

Modelling escaping atmospheres of highly irradiated exoplanets

Proefschrift

ter verkrijging van
de graad van doctor aan de Universiteit Leiden,
op gezag van waarnemend rector magnificus,
volgens besluit van het college voor promoties
te verdedigen op woensdag 25 februari 2026
klokke 10:00 uur

door

Andrew Patrick Allan

Promotores:

Prof.dr. A. A. Vidotto

Prof.dr. I.A.G. Snellen

Promotiecommissie:

Prof.dr. S. Viti

Prof.dr. M. Hogerheijde

Dr. Y. Miguel

Prof.dr. E. Gallo (University of Michigan)

Dr. L. Fossati (Space Research Institute, Austrian Academy of Sciences)

Cover designed by Andrew Allan.

The stellar background is an image of the Sun, modified for the purpose of this cover. The original¹ was a high-resolution composite of 200 individual images observed at 17.4 nm by the Solar Orbiter's Extreme Ultraviolet Imager (EUI) on March 9th 2025.

Credit for the original EUI composite: ESA & NASA/Solar Orbiter/EUI Team, E. Kraaikamp (Royal Observatory of Belgium).

Printed by: Proefschriften.nl

¹downloaded from here: https://www.esa.int/ESA_Multimedia/Images/2025/04/Solar_Orbiter_s_widest_high-res_view_of_the_Sun

CONTENTS

1	Introduction	1
1.1	Observing atmospheric escape	2
1.1.1	Inferring atmospheric escape from the demographics of exoplanets	2
1.1.2	Observing atmospheric escape through transmission spectroscopy	3
1.1.2.1	Hydrogen transmission spectroscopy	4
1.1.2.2	Helium transmission spectroscopy	6
1.2	Modelling atmospheric escape	9
1.2.1	The energy-limited approximation	9
1.2.2	Modelling atmospheric escape via fluid dynamics . . .	10
1.2.2.1	The isothermal Parker wind approximation .	11
1.2.2.2	Self-consistent atmospheric escape modelling	11
1.3	Modelling the observability of escaping atmospheres	12
1.4	Atmospheric escape with evolution	13
1.4.1	Evolution over the lifetime of a system	13
1.4.2	Evolution over shorter timescales: stellar activity cycles	13
1.5	Future Outlook	16
1.5.1	From an observational perspective	16
1.5.2	From a theoretical perspective	17
1.6	Outline of this thesis	18
2	Evolution of atmospheric escape in close-in giant planets and their associated Ly-α and H-α transit predictions	21
2.1	Introduction	22
2.2	Evolution of planetary radii and stellar EUV flux	23
2.3	Atmospheric escape and transit calculations	25
2.3.1	Hydrodynamic escape model	25
2.3.2	Comparison to energy-limited escape	30
2.3.3	Transit calculations	31
2.4	Evolution of atmospheric escape in close-in giants	33
2.4.1	Total mass lost during evolution	36
2.5	Spectroscopic transits in hydrogen lines	38
2.5.1	Ly α transits	38
2.5.2	H α transits	42
2.6	Discussion and conclusions	46

3	Evolution of helium triplet transits of close-in gas giants orbiting K-dwarfs	51
3.1	Introduction	52
3.2	Atmospheric escape model through photoionisation	54
3.2.1	Fluid dynamic equations	55
3.2.2	Calculating helium state populations	60
3.2.3	Photoionisation and heating processes with hydrogen and helium	63
3.2.4	Cooling processes with hydrogen and helium	65
3.2.5	Test case: solving helium populations in post-processing	66
3.3	Model inputs: evolution of high-energy stellar flux and planetary radii	68
3.4	The evolution of atmospheric escape	71
3.4.1	Effect of helium abundance on hydrodynamics	77
3.4.2	Effect of helium energetics on hydrodynamics	79
3.5	The observability of helium transits	80
3.5.1	The ray-tracing model for transmission spectroscopy	80
3.5.2	The evolution of helium 1083 nm transmission spectroscopy	81
3.5.3	Effect of helium abundance on 1083 nm observability	84
3.5.4	Effect of helium energetics on 1083 nm observability	87
3.6	Discussion and conclusions	87
3.6.1	Summary of main findings	87
3.6.2	Do we observe larger helium absorption at younger ages?	89
4	Helium escape signatures are generally strongest during younger ages but this age dependence is lost in the diversity of observed exoplanets	95
4.1	Introduction	96
4.2	Modelling approach	98
4.2.1	Sample of modelled systems	98
4.2.2	Determining the hydrodynamic atmospheric base	102
4.3	Results & discussion	105
4.3.1	General hydrodynamic predictions	105
4.3.2	He triplet transmission spectroscopy predictions	107
4.3.3	Relations with the helium triplet signature	112
4.4	Conclusions	117
5	The effects of stellar activity cycles on planetary atmospheric escape and the He I 1083 nm transit signature	125
5.1	Introduction	126
5.2	Stellar XUV activity cycles	128
5.2.1	The XUV cycle of the Sun	129

5.2.2	The XUV cycle of ι Hor	132
5.3	Modelling planetary atmospheric escape and the He I 1083 nm transit signature	133
5.4	Findings of our study	134
5.4.1	The effect of a solar-like activity cycle on the atmo- spheric escape of highly irradiated exoplanets	134
5.4.2	The effects of a solar-like activity cycle on the He I 1083 nm transit signature of highly irradiated exoplanets	135
5.4.3	Atmospheric escape with ι Hor as a stellar host	139
5.5	Discussion	144
5.5.1	A stellar XUV cycle can cause conflicting He I 1083 nm detections and non-detections of atmospheric escape	144
5.5.2	Comparing our model predictions to those in the lit- erature	145
5.6	Conclusions	146
	English summary	159
	Nederlandse samenvatting	161
	Publications	165
	Curriculum Vitae	167
	Acknowledgements	169

1 | INTRODUCTION

Since the first discovery of exoplanets orbiting solar-like stars (Mayor & Queloz 1995), almost 6000 exoplanets have been confirmed.¹ Due to observational biases in their detection techniques, the majority of these planets lie very close to their host stars, receiving an enhanced level of stellar radiation compared to planets in the solar system. These extreme systems can experience strong mass loss, through atmospheric escape. While there are a variety of processes by which a planet can lose its atmosphere, the thermal process of hydrodynamic escape is studied in this thesis. This atmospheric escape process is responsible for the most extreme rates of escape found for highly irradiated exoplanets. Depicted in Figure 1.1 below, hydrodynamic escape results from extreme ultraviolet (hereby EUV) radiation heating the upper planetary atmosphere. This high-energy radiation photoionises neutral hydrogen and to a lesser extent helium, in the planetary atmosphere, with any excess energy carried by the photon being converted into thermal energy via collisions of the ejected electron. This photoionisation heating drives a pressure gradient which results in the bulk outflow or escape of atmospheric material (Catling & Kasting 2017).

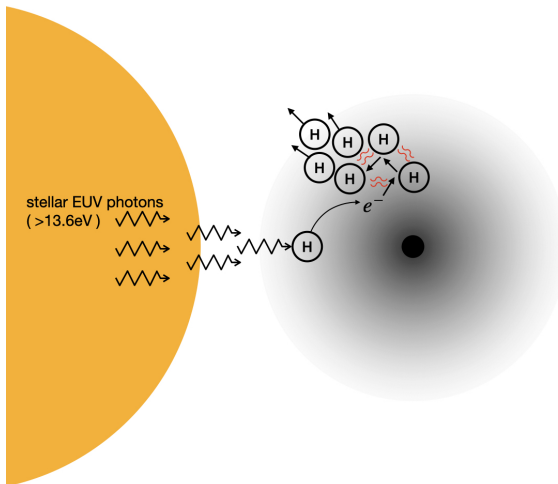


Figure 1.1: A sketch of the hydrodynamic escape of a planetary atmosphere. High-energy radiation from the star photoionises hydrogen in the upper-atmosphere of a close-orbiting gaseous exoplanet. Excess kinetic energy carried by the ejected electron is converted to thermal energy through various collisions.

¹5989 confirmed exoplanets as of August 28, 2025:
https://exoplanetarchive.ipac.caltech.edu/docs/counts_detail.html

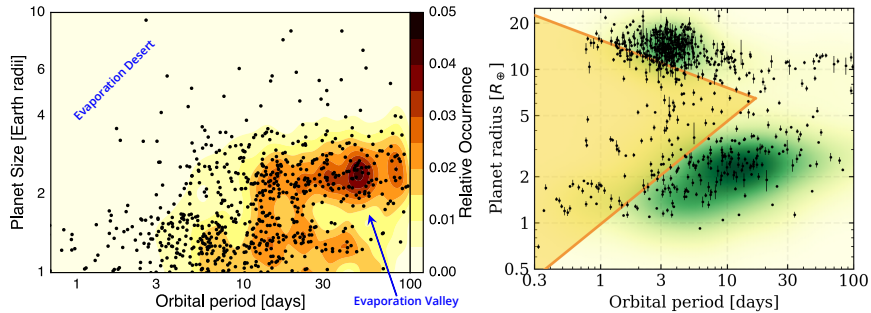


Figure 1.2: Left panel: The relative occurrence of planets observed by the California-Kepler-Survey, corrected for observational bias. The radius valley, or evaporation valley, is prominent in the lower right corner. Figure obtained from Owen (2019) and is a modified version of the original by Fulton et al. (2017). Right panel: The Neptunian desert (yellow triangle Mazeh et al. 2016) plotted over the population of confirmed exoplanets (as of May 3rd 2023, black markers) the population density of which is given by the colour gradient, with darker green corresponding to a higher density. The figure was obtained from Cloutier (2024) and is a modified version of the original by Osborn et al. (2023).

1.1 Observing atmospheric escape

1.1.1 Inferring atmospheric escape from the demographics of exoplanets

The importance of atmospheric escape is often discussed in the context of its potential role in shaping the demographics of the observed exoplanet population. Key to this discussion, are two observed phenomena, known as the radius valley² and the Neptunian desert³. Prior even to its confirmation by the California-Kepler-Survey (Fulton et al. 2017), the radius valley was predicted by atmospheric escape modelling (Owen & Wu 2013; Lopez & Fortney 2013). Displayed prominently in the left panel of Figure 1.2, it is a valley of low occurrence for 1.5-2 R_{\oplus} -sized planets orbiting close-in to their host star. Planets with radii placing them below the valley are thought to have been unable to retain their atmosphere during their early evolution when escape is strongest (see section 1.4.1), becoming stripped cores, while those above the valley are believed to still have their atmospheres (Owen & Wu 2017; Jin & Mordasini 2018; Rogers et al. 2021).

The Neptunian desert is better shown in the right panel of Figure 1.2. This desert is a significant dearth of Neptune-sized exoplanets orbiting close-

²aka the evaporation valley

³aka the sub-Jovian Desert

in to their host star. The paucity of planets in the Neptunian desert was first highlighted by cluster analysis of the known transiting exoplanets (Szabó & Kiss 2011), with the desert boundaries later being refined by Mazeh et al. (2016). Considering the high levels of XUV flux within the desert, various studies sought out explaining the observed feature with atmospheric escape (e.g. Kurokawa & Nakamoto 2014; Owen & Lai 2018; Ionov et al. 2018), finding that the lower edge of the desert could be produced by the loss of the atmosphere, similar to the radius valley. The origin of the desert’s upper edge however is less understood, with modelling by Kurokawa & Nakamoto (2014) being consistent with atmospheric escape, while Owen & Lai (2018); Ionov et al. (2018) later demonstrated a stability against catastrophic atmospheric loss for the larger planets of the deserts upper edge. Vissapragada et al. (2022) further supported this stability by observing planets near the deserts edge using the He I 1083 nm transit signature associated with atmospheric escape (described in section 1.1.2.2). The resulting atmospheric escape rate predictions were inconsistent with such planets catastrophically losing their atmosphere. A process other than, or perhaps in addition to, atmospheric escape is hence likely responsible for the upper edge of the Neptunian desert, such as the formation and/or migration of these larger gas giant planets (Bailey & Batygin 2018; Matsakos & Königl 2016).

1.1.2 Observing atmospheric escape through transmission spectroscopy

The transit method is currently the most popular method used to detect exoplanets, finding 4438 of the 5989 confirmed planets detected so far⁴. During planetary transit, the planet passes in front of the stellar disk, partially blocking some of the stellar irradiation which otherwise would reach an observer. By observing a planetary transit with a spectrograph covering a wavelength range, we can detect absorptions specific to these wavelengths by material in the obscuring planetary atmosphere. This is the process of transmission spectroscopy, so-called due to the partial *transmission* of the stellar flux through the transiting planetary atmosphere at different wavelengths. Transmission spectroscopy is currently the main method used to observe escaping planetary atmospheres (Dos Santos 2023). The two subsequent subsections describe how this technique has been used to detect escaping hydrogen and helium from exoplanetary atmospheres. While not modelled in the works of this thesis, transmission spectroscopy has also allowed for detections of heavier elements in escaping atmospheres, such as C, O, Na, Mg and Fe (Vidal-Madjar et al. 2004; Fossati et al. 2010; Cubillos et al. 2020; Sreejith et al. 2023).

⁴as of August 28, 2025:

https://exoplanetarchive.ipac.caltech.edu/docs/counts_detail.html

1.1.2.1 Hydrogen transmission spectroscopy

Hydrogen is the most abundant element in the atmospheres of gas-giant exoplanets. It is also the lightest, rendering it particularly susceptible to atmospheric escape. Accordingly, searching for escaping atmospheres by using hydrogen transit features is a wise approach. On this endeavour, the hydrogen Lyman- α (hereby Ly- α) line centred on 1215.67 Å (in vacuum) has been highly successful, detecting atmospheres escaping from hot-Jupiters (Vidal-Madjar et al. 2003; Lecavelier Des Etangs et al. 2010) and warm-Neptunes (Kulow et al. 2014; Ehrenreich et al. 2015).

Figure 1.3 showcases the process of transmission spectroscopy via the hydrogen Ly- α line over different phases in the transit of a planet and its escaping atmosphere. During the transit, neutral hydrogen in its ground state within the obscuring atmosphere absorbs stellar Ly- α photons, resulting in a net reduction of the observed Ly- α flux. The core of the Ly- α line profile (shaded in blue) is unfortunately unusable to atmospheric studies on account of significant absorption by the Interstellar Medium (ISM) and contamination by Earth’s geocorona at these lower velocities (Wood et al. 2005). As Ly- α is also significantly absorbed by Earth’s atmosphere, Ly- α atmospheric escape detections are also limited to space-based observations, with the oversubscribed Hubble Space Telescope currently being the only option (Dos Santos 2023). A famous Ly- α detection of atmospheric escape, that of the warm-Neptune GJ 436b (Ehrenreich et al. 2015), is shown in Figure 1.4. This detection features strong absorption in the blue wing of the Ly- α profile both in-transit and post-transit. From the significant post-transit absorption the authors inferred the presence of a comet-like tail of escaping hydrogen akin to that of the schematic in Figure 1.3 (see also the modelling of Bourrier et al. 2016).

There has also been some success observing atmospheric escaping via another hydrogen feature, the H- α line at 6562.79 Å which traces neutral hydrogen in its first excited state (Yan & Henning 2018; Wyttenbach et al. 2020; Czesla et al. 2022; Orell-Miquel et al. 2024). Due to its wavelength in the optical, H- α observations can be made from the ground using various high-resolution facilities, such as ESPRESSO⁵ in Chile (Pepe et al. 2021). Its wavelength also means that the H- α line core is accessible, enabling the probing of slower moving atmospheric material deeper in the outflowing planetary atmosphere that is inaccessible by Ly- α transmission spectroscopy. H- α transit signatures do however suffer significant contamination by stellar H- α variability (Cauley et al. 2017). The typical depths of H- α transit absorptions are also considerably shallower than that of Ly- α absorptions due to a higher abundance of atmospheric hydrogen in its ground state than its first excited state. Tracing hydrogen’s first excited

⁵Echelle SPectrograph for Rocky Exoplanets and Stable Spectroscopic Observations spectrograph (ESPRESSO) at ESO’s Very Large Telescope.

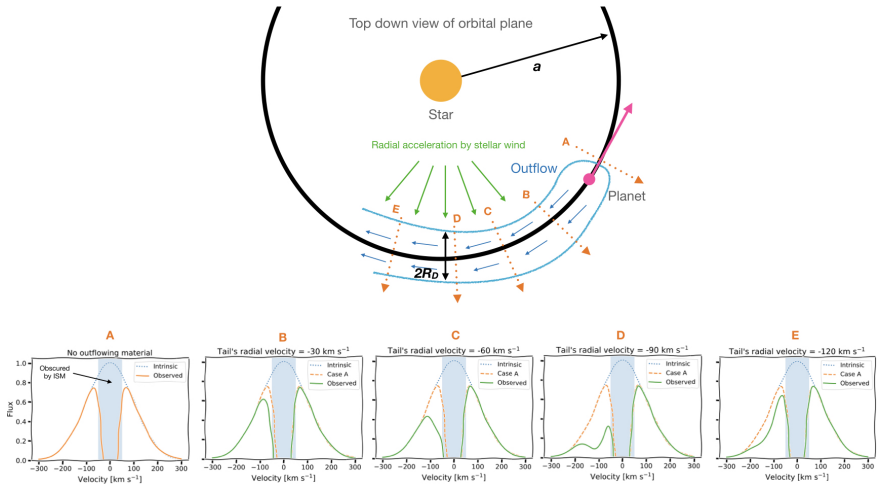


Figure 1.3: Schematic of the Ly- α transit of an exoplanet and its escaping atmosphere (Owen et al. 2023, slightly modified). Panel A shows the received flux centred on the Ly- α wavelength prior to obscuration by atmospheric material. The subsequent panels exhibit absorption in the blue wing of the Ly α transit signature. The shaded blue rectangles mark the wavelength regions contaminated by ISM absorption.

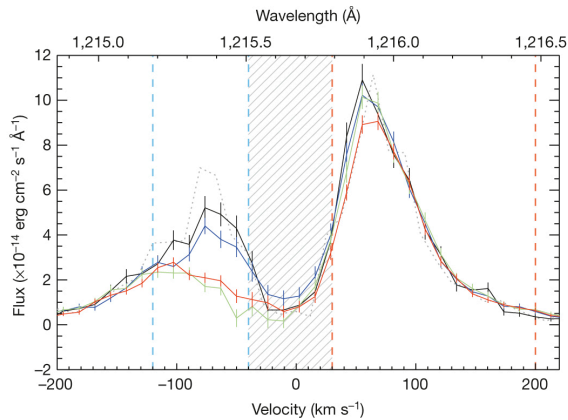


Figure 1.4: The hydrogen Ly- α signature of GJ 436b (Ehrenreich et al. 2015) averaged over an out-of-transit phase (black), pre-transit phase (blue), in-transit phase (green) and post-transit phase (red). The hatched region is inaccessible due to absorption by the ISM.

state also restricts H- α atmospheric escape detections to the hottest exoplanets, with many of the current detections being of ultra-hot-Jupiters (e.g., [Bello-Arufe et al. 2022](#); [Zhang et al. 2022d](#)).

1.1.2.2 Helium transmission spectroscopy

Currently, the most popular method of detecting atmospheric escape is transmission spectroscopy using the helium triplet signature at 1083 nm, hereby He I 1083 nm ([Spake et al. 2018](#); [Nortmann et al. 2018](#); [Allart et al. 2018, 2023](#); [Orell-Miquel et al. 2024](#)). This signature is comprised of three individual lines, with line-centre wavelengths in air of 1082.909, 1083.025, 1083.034 nm. It is produced by transitions from the 2^3S to the 2^3P state of neutral helium. He I 1083 nm detections of atmospheric escape are possible because the important 2^3S state is metastable, with radiative decays down to the ground 1^1S state suppressed with a lifetime of 2.2 hours ([Drake 1971](#)). The success of the He I 1083 nm signature at detecting atmospheric escape is due largely to its near-infrared (nIR) wavelength. This allows it to be observed using numerous high-resolution ground based telescopes, such as those listed in [Table 1.1](#). Lower-resolution narrowband photometric telescopes ([Vissapragada et al. 2020](#)) and space-based telescopes ([Spake et al. 2018](#)) can also be used to observe this signature of atmospheric escape. Another advantage over hydrogen's Ly- α signature is that the core of the He I 1083 nm signature is relatively unaffected by ISM absorption ([Indriolo et al. 2009](#)), as shown by the transmission spectrum of WASP-107b ([Kirk et al. 2020](#)), displayed in [Figure 1.5](#). Hence, slower escaping material deeper in the atmospheric outflow can be probed with the helium signature, rather than just the fast moving material traced by the line wings. The negligible ISM absorption also allows for He I 1083 nm atmospheric escape detections of more distant exoplanets, beyond that of the Ly- α signature, which is likely completely absorbed by the ISM for F, G and K-type stars beyond 60 pc ([Dos Santos 2023](#)).

[Figure 1.6](#) displays many of the He I 1083 nm confirmed detections (blue) and non-detections (red). Detections evidently have been made for various types of highly irradiated exoplanets, from larger hot-Jupiters (e.g, HD209458b [Alonso-Floriano et al. 2019](#)) to mini-Neptunes (e.g, TOI-560b [Zhang et al. 2022a](#)). However, with the majority being non-detections, it is also clear that predicting suitable candidates for He I 1083 nm detections is not straightforward. One complication is that the signature is not only dependent on the escaping atmosphere itself, but also on the intensity and spectral shape of the received stellar irradiation ([Oklopčič 2019](#)). In exoplanetary atmospheres, He I(2^3S) is populated predominantly by recombination from He $^+$. This introduces a He I(2^3S) population dependence on the level of EUV radiation received, with the ground state He I(1^1S) having a threshold ionisation wavelength of 504 Å. However, the received EUV

Table 1.1: High-resolution ground-based instruments used to search for escaping exoplanet atmospheres via He I 1083 nm transmission spectroscopy. \mathcal{R} refers to the instruments maximum resolving power in the near-IR wavelength range of the helium signature. The diameter is that of the primary mirror of the telescope.

name	\mathcal{R}	diameter	location
CARMENES ^a	80,400	3.5 m	Almería, Spain
GIARPS/TNG ^b	50,000 in nIR	3.58 m	La Palma, Spain
CRIRES+/VLT ^c	92,000	8.2 m	Atacama Desert, Chile
NIRPS/ESO 3.6m ^d	90,000	3.6 m	Atacama Desert, Chile
SPIRou/CFHT ^e	70,000	3.6 m	Maunakea, Hawaii
NIRSPEC/Keck ^f	25,000	10 m	Maunakea, Hawaii
IRD/Subaru ^g	70,000	8.2 m	Maunakea, Hawaii
HPF/HET ^h	55,000	10 m	Texas, US

^aCalar Alto high-Resolution search for M dwarfs with Exo-earths with Near-infrared and optical Echelle Spectrograph (Quirrenbach et al. 2014)

^bGIANO-B (nIR) + HARPS-N (visible) spectrographs of the Telescopio Nazionale Galileo (Claudi et al. 2016)

^cCryogenic high-resolution InfraRed Echelle Spectrograph+ of the Very Large Telescope (Dorn et al. 2023)

^dNear-InfraRed Planet Searcher of the European Southern Observatory 3.6m telescope (Bouchy et al. 2025)

^eSpectromètre InfraROUge of Canada France Hawaii Telescope (Donati et al. 2020)

^fNear Infrared Echelle Spectrograph (McLean et al. 1998; Martin et al. 2018)

^gInfraRed Doppler of the Subaru Telescope (Kotani et al. 2018)

^hHabitable-zone Planet Finder Spectrograph of the Hobby-Eberly Telescope (Mahadevan et al. 2012a)

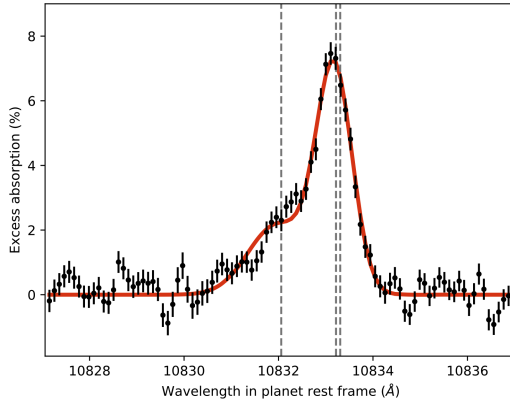


Figure 1.5: He I 1083 nm transmission spectrum of WASP-107b (black points) in terms of excess absorption relative to out-of-transit observations, made with NIRSPEC/KECK (Kirk et al. 2020). The three vertical dashed lines correspond to the lines of the helium triplet. The red line is the authors' fit to the data.

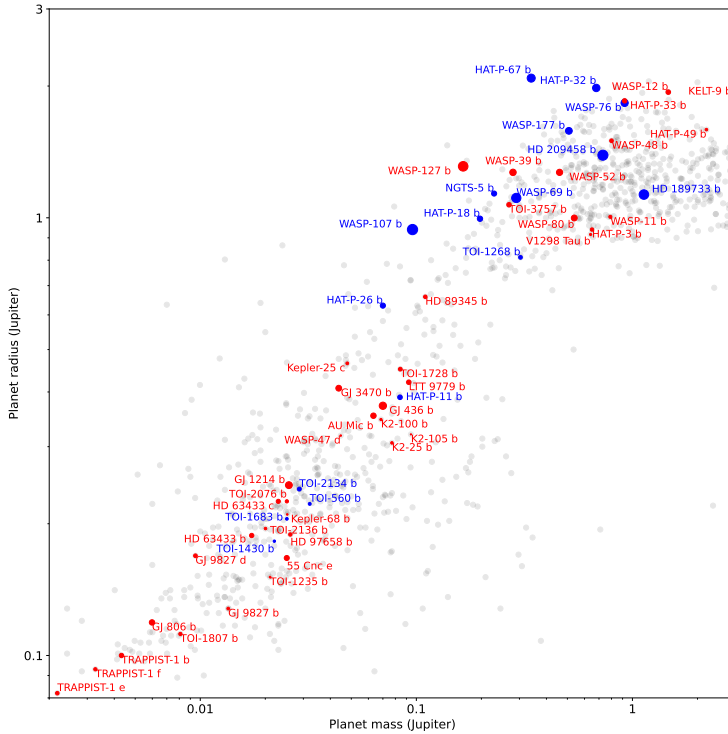


Figure 1.6: Planetary mass-radius diagram showing 17 He I 1083 nm detections in blue and 40 non-detections in red, superimposed over the population of confirmed planets in grey (Krishnamurthy & Cowan 2024). The symbol size reflects each planet’s Transmission Spectroscopy Metric (TSM Kempton et al. 2018).

flux, to which the physical process of atmospheric escape is highly sensitive in addition to the population of atmospheric He I(2^3S), is often poorly constrained. This is the result of ISM absorption limiting EUV observations to only nearby stars within a few tens of parsecs (Craig et al. 1997), with the EUV flux of more distant stars being inferred using easier to observe properties such as the X-ray flux (Sanz-Forcada et al. 2011). With a threshold ionisation wavelength of 2600 Å, the He I(2^3S) population is also dependent on the received flux of mid-UV photons. Hence, Oklopčić (2019) predicted that He I 1083 nm observations may have a preference for K-type host stars due to their favourable combination of relatively low mid-UV and high EUV flux. This K-type host favourability indeed remains apparent in the growing population of He I 1083 nm observations (Krishnamurthy & Cowan 2024). Another complication with He I 1083 nm transmission spectroscopy is in disentangling transit signature contributions by the escaping atmosphere from stellar He I(2^3S) variations, as will be explored in Chapter 5.

1.2 Modelling atmospheric escape

There are various approaches that can be taken to model the atmospheric escape of highly irradiated exoplanets in the hydrodynamic regime.

1.2.1 The energy-limited approximation

The most simplistic approach is to adopt the energy-limited approximation for the atmospheric mass-loss rate (Watson et al. 1981). In this approximation, some fraction ϵ of the EUV flux (F_{EUV}) intercepted by the planetary atmosphere is assumed to be converted into kinetic energy (see section 2.3.2 later for the derivation). The mass-loss rate of the escaping planetary atmosphere can then be approximated as:

$$\dot{M}_{\text{E-limited}} = \epsilon \frac{F_{\text{EUV}}(\pi R_{\tau=1}^2)}{KGM_{\text{pl}}/R_{\text{pl}}}. \quad (1.1)$$

where $R_{\tau=1}$ is the distance where optical depth unity to ionising photons is reached, K is a correction factor to account for stellar tidal forces (Erkaev et al. 2007, , eq. 2.9 later), G is the gravitational constant, M_{pl} and R_{pl} are the planetary mass and radius. Given its simplicity, this approach is popular with large population studies of atmospheric escape (Chen & Rogers 2016; Owen & Wu 2017). However, the energy-limited approximation can also be a poor indicator of the mass-loss rate obtained by more sophisticated atmospheric escape modelling (Salz et al. 2016a; Kubyshkina et al. 2018), such as those described in the next section.

1.2.2 Modelling atmospheric escape via fluid dynamics

As the name suggests, the motion of a hydrodynamically escaping exoplanetary atmosphere behaves as a fluid. Hence, it can be described by the equations of fluid dynamics. However, a requirement for hydrodynamic escape to occur is that the atmosphere be ‘collisional’. This is verified with a Knudsen number $K_n = \lambda_{\text{mfp}}/h \ll 1$, where λ_{mfp} and h are the mean free path of an atmospheric particle and the atmospheric scale height, respectively. The equations of fluid dynamics are coupled differential equations stating that momentum, energy and mass are conserved (presented in section 2.3.1). There are various mathematical solutions to these coupled differential equations, but only one which has physical significance for an escaping planetary atmosphere. In order to best illustrate this one critical solution, the equation for the conservation of momentum:

$$u \frac{du}{dr} = -\frac{1}{\rho} \frac{dP}{dr} - \frac{GM_{\text{pl}}}{r^2} + \frac{3GM_* r}{a^3}, \quad (1.2)$$

is rearranged to the equivalent form of eq. 1.7. Above, u , r , ρ and P refer to the atmospheric profiles of velocity, distance, density and thermal pressure, a is the orbital distance, and M_* is the stellar mass. While the required intermediary algebraic steps are omitted for the sake of brevity, the key steps can be summarised as follows:

- Obtaining $\frac{dP}{dr}$ from the ideal gas law using the product rule,

$$\frac{dP}{dr} = \frac{k_B}{m} \left(T \frac{d\rho}{dr} + \rho \frac{dT}{dr} \right), \quad (1.3)$$

where T is the atmospheric temperature profile.

- Rearranging the conservation of energy (eq. 2.2 later) for $\rho \frac{dT}{dr}$, substituting this into eq. 1.3 above, and recalling that the sonic velocity is $c_s = \sqrt{\frac{\gamma k_B T}{m}}$, with $\gamma = 5/3$ being the ratio of specific heats for a monatomic ideal gas and k_B the Boltzmann constant,

$$\frac{dP}{dr} = c_s^2 \frac{d\rho}{dr} + \frac{(\gamma - 1)}{u} (Q - C), \quad (1.4)$$

where Q and C are atmospheric heating and cooling terms.

- Substituting $\frac{dP}{dr}$ (eq. 1.4) into the momentum equation (eq. 1.2):

$$u \frac{du}{dr} = -\frac{c_s^2}{\rho} \frac{d\rho}{dr} - \frac{(\gamma - 1)}{\rho u k_B} (Q - C) - \frac{GM_{\text{pl}}}{r^2} + \frac{3GM_* r}{a^3}. \quad (1.5)$$

- Obtaining $\frac{1}{\rho} \frac{d\rho}{dr}$ from mass continuity (eq. 2.4 later):

$$\frac{1}{\rho} \frac{d\rho}{dr} = -\frac{2}{r} - \frac{1}{u} \frac{du}{dr}. \quad (1.6)$$

- Substituting $\frac{1}{\rho} \frac{d\rho}{dr}$ above into eq. 1.5 and solving for $\frac{du}{dr}$ to reach the rearranged but equivalent form of the momentum equation:

$$\frac{du}{dr} = u \left(\frac{2c_s^2}{r} - \frac{(\gamma - 1)}{\rho u k_B} (Q - C) - \frac{GM_{\text{pl}}}{r^2} + \frac{3GM_* r}{a^3} \right) / (u^2 - c_s^2). \quad (1.7)$$

As mentioned, there are numerous mathematical solutions to eq. 1.7. However, key to atmospheric escape modelling, there is only one ‘critical solution’ which begins at a sub-sonic initial velocity and accelerates to supersonic velocities at larger distances (Parker 1958). In other words, at some critical atmospheric distance, the numerator on the right-hand side of eq. 1.7 sums to 0, when the sum of forces balance. In order for the acceleration to remain positive throughout the atmospheric outflow, the denominator must also equal 0, therefore $u = c_s$ at this critical point.

1.2.2.1 The isothermal Parker wind approximation

A common approach for solving the fluid dynamic equations is to use the isothermal Parker wind approximation (Parker 1958). This greatly simplifies the energy conservation equation by assuming an energy balance that results in a constant atmospheric temperature profile, rather than a more physically-informed balance of various heating and cooling processes. An isothermal Parker wind solution has been assumed in various modelling studies of atmospheric escape (Oklopčić & Hirata 2018; Lampón et al. 2020) and has become popular amongst observational He I 1083 nm studies (Kirk et al. 2022; Allart et al. 2023) given the usability of the publicly available atmospheric escape code P-WINDS (Dos Santos et al. 2022). The isothermal Parker wind approximation does however result in a degeneracy in the atmospheric mass-loss rate and temperature. As demonstrated by Linssen et al. (2022), it is possible to partially break this degeneracy by cross-validating the assumed temperature with the temperature profile obtained using a separate photoionization code (such as CLOUDY, Ferland et al. 1998, 2017).

1.2.2.2 Self-consistent atmospheric escape modelling

The equations of fluid dynamics can also be solved self-consistently using numerical modelling (Murray-Clay et al. 2009; Salz et al. 2015; Caldiroli et al. 2021; Allan et al. 2024). This approach allows various atmospheric heating and cooling processes to affect the atmospheric escape predictions

via the energy conservation equation (eq. 2.2). 1-D self-consistent atmospheric escape modelling has been used to interpret atmospheric escape from He I 1083 nm transit signatures (e.g., Alam et al. 2024; D’Arpa et al. 2024). The 1-D modelling approach is better suited to He I 1083 nm observations than hydrogen Ly- α observations, with the latter tracing atmospheric material at greater heights, where 3-D physical effects such as interaction with the stellar wind (Carolan et al. 2021a) can have a greater influence. That said, 3-D effects do still impact the He I 1083 nm transit signatures, however, they are often omitted from atmospheric modelling on account of the required computational complexity, as discussed further in section 1.5.

In obtaining the results of the coming chapters, we performed 1-D atmospheric escape modelling, self-consistently solving the energetics of hydrogen (chapter 2) as well as helium (chapters 3 – 5). As will later be explained, our model achieves this through solving the fluid dynamics equations numerically, iterating through different initial velocities u_0 at the base of the modelled atmosphere until the solution passes through the mentioned critical point of eq. 1.7.

1.3 Modelling the observability of escaping atmospheres

In order to predict a transit signature of an escaping exoplanetary atmosphere, the population of atmospheric material in the state relevant to the specific observation must first be determined. This refers to helium in the 2^3S state for the He I 1083 nm transit signature, and the ground and first excited states of hydrogen for Ly- α and H- α signatures, respectively. On account of hydrogen’s dominant contribution to atmospheric heating, the population of neutral hydrogen is often determined self-consistently along with the equations of fluid dynamic via the inclusion of an additional equation concerning the balance of hydrogen ionisation (eq. 2.3). Determining the He I (2^3S) population on the other hand is more complex. As shown later by the schematic of Figure 3.1, the populations of helium in the considered 1^1S , 2^1S , 2^3S , singly ionised and doubly ionised states are affected by numerous processes including photoionisation, collisional ionisation, recombination, collisional excitation, radiative decays and charge exchange. The dominant processes regarding the observationally important 2^3S state are population via recombination from He⁺ and depopulation by both photoionisation and collisional excitation (Oklopčić 2019). The He I (2^3S) population can either be solved in post-processing (Oklopčić & Hirata 2018; Lampón et al. 2020; MacLeod & Oklopčić 2022; Dos Santos et al. 2022) or self-consistently with the dynamics of atmospheric escape (Shaikhislamov et al. 2021; Wang & Dai 2021a; Biassoni et al. 2024). In our modelling, we

take the self-consistent approach (Allan et al. 2024), allowing for processes involving helium to influence the energetics of atmospheric escape.

Once the population of the observationally relevant state has been determined, the next step is to simulate this material obscuring the stellar disk in a planetary transit. This is achieved via ray-tracing modelling, in which the level of irradiation absorbed by the obscuring atmospheric material is calculated. Our similar ray-tracing methodologies for predicting hydrogen and helium transit signatures are detailed in sections 2.3.3 and 3.5.1, respectively.

1.4 Atmospheric escape with evolution

1.4.1 Evolution over the lifetime of a system

As a star ages, it ‘spins-down’; its rotation slows due to the loss of angular momentum through its stellar wind (Skumanich 1972). The upper-panel of Figure 1.7 shows this spin-down for a $0.75 M_{\odot}$ star, according to a rotational evolution model constrained by observed rotation distributions of stellar clusters (Johnstone et al. 2021). This spin-down is shown for an initially fast (blue), medium (green) or slow (red) rotating star, with the rotation rate converging to similar values beyond a few Gyr. As seen in the lower panel, the stellar spin-down leads to a declining X-ray and EUV emission with evolution. This declining high-energy stellar flux contributes to weaker atmospheric escape at older system ages due to a reduction in atmospheric heating (Tu et al. 2015; Johnstone et al. 2015b).

Also affecting the evolution of atmospheric escape, the planetary radius shrinks as the planet cools down with time (Fortney & Nettelmann 2010; Kubyshkina et al. 2020). This shrinking has a twofold effect on reducing the atmospheric escape with evolution. Firstly, it causes larger gravitational potentials, enhancing the planet’s ability to retain its atmosphere. Secondly, it reduces the collecting area for potential XUV photoionisations, further reducing atmospheric heating with evolution. The combined effect of the spin-down of the host star and the shrinking of the planetary radius hence leads to stronger rates of atmospheric escape when a planet is younger. The associated hydrogen and helium transit absorptions are consequently deeper when a planet is younger, as will be later shown in Chapters 2 and 3.

1.4.2 Evolution over shorter timescales: stellar activity cycles

In addition to changes in the high-energy radiation over the long-term (Gyr scale) evolution of stars, shorter timescale processes can also affect the high-energy radiation. The Sun, for example, exhibits a cycle in which its ac-

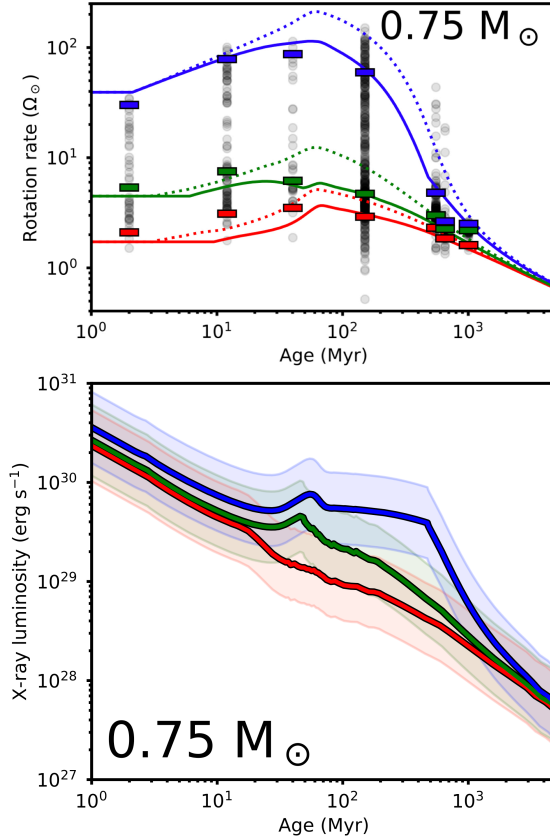


Figure 1.7: The predicted spin-down (upper-panel) and X-ray luminosity evolution (lower-panel) of a $0.75 M_{\odot}$ star, based on a rotational evolution model constrained by observed rotational distributions of stellar clusters (Johnstone et al. 2021). The red, green and blue profiles indicate initially slow, medium and fast rotating stars. In the upper panel, solid and dotted lines display envelope and core rotation rate, respectively. The grey circles show observed rotation rates while the rectangles show the 5th, 50th, and 95th percentiles. In the lower panel, the respective shaded areas show one standard deviation of the spread around the displayed best-fit relation.

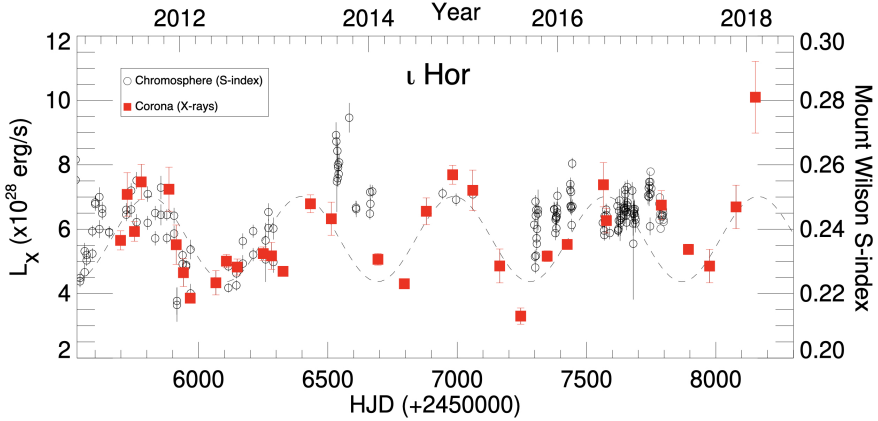


Figure 1.8: The activity cycle of ι Hor, as shown by its X-ray luminosity in red and its S-index in grey (Sanz-Forcada et al. 2013, 2019, figure is from the latter). The S-index data (Metcalf et al. 2010) are a measure of the emission of the Ca II H&K lines, relative to nearby spectral continuum regions (Wilson 1968).

tivity rises and falls, with a period of approximately 11 years. This cyclic behaviour is apparent in various forms of stellar activity such as the size and number of its sunspots (Schwabe 1844), the associated magnetic field strength (Hale et al. 1919) and the emitted flux across various wavelengths (Yeo et al. 2014). On the latter, satellite missions such as NASA’s Solar Radiation and Climate Experiment (SORCE, Woods et al. 2021), have captured the activity cycle of the Sun at EUV wavelengths.

Activity cycles have also been detected in stars beyond the Sun (for a recent review, see Jeffers et al. 2023). Long-term monitoring programs such as that of the Mount Wilson observatory (Wilson 1978; Baliunas et al. 1995) have detected activity cycles in over 1000 stars via the chromospheric Ca II H&K lines at visible wavelengths. Boro Saikia et al. (2018) created a catalogue of 4454 cool stars exhibiting cyclic activity behaviour, combining data from various surveys. While most stellar cycles have been found with the Ca II H&K lines, a handful of stars have had their activity cycles detected at X-ray wavelengths (Wargelin et al. 2024). Figure 1.8 displays the activity cycle of ι Hor. The cycle is seen in its S-index (Metcalf et al. 2010), a traditional activity tracer relating to the Ca II H&K lines, as well as its X-ray luminosity (Sanz-Forcada et al. 2013, 2019). The star ι Hor is a young (~ 600 Myr Sanz-Forcada et al. 2013, and references therein) solar analogue with spectral type \sim F8V/G0V (Vauclair et al. 2008). Compared to the Sun’s 11 year activity cycle, its displayed ~ 1.6 year cycle is notably shorter and the amplitude of its variations are also weaker.

Stellar activity cycles are capable of influencing the atmospheric escape

of highly irradiated exoplanets and their associated transit signatures. Large amplitude flux variations at EUV wavelengths, shown later in Figure 5.7, are highly relevant in this regard, considering the high sensitivity of atmospheric escape to the EUV flux. Hazra et al. (2020) utilised solar EUV observations as input to their atmospheric escape modelling. From this, they demonstrated that the atmospheric escape and the associated hydrogen H- α transit signature of a hot-Jupiter exoplanet varies substantially with the phase of the stellar activity cycle, with the rate of escape and H- α signature being stronger when closer to a maximum activity phase. In their recent modelling, Taylor et al. (2025) similarly demonstrated a sensitivity of the He I 1083 nm signature of the hot-Jupiter HD209458b to a Sun-like activity cycle. Chapter 5 later explores the influence of stellar cycles on the atmospheric escape and He I 1083 nm signature of four classifications of exoplanets, at two close-in orbital distances.

1.5 Future Outlook

Going forward, both observational and theoretical advancements will enhance our current understanding of the atmospheric escape of highly irradiated exoplanets.

1.5.1 From an observational perspective

From an observational perspective, we will benefit from new observing facilities such as the concept instrument LUMOS (LUVOIR⁶ Ultraviolet Multi-Object Spectrograph France et al. 2017), proposed for NASA’s next-generation Habitable Worlds Observatory. An instrument like LUMOS would be capable of detecting atmospheric escape via UV transmission spectroscopy of the hydrogen Ly- α line as well as various metal lines (Dos Santos et al. 2025). Towards higher wavelengths, the high-resolution ($\mathcal{R}=100,000$) spectrograph ANDES (ArmazoNes high Dispersion Echelle Spectrograph, Marconi et al. 2024), a second generation instrument planned for ESO’s future Extremely Large Telescope, would be capable of detecting atmospheric escape via He I 1083 nm and hydrogen H- α transmission spectroscopy (Palle et al. 2025). With the large 39-m diameter of the ELT’s primary mirror, ANDES could advance the observing capabilities of the current high-resolution nIR ground-based facilities (see table 1.1) towards detecting fainter escaping He I 1083 nm signatures. The future NIGHT (Near-Infrared Gatherer of Helium Transits Farret Jentink et al. 2024b) high-resolution spectrograph will be dedicated specifically to surveying and temporally monitoring

⁶The Large UV Optical IR Surveyor (LUVOIR) concept has since merged into the Habitable Worlds Observatory.

He I 1083 nm in stellar and planetary atmospheres. It will be capable of detecting 1% absorptions of 118 known exoplanets in a single transit (Farret Jentink et al. 2024a).

Observing atmospheric escape simultaneously with numerous tracers will also push our understanding further. This has already been demonstrated by the GIARPS observing mode of the TNG (Claudi et al. 2017), which combines high-resolution nIR and visible observations from the GIANO-B and HARPS-N spectrographs, respectively. This combined spectral coverage of the He I 1083 nm and hydrogen H- α transit signatures is particularly useful for constraining the level of stellar activity contamination (Guilluy et al. 2020, 2024). Going forward, re-observing the current population of He I 1083 nm observed planets (including non-detections) with a simultaneous H- α observation would allow us to better understand the impact of stellar activity. Combining more signatures of atmospheric escape, for example metal lines that have already been detected in some exoplanets (Vidal-Madjar et al. 2004; Fossati et al. 2010), as well as potentially new lines such as those identified by the modelling of Linszen & Oklopčić (2023), would further aid detections of atmospheric escape. By simultaneously observing various signatures arising from different regions of the escaping atmosphere, we would obtain a better picture of its physical properties.

In addition to advancements in observing the signatures of escaping atmospheres, placing tighter constraints on the EUV flux received by planetary atmospheres would also significantly improve our ability to infer properties of their escape. On this, future missions such as NASA's planned cubesat mission MANTIS⁷ (Monitoring Activity from Nearby sTars with UV Imaging and Spectroscopy, Indahl & Wilson 2022) will move us towards a better understanding of the EUV environments of escaping planetary atmospheres.

1.5.2 From a theoretical perspective

On the theoretical front of exoplanetary atmospheric escape, there is also ample room for advancements. Models incorporating the He I 1083 nm transit signature are particularly suitable for further study, given their relative novelty and the rapid observational growth. Towards this end, there has been a recent push towards revising the commonly adopted network of processes relevant to populating the metastable 2^3S state. For example, García Muñoz (2025) updated the rate coefficient for the Penning ionisation of H with He I(2^3S) and highlighted additional processes involving H₂, some molecular ions and photoelectrons. Taylor et al. (2025) reassessed various excitation and de-excitation rates and also demonstrated a He I 1083 nm sensitivity to the diffusive separation of helium. The latter finding strength-

⁷mission website: <https://lasp.colorado.edu/missions/mantis/>

ens the known sensitivity to helium fractionation (Xing et al. 2023; Schulik & Owen 2025). However, accounting for helium fractionation rather than assuming a constant He/H atmospheric fraction, requires computationally expensive multi-fluid modelling. Other relevant but often omitted physical processes include the interaction between the escaping atmosphere and the stellar wind (MacLeod & Oklopčić 2022), the interaction with a planetary magnetic field (Khodachenko et al. 2021b; Schreyer et al. 2024) and day-to-night-side variations (Nail et al. 2024). Being 3-D by nature, modelling these three mentioned processes also requires considerable computational expense. Accordingly, they have mostly been studied in isolation, neglecting other processes known to be relevant to the escape and He I 1083 nm signature. Furthermore, they have been studied for only a handful of chosen exoplanets. Going forward, it will be necessary to better account for such processes in theoretical modelling. Knowledge regarding how they act in combination with other relevant processes and how their behaviour depends on the diverse environments of planets with detected escape, are worth exploring further. Answering such questions will first be necessary before we can fully avail of the atmospheric escape information contained within the fast-growing collection of He I 1083 nm transit observations.

1.6 Outline of this thesis

This thesis presents a study into the atmospheric escape of highly irradiated exoplanets and their associated hydrogen and helium transit signatures, using 1-D, self-consistent, hydrodynamic modelling.

Chapter 2: Evolution of atmospheric escape in close-in giant planets and their associated Ly- α and H- α transit predictions

In this first study, published in Allan & Vidotto (2019), we assumed a purely hydrogen composition for our modelled escaping atmospheres. Self-consistently solving the equations of fluid dynamics, we predicted the atmospheric escape over the evolution of two highly irradiated gas-giants, with masses of 0.3 and $1M_{\text{Jup}}$. The atmospheric escape was shown to be strongest while the planets were youngest, on account of receiving a higher flux of XUV irradiation as well as their more inflated planetary radii. The associated hydrogen Ly- α and H- α transit signatures were also shown to be stronger at younger ages, with more atmospheric material obscuring the stellar disk during planetary transit.

Chapter 3: Evolution of helium triplet transits of close-in gas giants orbiting K-dwarfs

In the next study, published in [Allan et al. \(2024\)](#), we expanded our evolutionary study of atmospheric escape so as to also include the He I 1083 nm transit feature, currently the most popular signature of escaping exoplanetary atmospheres. The simulation of this helium signature required significant upgrades to our previous modelling approach, such as the transitions between the helium 1^1S , 2^1S , 2^3S , singly and doubly ionised states, as well as their contributions to atmospheric heating and cooling. Taking inspiration from the sample of observations, we modelled the evolution of atmospheric escape of a highly irradiated $0.3 M_{\text{Jup}}$ gas giant orbiting a K-dwarf star. On account of the various possible photoionisations, we upgraded our previously monochromatic stellar flux implementation to now consider separate X-ray, hard and soft extreme-ultraviolet (UV), and mid-UV fluxes. Our upgraded model self-consistently solved the hydrodynamic escape and the population of the observationally important He I (2^3S) state. As with the hydrogen signatures of the previous study, the He I 1083 nm transit absorptions were shown to be strongest at younger planetary ages, due to higher rates of atmospheric escape.

Chapter 4: Helium escape signatures are generally strongest during younger ages but this age dependence is lost in the diversity of observed exoplanets

Having established that atmospheric escape and the associated He I 1083 nm signature are stronger when a planet is younger, we then modelled the escape and He I 1083 nm signatures of 12 young (<1 Gyr) exoplanets which already had attempted He I 1083 nm transmission spectroscopy. This was in part to understand why several of the young planets that had been observed had yielded weak or non-detections in their He I 1083 nm transit absorptions. The resulting He I 1083 nm model predictions aligned relatively well with the observations. We concluded that for any given planet, stronger atmospheric escape during younger ages produces deeper He I 1083 nm absorption, as demonstrated in Chapter 3. However, for a population of exoplanets, the relation between younger ages and stronger He I 1083 nm absorptions is lost to the broad diversity of their various other system parameters. We noted agreement with our model predictions and the empirical trend noted in the literature between $EW \cdot R_*^2$ and $F_{\text{xuv}} \cdot R_{\text{pl}}^2 / \Phi_g$. We also further refined our model of atmospheric escape, highlighting that coupling between the lower and upper atmospheres is necessary for a robust prediction of the He I 1083 nm signature. This work was published in [Allan & Vidotto \(2025\)](#).

Chapter 5: The effects of stellar activity cycles on planetary atmospheric escape and the He I 1083 nm transit signature

This final chapter describes our study into the effects that a stellar activity cycle has on the planetary atmospheric escape and the He I 1083 nm transit signature (Allan et al. 2025, now in press). We considered two stellar activity cycles, that of the Sun using space-based XUV spectral irradiance observations over solar cycle 24, as well as reconstructing the XUV activity cycle of the star ι Hor from X-ray observations and photospheric modelling. For the Sun-like activity cycle, which exhibits substantial variations in the flux emitted at EUV wavelengths, the atmospheric escape and He I 1083 nm transit signatures of four considered types of highly irradiated exoplanets were found to be significantly stronger during a maximum phase of the activity cycle. This is the result of substantially larger activity cycle variations in the received EUV flux responsible for atmospheric escape, compared to the concurrent variations in the mid-UV flux, capable of photoionising helium out of the 2^3S state. We found the atmospheric escape and He I 1083 nm signature of further orbiting planets to be more affected by stellar activity cycles. We proposed that stellar cycles could explain some of the conflicting He I 1083 nm observations, with detections being more likely when the stellar host is closer to a phase of activity maximum.

2

EVOLUTION OF ATMOSPHERIC ESCAPE IN CLOSE-IN GIANT PLANETS AND THEIR ASSOCIATED LY- α AND H- α TRANSIT PREDICTIONS

A. P. Allan, A. A. Vidotto, 2019, *Monthly Notices of the Royal Astronomical Society*, Volume 490, Issue 3, December 2019, Pages 3760–3771.

Abstract

Strong atmospheric escape has been detected in several close-in exoplanets. As these planets consist mostly of hydrogen, observations in hydrogen lines, such as Ly α and H α , are powerful diagnostics of escape. Here, we simulate the evolution of atmospheric escape of close-in giant planets and calculate their associated Ly α and H α transits. We use a one-dimensional hydrodynamic escape model to compute physical properties of the atmosphere and a ray-tracing technique to simulate spectroscopic transits. We consider giant (0.3 and $1M_{\text{jup}}$) planets orbiting a solar-like star at 0.045au, evolving from 10 to 5000 Myr. We find that younger giants show higher rates of escape, owing to a favourable combination of higher irradiation fluxes and weaker gravities. Less massive planets show higher escape rates ($10^{10} - 10^{13}$ g/s) than those more massive ($10^9 - 10^{12}$ g/s) over their evolution. We estimate that the $1M_{\text{jup}}$ planet would lose at most 1% of its initial mass due to escape, while the $0.3M_{\text{jup}}$ planet, could lose up to 20%. This supports the idea that the Neptunian desert has been formed due to significant mass loss in low-gravity planets. At younger ages, we find that the mid-transit Ly α line is saturated at line centre, while H α exhibits transit depths of at most 3 – 4% in excess of their geometric transit. While at older ages, Ly α absorption is still significant (and possibly saturated for the lower mass planet), the H α absorption nearly disappears. This is because the extended atmosphere of neutral hydrogen becomes predominantly in the ground state after ~ 1.2 Gyr.

2.1 Introduction

Following the first detection of an exoplanetary atmosphere around the hot-Jupiter HD209458 b (Charbonneau et al. 2002), there has been a plethora of studies aimed at better understanding the atmospheres of exoplanets. Whether a planet can retain an atmosphere for a significant time period is essential for its habitability, as atmospheres regulate the planetary surface temperature, as well as absorb harmful solar or cosmic rays (e.g., [Kasting et al. 1993](#); [Lammer et al. 2009](#)). Consequently, studies regarding the stability of planetary atmospheres are critical in the ongoing searches for habitable planets.

A planet that is too close to its host star, however, receives intense high-energy (i.e., X-rays and ultraviolet, UV) irradiation, which can cause atmospheres to heat, expand and ‘evaporate’. For many years now, the Hubble Space Telescope (HST) has been a key instrument for observing escaping planetary atmospheres in the UV (e.g. [Vidal-Madjar et al. 2003](#)). Major advancements in the field can be expected with new missions soon to be launched, such as the Colorado Ultraviolet Transit Experiment ([Fleming et al. 2017](#)), and the James Webb Space Telescope. Predicting prime candidates for future observations of escaping atmospheres is therefore important both to guide these observations as well as for interpreting their findings.

Strong atmospheric escape has been detected in several close-in exoplanets so far using transmission spectroscopy in the UV (e.g., [Vidal-Madjar et al. 2003](#); [Fossati et al. 2010](#); [Kulow et al. 2014](#); [Ehrenreich et al. 2015](#); [Bourrier et al. 2016](#)). In particular, as the composition of gas giants consists predominantly of hydrogen, their atmospheres show strong absorption in the Ly α line. Unfortunately, the centre of this line is contaminated in our geocorona and can be significantly absorbed by neutral hydrogen in the interstellar medium ([Wood et al. 2002](#); [Ben-Jaffel 2008](#)). This renders the line core unusable and the signatures of escaping atmospheres can only be observed in the wings of the Ly α line.

Another promising line for conducting transmission spectroscopy is H α , as this line can be observed with ground-based spectrographs and it does not suffer contamination at the line centre, thus allowing us to probe the accelerating material at the bottom of the escaping atmosphere. However, as the number of hydrogen atoms initially in the first excited state ($n = 2$) can be much lower than the population at ground level ($n = 1$), transit depths in H α are expected to be smaller than in Ly α transits ([Jensen et al. 2012](#); [Cauley et al. 2015](#)). Another complication is that an active host star shows variability in H α , making it harder to disentangle signatures from the star and from the planetary atmosphere ([Cauley et al. 2017](#)). Recently, escaping atmospheres were detected using the metastable helium triplet at $\sim 10830\text{\AA}$ ([Nortmann et al. 2018](#); [Allart et al. 2019](#); [Alonso-Floriano et al.](#)

2019), opening up new possibilities for probing planetary atmospheres with ground-based instrumentation in the infrared, such as with CARMENES (Quirrenbach et al. 2014) and SpIRou (Cloutier et al. 2018).

The reason why atmospheres of close-in giants are more susceptible to strong evaporation relies on two factors: 1) the intense high-energy irradiation they receive from their host stars, due their close proximity to the host, and 2) on their relatively low gravitational potential, required for a planet to ‘hold on’ to their atmospheres. Young exoplanets are more susceptible to escape, because young stars have higher X-ray and UV fluxes (Ribas et al. 2005; Johnstone et al. 2015b) and because planets at young ages are more ‘puffed up’, and thus have a lower gravitational potential. As the system evolves and the high-energy flux decreases with time, escape rates are expected to decrease.

In this paper, we model the evolution of atmospheric escape on close-in giant planets. In particular, we focus on two different types of gas giants: a Jupiter-mass planet and a Saturn-mass planet (1 and 0.3 M_{jup} , respectively). In both cases, we consider these planets to be at an orbital distance of 0.045 au or, equivalently, at a 3.5 day orbit around a solar mass star. This distance is just inside the short-period ‘Neptunian desert’, which shows a lack of planets with masses between 0.03 and 0.3 M_{jup} at orbital periods $\lesssim 5\text{--}10$ days (Mazeh et al. 2016). The paucity of detected planets within this desert is suggestive of significant mass loss in planets with masses $\lesssim 0.3 M_{\text{jup}}$. This will indeed be demonstrated in our results.

Our paper is presented as follows. Section 2.2 presents the two main inputs required in our study of the evolution of atmospheric escape: a prescription for how the high-energy flux of the host star evolves during the main-sequence phase and a prescription describing the contraction of the planet after its formation. These two factors are then considered in our atmospheric escape models, which are described in Section 2.3, along with a description of the ray tracing technique used to simulate the spectroscopic transits. Our results are shown in Section 2.4: for each age ranging from 10 to 5000 Myr, we calculate the physical properties of the escaping atmospheres and predict their Ly α and H α transit profiles, which can be compared to observations. Section 2.6 presents a discussion of our results and our conclusions.

2.2 Evolution of planetary radii and stellar EUV flux

The evolution of atmospheric escape of a close-in planet depends on two important factors:

1. as the host star evolves, its activity declines due to spin down, resulting

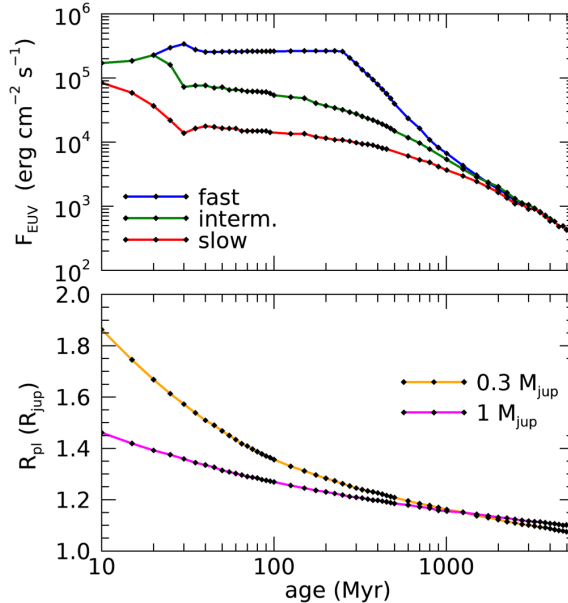


Figure 2.1: Top: EUV flux received at an orbital distance of 0.045 au from a solar-like star with respect to planetary age. Line colour indicates stellar rotation: slow (red), intermediate (green), fast (blue). From [Johnstone et al. \(2015b\)](#). Bottom: Planetary radius with respect to age for both a $1-M_{\text{jup}}$ (magenta) and a $0.3-M_{\text{jup}}$ (orange) close-in giant orbiting a solar-like star at 0.045 au. From [Fortney & Nettelmann \(2010\)](#). The black diamonds show our sampled increments.

in declining fluxes in the extreme ultraviolet (EUV) and

2. as the planet evolves, cooling causes it to contract with time.

Therefore, to simulate the evolution of a close-in giant, we couple evolving predictions of EUV flux ([Johnstone et al. 2015b](#)) and planetary radius ([Fortney & Nettelmann 2010](#)) with our hydrodynamic escape model, which will be described in Section 2.3. The evolution of these input parameters are shown in Figure 2.1 and described next.

The EUV emitted from the host star originates from its magnetically heated, chromospheric and coronal plasma (e.g., [Jardine et al. 2006](#)). Given that magnetic activity is linked to rotation, the EUV flux depends on the host star’s rotational evolution. In rotational evolution studies, it is common to separate stars in different rotational tracks: those representing stars born as slow, intermediate or fast rotators ([Gallet & Bouvier 2013](#); [Johnstone et al. 2015a](#)). Due to the rotation-activity relations, stars that are born as slow rotators have overall lower EUV flux throughout their lives than those that were born as fast rotators ([Tu et al. 2015](#)). As the host star evolves, its

magnetic activity declines due to spin down (Vidotto et al. 2014). At ~ 1 Gyr, the rotational evolution paths for solar-mass stars converge to a unique solution (Skumanich 1972; Gallet & Bouvier 2013). This convergence is thus also predicted to occur in the evolution of the EUV flux (F_{EUV}).

Here, similarly to Johnstone et al. (2015b), we consider three host star rotational evolutions, resulting in three differing EUV flux evolutions for fast, intermediate and slow rotators (Figure 2.1, top). This allows us to study the influence of initial conditions of the star’s rotation on atmospheric escape of an orbiting close-in giant.¹

A planetary evolution model is required to calculate the change in planetary radius R_{pl} with time. Here, we use the results from Fortney & Nettelmann (2010) to describe the evolution of a $1-M_{\text{jup}}$ planet (magenta line in the bottom panel of Figure 2.1) and of a $0.3-M_{\text{jup}}$ planet (orange line). These curves represent the calculations with no core in Fortney & Nettelmann (2010), for planets orbiting a solar-like star at 0.045 au, and they do not account for the mass loss. Ideally, as the atmosphere is removed from the planet, one would also need to take into account the reduction in the total mass of the planet, and consequently the corresponding change in radius. For example, this could be done by coupling atmospheric losses to planetary evolution models in a self-consistent way. This is left for a future work. Although mass loss is not self-consistent considered in the adopted radius evolution curves, it is unlikely that this would affect the $1-M_{\text{jup}}$ planet, as total mass lost represents a small fraction of the total planetary mass, as we will see further on. However, this correction is more relevant for the $0.3-M_{\text{jup}}$, as lower-mass planets have stronger evaporation. We will discuss this further in Section 2.4.

2.3 Atmospheric escape and transit calculations

2.3.1 Hydrodynamic escape model

Because of the strong mass-loss rates inferred in observations ($> 10^9$ g/s, Ehrenreich & Désert 2011), atmospheric escape in close-in planets can be described using a fluid approximation. For escape to be considered in this regime, the atmosphere has to be collisional, whose indicator is given by the Knudsen number, $K_n = \lambda_{\text{mfp}}/h$, which is the ratio between the mean free

¹The values predicted by Johnstone et al. (2015b) results in $F_{\text{EUV}} = 6.7 \text{ erg s}^{-1} \text{ cm}^{-2}$ at 1 au assuming a solar-like star at the approximate solar age. To match the observed flux of $1 \text{ erg s}^{-1} \text{ cm}^{-2}$ from Ribas et al. (2005), we normalise the curves in Johnstone et al. (2015b) by dividing them by 6.7. The flux of $1 \text{ erg s}^{-1} \text{ cm}^{-2}$ is also the one adopted in the fiducial case of Murray-Clay et al. (2009), on which our hydrodynamic model is based.

path of an atmospheric particle λ_{mfp} and the atmospheric scale height h . The motion of a planetary atmosphere for which $K_n \ll 1$ is best described by a fluid, in an escape process known as hydrodynamic escape. This escape process occurs when heating in the collisional region of an atmosphere causes an upward pressure gradient force, which drives a bulk, radial outflow (Catling & Kasting 2017).

Our numerical model is based on the model presented in Murray-Clay et al. (2009). We treat the escaping atmosphere as a fluid, solving the equations of fluid dynamics in a co-rotating frame. These coupled differential equations are ionisation balance as well as the conservation of mass, energy and momentum. To achieve convergence of the wind solution, we use a shooting method based on the model of Vidotto & Jatenco-Pereira (2006).

In steady state, the momentum equation in spherical symmetry can be written as

$$u \frac{du}{dr} = -\frac{1}{\rho} \frac{dP}{dr} - \frac{GM_{\text{pl}}}{r^2} + \frac{3GM_* r}{a^3}, \quad (2.1)$$

where r is the radial coordinate from the centre of the planet, ρ and u represent the atmospheric mass density and velocity, respectively, and P is the thermal pressure. The first term on the right side of Equation (2.1) is the thermal pressure gradient while the second term represents attraction due to gravity. This equation is analogous to the momentum equation for a stellar wind (Parker 1958) with an additional term on the right side due to tidal effects. The tidal term is the sum of the centrifugal force and differential stellar gravity along the ray between the planet and star (García Muñoz 2007). In this paper, we use the terms ‘hydrodynamic escape’ and ‘planetary wind’ interchangeably.

Conservation of energy requires that

$$\rho u \frac{d}{dr} \left[\frac{k_B T}{(\gamma - 1)m} \right] = \frac{k_B T}{m} u \frac{d\rho}{dr} + Q - C, \quad (2.2)$$

where k_B is the Boltzmann constant, T the temperature, $\gamma = 5/3$ is the ratio of specific heats for a monatomic ideal gas and m is the mean particle mass, which ranges from $0.5m_H$ to $1m_H$, for a fully ionised to fully neutral atomic hydrogen plasma, respectively. Here, m_H is the mass of atomic hydrogen. The term on the left indicates the change in the internal energy of the fluid. The first term on the right represents cooling due to gas expansion, while the second (Q) and third (C) are heating and cooling terms. This equation is, again, typically used in stellar wind models, although with different heating and cooling terms (Vidotto & Jatenco-Pereira 2006).

Our planetary wind model assumes that the EUV flux is concentrated at one photon energy $e_{\text{in}} = 20 \text{ eV}$, thus the volumetric heating rate [erg/s/cm^3] can be written as $Q = \epsilon F_{\text{EUV}} e^{-\tau} \sigma_{\nu_0} n_n$, where F_{EUV} is the EUV flux received by the planet, τ the optical depth to ionising photons, n_n the

number density of neutral hydrogen and σ_{ν_0} is the cross-section for the photoionisation of hydrogen given by $\sigma_{\nu_0} = 6 \times 10^{-18} (e_{\text{in}}/13.6\text{eV})^{-3} = 1.89 \times 10^{-18} \text{cm}^2$ (Spitzer 1978). Of the total received energy flux F_{EUV} , a fraction ϵ is converted to thermal energy to heat the atmosphere. In our simulations, we follow the approach by Murray-Clay et al. (2009) and assume $\epsilon = 1 - 13.6 \text{ eV}/e_{\text{in}} = 0.32$.

We assume that the escaping atmospheric gas cools by radiative losses resulting from collisional excitation, also known as Ly α cooling. The volumetric cooling rate is $C = 7.5 \times 10^{-19} n_+ n_n \exp[-1.183 \times 10^5/T]$, where n_+ is the number density of protons, which is equivalent to the number density of electrons in a purely hydrogen plasma.

The ionisation balance is given by

$$\frac{n_n F_{\text{EUV}} e^{-\tau} \sigma_{\nu_0}}{e_{\text{in}}} = n_+^2 \alpha_{\text{rec}} + \frac{1}{r^2} \frac{d}{dr} (r^2 n_+ u), \quad (2.3)$$

where the rate of photoionisations (first term) balances the sum of the rates of radiative recombinations (second term) and of the advection of ions (third term). Here, $\alpha_{\text{rec}} = 2.7 \times 10^{-13} (T/10^4)^{0.9}$ is the case B radiative recombination coefficient for hydrogen ions (Storey & Hummer 1995; Osterbrock & Ferland 2006). The ionised fraction is given as $F_{\text{ion}} = n_+/n_H$, where $n_H = n_+ + n_n$ is the total number density of hydrogen.

Finally, the conservation of mass requires that

$$\frac{d(r^2 \rho u)}{dr} = 0. \quad (2.4)$$

Our simulated planetary outflow originates from the sub-stellar point of the planet, which is the point closest to the star. We then apply our calculated solution over 4π steradians rendering it an upper limit to atmospheric escape (Murray-Clay et al. 2009; Johnstone et al. 2015b). Therefore, from Equation (2.4), we have that the mass-loss rate of the escaping atmosphere is $\dot{M} = 4\pi r^2 \rho u$.

Similarly to stellar wind theory, the initially subsonic flow is accelerated transonically until it reaches an asymptotic speed, known as the terminal velocity u_{term} . Convergence is reached once the values of the mass-loss rate and terminal velocity between two subsequent runs are below 1%. We then calculate the Knudsen number K_n for each run of our simulations, so as to ensure that the atmosphere remains collisional throughout all our simulations.

Figure 2.2 shows typical solutions of our simulations, where we show radial profiles of various atmospheric parameters for $1 M_{\text{jup}}$ (magenta) and $0.3 M_{\text{jup}}$ (orange) planets orbiting a solar mass star at 0.045 au. The adopted radii for these illustrative simulations are $1.1 R_{\text{jup}}$. For both these planets, we assume an $F_{\text{EUV}} = 480 \text{ erg cm}^{-2} \text{ s}^{-1}$. In addition to these parameters, which determine the physical properties of the planetary systems,

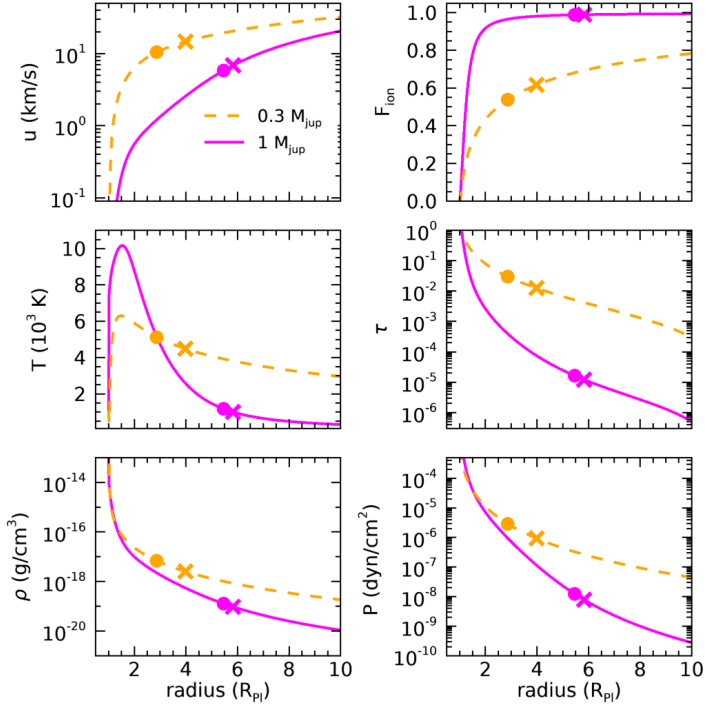


Figure 2.2: Radial profiles of various atmospheric properties for two simulated close-in planets with masses $1 M_{jup}$ (magenta, solid line) and $0.3 M_{jup}$ (orange, dashed line) and radius $1.1 R_{jup}$. The planets orbit a solar-like star at 0.045 au, and receive an incident flux $F_{EUV} = 480 \text{ erg cm}^{-2} \text{ s}^{-1}$, consistent with a 4.5 Gyr-old star. Left panels, from top to bottom: wind velocity u , temperature T , total mass density ρ . Right panels, from top to bottom: fraction of ionised hydrogen F_{ion} , optical depth to ionising photons τ and thermal pressure P . The distance at which $\tau = 1$ is reached at $\sim 1.1 R_{pl}$ for the cases presented above. The circle and cross indicate the sonic point and Roche lobe boundary, respectively.

our hydrodynamic models require values of the temperature T_0 and density ρ_0 at the base of the escaping atmosphere (here, assumed at $1 R_{\text{pl}}$). For all of our simulations, we assume these parameters are $T_0 = 1000$ K and $\rho_0 = 4 \times 10^{-13}$ g cm $^{-3}$, similar to values adopted in Murray-Clay et al. (2009). Note that, although T_0 and ρ_0 are free parameters of the model, Murray-Clay et al. (2009) demonstrated that large variations in these values had negligible effect on the resulting simulated escape. We confirmed their results with our models as well.

The left panels of Figure 2.2 show profiles of planetary wind velocity u , temperature T , and total mass density ρ , while the right panels show fraction of ionised hydrogen F_{ion} , optical depth to ionising photons τ and thermal pressure P . In each of the panels, the cross represents the Roche lobe boundary

$$R_{\text{Roche}} = \frac{a}{R_{\text{pl}}} \left(\frac{M_{\text{pl}}}{3M_*} \right)^{1/3}. \quad (2.5)$$

Atmospheric particles are no longer gravitationally bound to the planet for $r > R_{\text{Roche}}$, with stellar tidal gravity dominating over planetary gravity. Note that each of our calculations extend out to $10 R_{\text{pl}}$, which is above R_{Roche} . The circle indicates the sonic point R_{sonic} , which is the distance at which the planetary wind reaches the sound speed $c_s = \sqrt{5k_B T/3m}$. It is evident from the velocity profile that our simulated wind becomes transonic within the Roche lobe boundary. This is also the case for our simulated planets featured in the subsequent sections during all evolutionary stages.

Figure 2.2 shows a steep drop in density and pressure with simultaneous sharp rises in T and F_{ion} , occurring below $1.5R_{\text{pl}}$. These strong variations in the atmospheric structure are the result of strong absorption of stellar EUV radiation at this distance (region with high optical depth τ), which leads to the photoionisation of atmospheric hydrogen, as seen in the dramatic increase of F_{ion} from $\simeq 0\%$ to 75% (30%) at $1.5R_{\text{pl}}$ for a $1-M_{\text{jup}}$ ($0.3-M_{\text{jup}}$) planet. Ejected free electrons then heat the planetary atmosphere through collisions, causing the sharp temperature increase. The high temperatures cause the atmosphere to expand and escape hydrodynamically. At large distances, the temperature drops due to the expansion of the atmosphere (adiabatic cooling). This energy sink dominates over heating once the atmosphere becomes sufficiently ionised. Ly α cooling also acts against the heating and is at its strongest at higher atmospheric temperatures due to increased collisional excitation (Salz et al. 2016b).

Comparing the curves for the $1-M_{\text{jup}}$ and $0.3-M_{\text{jup}}$ planets in Figure 2.2, we see that the wind of the more massive planet has lower velocities due to its higher gravitational potential. Its atmosphere is also more rarefied, as seen by the density and optical depth curves. Its temperature, nevertheless, reaches higher values, leading to a more ionised atmosphere. The mass-loss rates of the $1-M_{\text{jup}}$ planet is 1.7×10^9 g s $^{-1}$, 26 times lower than the

mass-loss rate of $4.4 \times 10^{10} \text{ g s}^{-1}$, for the $0.3\text{-}M_{\text{jup}}$ planet. Altogether, the lower gravitational potential of the less massive planet results in stronger planetary winds, with higher velocities and mass-loss rates.

2.3.2 Comparison to energy-limited escape

The energy limited approximation (Watson et al. 1981) is often adopted for calculating mass-loss rates of atmospheric escape in place of more computationally heavy hydrodynamic models. This approximation can be derived as follows. We first assume energy balance between the final kinetic energy of the planetary wind and the input energy due to irradiation

$$E_{\text{kinetic,output}} = E_{\text{irradiation,input}} \quad (2.6)$$

For the input energy, a fraction ϵ of the stellar high-energy flux F_{EUV} intercepted by a planet with a cross section of πR_{pl}^2 is assumed to drive a flow that reaches a kinetic energy $\dot{M}u_{\text{term}}^2/2$, where u_{term} is the terminal velocity.

$$\frac{\dot{M}u_{\text{term}}^2}{2} = \epsilon F_{\text{EUV}}(\pi R_{\text{pl}}^2). \quad (2.7)$$

where \dot{M} is the mass-loss rate of the planetary wind. We further assume that the terminal velocity u_{term} is on the order of the surface escape velocity $v_{\text{esc}} = (2GM_{\text{pl}}/R_{\text{pl}})^{1/2}$, we have thus that the mass-loss rate derived in the energy-limit approximation is

$$\dot{M}_E = \epsilon \frac{F_{\text{EUV}}(\pi R_{\text{pl}}^2)}{GM_{\text{pl}}/R_{\text{pl}}}. \quad (2.8)$$

Using an efficiency of $\epsilon = 0.32$, for the $1\text{-}M_{\text{jup}}$ and $0.3\text{-}M_{\text{jup}}$ planets presented in Figure 2.1, we find energy limited mass-loss rates of $\dot{M}_E = 1.9 \times 10^9 \text{ g s}^{-1}$ and $6.2 \times 10^9 \text{ g s}^{-1}$, respectively. The energy-limit approximation overestimates the mass-loss rate computed from hydrodynamical models for the $1\text{-}M_{\text{jup}}$ planet by only a factor of 1.1. However, it underestimates by a factor of 1/7 the mass-loss rate of the $0.3\text{-}M_{\text{jup}}$ planet. Examining Equations (2.7) and (2.8), we expect that $\dot{M}_E > \dot{M}$, when the terminal velocities of the wind are $u_{\text{term}} < v_{\text{esc}}$. Indeed, for the $1\text{-}M_{\text{jup}}$ planet, terminal velocities are $\sim 20 \text{ km/s}$, compared to an escape velocity of $\sim 60 \text{ km/s}$. On the other hand, we expect that $\dot{M}_E < \dot{M}$, when the terminal velocities of the wind are $u_{\text{term}} > v_{\text{esc}}$. This is the case for the $0.3\text{-}M_{\text{jup}}$ planet, where the terminal velocities are above 32 km/s and escape velocity is $\sim 30 \text{ km/s}$.

Recent studies showed that the energy-limited approximation can be a poor indicator of the mass lost in atmospheric escape processes (e.g. Salz et al. 2016a; Kubyschkina et al. 2018) and can underestimate the mass-loss rate of low density, highly irradiated exoplanets planets in the boil-off regime

(Kubyskhina et al. 2018). To better reconcile the analytical expression with hydrodynamic models, a correction factor K is often considered in the denominator of Equation (2.8) to account for stellar tidal forces that reduces the effect of the planetary gravitational potential (Erkaev et al. 2007)

$$K = 1 - \frac{3R_{\text{pl}}}{2R_{\text{Roche}}} + \frac{R_{\text{pl}}^3}{2R_{\text{Roche}}^3}. \quad (2.9)$$

Additionally, the cross section of the planet is assumed to be $\pi R_{\tau=1}^2$, where $R_{\tau=1}$ refers to the distance where optical depth unity to ionising photons is reached. These two additional factors can reduce the discrepancy between the hydrodynamic calculations and the analytical limit, hence

$$\dot{M}_E^{\text{corr}} = \epsilon \frac{F_{\text{EUV}}(\pi R_{\tau=1}^2)}{KGM_{\text{pl}}/R_{\text{pl}}}. \quad (2.10)$$

However, to calculate $R_{\tau=1}$, one needs to compute the density and optical depth profiles through hydrodynamic simulations or from a derived prescription based in such simulations. For our examples presented in Figure 2.2, using $R_{\tau=1}$ from our simulations, and the tidal correction factor K , we find \dot{M}_E^{corr} that are factors of 1.6 and 0.25 the values from our hydrodynamical models. In these cases, the ‘correction’ made the discrepancy smaller for the $0.3-M_{\text{jup}}$ planet (from $1/7$ to $1/4$), but increased the discrepancy for the $1-M_{\text{jup}}$, when we adopted Equation (2.10) instead of (2.8). In the comparisons done further on in this paper, we compute energy-limited mass loss from Equation (2.10).

2.3.3 Transit calculations

After solving for the hydrodynamic equations for the planetary outflow, we use a ray tracing model to simulate planetary transits as observed in both Ly α and H α . This model is described in Vidotto et al. (2018), here modified for Ly α and H α transitions. In the ray tracing model presented here, we upgrade from a Doppler line profile to a Voigt line profile. As the ray tracing model from Vidotto et al. (2018) is three-dimensional, we create a three-dimensional Cartesian grid with 201 evenly spaced cells in each direction. This grid is centred on the planet and each cell is ‘filled’² with the one dimensional hydrodynamic calculations of u , T , and ρ , taking into account that Doppler shifts result from the projection of the wind velocities along the line-of-sight. One of the axis of the grid is aligned along the observer-star line, so that the grid seen in the plane-of-the-sky is a square of 201×201 cells.

To calculate a frequency-dependent transit, we use 51 velocity channels from $u_{\text{channel}} = -500$ km/s to $+500$ km/s, using increments of 50 km/s

²Similar to a solid of revolution.

for the outer velocities ($|u_{\text{channel}}| = 100$ to 500 km/s), while we improve the resolution at line centre (35 channel increments within ± 100 km/s). With this, the frequency-dependent optical depth along a single ray in the direction connecting the observer to the star-planet system is

$$\tau_\nu = \int n_n \sigma \phi_\nu dz, \quad (2.11)$$

where σ is the absorption cross-section at the line centre, ϕ_ν the Voigt line profile. The subscript ‘ ν ’ indicates that the line profile and the optical depth are dependent on the frequency (or velocity channel) of the observation. We calculate σ for both Ly α and H α transitions using

$$\sigma = \frac{\pi e^2 f}{m_e c} \quad (2.12)$$

where f is the oscillator strength of the transition, m_e the electron mass, e the electron charge and c the speed of light. Our values of f for each of these transitions were obtained from the NIST Catalogue³, which gives $f = 0.416410$ for Ly α and $f = 0.64108$ for H α . The Voigt line profile ϕ_ν is a convolution of a Gaussian and Lorentzian line profile accounting for both Doppler and natural broadening

$$\phi_\nu = \frac{\lambda_0}{\sqrt{\pi} u_{\text{th}}} \frac{\xi}{\pi} \int_{-\infty}^{\infty} \frac{e^{-w^2}}{\chi^2 + (\Delta u / u_{\text{th}} - w)^2} dw \quad (2.13)$$

where λ_0 is the wavelength at line centre ($\lambda_0 = 1215.67\text{\AA}$ for Ly α ; $\lambda_0 = 6562.79\text{\AA}$ for H α), $u_{\text{th}} = (2k_B T / m_H)^{1/2}$ and m_H is the mass of atomic hydrogen. $\chi = A_{ji} \lambda_0 / (4\pi u_{\text{th}})$ is the damping parameter, where A_{ji} is the transition rate ($A_{ji} = 4.69860 \times 10^8 \text{ s}^{-1}$ for the Ly α transition; $A_{ji} = 4.4101 \times 10^7 \text{ s}^{-1}$ for the H α one; values from NIST). The velocity offset from the line centre is $\Delta u = u_{\text{channel}} - u_{\text{LOS}}$, where u_{LOS} is the line of sight flow velocity of the escaping wind. We make use of IDL’s inbuilt `voigt` function to calculate ϕ_ν .

In computing the transmitted spectrum, we neglect centre-to-limb variations in the stellar disc and assume that, for a given frequency, the stellar disc emits a uniform specific intensity I_\star . The fraction of ‘transmitted’ specific intensity at a given frequency during transit is hence

$$\frac{I_\nu}{I_\star} = e^{-\tau_\nu}. \quad (2.14)$$

$1 - I_\nu / I_\star$, therefore, represents the fraction of absorbed specific intensity as a result of the absorption from both the planet disc and its atmosphere. To

³<https://www.nist.gov/pml/atomic-spectra-database>

calculate the total absorption, we then integrated over all rays. Given our three-dimensional grid construction, the grid projected in the plane of the sky has 201×201 cells. We therefore shoot 51 frequency-dependent rays through each of the 201^2 grid elements. Given that the grid is larger than the projected area of the stellar disc, rays emitted from pixels outside the stellar disc are assigned a zero specific intensity.

Therefore, integrating over all these rays and dividing by the ‘flux’ of star (πR_\star^2) allows us to calculate the transit depth

$$\Delta F_\nu = \frac{\int \int (1 - e^{-\tau_\nu}) dx dy}{\pi R_\star^2}. \quad (2.15)$$

where dx and dy are the sizes of each cell. By construction, $dx = dy = 2 \times 10R_{\text{pl}}/201 \simeq 0.1R_{\text{pl}}$ (the factor of 2 comes from the ‘solid of revolution’ method used and $10R_{\text{pl}}$ is the extension of the hydrodynamical computations). In practice, ΔF_ν represents the ratio of a frequency-dependent effective area of the planet $\pi(R_{\text{pl},\nu}^{\text{eff}})^2$, i.e., planet disc plus its absorbing atmosphere, by the stellar area

$$\Delta F_\nu = \frac{\pi(R_{\text{pl},\nu}^{\text{eff}})^2}{\pi R_\star^2}. \quad (2.16)$$

Because of the nature of our spherically symmetric model, the effective area of the planet is that of a circle, but in 3D models, this area could take a different form (e.g. Vidotto et al. 2018). Here, we assume a transit along the centre of the stellar disc resulting in an impact parameter $b = 0$. Assuming circular orbit, this gives a transit duration of

$$t_{\text{dur}} \approx \frac{P_{\text{orb}} R_\star}{\pi a} = \frac{2R_\star}{\sqrt{GM_\star/a}} = 2.75 \text{ h}, \quad (2.17)$$

where P_{orb} is the orbital period.

2.4 Evolution of atmospheric escape in close-in giants

To probe the evolution of the atmospheric escape, we perform escape simulations for two planet masses (0.3 and $1 M_{\text{Jup}}$) orbiting stars that were born as slow, intermediate and fast rotators. This results in six different evolutionary tracks. For each track, we have more than 50 models sampling ages from 10 Myr to 5 Gyr. The ages sampled are shown as diamonds in Figure 2.1. In total, we ran more than 300 models to compute the evolution of atmospheric escape. For each of these models, we also predict Ly α and H α transit signals. The stellar mass ($M_\star = 1M_\odot$), radius ($R_\star = 1R_\odot$) and

orbital distance ($a = 0.045$ au) are fixed in our study. In Figure 2.3, we present the evolution of three atmospheric properties predicted using our models: the mass-loss rate (top panels), terminal velocities (middle) and the position of the sonic point (bottom). The results for our $1-M_{\text{jup}}$ and $0.3-M_{\text{jup}}$ planets are shown on the left and right panels, respectively.

The evolution of \dot{M} for the three considered host star rotations are shown as solid lines in the top panels of Figure 2.3. We see that close-in giants experience greater levels of mass loss during younger evolutionary stages and that their mass-loss rates decrease with time. This is the result of the lowered EUV flux incident on the planetary atmosphere as well as the contracting planetary radius with evolution (Figure 2.1). The lowered EUV flux leads to a reduced level of heating in the atmosphere due to a lower number of photoionisations. This ultimately weakens the hydrodynamic wind as the planet evolves, resulting in the declining curves of \dot{M} .

The contracting planetary radius with evolution results in a strengthening planetary gravitational force on atmospheric particles. This acts to further reduce the atmospheric escape experienced with evolution by improving the planet's ability to retain its atmospheric particles. A weaker gravitational potential is directly responsible for the stronger escape experienced by the lower mass $0.3-M_{\text{jup}}$ planet, as compared to the $1-M_{\text{jup}}$ planet. Both its lower mass and larger radii are responsible for this.

Although not considered in our models, the decreasing planetary mass resulting from atmospheric escape will soften the effect of the growing planetary gravity with age. We do not include this decrease in mass in our simulations. As a result, our mass-loss rates increasingly underestimate the true mass-loss rate as the planet ages due to a growing overestimation of planetary gravity. Fortunately, we can assume that the resulting inaccuracy is of minor importance as the effect of the neglected mass variation on the planetary gravity is negligible in comparison to that resulting from the radius variation during evolution (Section 2.4.1).

We used the evolutionary curves from Fortney & Nettelmann (2010), which did not consider the presence of a core. By considering a $25-M_{\oplus}$ core, Fortney & Nettelmann (2010) predicted planets with smaller radii than those without a core. In our models, this smaller radius would lead to stronger planetary gravity and consequently to a somewhat weaker mass loss. However, this would not change the trends we present in Figure 2.3.

The significantly steeper \dot{M} curves for the close-in giant orbiting a fast-rotating star (blue) further demonstrates the significance of stellar activity on atmospheric escape. Stellar rotation determines the EUV emission, with faster rotation producing higher emission, until a saturation plateau is reached for a fast rotating star (Figure 2.1). The \dot{M} curves for the three rotations become indistinguishable after ~ 1 Gyr, owing to a convergence of the received EUV flux at this age.

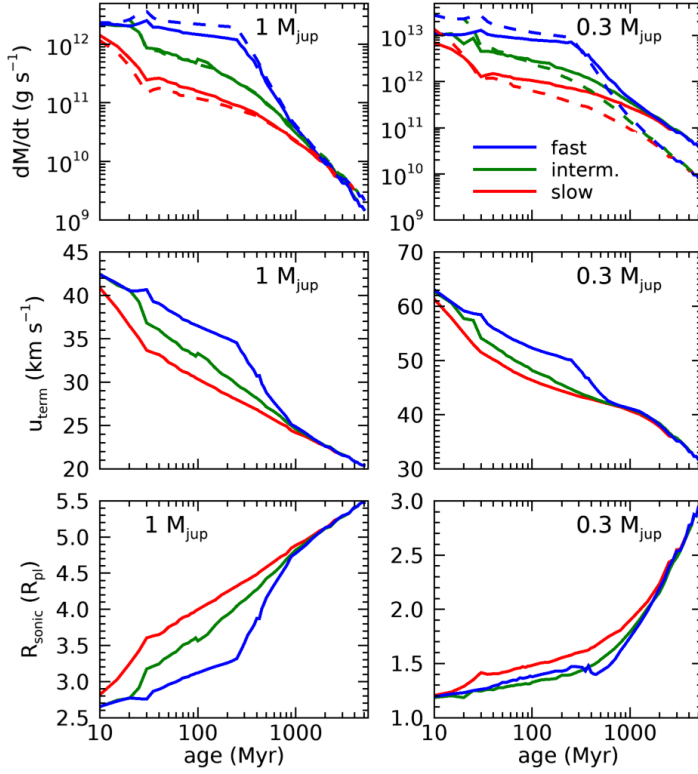


Figure 2.3: Evolution of atmospheric properties for a $1-M_{\text{jup}}$ (left) and $0.3-M_{\text{jup}}$ (right) planets orbiting a $1-M_{\odot}$ star at 0.045 au, of slow (red), intermediate (green) or fast (blue) rotation. The panels are: mass-loss rate \dot{M} (upper), terminal velocity u_{term} (centre) and radial distance to the sonic point R_{sonic} (lower). Dashed lines show \dot{M} predicted by the energy-limited approximation (Equation 2.10). We present analytical fits to these results in Appendix 2.6.

The dashed lines in the upper panels of Figure 2.3 show the mass-loss rates estimated using the energy limit approximation (Equation 2.10). For the $1-M_{\text{jup}}$ planet, the energy limited approximation overestimates the mass loss when orbiting a fast rotating host star (i.e., in the case of high F_{EUV}), while it underestimates mass-loss rates in the case of planets orbiting slowly rotating hosts. The results for the hydrodynamic case and the energy-limit case agree quite well after ~ 500 Myr. For the case of the $0.3-M_{\text{jup}}$ planet, the situation is quite different, in which we see that the estimates of \dot{M} provided by the energy-limited approximation are very different from the hydrodynamical calculation.

The middle panels of Figure 2.3 show the terminal velocity u_{term} of the planetary outflow, where we see that at younger ages, larger terminal velocities are reached. We define u_{term} here as the velocity of atmospheric particles leaving the planetary atmosphere at our maximum simulated distance of $10 R_{\text{pl}}$. As with the curves of \dot{M} , we see a decline of the u_{term} as the planet ages. However, while mass-loss rates vary by more than 3 orders of magnitude from 10 to 5000 Myr, the terminal velocities only vary by a factor of ~ 2 . Both \dot{M} and u_{term} decline with age due to a combination of an increasingly weaker atmospheric heating and an improved ability of the planet to retain its atmospheric particles causing weaker, slower hydrodynamic winds at later evolutionary stages. The velocity of escaping neutral hydrogen atoms is of particular importance for Ly α observations as only absorption in line wings are observable (Section 2.5.1).

The bottom panels of Figure 2.3 show the evolution of the sonic point R_{sonic} , which climbs to higher positions of the atmosphere with evolution. The sonic point occurs when the wind velocity reaches the speed of sound, $u = c_s$. With evolution, there is a slower rise in the wind velocity with distance (i.e., lower acceleration). As a result, the wind must travel a greater distance before it reaches the sound speed c_s . With age, c_s will also be slightly lowered due to overall lower atmospheric temperatures, but this only partially counteracts the effects of the lower wind acceleration. As a result, the variations in wind velocity profiles dominate in setting the growth of R_{sonic} with evolution.

We draw attention to the striking resemblance of each of the curves of Figure 2.3 to the curves of the received F_{EUV} included in Figure 2.1, demonstrating a strong dependence of \dot{M} and u_{term} on the irradiation level of the planetary atmosphere. We present analytical fits to these results in Appendix 2.6.

2.4.1 Total mass lost during evolution

Figure 2.4 shows the total mass lost calculated over the simulated life of the 1- (top panel) and $0.3-M_{\text{jup}}$ (bottom) planets. We calculate the total mass lost by integrating mass-loss rates given in Figure 2.3 with respect to

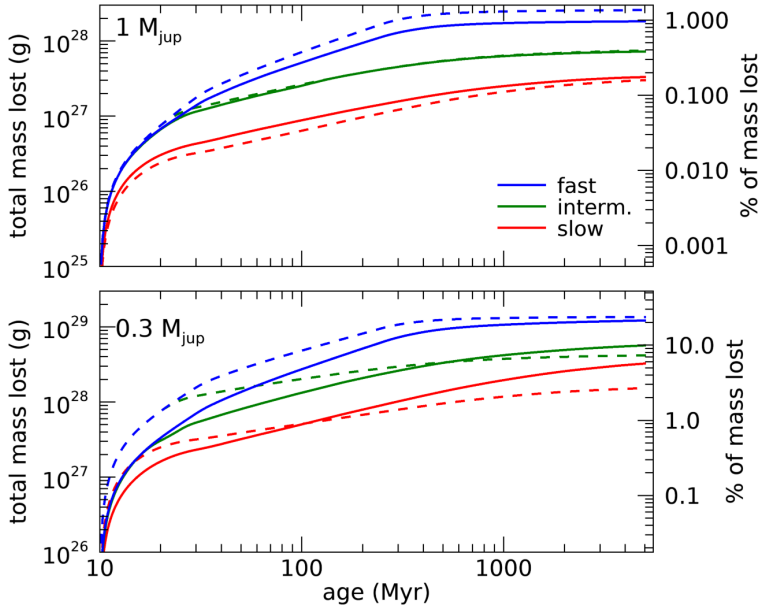


Figure 2.4: Total planetary mass lost after the age of 10 Myr for a 1- (top) and 0.3- (bottom) M_{jup} planets orbiting a slow (red), intermediate (green), and fast (blue) rotating host. Solid and dashed lines are mass lost calculated using the hydrodynamic model and energy-limited case, respectively.

time. Figure 2.4 shows the largely differing mass losses resulting from the three considered rotations of the host star. The total mass lost is clearly dependent on stellar rotation and mass loss is greatest for planets orbiting faster rotating hosts. The mass loss experienced by each planet levels off with age due to the slowing mass-loss rates with evolution shown in Figure 2.3.

Past studies predicted that atmospheric escape does not play an influential role in the overall evolution of hot-Jupiters (Murray-Clay et al. 2009; Owen & Wu 2013; Ehrenreich et al. 2015). In spite of the large mass-loss rates observed, the planetary mass is still very large, constituting essentially an unending atmospheric reservoir. Indeed, over its entire evolution, we predict that the $1\text{-}M_{\text{jup}}$ planet would lose at most 1% of its initial mass. We therefore expect hydrodynamic escape to have a negligible effect on mass of highly irradiated Jupiter-mass planets, owing to their large mass reservoir.

However, for the $0.3\text{-}M_{\text{jup}}$ planet, our results indicate the opposite – mass lost due to hydrodynamic escape is considerably large, and could potentially shape the planet’s evolution. In this case, the total mass lost can reach more than 20%. For orbital distances even shorter than the 0.045 au

considered in this work, mass-loss rates are expected to increase even more, giving support to the idea that close-in rocky planets might have begun their evolution as Neptune-like planets, but eventually evaporated the entirety of their atmospheres (Ehrenreich et al. 2015).

Regardless of the planetary mass, orbiting a faster rotating host star leads to greater losses, with a slow rotator host producing ~ 4 to 5 times less lost mass than a fast rotating host. The dashed lines in Figure 2.4 show the total mass lost calculated using the energy-limit approach. This approximation overestimates the total mass lost when orbiting a fast rotating host star, while it underestimates the loss for planet orbiting a slow host.

2.5 Spectroscopic transits in hydrogen lines

We use the solutions of the hydrodynamic calculations presented in the previous Section to calculate spectroscopic transits in Ly α and H α . To model these transits, we need to know the density of neutral hydrogen in the ground state $n = 1$ (hereby N_1) and in the first excited state $n = 2$ (N_2), respectively. For that, we solve the statistical equilibrium equation in the coronal-model approximation (Del Zanna & Mason 2018). In this approximation, the spontaneous radiative decay balances the excitation process, and collisional de-excitation is neglected. Only direct excitations from the ground state $n = 1$ are included. To perform this calculation, we use the CHIANTI software (v 9.0.1, Dere et al. 2019)⁴ written in IDL (more specifically, we use the `ch_pops` procedure). In practice, the population calculation requires the temperature and electron density, which are outputs from our hydrodynamic calculations. Note that for all our simulations, the ratio N_2/N_1 is quite low, with values not exceeding $1 - 2 \times 10^{-5}$ for the young planets, and maximum values well below that for the older planets.⁵ However, as hydrogen is so abundant, we still predict a reasonably large transit in H α , as we will show in Section 2.5.2.

2.5.1 Ly α transits

Figure 2.5 shows our predicted transit signatures in the Ly- α line for the $1-M_{\text{jup}}$ planet. For each block of three panels in Figure 2.5, colour indicates the planetary age as given by the relevant colour bar. In the three upper plots (a-c), we show the line profiles of hot-Jupiters orbiting a slowly rotating

⁴We use `sun_photospheric_2015_scott.abund` for the photospheric abundance file and ion equilibrium file `chianti.ioneq`.

⁵We also computed the ratio N_2/N_1 using the Boltzmann equilibrium equation, and found ratios larger than the ones found by solving the statistical equilibrium equation. The Boltzmann equation predicted larger H α transits, therefore representing an upper limit for the transit calculations. In general, though, these transit depths were not larger by more than a factor of 2 of the ones shown in the present paper.

host; the central plots (d-f) consider an intermediate rotator, while lower plots (g-i) correspond to a fast rotating host star. The lightcurves resulting from the geometric transit of the planet itself are shown in panels a, d and g. Therefore, these plots simply reveal the transit effect of the evolving planetary radius, where the transit depths can be converted in $(R_{\text{pl}}/R_*)^2$.

Panels b, e and h of Figure 2.5 display predicted transit lightcurves as observed at the Ly α line centre. These lightcurves feature considerably deeper transits than those resulting from the geometric transit, as neutral hydrogen in the extended atmospheres absorbs strongly in Ly α . In addition, the typical Ly α transit duration is approximately 2 hours longer than the geometric transit, with young planets producing even longer durations. These plots show the evolution of the atmospheric size: as the atmospheres of younger close-in giants are inflated further than those of older planets, they occult more of the stellar disc, thus resulting in a greater transit duration and depth in Ly α .

As Ly α observations are not possible at the line centre, in panels c, f and i of Figure 2.5, we show the predicted Ly α line profile at mid-transit. In these panels, we show the occulted flux ΔF_ν (Equation 2.15) as a function of wavelength and Doppler velocity. These profiles show saturation of Ly α absorption at line centre and larger absorption in the line wings for younger planets. This is a direct result of the stronger atmospheric escape experienced by these planets, resulting in higher velocities of the escaping neutral hydrogen atoms. The symmetric line profiles are a result of our hydrodynamical models being spherically symmetric. A more realistic simulation, including for example interaction with stellar wind and acceleration due to radiation pressure, would present asymmetries in blue and red wings of the line profile (e.g., Kislyakova et al. 2014; Bourrier et al. 2016; Villarreal D’Angelo et al. 2018; Vidotto et al. 2018; McCann et al. 2019; Esquivel et al. 2019).

Across the three considered host-star rotations, a faster rotating host leads to longer and deeper Ly α transits (line centre) for a given planetary age below ~ 800 Myr. These younger planets also show wider line profiles at mid-transit, when orbiting fast-rotating stars. This is because planets orbiting more active stars receive more F_{EUV} , which then creates stronger evaporation.

In Figure 2.6, we present the same analysis as that shown in Figure 2.5, only now we consider the $0.3-M_{\text{Jup}}$ planet. It is clear that each of the Ly α transit profiles exhibit more extreme characteristics for this less massive planet: longer duration, deeper transits and wider line profiles. These are due to both a greater inflation of the atmosphere and faster moving neutral hydrogen atoms.

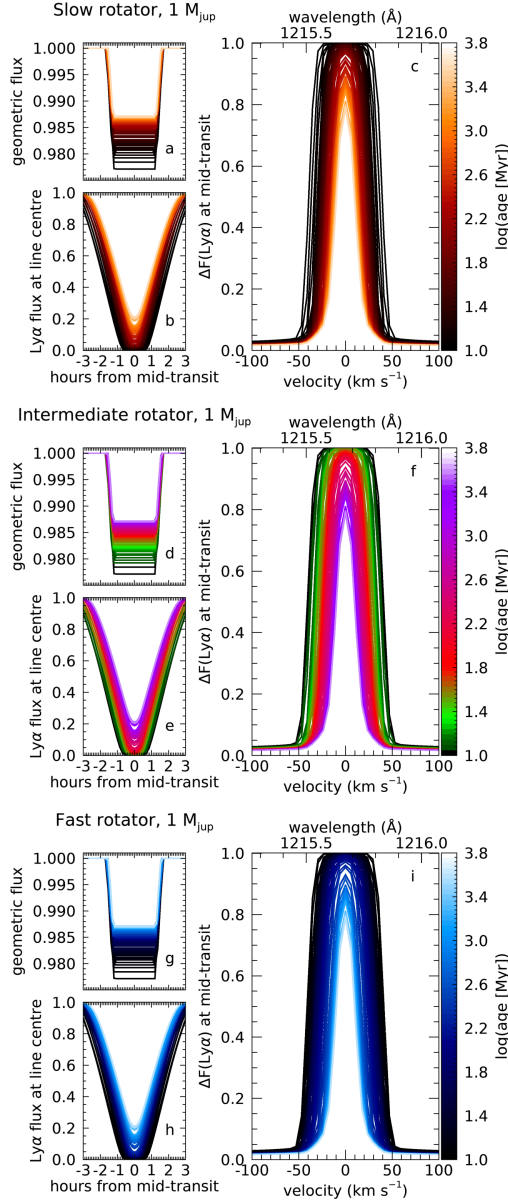


Figure 2.5: Ly α transit simulations for the $1 M_{\text{Jup}}$ planet. Results are separated into three blocks related to the host star stellar rotation: slow (a-c), intermediate (d-f) and fast (g-i) rotators. Panels a, d, and g show the lightcurves of the geometric transit. Panels b, e and h show the lightcurves as observed in Ly α line centre. Panels c, f and i are the mid-transit obscured flux (ΔF_{ν} , Equation 2.15) of the Ly α line profile, as a function of Doppler velocity and wavelength. Note that ΔF_{ν} does not reach zero and is offset by a couple % due to the absorption of the opaque disc of the planet. For each plot, colour represents age, which are indicated in the colour-bars.

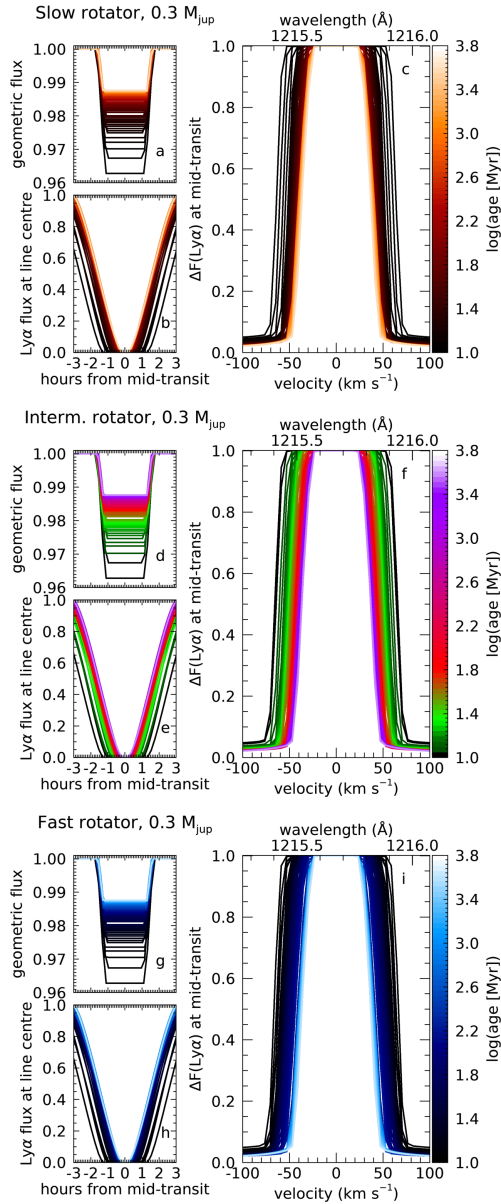


Figure 2.6: Same as in Figure 2.5, but for the $0.3 M_{\text{Jup}}$ planet.

2.5.2 H α transits

Similar to our predictions of Ly α transits, here we present our estimates of H α transits. An advantage of observing in H α is that the line centre is not contaminated as in the Ly α line and, perhaps, most importantly, they can be conducted with ground-based spectrographs.

Figure 2.7 shows the H α transits for the $1-M_{\text{jup}}$ and $0.3-M_{\text{jup}}$ planets, left and right panels respectively, in a similar design as Figures 2.5 and 2.6. We omit here the intermediate rotator for brevity and only show results for the slow (top panels) and fast (bottom) host-star rotations. The trends in the H α transits are *qualitatively* similar to the ones seen in the Ly α ones: the H α transits exhibit greater depths and duration than the geometric lightcurves due to absorption of H α photons by neutral hydrogen in the first excited state in the evaporating atmosphere. Likewise, we find that younger planets produce deeper, longer and broader H α transits compared to their older counterparts. For a given age below ~ 800 Myr ($\log(\text{age}) = 2.9$), the obscuration is larger for planets orbiting fast rotators, due to the higher F_{EUV} of these stars. However, Ly α and H α transits are *quantitatively* different.

Contrary to the saturation often seen in Ly α for several ages and host star rotations, H α absorption is considerably weaker. This is due to the significantly lower density of hydrogen in the first excited state $n = 2$ compared to the ground state $n = 1$. As a result, the transit depths we predict in our models reach, at line centre, at most $\Delta F_{\nu} \sim 5 - 8\%$ (a $\sim 3 - 4\%$ excess from the geometric transit) at very young ages reducing, at older ages, to fractions of a percent above the geometric transit, for the $1-M_{\text{jup}}$ planet, or no excess absorption at all for the $0.3-M_{\text{jup}}$ planet. The left panels in Figure 2.8 show the evolution of the H α excess flux, i.e., above the geometric transit, for the planets simulated here.

Our results, therefore, indicate that H α transits could be more easily detected in planets orbiting young and/or active stars. An extended H α transit has indeed been observed for HD189733b, which orbits a relatively active star (Jensen et al. 2012). These authors report a planet size in H α that is $\sim 1.4R_{\text{pl}}$, or $\Delta F_{\nu} \simeq 4.7\%$ at line centre at mid-transit. These values are actually not too dissimilar to our models of the $1-M_{\text{jup}}$ planet at younger ages. H α was also detected in the atmosphere of KELT-9b (Yan & Henning 2018; Cauley et al. 2019). Although the host is not an active star, it has a strong EUV flux due to its early spectral type. As a result, KELT-9b shows a wide H α line profile (~ 50 km/s) and a transit depth of 1.8% (1.15% in excess of the geometric transit of 0.68%, Yan & Henning 2018). Conversely, an H α extended transit was not detected in the less active KELT-3 system (Cauley et al. 2017).

Our models predict that lower gravity giants, like our $0.3-M_{\text{jup}}$ case, would show a larger H α obscuration than the more massive planets at young

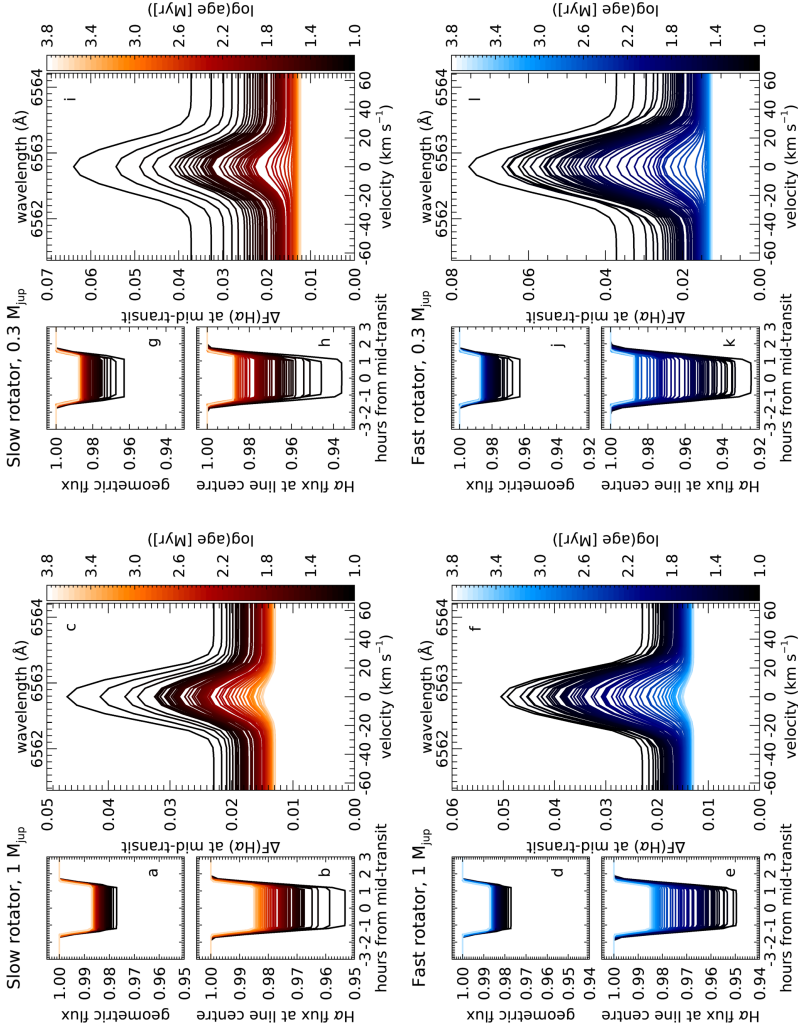


Figure 2.7: Same as in Figure 2.5, but for the H α transits of the $1 M_{\text{Jup}}$ planet (left) and $0.3 M_{\text{Jup}}$ planet (right). The host stars are assumed to start their lives as slow (top), and fast (bottom) rotators.

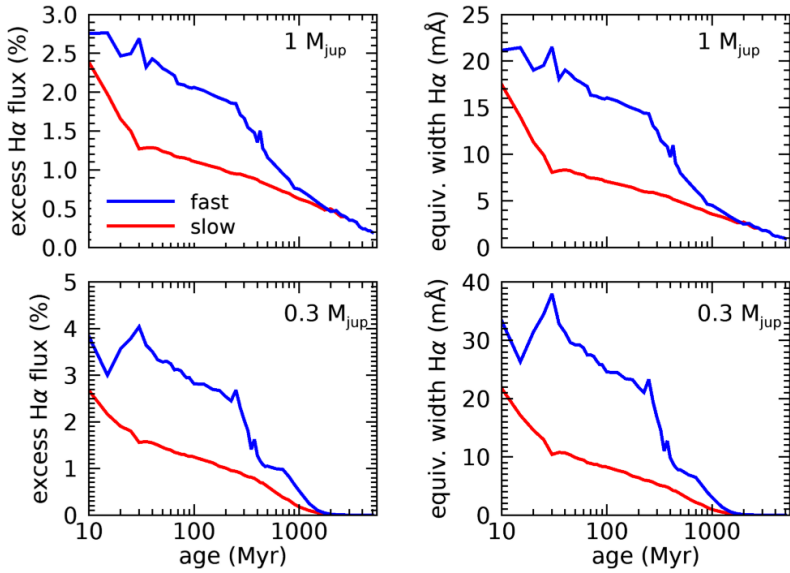


Figure 2.8: Left: Evolution of transit depths, in excess of the geometric transit, in the H α line at line centre and at mid-transit. Right: Evolution of the mid-transit equivalent width (Equation 2.18), integrated over ± 500 km/s. Top panels are for the $1 M_{\text{jup}}$ planet simulations while the bottom panels are for the $0.3 M_{\text{jup}}$ case. Red and blue curves represent the rotation of the host star, slow and fast, respectively.

ages (compare top and bottom panels in Figure 2.8). However, at older ages, the situation is reversed, with the $0.3-M_{\text{jup}}$ showing no excess $\text{H}\alpha$ flux above ~ 1.2 Gyr. This is because the extended atmosphere of neutral hydrogen becomes almost entirely in the ground state at older ages. Our result agrees with the lack of absorption observed in the $\text{H}\alpha$ transits of GJ436b (Cauley et al. 2017), in spite of its impressively long and extended transit in $\text{Ly}\alpha$ (Kulow et al. 2014; Ehrenreich et al. 2015; Lavie et al. 2017). This situation can occur when temperatures are not high enough to excite hydrogen. Indeed, GJ436b has a relatively small EUV flux ($F_{\text{EUV}} = 10^3$ erg/cm²/s, Ehrenreich et al. 2015). In our simulations, this flux is reached at an age of ~ 3 Gyr, when we already see a lack in $\text{H}\alpha$ absorption.

We also calculate the equivalent width of our $\text{H}\alpha$ transmission spectra as

$$W_{\text{H}\alpha} = \int_{v_i}^{v_f} (\Delta F_\nu - \Delta F_{\text{geom}}) dv, \quad (2.18)$$

where v_i and v_f represent the velocity range over which the integration is performed and ΔF_{geom} is the geometric transit depth ($R_{\text{pl}}^2/R_\star^2$), which is wavelength-independent. Equation (2.18) is thus the integral of the ‘excess’ transit over a velocity (or wavelength) range. We integrate over our entire simulated velocity range of ± 500 km/s or, equivalently, $\pm 10.9 \text{ \AA}$. However, we note that decreasing the range of integration to ± 50 km/s ($\pm 1 \text{ \AA}$) gives the same equivalent width – this is because the bulk of our predicted absorption occurs within ± 50 km/s.

The right panels of Figure 2.8 show the evolution of $W_{\text{H}\alpha}$ for the 1- (top) and $0.3-M_{\text{jup}}$ (bottom) planets, respectively. Equivalent widths are larger at younger ages for both mass planets, reaching 20 – 40 m \AA for planets orbiting active, young stars. Our values are lower than, but still similar to, the ~ 65 m \AA observed for the hot-Jupiter HD189733b (Jensen et al. 2018).

Both the excess transit and the equivalent width of the $\text{H}\alpha$ line (Figure 2.8) show trends that are similar to the F_{EUV} evolution with rotation of the host (Figure 2.1 top): the curve for fast rotator lies above the curve for slow rotator. However, contrary to the saturation of flux seen at early ages, which is also reflected in the curves of \dot{M} (Figure 2.3), the $\text{H}\alpha$ line shows neither a plateau-like saturation in transit depth nor in the equivalent width (Figure 2.8). This can be seen in Figure 2.9, where we plot the excess transit versus the escape rates. At younger ages, from 10 to 400 Myr (between crosses and squares), we see relatively small variations in \dot{M} for planets around fast rotating stars (in the saturated regime), but a significant drop in excess absorption.

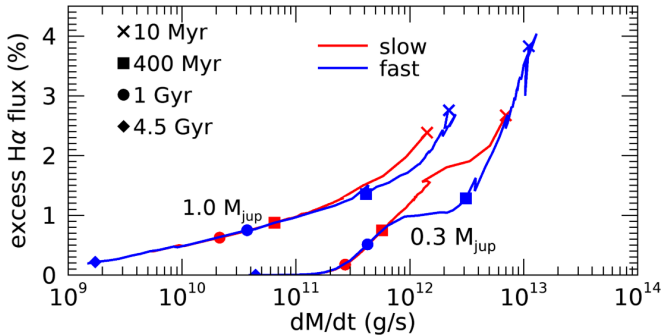


Figure 2.9: Transit depths, in excess of the geometric transit, in the $H\alpha$ line at line centre and at mid-transit versus the predicted escape rate. Symbols mark different evolutionary stage, with the younger systems at the top right of the curves and evolving as going towards the bottom left. The left (right) most curves are for the $1-M_{\text{jup}}$ ($0.3-M_{\text{jup}}$) planet simulations.

2.6 Discussion and conclusions

In this work, we studied the evolution of atmospheric escape in close-in giants. For that, we modelled escape of a higher gravity planet ($1.0 M_{\text{jup}}$) and a lower gravity one ($0.3 M_{\text{jup}}$). Both planets were assumed to be at 0.045 au, orbiting stars whose EUV fluxes evolve from early ages (10 Myr) to about 5 Gyr. Given that the host star’s fluxes evolve differently depending on their initial rotation, we considered three evolutionary paths for the EUV flux, by following host stars that initiated their lives as slow, intermediate or fast rotators (Johnstone et al. 2015b). In our models, we also took into account contraction of the planet during its evolution (Fortney & Nettelmann 2010).

To probe the entire evolution, for the two different planet masses, and three different stellar rotations, we run more than 300 simulations of atmospheric escape, using a hydrodynamic escape model. We found that younger planets experience higher levels of atmospheric escape, owing to a favourable combination of higher irradiation levels and weaker planetary gravity (due to their larger radii). Lesser mass planets experience even higher escape rates than the more massive ones. Altogether, the lower gravitational potential of the less massive planet results in stronger planetary winds, with higher velocities and mass-loss rates.

In spite of the relatively large escape rates ($10^9 - 10^{12}$ g/s), we estimated that, over 5 Gyr, the $1-M_{\text{jup}}$ planet would lose at most 1% of its initial mass due to escape. However, for the $0.3-M_{\text{jup}}$ planet ($10^{10} - 10^{13}$ g/s), up to 20% of its mass could evaporate through hydrodynamic escape. This strong

escape in the lower mass planet is in line with observations of the short-period ‘Neptunian desert’, which shows a lack of planets at $\lesssim 5\text{--}10\text{-day}$ orbit, with masses between 0.03 and $0.3 M_{\text{jup}}$ (Mazeh et al. 2016). The desert is suggestive of significant mass loss in planets with masses $\lesssim 0.3 M_{\text{jup}}$, which is indeed confirmed by our models.

Using the results of our hydrodynamic models, we then computed spectroscopic transits in both $\text{Ly}\alpha$ and $\text{H}\alpha$ lines. The $\text{Ly}\alpha$ line is saturated at line centre and at mid-transit (we assume no impact parameter for simplicity), while $\text{H}\alpha$ transits produce transit depths of at most $3\text{--}4\%$ in excess of their geometric transit at younger ages. Planets older than 200 Myr (or 600 Myr, if orbiting around fast rotating star) would have $\text{H}\alpha$ absorption $\lesssim 1\%$ in excess of the geometric transit. While at older ages ($\gtrsim 1.2$ Gyr), $\text{Ly}\alpha$ absorption is still significant (and the line could even be saturated, as in the case of the lower mass planet), the $\text{H}\alpha$ absorption nearly disappears. This is because the extended atmosphere of neutral hydrogen becomes almost entirely in the ground state at such ages.

Our models, however, predict line profiles that are symmetric, in contrast to asymmetric profiles derived from observations (e.g., HD189733b (Lecavelier des Etangs et al. 2012); HD209458b (Vidal-Madjar et al. 2003; Ben-Jaffel 2008); GJ436b (Ehrenreich et al. 2015)). This is because our escape models are spherically symmetric. To overcome this limitation, we would need to consider additional physical ingredients in our models, such as charge-exchange between stellar wind protons and atmospheric neutrals, acceleration of neutral atoms due to radiation pressure and interaction of planetary flows with a stellar wind. Several multi-dimensional simulation studies have moved into this direction (e.g., Kislyakova et al. 2014; Khodachenko et al. 2015; Bourrier et al. 2016; Villarreal D’Angelo et al. 2018; Vidotto et al. 2018; McCann et al. 2019; Esquivel et al. 2019; Daley-Yates & Stevens 2019; Debrecht et al. 2019; Carolan et al. 2019). These physical mechanisms are also required to reproduce the large velocities seen in $\text{Ly}\alpha$. While these model provide more physical intuition in the details of the atmospheric escape, they can be computationally expensive.

The advantage of our models, versus more complex ones, is thus the ability of computing a large number of simulations due to their low computational cost. As a result, we can make general predictions that could help guide observations. We showed here that younger systems show deeper transits as well as larger widths in both $\text{H}\alpha$ and $\text{Ly}\alpha$ lines. In theory, this indicates that atmospheric escape is easier to detect during early ages. However, in practice, at younger ages, stars are more active, generating variability that could mimic signatures of atmospheric transits (Barnes et al. 2016; Jensen et al. 2018). This effect makes escape observations at young ages and/or around active stars more difficult to interpret and, thus, models, like ours, can assist in the interpretations of transit signatures.

Table 2.1: Coefficients to fits given in Equations (2.19) and (2.20) for the three considered host star rotations at various ages, as shown in Figure 2.3, for the $1-M_{\text{jup}}$ planet.

age range [Myr]	a	b	c	d
Slow				
10 – 30	13.8	1.58	1.71	0.107
30 – 250	12.2	0.532	1.66	0.0902
250 – 5000	14.4	1.37	1.79	0.175
Intermediate				
10 – 30	13.1	0.714	1.78	0.128
30 – 250	12.9	0.621	1.71	0.0991
250 – 5000	15.5	1.69	1.75	0.116
Fast				
10 – 30	12.2	-0.0918	1.94	0.174
30 – 250	12.7	0.287	1.70	0.0695
250 – 5000	17.4	2.24	1.67	0.0414

Acknowledgements

We acknowledge funding from the Irish Research Council Consolidator Laureate Award 2018. CHIANTI is a collaborative project involving George Mason University, the University of Michigan (USA), University of Cambridge (UK) and NASA Goddard Space Flight Center (USA). The authors thank C. Villarreal D’Angelo and A. Esquivel for their insightful comments and discussion.

Appendix

Analytical fits to mass-loss rates and terminal velocities

Here, we present power-law fits of the evolutionary curves of mass-loss rate and terminal velocity presented in Figure 2.3. These quantities take the form

$$\frac{\dot{M}}{[\text{g/s}]} = 10^a \left(\frac{\text{age}}{[\text{Myr}]} \right)^{-b} \quad (2.19)$$

$$\frac{u_{\text{term}}}{[\text{km/s}]} = 10^c \left(\frac{\text{age}}{[\text{Myr}]} \right)^{-d} \quad (2.20)$$

where a , b , c and d are shown in Tables 2.1 and 2.2. These expressions give errors of up to 1.5% for \dot{M} and 1.6% for u_{term} .

Equation 2.19 offers an alternative to the widely used energy-limited approximation for \dot{M} . In addition, a priori knowledge of the effective radius

Table 2.2: The same as in Table 2.1, but for the $0.3-M_{\text{jup}}$ planet.

age range [Myr]	a	b	c	d
Slow				
10 – 30	14.4	1.52	1.91	0.104
30 – 250	12.7	0.342	1.82	0.0758
250 – 5000	14.3	0.977	1.95	0.160
Intermediate				
10 – 30	13.7	0.630	1.91	0.106
30 – 250	13.4	0.488	1.86	0.0897
250 – 5000	15.3	1.26	1.93	0.125
Fast				
10 – 30	12.9	-0.138	2.02	0.136
30 – 250	13.4	0.227	1.85	0.0662
250 – 5000	17.0	1.76	1.87	0.0716

$R_{\tau=1}$ included in the energy limited approximation (Equation 2.10) is not required by our expression for mass-loss rates.



3 | EVOLUTION OF HELIUM TRIPLET TRANSITS OF CLOSE-IN GAS GIANTS ORBITING K-DWARFS

A. P. Allan, A. A. Vidotto, C. Villarreal D'Angelo, L. A. Dos Santos, F. A. Driessen, *Monthly Notices of the Royal Astronomical Society*, Volume 527, Issue 3, January 2024, Pages 4657–4676.

Abstract

Atmospheric escape in exoplanets has traditionally been observed using hydrogen Lyman- α and H- α transmission spectroscopy, but more recent detections have utilised the metastable helium triplet at 1083 nm. Since this feature is accessible from the ground, it offers new possibilities for studying atmospheric escape. Our goal is to understand how the observability of escaping helium evolves during the lifetime of a highly irradiated gas giant. We extend our previous work on 1-D self-consistent hydrodynamic escape from hydrogen-only atmospheres as a function of planetary evolution to the first evolution-focused study of escaping hydrogen-helium atmospheres. Additionally, using these novel models we perform helium triplet transmission spectroscopy. We adapt our previous hydrodynamic escape model to now account for both hydrogen and helium heating and cooling processes and simultaneously solve for the population of helium in the triplet state. To account for the planetary evolution, we utilise evolving predictions of planetary radii for a close-in $0.3 M_{\text{Jup}}$ gas giant and its received stellar flux in X-ray, hard and soft EUV, and mid-UV wavelength bins assuming a K dwarf stellar host. We find that the helium triplet signature diminishes with evolution. Our models suggest that young ($\lesssim 150$ Myr), close-in gas giants (~ 1 to $2 R_{\text{Jup}}$) should produce helium 1083 nm transit absorptions of $\sim 4\%$ or $\sim 7\%$, for a slow or fast-rotating K dwarf, respectively, assuming a 2% helium abundance.

3.1 Introduction

Highly irradiated exoplanets undergo extreme atmospheric escape. This occurs mainly through the process of hydrodynamic escape, in which photoionisations of hydrogen (and, to a lesser extent, helium) atoms by X-ray and extreme-ultraviolet (hereafter XUV) photons heat the atmosphere causing its expansion and ultimately a bulk outflow of the material. This escape process can be modelled by treating the atmosphere as a collisional fluid (Yelle 2004; Murray-Clay et al. 2009). In addition to the stellar XUV heating, heating from the planet interior can also contribute to the atmospheric escape mechanism (Ginzburg et al. 2018; Kubyshkina et al. 2020; Kubyshkina & Vidotto 2021; Kubyshkina & Fossati 2022).

Intense atmospheric escape can affect a planet’s overall evolution and structure. The level of atmospheric escape in highly irradiated gas giant planets declines substantially with planetary evolution (e.g. Owen 2019; Allan & Vidotto 2019; Pezzotti et al. 2021b). A reduction in the stellar XUV flux received with age and a growing planetary gravitational force are responsible for this. Failure to account for how atmospheric escape varies with evolution can lead to significant inaccuracies in the predicted atmospheric structure and escape. Strong atmospheric escape over the lifetime of a planet is one of the explanations offered for apparent trends in the detected population of exoplanets, namely the ‘hot-Neptune desert’ (Mazeh et al. 2016; Owen & Lai 2018) and the ‘radius valley’ (Fulton et al. 2017). Planetary evolution not only impacts the physical process of escape but additionally its corresponding observable signatures. In Allan & Vidotto (2019), we found that the hydrogen Lyman- α and H- α signatures of atmospheric escape weaken significantly over the evolution of highly irradiated gas giants with primordial hydrogen atmospheres.

Since our previous evolution study, there has been an explosion of detections of atmospheric escape using a new spectroscopic signature, the metastable helium triplet at 1083 nm (for theoretical studies, see Seager & Sasselov 2000; Oklopčić & Hirata 2018). This signature’s ability to be observed using ground-based (in addition to space-based) facilities is greatly responsible for its popularity, and it presents a great advantage over the more traditional hydrogen Lyman- α signature, which is observable only from space. Additionally, the Lyman- α line suffers from strong interstellar medium absorption and contamination by geocoronal emission, rendering the line core unusable in atmospheric escape analysis.

Since the first detections of escaping helium (Nortmann et al. 2018; Spake et al. 2018; Allart et al. 2018), there have been over a dozen detections (e.g., Allart et al. 2019; Alonso-Floriano et al. 2019; Kirk et al. 2020; Spake et al. 2021; Guilluy et al. 2020; Fu et al. 2022), as well as many constraint-setting non-detections, (e.g., Zhang et al. 2021; Krishnamurthy

et al. 2021; Fossati et al. 2022). For a recent compilation of detections and non-detections, we refer the reader to Dos Santos (2023).

Of the helium 1083 nm detections, K-type host stars appear to be favoured. This has been explained by their relatively low mid-UV flux, which depopulates the helium triplet state, and a high EUV flux, which populates the state through photoionisations followed by recombinations (Oklopčić 2019). Due to the favourability of K-type hosts, both models and observations of their spectra are important for interpreting escaping helium detections (France et al. 2016; Johnstone et al. 2021; Poppenhaeger 2022; Richey-Yowell et al. 2022). An important consideration is that there is no ‘typical’ XUV flux that fits all K dwarfs (see, e.g., Loyd et al. 2016; Youngblood et al. 2016; Sanz-Forcada 2022). In cool dwarf stars, the high-energy radiation originates in the chromosphere and corona, and they are ultimately related to the magnetic activity of the star (e.g. Vidotto et al. 2014; Toriumi & Airapetian 2022; Namekata et al. 2023). Because activity decays substantially with age, the XUV flux of K dwarfs is significantly affected with evolution (Johnstone et al. 2021; Pezzotti et al. 2021a).

In the context of predicting helium transit signatures, many of the existing models adopt a one-dimensional (1-D) Parker wind solution (Parker 1958), assuming either an isothermal atmosphere or a constant speed of sound (Oklopčić & Hirata 2018; Lampón et al. 2021; Dos Santos et al. 2022), and thus neglecting the self-consistent calculation of the energetics of the flow. However, such models often result in a degeneracy between the temperature and the mass-loss rate. Linssen et al. (2022) reduce this degeneracy, by linking isothermal Parker wind solutions with the detailed photoionisation code CLOUDY (Ferland et al. 1998, 2017), in order to rule out regions of the explored temperature -mass loss parameter space, without requiring the added complexity of self-consistently modelling the escape, by solving the coupled hydrodynamic and radiative processes consistently. The latter is instead the approach of the 1-D models of TPCI (Salz et al. 2015) and ATEs (Caldiroli et al. 2021), which is more similar to our approach.

In this paper, we compute atmospheric hydrodynamic escape solutions using a single, non-isothermal hydrodynamic model, which self-consistently incorporates energetic balance through different heating and cooling mechanisms. As will be detailed, we have modified the hydrogen-only model of Allan & Vidotto (2019) to achieve this. Our model still assumes spherical symmetry (i.e, it is 1-D). Because three-dimensional (3-D) models naturally account for asymmetries arising from a variety of processes, such as interactions with the stellar wind, magnetism and day-to-night side variations (Villarreal D’Angelo et al. 2014, 2018; McCann et al. 2019; Carolan et al. 2020, 2021a), they are more realistic than 1-D models. A wealth of information on the helium signature of escape has already been gained from 3-D models (Shaikhislamov et al. 2021; Khodachenko et al. 2021a; MacLeod & Oklopčić 2022; Wang & Dai 2021b,a; Rumenskikh et al. 2022; Yan et al.

2022). However, their long computational time leaves 3-D models poorly suited for evolution studies, like ours, that require numerous models at differing ages.

Here, we model the long-term evolution of atmospheric escape of planets orbiting K dwarfs, taking into account both the evolution of the host star and the planet. The main goal is to study the evolution of the helium 1083 nm signature. To the best of our knowledge, this study is the first with this goal. Our model computes self-consistently the ionisation of hydrogen, as well as both the single and double ionisation of helium and its population in the 1^1S , 2^1S and 2^3S states. In section 3.2, we describe this model. Section 3.3 outlines our planetary evolution set-up, while section 3.4 showcases how the physical process of atmospheric escape varies with evolution. In section 3.5, we present our ray-tracing technique for simulating helium 1083 nm transmission spectroscopic transits and the resulting transit predictions with evolution. Finally, section 3.6 summarises the main findings of our study.

3.2 Atmospheric escape model through photoionisation

One of the main drawbacks of describing atmospheric escape using a Parker wind model is that the solution of these types of models are highly sensitive to the assumed isothermal temperature (Parker 1958). Additionally, the escape rates also depend strongly on the assumed base densities. While Parker-type models are extremely useful, allowing for quick predictions for atmospheric escape (e.g. Dos Santos et al. 2022), they omit important physics such as heating and cooling processes, which produce non-isothermal temperature structures, which can then affect the derived signatures of spectroscopic transits.

To model the evolution of atmospheric escape, we update the photoionisation driven escape model described in Allan & Vidotto (2019, see also Murray-Clay et al. 2009) to now include helium in addition to hydrogen. Original and current model versions are both non-isothermal, 1-D, spherically symmetric and treat the escaping atmosphere as a fluid. They solve the equations of fluid dynamics in a co-rotating frame using a shooting method approach (e.g. Vidotto & Cleary 2020). Additionally, the new helium-incorporated version presented in this work

- tracks the state of helium, accounting for transitions between the helium 1^1S , 2^1S , 2^3S , singly and doubly ionised states (displayed in Figure 3.1).
- Considers heating and cooling due to hydrogen and helium.

- Reads separate X-ray, mid-UV, hard and soft EUV fluxes.
- Considers photons emitted in direct recombinations and radiative decays to the helium (1^1S) state.

Previously, we considered only photoionisations arising from a given monochromatic flux of EUV photons, implying that the input flux of EUV photons was concentrated at a representative photon energy of 20 eV. Here, we drop the monochromatic approximation and instead utilise four separate energy flux bins, each with their own representative energies (e_λ). Going beyond a monochromatic flux is necessary for our present work due to the differing minimum photoionisation energies of hydrogen and the considered helium states. Furthermore, the individual flux bins each have their own unique dependencies on age. Table 3.1 lists the hydrogen and helium photoionisations we consider and their respective cross-sections (σ_λ) and excess kinetic energy factors (ϵ_λ). The wavelength ranges covered by these chosen flux bins are X-ray (0.517-12.4 nm), hard EUV (hEUV, 10-36 nm), soft-EUV (hereafter sEUV, 36-92 nm) and mid-UV (91.2-320 nm). We set their representative energies e_λ as 248, 40, 20 and 7 eV, respectively. Some of our bin selections are consistent with values used in other models in the literature such as Murray-Clay et al. (2009); Kubyshkina et al. (2018); Wang & Dai (2021a,b). Table 3.1 also lists parameters for three additional photoionising sources, photons with energies 24.6, 21.2 and 10.3 eV arising from helium state transitions in the planetary atmosphere, rather than originating directly from the assumed stellar source. Photoionisations in the model are discussed in more detail in section 3.2.3.

3.2.1 Fluid dynamic equations

We model the escaping planetary atmosphere by treating it as a non-isothermal outflow, utilising the equations of fluid dynamics. These equations enforce the conservation of momentum, energy, and mass. In steady state, the momentum equation in spherical symmetry can be written as

$$u \frac{d(u)}{dr} = -\frac{1}{\rho} \frac{dP}{dr} - \frac{GM_{\text{pl}}}{r^2} + \frac{3GM_* r}{a^3}, \quad (3.1)$$

where r is the radial coordinate from the centre of the planet, ρ and u represent the atmospheric mass density and velocity, respectively, and P is the thermal pressure. The masses of star and planet are M_* and M_{pl} , and the orbital distance is a . The first term on the right hand side of Equation 3.1 is the thermal pressure gradient while the second term represents attraction due to gravity. This equation is analogous to the momentum equation for a stellar wind (Parker 1958) with an additional term on the right side due

Table 3.1: Considered photoionisation processes and their respective excess kinetic energy factors ϵ_λ , cross-section σ_λ and their relevant reference. References correspond to: (Spitzer 1978)^a, (Osterbrock & Ferland 2006)^b, (Brown 1971)^c, (Norcross 1971)^d, (Verner et al. 1996)^e.

ID	absorber	photon energy	ϵ_λ	σ_λ (cm ²)	ref.
(3.1.1)	H ⁰	sEUV: 20 eV	0.32	2.21×10^{-18}	a,b
(3.1.2)	H ⁰	hEUV: 40 eV	0.66	8.29×10^{-20}	a,b
(3.1.3)	H ⁰	X-ray: 248 eV	0.95	1.10×10^{-21}	a,b
(3.1.4)	H ⁰	24.6 eV	0.45	1.24×10^{-18}	a,b
(3.1.5)	H ⁰	21.2 eV	0.36	1.87×10^{-18}	a,b
(3.1.6)	He(1 ¹ S)	hEUV: 40 eV	0.36	2.15×10^{-18}	c
(3.1.7)	He(1 ¹ S)	X-ray: 248 eV	0.90	3.00×10^{-20}	c
(3.1.8)	He(1 ¹ S)	24.6 eV	0	2.42×10^{-19}	c
(3.1.9)	He(2 ³ S)	mid-UV: 7 eV	0.31	3.68×10^{-18}	d
(3.1.10)	He(2 ³ S)	sEUV: 20 eV	0.76	5.48×10^{-19}	d
(3.1.11)	He(2 ³ S)	hEUV: 40 eV	0.88	9.00×10^{-19}	d
(3.1.12)	He(2 ³ S)	24.6 eV	0.80	4.26×10^{-19}	d
(3.1.13)	He(2 ³ S)	21.2eV	0.77	4.97×10^{-19}	d
(3.1.14)	He(2 ³ S)	10.3eV	0.54	1.95×10^{-18}	d
(3.1.15)	He(2 ¹ S)	mid-UV: 7 eV	0.43	3.63×10^{-18}	d
(3.1.16)	He(2 ¹ S)	sEUV: 20 eV	0.80	3.35×10^{-19}	d
(3.1.17)	He(2 ¹ S)	hEUV: 40 eV	0.90	1.00×10^{-18}	d
(3.1.18)	He(2 ¹ S)	24.6 eV	0.84	2.42×10^{-19}	d
(3.1.19)	He(2 ¹ S)	21.2eV	0.81	3.03×10^{-19}	d
(3.1.20)	He(2 ¹ S)	10.3eV	0.61	1.71×10^{-18}	d
(3.1.21)	He ⁺	X-ray: 248 eV	0.78	2.09×10^{-20}	e

to tidal effects. The tidal term is the sum of the centrifugal force and differential stellar gravity along the line between the planet and star (García Muñoz 2007).

Conservation of energy requires that

$$\rho u \frac{d}{dr} \left(\frac{k_B T}{(\gamma - 1)m} \right) = \frac{k_B T}{m} u \frac{d\rho}{dr} + Q - C, \quad (3.2)$$

where k_B is the Boltzmann constant, T is the gas temperature, $\gamma = 5/3$ and m is the mean particle mass. The term on the left indicates the change in the internal energy of the fluid. The first term on the right represents cooling due to gas expansion (adiabatic cooling), while the second (Q) and third (C) are heating and cooling terms, which in this work accounts for a number of physical process involving hydrogen and helium species (see sections 3.2.3 and 3.2.4). This equation is, again, typically used in stellar wind models, although with different heating and cooling terms (Vidotto & Jatenco-Pereira 2006).

The conservation of mass requires that

$$\frac{d(r^2 \rho u)}{dr} = 0. \quad (3.3)$$

Our simulated planetary outflow originates from the sub-stellar point of the planet, which is the point closest to the star. We then apply our calculated solution over 4π steradians rendering it an upper limit to atmospheric escape (Murray-Clay et al. 2009; Johnstone et al. 2015b). Therefore, from Equation 3.3, we have that the mass-loss rate of the escaping atmosphere is $\dot{m} = 4\pi r^2 \rho u$.

We also solve the equation of ionisation balance of hydrogen

$$u \frac{d(n_{\text{H}^+})}{dr} = \Phi [\text{H}^0] + \Psi [\text{H}^0] - \alpha_B [\text{H}^0]. \quad (3.4)$$

This equation states that the advection of hydrogen ions (first term) is balanced by the combined rate of photo-ionisation ($\Phi [\text{H}^0]$, see Equation 3.10 and Table 3.1) and collisional-ionisation ($\Psi [\text{H}^0]$, Table 3.2) of neutral hydrogen with the radiative recombinations ($\alpha_B [\text{H}^0]$, also see Table 3.2).

Altogether, the fluid dynamic equations (Equations 3.1-3.3), the hydrogen ionisation balance equation (Equation 3.4) and the four additional helium population equations (see next section, Equations 3.5 - 3.8) form a system of coupled differential equations. There is only one physical solution for this system: a transonic wind beginning at the base of the atmosphere with a subsonic velocity, passing through the sonic point and thereby reaching supersonic velocities (Parker 1958). Contrary to isothermal wind models, we do not know a priori the location of the sonic point nor the initial wind velocity, therefore we follow a numerical approach in solving the

coupled differential equations utilising a ‘shooting method’ combined with a fourth order Runge-Kutta solver and an iteration scheme. Our initial solution assumes a hydrostatic atmosphere for the density, and the shooting method finds the solution that passes through the sonic point. This new solution provides a different density profile than initially assumed, so using this newly found density structure, we again search for the solution that passes through the sonic point through the shooting method. In this way, the density, temperature, velocity and optical depth profiles are updated with each set of iterations of the shooting method, iteratively approaching to a converged solution. We consider this solution to have been reached once the predicted mass-loss rate and terminal velocity of two subsequent model results agree to within 1%. All atmospheric profiles are calculated with a resolution of $10^{-6}R_{\text{pl}}$ below the sonic point, and $2 \times 10^{-5}R_{\text{pl}}$ above.

The necessary free parameters of our model include the temperature $T_0 = 1000$ K and density $\rho_0 = 4 \times 10^{-14}$ g cm $^{-3}$ at the base of the atmosphere, chosen to be at $1 R_{\text{pl}}$. [Allan & Vidotto \(2019\)](#) and [Murray-Clay et al. \(2009\)](#) found that large variations in these values had a negligible effect on the resulting simulated escape. This is similar in our models as will be further discussed in Appendix A. Our model must also be given initial guesses for the abundances by number at the base of the atmosphere for ionised hydrogen, singly- and doubly- ionised helium as well as its 1^1S , 2^1S and 2^3S states. These initial guesses were 10^{-5} , 10^{-5} , 10^{-7} , ~ 1 , ~ 0 and ~ 0 , meaning that initially both hydrogen and helium are predominantly neutral, with helium being nearly entirely in its singlet state. To ensure the validity of the hydrodynamic escape we model, once the solution is found, we confirm that the atmosphere remains within the collisional regime with a Knudsen number (ratio of mean free path to atmospheric scale height) < 1 . In the non-collisional regime, particle models such as those used in [Bourrier & Lecavelier des Etangs \(2013\)](#); [Bourrier et al. \(2016\)](#); [Allart et al. \(2018\)](#); [Spake et al. \(2018\)](#); [Allart et al. \(2019\)](#) are better suited to model atmospheric escape. Our models are computed all the way to $10 R_{\text{pl}}$, but we note that in reality, the extent of the atmosphere could be larger or smaller, as its boundary should be set by the interactions with the wind of the host star (e.g. [Vidotto & Cleary 2020](#)), neglected in our study.

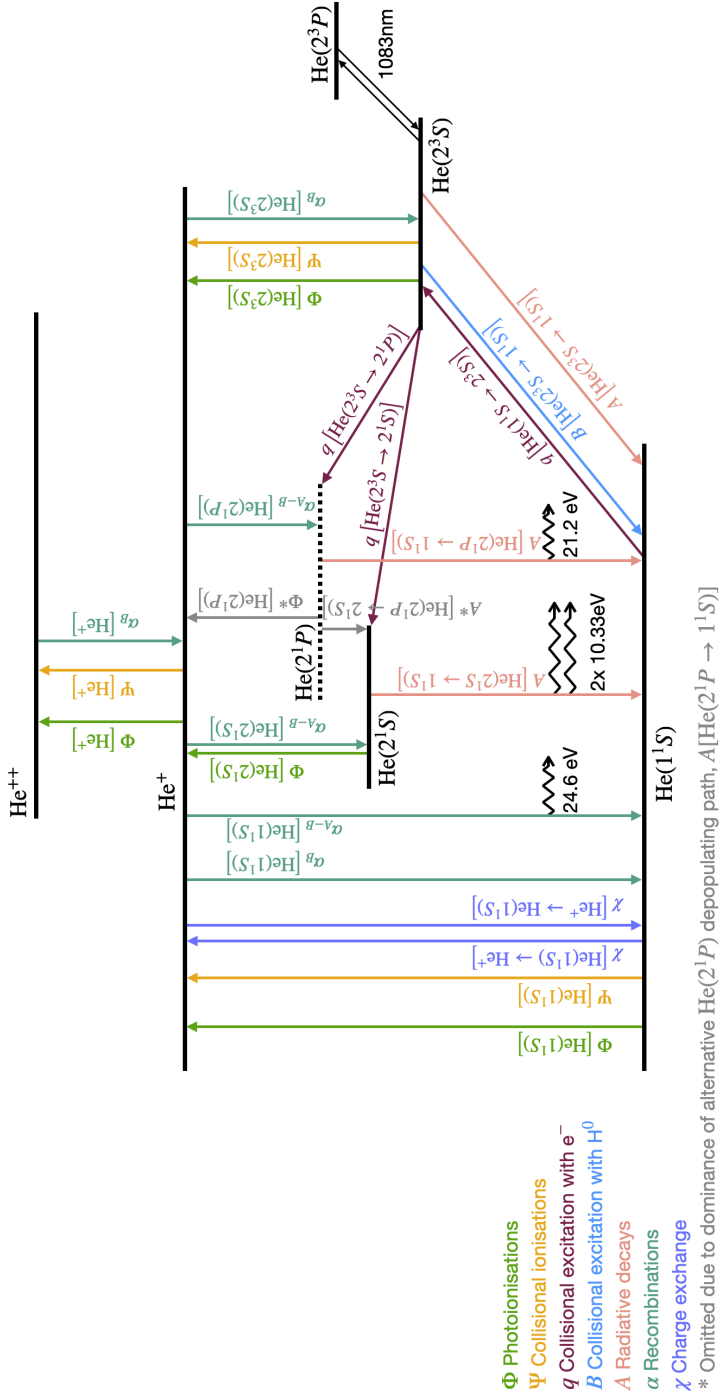


Figure 3.1: Schematic displaying the various helium processes considered in our modelling. See Table 3.2 for the rate equations and their relevant references.

3.2.2 Calculating helium state populations

In addition to Equations 3.1 to 3.4, we also solve four continuity equations for the populations of helium, in the helium singlet ground state, $\text{He}(1^1S)$

$$\begin{aligned}
 u \frac{d(f_{1^1S})}{dr} = & \alpha_B [\text{He}(1^1S)] + \alpha_{A-B} [\text{He}(1^1S)] \\
 & + B [\text{He}(2^3S \rightarrow 1^1S)] \\
 & + A [\text{He}(2^3S, 2^1S, 2^1P \rightarrow 1^1S)] \\
 & + \chi [\text{He}^+ \rightarrow \text{He}(1^1S)] - \chi [\text{He}(1^1S) \rightarrow \text{He}^+] \\
 & - q [\text{He}(1^1S \rightarrow 2^3S)] - \Phi [\text{He}(1^1S)] - \Psi [\text{He}(1^1S)],
 \end{aligned} \tag{3.5}$$

the helium triplet state, $\text{He}(2^3S)$

$$\begin{aligned}
 u \frac{d(f_{2^3S})}{dr} = & \alpha_B [\text{He}(2^3S)] + q [\text{He}(1^1S \rightarrow 2^3S)] \\
 & - q [\text{He}(2^3S \rightarrow 2^1S, 2^1P)] \\
 & - A [\text{He}(2^3S \rightarrow 1^1S)] - B [\text{He}(2^3S \rightarrow 1^1S)] \\
 & - \Phi [\text{He}(2^3S)] - \Psi [\text{He}(2^3S)],
 \end{aligned} \tag{3.6}$$

the helium 2^1S state, $\text{He}(2^1S)$

$$\begin{aligned}
 u \frac{d(f_{2^1S})}{dr} = & \alpha_{A-B} [\text{He}(2^1S)] + q [\text{He}(2^3S \rightarrow 2^1S)] \\
 & - A [\text{He}(2^1S \rightarrow 1^1S)] - \Phi [\text{He}(2^1S)],
 \end{aligned} \tag{3.7}$$

and the singly ionised helium state, He^+

$$\begin{aligned}
 u \frac{d(f_{\text{He}^+})}{dr} = & \Phi [\text{He}(1^1S, 2^1S, 2^3S)] + \Psi [\text{He}(1^1S, 2^3S)] \\
 & + \alpha_B [\text{He}^+] - \alpha_B [\text{He}(1^1S)] - \alpha_{A-B} [\text{He}(1^1S)] \\
 & - \alpha_{A-B} [\text{He}(2^1S)] - \alpha_{A-B} [\text{He}(2^1P)] \\
 & - \alpha_B [\text{He}(2^3S)] - \Phi [\text{He}^+] - \Psi [\text{He}^+] \\
 & + \chi [\text{He}(1^1S) \rightarrow \text{He}^+] - \chi [\text{He}^+ \rightarrow \text{He}(1^1S)].
 \end{aligned} \tag{3.8}$$

These state that the fractions of helium in its 1^1S , 2^3S , 2^1S , and singly ionised states f_{1^1S} , f_{2^3S} , f_{2^1S} and f_{He^+} respectively, are determined by the balance of the processes directly populating and depopulating these states. These processes (de-)populating the helium states are defined as follows

- Φ - photoionisations (out of the state in parentheses) by capable stellar XUV and mid-UV photons as well as by photons released in the planetary atmosphere through helium transitions,

- ψ - collisional ionisations (out of the state in parentheses),
- α - recombinations (into the state in parentheses),
- q - collisional excitation with a free electron,
- B - collisional excitation with H^0 ,
- A - radiative decays,
- χ - charge exchange.

Table 3.2 lists all of their corresponding rate equations for these helium states in addition to that for hydrogen. Figure 3.1 visualises the considered paths for the helium states. The helium number densities in each state are obtained by multiplying their respective fraction by the total number density of helium n_{He} . Our model considers free electrons produced from both hydrogen and helium ionisations while maintaining a neutral net charge for the global modelled atmosphere. We also calculate the fraction of doubly-ionised helium, assuming its number density to be $n_{\text{He}^{++}} = n_{\text{He}} - n_{1^1S} - n_{2^3S} - n_{2^1S} - n_{\text{He}^+}$. However, including He^{++} is found to have a negligible effect on the modelled hydrodynamics and observability of atmospheric escape.

Being a non-metastable and hence short-lived state (Wiese & Fuhr 2009), our model does not solve for the fraction of helium in the 2^1P state. Rather, we follow Oklopčić & Hirata (2018) in allowing electron collisional excitation from 2^3S to 2^1P , $q [\text{He}(2^3S \rightarrow 2^1P)]$ to populate the 1^1S state on account of the rapid decay, $A [\text{He}(2^1P \rightarrow 1^1S)]$. Lampón et al. (2020) and Dos Santos et al. (2022) also follow this assumption, which most importantly accounts for the depopulation of the 2^3S state. Additionally, our model considers recombinations into 2^1P , $\alpha_{A-B} [\text{He}(2^1P)]$, which is also set to populate 1^1S in our model’s helium equations. It should be noted that the rapid radiative decay from the 2^1P to 1^1S state $A [\text{He}(2^1P \rightarrow 1^1S)]$ releases a 21.2 eV photon (Eikema et al. 1996; Sun & Hu 2020), capable of photoionising hydrogen, helium 2^3S and 2^1S in our model¹. As will be discussed in section 3.2.3, our model considers such photoionisations.

¹The released 21.2 eV is also capable of photoionising $\text{He}(2^1P)$ however our model does not account for this particular photoionisation as we do not solve for the $\text{He}(2^1P)$ fraction. Given that the rapid radiative decay $A [\text{He}(2^1P \rightarrow 1^1S)]$ is an alternative depopulating path for $\text{He}(2^1P)$, we consider omitting these photoionisations to be reasonable. Furthermore, the cross section for the photoionisation of $\text{He}(2^1P)$ is between one and two orders of magnitudes less than that for 2^1S and 2^3S as shown in Figure 3.2.

3.2. ATMOSPHERIC ESCAPE MODEL THROUGH PHOTOIONISATION

62

Table 3.2: The populating and depopulating processes for the hydrogen and helium states considered in our model. Densities are given in cm^{-3} and temperature in K. $\text{He}(2^1P)^*$ is marked with an asterisk as a reminder that we do not solve for the fraction of helium in the 2^1P state, as it is short-lived (see section 3.2.2). α_B^* $[\text{He}(1^1S)]$ is marked with an asterisk to draw attention to the removal of helium 2^1P and 2^3S recombinations from this term. Letters correspond to the following references: (Brown 1971)^a, (Norcross 1971)^b, (Verner et al. 1996)^c, (Spitzer 1978)^d, (Osterbrock & Ferland 2006)^e, (Benjamin et al. 1999)^f, (Wiese & Fuhr 2009)^g, (Eikema et al. 1996)^h, (Bergeson et al. 1998)ⁱ, (Hui & Gnedin 1997)^j, (Caldiroli et al. 2021)^k, (Storey & Hummer 1995)^l, (Bray et al. 2000)^m, (Lampón et al. 2020)ⁿ, (Roberge & Dalgarno 1982)^o, (Oklopčić & Hirata 2018)^p, (Cen 1992)^q, (Koskinen et al. 2013)^r, (Drake 1971)^s.

populates	depopulates	rates (s^{-1})	reference
He ⁺ He ⁺ He ⁺ He ⁺⁺ H ⁺	He(1 ¹ S) He(2 ³ S) He(2 ¹ S) He ⁺ H ⁰	photoionisation by stellar XUV and mid-UV photons Equation 3.10 and Table 3.1 for rate, caused by $\lambda_{\text{hEUV}/X\text{-ray}}$ Equation 3.10 and Table 3.1 for rate, caused by $\lambda_{\text{s/hEUV}/\text{mid-UV}}$ Equation 3.10 and Table 3.1 for rate, caused by $\lambda_{\text{s/hEUV}/\text{mid-UV}}$ Equation 3.10 and Table 3.1 for rate, caused by $\lambda_{X\text{-ray}}$ Equation 3.10 and Table 3.1 for rate, caused by $\lambda_{\text{s/hEUV}/X\text{-ray}}$	a b b c d,e
H ⁺ / He ⁺ H ⁺ / He ⁺ He ⁺	H ⁰ / He(1 ¹ S, 2 ¹ S, 2 ³ S) H ⁰ / He(2 ¹ S, 2 ³ S) He(2 ¹ S, 2 ³ S)	photoionisation by planetary-atmosphere-produced photons $\zeta_{\text{sp},24.6\text{ eV}} \alpha_{A-B} [\text{He}(1^1S)]$ $\zeta_{\text{sp},21.2\text{ eV}} A [\text{He}(2^1P \rightarrow 1^1S)]$ $2 \zeta_{\text{sp},10.3\text{ eV}} A [\text{He}(2^1S \rightarrow 1^1S)]$	e, f g, h e, i
He(2 ³ S) He(2 ¹ S) He(2 ¹ P)* He(1 ¹ S) He(1 ¹ S) He ⁺ H ⁰	He ⁺ He ⁺ He ⁺ He ⁺ He ⁺ He ⁺⁺ H ⁺	recombination $\alpha_B [\text{He}(2^3S)] = 2.10 \times 10^{-13} (T/10^4)^{-0.778} n_e f_{\text{He}^+}$ $\alpha_{A-B} [\text{He}(2^1S)] = 5.55 \times 10^{-15} (T/10^4)^{-0.451} n_e f_{\text{He}^+}$ $\alpha_{A-B} [\text{He}(2^1P)] = 1.26 \times 10^{-14} (T/10^4)^{-0.695} n_e f_{\text{He}^+}$ $\alpha_B \cdot [\text{He}(1^1S)] = 6.23 \times 10^{-14} (T/10^4)^{-0.827} n_e f_{\text{He}^+} - \alpha_{A-B} [\text{He}(2^1P)] - \alpha_{A-B} [\text{He}(2^1S)]$ $\alpha_{A-B} [\text{He}(1^1S)] = 1.54 \times 10^{-13} (T/10^4)^{-0.486} n_e f_{\text{He}^+}$ (emits 24.6 eV photon) $\alpha_B [\text{He}^+] = 5.506 \times 10^{-14} (1263030/T)^{1.5} (1 + (460960/T)^{0.407})^{-2.242} n_e f_{\text{He}^{++}}$ $\alpha_B [\text{H}^0] = 2.7 \times 10^{-13} (T/10^4)^{-0.9} n_e f_{\text{H}^+}$	f f f f f j, k l, e
He(2 ¹ S) He(2 ¹ P)* He(1 ¹ S) He(2 ³ S)	He(2 ³ S) He(2 ³ S) He(2 ³ S) He(1 ¹ S)	collisional (de-)excitation $q [\text{He}(2^3S \rightarrow 2^1S)] = 2.6 \times 10^{-8} n_e f_{2^3S}$ $q [\text{He}(2^3S \rightarrow 2^1P)] = 4.0 \times 10^{-9} n_e f_{2^3S}$ $B [\text{He}(2^3S \rightarrow 1^1S)] = 5.0 \times 10^{-10} n_{\text{H}^0} f_{2^3S}$ $q [\text{He}(1^1S \rightarrow 2^3S)] = 4.5 \times 10^{-20} n_e f_{1^1S}$	m, p m, p n, p m, p
H ⁺ He ⁺ He ⁺ He ⁺⁺	H ⁰ He(1 ¹ S) He(2 ³ S) He ⁺	collisional ionisation $\Psi [\text{H}^0] = (1.27 \times 10^{-21} T^{0.5} \exp[-157809.1/T] n_e f_{\text{H}^0}) / (\epsilon_{\text{ion, H}^0} [\text{erg}])$ $\Psi [\text{He}(1^1S)] = (9.38 \times 10^{-22} T^{0.5} \exp[-285335.4/T] n_e f_{1^1S}) / (\epsilon_{\text{ion, He}(1^1S)} [\text{erg}])$ $\Psi [\text{He}(2^3S)] = (6.41 \times 10^{-21} T^{0.5} \exp[-55338/T] n_e f_{2^3S}) / (\epsilon_{\text{ion, He}(2^3S)} [\text{erg}])$ $\Psi [\text{He}^+] = (4.95 \times 10^{-22} T^{0.5} \exp[-631515/T] n_e f_{\text{He}^+}) / (\epsilon_{\text{ion, He}^+} [\text{erg}])$	q q q q
He(1 ¹ S), H ⁺ He ⁺ , H ⁰	He ⁺ , H ⁰ He(1 ¹ S), H ⁺	charge exchange $\chi [\text{He}^+ \rightarrow \text{He}(1^1S)] = 1.25 \times 10^{-15} (300/T)^{-0.25} n_{\text{H}^0} f_{\text{He}^+}$ $\chi [\text{He}(1^1S) \rightarrow \text{He}^+] = 1.75 \times 10^{-11} (300/T)^{0.75} \exp[-128000/T] n_{\text{H}^+} f_{1^1S}$	r, n r, n
He(1 ¹ S) He(1 ¹ S) He(1 ¹ S)	He(2 ³ S) He(2 ¹ S) He(2 ¹ P)*	radiative decay $A [\text{He}(2^3S \rightarrow 1^1S)] = 1.272 \times 10^{-4} f_{2^3S}$ $A [\text{He}(2^1S \rightarrow 1^1S)] = 51.3 f_{2^1S}$ (emits two 10.3 eV photons) $A [\text{He}(2^1P \rightarrow 1^1S)] = 1.7989 \times 10^2 f_{2^1P}$ $\approx q [\text{He}(2^3S \rightarrow 2^1P)] + \alpha_{A-B} [\text{He}(2^1P)]$ (emits 21.2 eV photon)	s e g assumed here

We use Case-B coefficients in our calculations of hydrogen and the helium 2^3S , 2^1S , 2^1P states. Direct recombinations (i.e. Case-A – Case-B) are not considered for these mentioned states, given their low energies and the high probability for the photon released in the process to photoionise a species identical to that formed in the recombination, resulting in no net variation in the ionisation fraction. Direct recombinations to He(1^1S) state however are different in that they release a higher energy 24.6 eV photon (Benjamin et al. 1999; Osterbrock & Ferland 2006), capable of photoionising both the more abundant hydrogen in addition to the various helium states. Accordingly, we calculate both direct and non-direct recombinations for He(1^1S), in order to obtain the rate of the 24.6 eV photoionisations, as will be discussed in section 3.2.3.

In short, our model considers hydrogen and helium photoionisation, collisional ionisation, recombination, collisional (de-) excitation, charge exchange and radiative decays. Our model solves the four helium populations equations (Equations 3.5 to 3.8) simultaneously with Equations 3.1 to 3.4.

To model the escape of a primordial hydrogen and helium atmosphere, the helium to hydrogen number abundance must be known. Models have typically assumed this to be constant throughout their atmosphere, which we also assume. Some typically derived values are: He/H \sim 0.02/0.98 for HD209458b (Lampón et al. 2020; Khodachenko et al. 2021b); He/H \sim 0.016/0.984 (Shaikhislamov et al. 2021) and He/H \sim 0.015/0.985 (Lampón et al. 2021) for GJ3470b; He/H \sim 0.008/0.992 (Lampón et al. 2021) and He/H \sim 0.005/0.995 (Rumenskikh et al. 2022) for HD189733b. All of the mentioned helium abundances fall below the solar value of approximately 0.1. Models of WASP-107b were the first to obtain a He/H number abundance close to the solar value, with a predicted helium abundance of 0.075-0.15 (Khodachenko et al. 2021a). In our models, we use helium number abundances of 0.02 and 0.1 to investigate how this affects the predicted transits.

3.2.3 Photoionisation and heating processes with hydrogen and helium

Photoionisations are not only important for determining the population of atmospheric hydrogen and helium states. If a given photon has an energy in excess of the photoionisation energy, this excess is transferred to an electron in the form of kinetic energy. This collisional process acts to heat up the atmosphere.

The amount of photoionisations and heating that is deposited in the atmosphere depends on the individual optical depths τ_λ for each of the

considered photoionisations

$$\tau_\lambda = \int_{\text{top}}^{1R_{\text{pl}}} n \sigma_\lambda dr, \quad (3.9)$$

where n is the number density of the absorber (neutral hydrogen, helium singlet or triplet) and σ_λ is the absorber- and wavelength-dependent photoionisation cross section (Table 3.1). The integration is performed for distances r starting at the top of the atmosphere ($10R_{\text{pl}}$, in our models) until the bottom of the atmosphere at $1R_{\text{pl}}$. The rate of one of the considered photoionisations is then

$$\Phi_\lambda = F_\lambda \zeta_{\text{sp},\lambda} e^{-\tau_\lambda} \sigma_\lambda \frac{1}{e_\lambda}, \quad (3.10)$$

where F_λ is the energy flux at e_λ and $\zeta_{\text{sp},\lambda}$ is a weighting factor we introduce to prevent the same photon from being able to photoionise both hydrogen and helium, where ‘sp’ refers to the specific species being photoionised. The fraction of photons which photoionise hydrogen rather than helium from a given flux bin with e_λ is (see Equation 2.21 of [Osterbrock & Ferland 2006](#))

$$\zeta_{\text{H}^0,\lambda} = \frac{n_{\text{H}^0} \sigma_{\text{H}^0,\lambda}}{n_{\text{H}^0} \sigma_{\text{H}^0,\lambda} + n_{\text{He}^0} \sigma_{\text{He},\lambda}}. \quad (3.11)$$

We use similar weighting factor expressions for each considered photoionisation process in our model. For example, Table 3.1 shows that the X-ray flux bin can photoionise H^0 , $\text{He}(1^1\text{S})$ and He^+ . Hence, the weighting factor for an X-ray photon to photoionise $\text{He}(1^1\text{S})$, $\zeta_{\text{He}(1^1\text{S}),\text{X-ray}}$ in our model is given by

$$\frac{n_{\text{He}(1^1\text{S})} \sigma_{\text{He}(1^1\text{S}),\text{X-ray}}}{n_{\text{He}(1^1\text{S})} \sigma_{\text{He}(1^1\text{S}),\text{X-ray}} + n_{\text{H}^0} \sigma_{\text{H}^0,\text{X-ray}} + n_{\text{He}^+} \sigma_{\text{He}^+,\text{X-ray}}}.$$

This important consideration to prevent from double-counting photons is often not included in hydrogen-helium atmospheric escape models. The rate of the heating associated with a photoionisation is calculated as

$$Q_\lambda = \epsilon_\lambda e_\lambda \Phi_\lambda n = \epsilon_\lambda F_\lambda \zeta_{\text{sp},\lambda} e^{-\tau_\lambda} \sigma_\lambda n. \quad (3.12)$$

Combined, the terms $F_\lambda \zeta_{\text{sp},\lambda} e^{-\tau_\lambda}$ account for the remaining supply of capable photons at a given distance into the atmosphere. $\epsilon_\lambda = 1 - (e_{\text{ion}}/e_\lambda)$ accounts for how much energy the photon with e_λ has in excess of the photoionisation energy cost ($e_{\text{ion}} = 13.6, 24.6, 4.0, 4.8, 54.4$ eV for H^0 , helium 1^1S , 2^1S , 2^3S and He^+ , respectively). Values of ϵ_λ are listed in Table 3.1. Finally, the combined $\sigma_\lambda n$ terms account for the availability of potential absorbers. The total photoionisation heating Q , included in Equation 3.2, is then the sum of the heating due to each of the considered species.

In addition to the considered stellar flux, our model also accounts for 24.6 eV and 21.2 eV photons released in recombinations and radiative decay from He(2¹P) to He(1¹S). It also accounts for the release of two 10.3 eV (Bergeson et al. 1998) photons released in the radiative decay from helium’s 2¹S to 1¹S state. We assume the photoionisation rates by these photons to be given by the rate of the process from which they are released ($\times 2$ for the two-photon process), as shown in Table 3.2. In doing so, we assume that all of these photons are re-absorbed by the planetary atmosphere and do not escape. Given that these photons are predominantly released in the optically thick inner-most region of the atmosphere, we consider this assumption to be reasonable. To determine the fractions of which of the viable atmospheric species are absorbed by these photons, we again utilise the weighting factor given by Equation 3.11. For example, the modelled rate of the released 24.6 eV photons which photoionise hydrogen is $\zeta_{\text{H}^0, 24.6 \text{ eV}} \alpha_{A-B} [\text{He}(1^1S)]$. As will be shown, this contributes non-negligibly to the overall photoionisation of hydrogen and heating in the inner-most region of the modelled planetary atmosphere.

Cecchi-Pestellini et al. (2006) showed that X-rays can play a large role in heating the upper layers of planetary atmospheres, particularly those which orbit closely to young (high X-ray flux) stars. Owing to their large photon energies, primary X-ray photoionisations are followed by subsequent photoionisations caused by released energetic secondary photo- and Auger-electrons (Güdel 2015). Heating by X-rays is dominated by such secondary photo-electron generation from the K-shells of metals, with oxygen and carbon being the most important (Owen & Jackson 2012). Few works (Cecchi-Pestellini et al. 2006; Shematovich et al. 2014; Locci et al. 2022) have modelled the secondary electron photoionisation cascade. As our model considers only hydrogen and helium and not heavier elements important for such processes, secondary photoionisations are omitted from our model (as is the case for the models of Oklopčić & Hirata 2018; Lampón et al. 2020; Dos Santos et al. 2022). Hence, it should be noted that our models may underestimate the number of photoionisations by X-rays, particularly when the host star is a young, initially fast rotator. A recent work by Gillet et al. (2023) studies the effects of secondary ionisation by photoelectrons and stresses that such ionisations should be taken into account in 1-D hydrodynamic modelling, reporting a reduction in the predicted mass-loss rate of 43% upon its inclusion for a $0.69M_{\text{Jup}}$ planet orbiting the K1V host HD97658 at 0.074 au.

3.2.4 Cooling processes with hydrogen and helium

In addition to heating, our energy equation (Equation 3.2) also includes various hydrogen and helium cooling contributions. These are collisional ionisation, collisional excitation, recombination and Bremsstrahlung. The

volumetric cooling rates were obtained from [Black \(1981\)](#) and [Cen \(1992\)](#) and are listed in [Table 3.3](#). To obtain the stated cooling contribution processes ([3.3.4](#)) and ([3.3.10](#)), we rearranged the respective rate equations given in [Table 3](#) of [Black \(1981\)](#) so as to use our own helium triplet number density rather than an approximation given by [Equation 11](#) of [Black \(1981\)](#). Rearranging and substituting this equation into their rate equations gives the cooling rate equations listed in [Table 3.3](#). The sum of all the volumetric cooling rates listed in [Table 3.3](#) results in C , which is included in [Equation 3.2](#).

3.2.5 Test case: solving helium populations in post-processing

For comparative purposes, we also present a representative model in which the helium equations are solved in a post-processing step (as is the case for the models of [Oklopčić & Hirata 2018](#); [Lampón et al. 2020](#); [Dos Santos et al. 2022](#)). If solved in a post-processing step, helium heating and cooling contributions can not be included in the energy equation ([Equation 3.2](#)) as to calculate these contributions requires knowledge of the helium populations. Hence, whether the helium population equations are solved simultaneously with the fluid dynamic equations or in a post-processing step can impact the predicted atmospheric escape, the results of which will be discussed in [sections 3.4.2](#) and [3.5.4](#).

Our post-processing test model

- assumes an initially fast rotating stellar host.
- Assumes a constant helium number abundance of 10%.
- Allows heating by photoionisation of hydrogen only.
- Allows photoionisation by stellar XUV and mid-UV photons only, ignoring photons released in the planetary atmosphere as a result of helium transitions.
- Neglects photoionisation weighting factors (see [Equation 3.11](#)), meaning that a single photon could possibly photoionise hydrogen, as well as any of the viable considered helium states in the model.
- Includes only three cooling processes: recombination, collisional ionisation and excitation of hydrogen.
- Considers only electrons arising from hydrogen photoionisations.

While these terms are chosen to be similar to the post-processing 1-D models of [Oklopčić & Hirata \(2018\)](#); [Lampón et al. \(2020\)](#); [Dos Santos](#)

Table 3.3: Cooling processes included in our model. The sum of the cooling rates (C) are included in Equation 3.2. Densities are given in cm^{-3} and temperatures in K. References: (Black 1981)^a, (Cen 1992)^b, (Murray-Clay et al. 2009)^c, (Allan & Vidotto 2019)^d.

ID	volumetric cooling rates [$\text{erg cm}^{-3} \text{ s}^{-1}$]	reference
(3.3.1)	Collisational ionisation cooling $1.27 \times 10^{-21} T^{0.5} \exp[-157809.1/T] n_e n_{\text{H}^0}$	a,b
(3.3.2)	$9.38 \times 10^{-22} T^{0.5} \exp[-285335.4/T] n_e n_{\text{He}(1\text{S})}$	a,b
(3.3.3)	$4.95 \times 10^{-22} T^{0.5} \exp[-631515/T] n_e n_{\text{He}^+}$	a,b
(3.3.4)	$6.41 \times 10^{-21} T^{0.5} \exp[-55338/T] n_e n_{\text{He}(2\text{S})}$	a,b, see Section 3.2.4
(3.3.5)	Recombination cooling $\left(8.70 \times 10^{-27} T^{0.5} \left(\frac{T}{10^3}\right)^{-0.2}\right) / \left(1 + \left(\frac{T}{10^6}\right)^{0.7}\right) n_e n_{\text{H}^+}$	b
(3.3.6)	$1.55 \times 10^{-26} T^{0.3647} n_e n_{\text{He}^+}$	a,b
(3.3.7)	$\left(3.48 \times 10^{-26} T^{0.5} \left(\frac{T}{10^3}\right)^{-0.2}\right) / \left(1 + \left(\frac{T}{10^6}\right)^{0.7}\right) n_e n_{\text{He}^{++}}$	b
(3.3.8)	Dielectronic recombination cooling $1.24 \times 10^{-13} T^{-1.5} \exp[-470000/T] (1 + 0.3 \exp[-94000/T]) n_e n_{\text{He}^+}$	a,b
(3.3.9)	Collisational excitation cooling $7.5 \times 10^{-19} \exp[-118348/T] n_e n_{\text{H}^0}$	a,b,c,d
(3.3.10)	$5.54 \times 10^{-17} T^{-0.397} \exp[-473638/T] n_e n_{\text{He}^+}$	a,b
(3.3.11)	$1.16 \times 10^{-20} T^{0.5} \exp[-13179/T] n_e n_{\text{He}(2\text{S})}$	a,b, see Section 3.2.4
(3.3.12)	Free-free emission (Bremsstrahlung) $1.42 \times 10^{-27} T^{0.5} (3/2) [n_{\text{H}^+} + n_{\text{He}^+} + 4n_{\text{He}^{++}}] n_e$	a,b

et al. (2022), the specific modelling differs from each of these works in numerous ways. For example, they assume a Parker wind in their modelling of the atmospheric escape and hence do not calculate the heating due to photoionisations. However, P-WINDS (Dos Santos et al. 2022) allows the user to input a more complex and self-consistent atmospheric structure, rather than assume a Parker wind, as done for HD 189733 b in Dos Santos et al. (2023). Additionally, there are some minor variations in a number of the assumed rates between states (see Table 3.2).

3.3 Model inputs: evolution of high-energy stellar flux and planetary radii

Allan & Vidotto (2019) previously showed that the evolution of atmospheric escape for a close-in planet depends on two important factors:

1. as the host star evolves, its activity declines due to spin down (Skumanich 1972; Kawaler 1988; Vidotto et al. 2014), resulting in declining fluxes in the XUV (Jackson et al. 2012; Johnstone et al. 2015b, 2021) and
2. as the planet evolves, cooling causes it to contract with time (Fortney & Nettelmann 2010).

The level of atmospheric escape and consequently the observational signatures of escaping hydrogen in the Lyman- α and H- α lines were found to vary strongly with the evolution of the modelled planets, with younger planets exhibiting greater escape and deeper absorptions in both lines. This is the result of a favourable combination of higher irradiation fluxes and weaker gravities at young ages. In a continuation of this work, we now study how the helium 1083 nm signature evolves over the lifetime of a planet.

In order to incorporate the decline in XUV flux in this current work, we look to the physical rotational evolution model of Johnstone et al. (2021) that is constrained by observed rotation distributions in young stellar clusters. Their study offers publicly available evolutionary tracks of stellar flux for a wide variety of stellar mass, age and initial rotation. We use their tracks of X-ray, hEUV, sEUV flux and stellar radius evolution for a 0.7- M_{\odot} star, chosen to be representative of a K-dwarf star as detections of 1083 nm seem to favour such a host. We obtain tracks for both their ‘slow’ and ‘fast’ initial stellar rotation definitions corresponding to the 5th and 95th percentiles of their observed 150 Myr rotation distribution. In Allan & Vidotto (2019), we normalised the XUV flux tracks of Johnstone et al. (2015b) so that the solar XUV flux was reproduced at the solar age. Similarly, we now normalise the Johnstone et al. (2021) XUV flux tracks so that

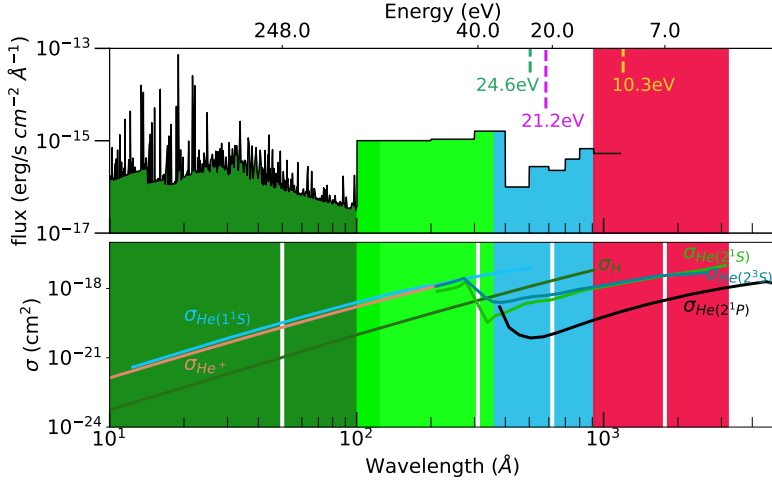


Figure 3.2: [Upper-panel] MUSCLES spectrum of HD 85512 used to normalise the high-energy evolution tracks of [Johnstone et al. \(2021\)](#), shown in Figure 3.3. The energy of the three considered photons produced due to helium transitions in the planetary atmosphere are marked by the dashed lines. [Lower-panel] Photoionisation cross-sections for hydrogen and considered helium states. Note that while He(2¹P) photoionisations are not considered in the model, its cross-section profile is shown here for comparison to that of the 2¹S and 2³S helium states. The four shaded regions indicate the wavelength channels of X-ray, hEUV, sEUV and mid-UV going from left to right. The representative energies of each of these flux bins is marked by the vertical solid white lines in the lower-panel.

they reproduce the XUV flux of spectral type K6 star HD 85512, utilising a spectrum obtained from the Measurements of the Ultraviolet Spectral Characteristics of Low-mass Exoplanetary Systems (MUSCLES) Treasury Survey ([France et al. 2016](#)), shown in Figure 3.2. MUSCLES combines Hubble and ground-based observations and where necessary (such as in the mostly inaccessible EUV wavelength range) stellar spectral models. While other K dwarf spectra were obtained by MUSCLES, we choose HD85512 to perform this normalisation based on its relatively late age. By this age, the slow and fast rotators have converged to the same rotation rate, meaning that normalising the flux tracks at this age retains the original track ratios between slow and fast rotator. We assume an age of ~ 5600 Myr for HD 85512 ([Pepe et al. 2011](#)) and a distance of 11.28 pc ([Gaia Collaboration et al. 2016, 2022](#)) to calculate its surface flux in each of the considered bins (see star symbols in Figure 3.3).

Our resulting evolution X-ray, hEUV and sEUV input fluxes ([Johnstone et al. 2021](#)) are shown in the upper-panel of Figure 3.3. Solid and dashed tracks correspond to slow and fast initial rotators, respectively. For the

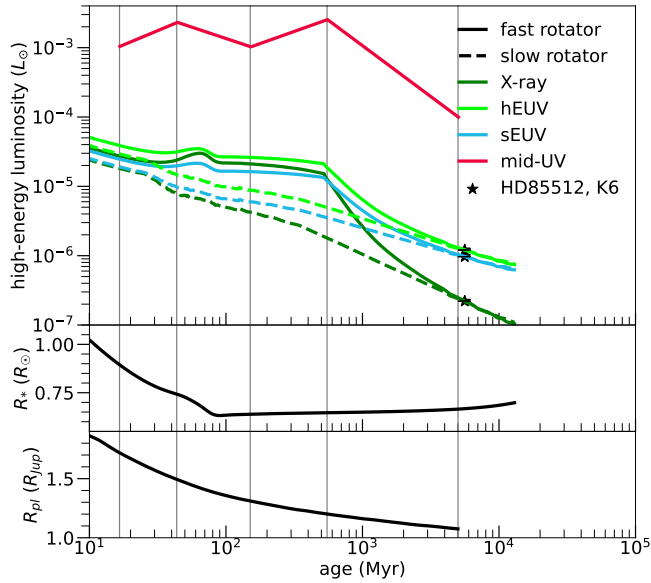


Figure 3.3: [Upper-panel] Evolution of high-energy stellar luminosity, where hEUV, sEUV and X-ray wavelength bins were obtained by normalising the predictions of [Johnstone et al. \(2021\)](#) for a $0.7-M_\odot$ by the K dwarf HD85512 (star symbols, from Figure 3.2). The mid-UV luminosity tracks combines the near-UV and far-UV fluxes from [Richey-Yowell et al. \(2022\)](#). [Central-panel] Stellar radius evolution for the same star, also obtained from the model of [Johnstone et al. \(2021\)](#). [Lower-panel] Planetary radius with respect to age for a $0.3-M_{jup}$ planet orbiting a solar-like star at 0.045 au ([Fortney & Nettelmann 2010](#)). The vertical grey lines indicate the sampled ages for our various classes of models.

near-UV and far-UV fluxes, we use the results from [Richey-Yowell et al. \(2022\)](#), but in our modelling we merge their near- and far-UV fluxes into a single ‘mid-UV flux’. We include the mid-UV flux due to the ability of these photons to photoionise helium out of the triplet state.

The central-panel of [Figure 3.3](#) shows the evolution of the stellar radius, also obtained from the model of [Johnstone et al. \(2021\)](#). Our evolving planetary radii inputs are shown in the lower-panel of [Figure 3.3](#). These are the same radii used in [Allan & Vidotto \(2019\)](#), corresponding to a $0.3 M_{\text{Jup}}$ gas giant planet orbiting a solar-like star at 0.045 au ([Fortney & Nettelmann 2010](#)). Note that these models neglect planetary-radius inflation. The close proximity to its host and the planetary mass puts this planet at the upper edge of the hot-Neptune desert ([Mazeh et al. 2016](#)). It should be noted that there is an inconsistency between the assumed stellar parameters in our flux (K dwarf) and radius evolution input (which assumes a G dwarf). In the future, it would be interesting to couple our hydrodynamic escape model to a planetary thermal evolution model as is done in [Kubyskhina et al. \(2020\)](#). This would allow us to also consider the decrease in planetary mass, which could be significant in case of strong atmospheric escape over time. This mass reduction would act to reduce the planetary gravity with evolution. As discussed in [Allan & Vidotto \(2019\)](#), omitting this shrinking mass with evolution in our modelling leads to our models slightly underestimating the true atmospheric escape progressively with planetary evolution, as the planetary gravity is progressively overestimated. This mass loss underestimation is minor due to the stronger dependence of the gravitational force with planetary radius compared to planetary mass, and planetary radius varying more than the mass with evolution.

3.4 The evolution of atmospheric escape

[Table 3.4](#) describes the four sets of evolution-sampled models we consider. This shows the initial stellar rotation, the He/H number abundance and whether or not helium heating and cooling processes are included. Hydrogen heating and cooling processes are included in all models. Helium heating and cooling, as well as the helium populations are self-consistently included in the top 3 models, while the model F10%PostProc does not include any helium heating or cooling terms (in the hydrodynamics model, the presence of the helium particles only affects the mean molecular weight of the gas) – in this case, the helium population is computed in a post-processing step. All models share the following common parameters: stellar mass $M_* = 0.7M_{\odot}$, orbital distance $a = 0.045$ au and planetary mass $M_{\text{pl}} = 0.3 M_{\text{Jup}}$, while the received stellar flux and the planetary and stellar radii evolve as given by [Figure 3.3](#).

[Figure 3.4](#) displays how the predicted mass-loss rate (upper-panel), cu-

Table 3.4: Description of the evolution model sets presented in this paper. Rotation refers to the initial stellar rotation (fast rotators have higher high-energy fluxes during their youth). The third column indicates the helium number abundance, with the remainder of the atmosphere being hydrogen. The listed heating and cooling processes correspond to the row IDs of Tables 3.1 and 3.3. Model F10%PostProc does not incorporate helium energetics in the hydrodynamic escape (although the mass of the helium particles affect the mean molecular weight) and instead computes the helium state fractions post-processingly, as described throughout section 3.2. All models share the following common parameters; $M_* = 0.7M_\odot$, $a = 0.045$ au, $M_{\text{pl}} = 0.3 M_{\text{Jup}}$. The received stellar flux and radius and the planetary radius vary with evolution following Figure 3.3.

model title	stellar rotation	He (%)	heating eqs	cooling eqs	helium population
S2%	slow	2	3.1.1 – 3.1.21	3.3.1 – 3.3.12	self-consistent
F2%	fast	2	3.1.1 – 3.1.21	3.3.1 – 3.3.12	self-consistent
F10%	fast	10	3.1.1 – 3.1.21	3.3.1 – 3.3.12	self-consistent
F10%PostProc	fast	10	3.1.1 – 3.1.3	3.3.1, 3.3.5, 3.3.9	post-processing

mulative mass lost (central-panel) and terminal velocity of the escaping atmosphere (lower-panel) vary as a function of age for each of our model sets. We calculate the cumulative mass lost by integrating the mass-loss rate profile with respect to planetary age. As found in [Allan & Vidotto \(2019\)](#), the diminishing XUV flux required to heat the planetary atmosphere combined with the growing gravitational force due to the shrinking planetary radii lead to the weakening of atmospheric escape as the planet evolves across all models. Variations with evolution are more extreme for the mass-loss rate compared to the terminal velocity. As discussed below, this is the result of the majority of heating occurring in the sub-sonic region of the atmosphere.

To investigate the evolution of the energetics of our models, the upper-panels of Figure 3.5 show how the considered photoionisation heating processes differ at young (left) compared to old (right) planetary ages as a function of distance. The lower-panels show the dominant cooling processes. The displayed individual heating and cooling contributions correspond to our F2% model (see Table 3.4). Q and C correspond to the total heating source and cooling sink contributions (see Equation 3.2) of this model. In each panel, the outflow velocity of the F2% model remains sub-sonic within the shaded regions, reaching supersonic velocities beyond. For comparison, we show also the total heating and cooling contributions of models F10% and F10%PostProc. It should be noted that the F10%PostProc heating profile could not simply be reproduced by summing the displayed hydrogen-only heating contributions of the F10% model. Firstly, this is because we account for the limited availability of photons as explained previously with Equation 3.11. Secondly, the heating affects the density distribution of neutrals which in turn affects the heating contributions.

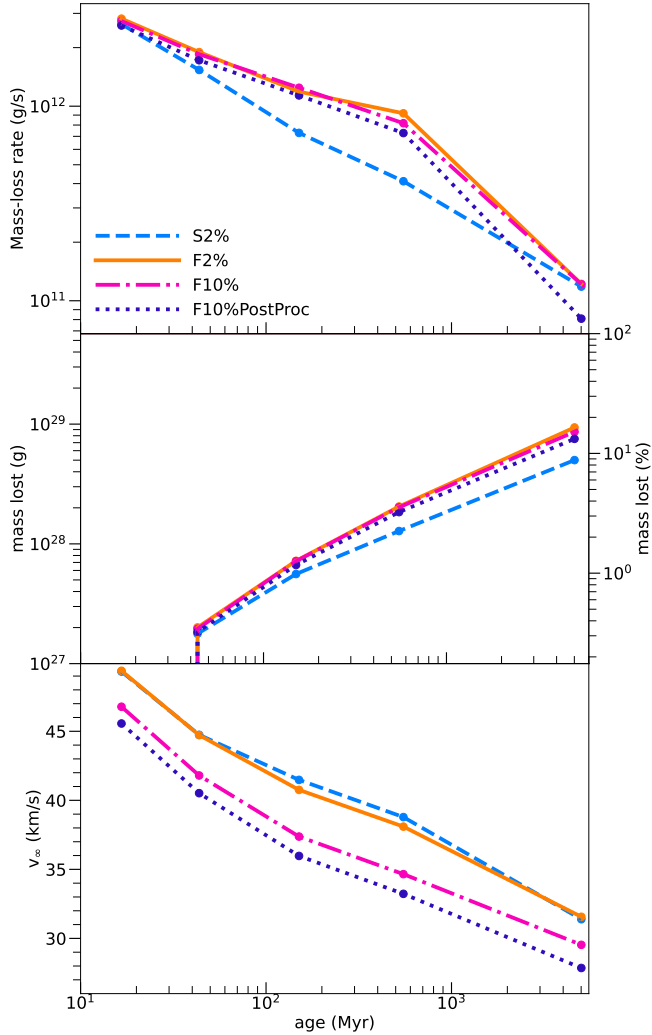


Figure 3.4: Mass-loss rate, cumulative mass lost and the terminal velocity of the escaping atmosphere as a function of planetary age are shown in the upper, central and lower-panels, respectively. The evolution model sets are described in Table 3.4.

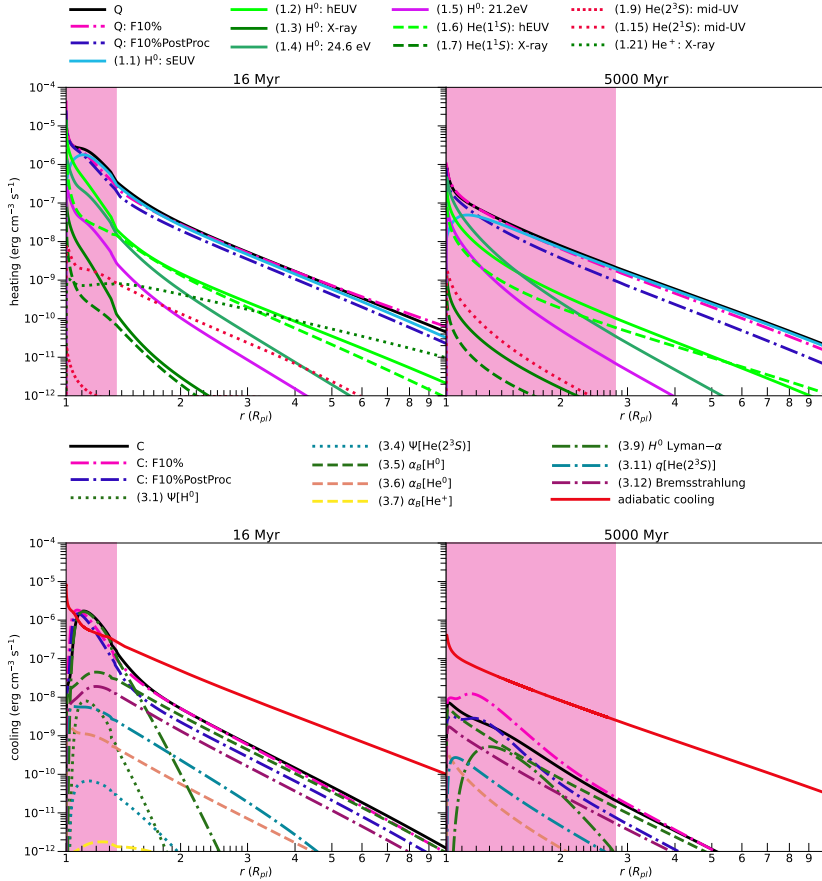


Figure 3.5: Volumetric heating rates (upper-panel) and volumetric cooling rate (lower-panel) profiles at young (left) and old (right) planetary ages. Shaded regions on the left of each panel highlight the sub-sonic region of the atmosphere. In both legend sets, the numbers in parentheses relate each process to their corresponding process number in Table 3.1 for heating and Table 3.3 for cooling. In all displayed panels there are processes that fall below the chosen y -axis range and hence are not included in the legend. The tables on the other hand list all of the included processes. The displayed individual heating and cooling contributions correspond to our F2% model (see Table 3.4). Q and C correspond to this model’s net heating source and cooling sink contributions (see Equation 3.2). For comparison, we show also the Q and C of models F10% and F10%PostProc.

We see in Figure 3.5 that the same heating process remains dominant above $\sim 1.1R_{\text{pl}}$ throughout the full planetary evolution: heating due to the photoionisation of neutral hydrogen by sEUV photons (ID: 3.1.1 of Table 3.1). Below $\sim 1.1R_{\text{pl}}$, heating from hydrogen photoionisations by hEUV photons (ID: 3.1.2) dominate over sEUV photons for the young planet, whereas at the oldest age, hydrogen photoionisation by the 24.6 eV photon (ID: 3.1.4), itself ejected in a direct recombination to $\text{He}(1^1\text{S})$, becomes the dominant heater below $\sim 1.1R_{\text{pl}}$. We found that the contribution of photoionisation of singlet state helium to the heating process, although not dominant, is not negligible for abundances of 2%, and is more important for higher abundances. Sections 3.4.1 and 3.4.2 will discuss the resulting effects of altering the assumed He/H number abundance and omitting helium energetics. Heating arising from photoionisations out of the helium triplet state is negligible.

Clearly, the majority of heating affects the sub-sonic region of the atmosphere. The heating contribution peaks within the sub-sonic region for the displayed young and old models. Accordingly, the temperature profile follows a similar behaviour, reaching peaks of approximately 11 250 K and 7750 K respectively as will later be shown in Figure 3.7. Due to the heating being mostly deposited in the sub-sonic region, heating variations with planetary evolution have a greater effect on the mass-loss rate, while having a lesser effect on the velocity of the outflowing atmosphere. This is indeed verified by Figure 3.4, with a decrease of over one order of magnitude in mass-loss rate while the terminal velocity decreases by 35% over the full evolution of our F2% model.

The lower-panels of Figure 3.5 show the dominant cooling processes. Similar to the heating processes, the net cooling peaks in the sub-sonic region of the atmosphere. Adiabatic cooling due to the expansion of the escaping atmosphere is more important than the cooling sink terms (composing C in Equation 3.2) for the old 5000-Myr model. Although not shown, this is also true for models F10% and F10%PostProc at the same age. At the young age of 16 Myr however, we see that collisional excitation of neutral hydrogen (dash-dotted green, ID: 3.3.9 in Table 3.3) more commonly referred to as Lyman- α cooling dominates at distances between 1.1 to 1.3 R_{pl} . Outside of this distance cooling due to adiabatic expansion again dominates. In their modelling with ATES, [Caldirolì et al. \(2021\)](#) show that adiabatic expansion dominates the atmospheric cooling in the case of their low-irradiation model of HD 97658 b, similar to our 5000 Myr model, while for their high-irradiation planet WASP-43 b, radiative cooling, predominantly Lyman- α cooling, dominates below 1.5 R_{pl} , similar to our 16 Myr planet. Our model's predicted heating and cooling behaviour also agrees reasonably well with that of [Zhang et al. \(2022a\)](#) obtained with TPCI ([Salz et al. 2015](#)) for the young mini-Neptune TOI 560.01. Assuming solar metallicity, they find adiabatic cooling to be more important than

radiative cooling at nearly all radii, with radiative cooling overtaking in the $\sim 2 - 3 R_{\text{pl}}$ region of the atmosphere. Their predicted heating is also dominated by neutral hydrogen photoionisations with smaller but non-negligible contributions from helium in agreement with our findings. Below $1.3 R_{\text{pl}}$, line heating and photoionisation of metals dominate their modelled heating.

Figure 3.6 shows the rates of the processes that directly populate (solid lines) or depopulate (dashed lines) the helium triplet state. Left and right panels correspond to ages 16 and 5 000 Myr, respectively. Again, only the dominant processes are displayed in the figure, the exhaustive list of considered processes is reserved for Table 3.2. While the relative rates between processes vary slightly with age, it is clear that the same triplet (de-)populating processes dominate throughout the planetary evolution. This also holds true at the intermediate ages not shown. At all distances, the dominant triplet-populating process is the recombination of ionised helium into the triplet state, $\alpha_B[\text{He}(2^3S)]$. Mostly balancing this process, is the de-excitation of triplet-state helium into the 2^1S helium state by means of a collision with a free electron ($q[\text{He}(2^3S \rightarrow 2^1S)]$). The general behaviour of the mentioned processes agree with the 1-D model of Oklopčić & Hirata (2018) and the 3-D models of Khodachenko et al. (2021a) and Rumenskikh et al. (2022) for WASP-107b and HD189733b, respectively. The depopulation of the triplet state due to both the photoionisation from mid-UV and sEUV photons is not a dominant process except in the very outer, more tenuous atmosphere, consistent with the findings of Oklopčić (2019) who shows that for stars cooler than spectral type G, collisional de-excitation from triplet to singlet state dominate. This is due to cooler K-dwarf stars having a smaller ratio of mid-UV : EUV flux, meaning a smaller ratio of triplet depopulating : escape driving flux, compared to warmer G type stars.

The triplet number density profile resulting from the balance of the mentioned populating and depopulating processes is shown in Figure 3.7, at young (upper-panel) and old (lower-panel) ages. The number densities of the other modelled helium states as well as neutral and ionised hydrogen (dotted profiles) are also included. The atmospheric temperature is shown by the solid profile. The temperature reached by the younger planet's atmosphere is larger due to the higher level of XUV flux received: the atmosphere of the 16-Myr old planet reaches a maximum temperature of 11 250 K, while the atmosphere of the 5-Gyr-old planet reaches a maximum temperature of 7 750 K. The level of hydrogen and helium ionisation is also larger at younger ages on account of the relatively larger incident flux. The number density of helium in the triplet state is greater for the younger planet. This is due to a higher rate of helium recombinations due to a larger availability of ionised helium at younger ages (Figure 3.6).

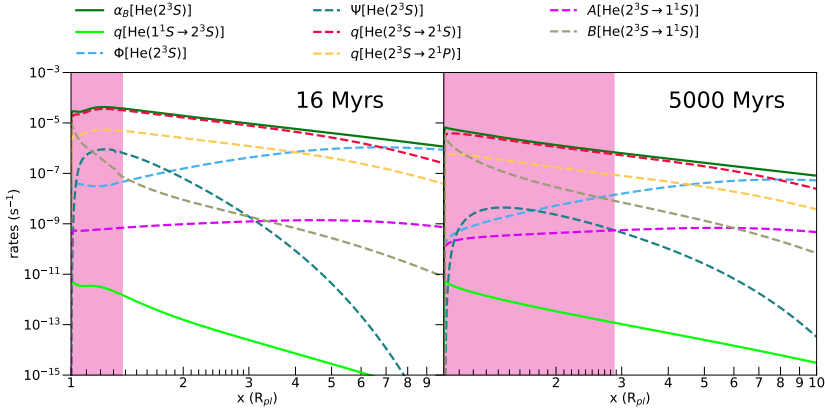


Figure 3.6: Rates of processes directly populating (solid) and depopulating (dashed) the helium triplet state at young (left) and old (right-panel) ages as a function of distance. Table 3.2 lists each considered transition. Here, only rates within the displayed y -axis range are listed in the Figure legend. The assumed planetary parameters are that of our F2% model (Table 3.4).

3.4.1 Effect of helium abundance on hydrodynamics

To investigate how the abundance of helium affects the hydrodynamic escape models, we run two set of models where we adopt helium number abundances of 0.02 (F2%) and 0.1 (F10%).

In Figure 3.5, individual heating contributions were shown only for the F2% model, with only the total Q profile of F10% on display. A deeper analysis into the heating for the F10% model reveals however that heating due to helium unsurprisingly plays a more significant role for a greater helium abundance (see Appendix 3.6.2 and Figure 3.12).

The nature of the atmospheric escape with evolution for models F2% and F10% is shown by their mass-loss rate and terminal velocities given in Figure 3.4 by the solid (F2%) and dash-dotted (F10%) tracks. Clearly, they both lead to very similar mass-loss rates, with both models resulting in similar cumulative loss of 15% (F10%) and 16% (F2%) of the planet’s initial mass over its entire evolution. The larger helium abundance produces also a slight decrease of 5-9% in terminal velocity maintained throughout the evolution as seen in the bottom panel of Figure 3.4. Slower terminal velocities are reached due to the heavier mean molecular weight combined with similar total heating and cooling profiles (see Figure 3.5). In conclusion, we find that increasing the assumed helium abundance leads to slightly slower outflows, which undergo slightly less atmospheric mass losses.

While the He/H range we consider here appears only to affect the hydrodynamics of escape trivially, there are two important effects resulting from

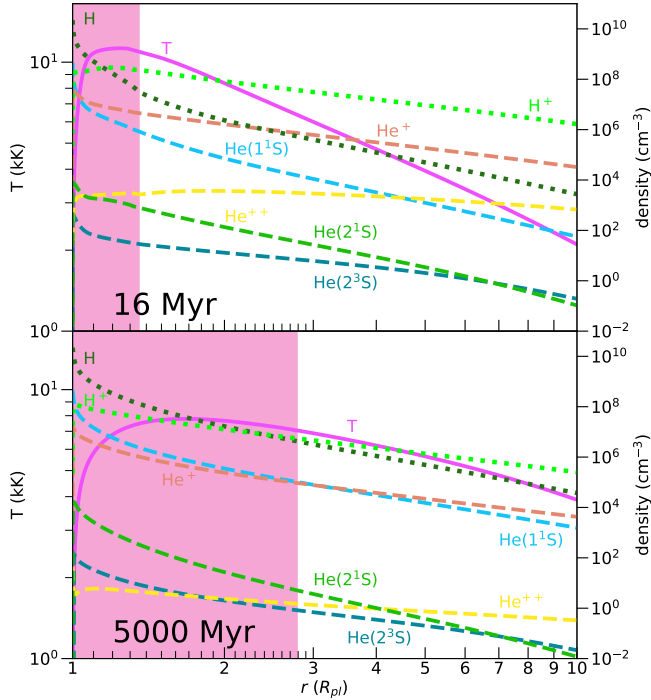


Figure 3.7: Temperature (left axis, solid line-style) and various number density profiles (right axis, dashed and dotted for helium and hydrogen, respectively). The upper-panel corresponds to an age of 16 Myr while the lower-panel shows 5000 Myr. The planetary parameters are that of our F2% model (see Table 3.4). Similar figures for our F10% and F10%PostProc are given in the Appendix.

the choice of the abundance. Firstly, the observability of helium transit is strongly dependent on the choice of helium abundance (Section 3.5.3). Secondly, if we omit the calculation of helium energetics, the choice of helium abundance can significantly affect the atmospheric escape. This will now be discussed.

3.4.2 Effect of helium energetics on hydrodynamics

The inclusion of helium affects the atmospheric dynamics in two ways. Firstly, it raises the mean molecular weight above that of a hydrogen-pure atmosphere. Intuitively, this effect acts to weaken atmospheric escape by raising the gravitational force experienced by the atmospheric material. This escape-reducing effect is straightforward to include in the modelling of atmospheric escape. Secondly, and more complex to model, is the effect of additional heating processes due to the inclusion of helium. In our modelling, we self-consistently incorporate the helium energetics, i.e. heating due to photoionisation from the 1^1S , 2^1S , 2^3S and singly ionised states, as well as cooling due to collisional excitation, and ionisation, recombination, and Bremsstrahlung in the fluid dynamic equations (Equations 3.1-3.3). To investigate the effects that self-consistently including helium energetics has, we compute the model set F10%PostProc which omits such effects for comparison, as described previously in section 3.2.5.

The top panels of Figure 3.5 show the total Q heating profiles of the model sets F10% (dash-dotted fuchsia) and F10%PostProc (dash-dotted purple). Comparing these, we see that close to the planet, the heating rates are comparable, but further away, the heating profile of the F10%PostProc model is considerably less. This leads to similar peak atmospheric temperatures, with models F10% and F10%PostProc reaching 11.2(8.8) kK and 11.3(8.3) kK at ages 16 (5 000) Myr, respectively, but a faster temperature decay with distance when omitting helium energetics (see Appendix 3.6.2, Figure 3.13). In order to better understand how the contribution of heating is affected by the specific model set-up, we calculate the net heating contributions for each model by integrating their volumetric heating rates over volume. Doing so reveals a $\sim 21\%$ heating reduction for the F10%PostProc model relative to the F10% model at the youngest age, growing to 45% for the oldest model age of 5 Gyr.

As reduced atmospheric heating drives less escape, our F10%PostProc model (purple dotted tracks in Figure 3.4) undergoes less mass loss compared to the F10% model (fuchsia dash-dotted), with respective losses of 13 and 15% of their initial mass over their evolution. The terminal velocity is also reduced by the omission of helium energetics, with reductions between 2.5 to 5.5% throughout the planetary evolution. The main barrier to the inclusion of helium energetics is that the helium populations must be solved simultaneously with the fluid dynamics equations rather than in a post-

processing step. This is because knowledge of the helium populations are required for calculating the helium heating and cooling terms, which ought to be included in the energy conservation equation. It is important to note however that even our model without helium heating is more sophisticated than Parker-type wind models, which assume ad-hoc constant temperatures throughout the atmosphere.

3.5 The observability of helium transits

3.5.1 The ray-tracing model for transmission spectroscopy

Here, we model transmission spectroscopy of the helium triplet at 1083 nm to investigate how the observability of this signature varies with long-term evolution. Our ray-tracing technique for modelling transmission spectroscopy is a helium-adapted version of a previous model described in [Allan & Vidotto \(2019, Lyman- \$\alpha\$ and H- \$\alpha\$ \)](#) and [Vidotto et al. \(2018, OI 130.22 nm\)](#). Hence, this section gives only a brief summary aimed at documenting the necessary modifications. For a more thorough description of the general model we refer the reader to [Allan & Vidotto \(2019\)](#).

As our ray tracing model is 3-D, we symmetrically fill a 3-D grid centred on the planet with our 1-D hydrodynamic calculations of atmospheric temperature, velocity and density. One of the grid axes is aligned along the observer–star line, so that the grid seen in the plane of the sky is a square of 201×201 cells. We also account for the line-of-sight velocity related to the orbital motion of the planet (assuming circular orbit) – this correction is more important for phases farther from mid-transit, as in mid-transit, the line-of-sight velocity of the planet’s orbital motion goes to zero.

The helium triplet is comprised of three individual lines, with line-centre wavelengths in air of 1082.909, 1083.025, 1083.034 nm. Hence, we model three individual wavelength-dependent transits for each of the triplet lines following the process described in detail in [Allan & Vidotto \(2019\)](#) for Lyman- α and H- α lines. We use the NIST database² ([Kramida et al. 2022](#)) to obtain the following line properties: the Einstein coefficient is $A_{ki} = 1.0216 \times 10^7 \text{ s}^{-1}$, the mentioned line centre wavelengths and their corresponding oscillator strengths f_{ik} , 0.059902, 0.17974, 0.29958. With these atomic parameters, we calculate a wavelength-dependent optical depth along a single ray in the direction connecting the observer to the star–planet system. In doing so, we use a Voigt line profile, a convolution of a Gaussian and Lorentzian line profile accounting for both Doppler and natural

²<https://physics.nist.gov/asd>

broadening

$$\phi_{\lambda_0} = \frac{\lambda_0}{\sqrt{\pi}u_{\text{th}}} \frac{\chi}{\pi} \int_{-\infty}^{\infty} \frac{e^{-w^2}}{X^2 + (\Delta u/u_{\text{th}} - w)^2} dw, \quad (3.13)$$

where λ_0 is the wavelength at line centre for the specific helium triplet line, $X = A_{ki}\lambda_0/(4\pi u_{\text{th}})$ is the damping parameter, $u_{\text{th}} = (2k_{\text{B}}T/m_{\text{He}})^{1/2}$ is the thermal velocity with m_{He} being the mass of atomic helium. The velocity offset from the line centre is $\Delta u = u_{\text{channel}} - u_{\text{LOS}}$, where u_{LOS} is the line of sight flow velocity of the escaping wind and u_{channel} represents the velocity ‘channel’ (related to wavelength via Doppler shifts) of the measurement. We slice our velocity calculations in 71 channels from -100 km/s to +100 km/s. In calculating this line profile, we make use of IDL’s inbuilt `voigt` function. From the wavelength-dependent optical depth, we calculate the wavelength-dependent absorption. By integrating this over all considered rays within the stellar disk, we find the total absorption. In this way, we calculate the transit depth contributions due to each of the three lines that make up the helium triplet. Finally, we sum these contributions to obtain the total helium triplet transit depth.

We assume a transit along the centre of the stellar disk (i.e., no impact parameter). We also neglect centre-to-limb variations in the stellar disc. With $M_* = 0.7M_{\odot}$, $a = 0.045$ au and the age-specific R_* shown in Figure 3.3, we obtain a transit duration between 2 to 2.4 hours for our models (see Equation 17 of [Allan & Vidotto 2019](#)).

3.5.2 The evolution of helium 1083 nm transmission spectroscopy

Figure 3.8 shows the plane-of-the-sky extinction computed for each of the individual lines of the helium triplet (shown here at mid-transit only). In each panel the stellar disk is outlined by the orange dashed circle. By integrating the extinction, we compute the excess absorption shown in Figure 3.9, where colour corresponds to various transit phases. At younger ages (upper-panel), the excess transit is larger and the transit depth is greatest at mid-transit as this is when the most dense atmospheric material occults the stellar disk. There is an asymmetry between pre- and post-mid-transit spectra as a result of the Doppler velocities of the atmospheric material due to the orbital motion. This asymmetry is greatest at times furthest from mid-transit as the majority of obscuring material is red-shifted (transit phase=+0.5, fourth contact ‘T4’) or blue-shifted (transit phase=-0.5, first contact ‘T1’). The degree of asymmetry would be even greater had we considered the interaction with a stellar wind ([Carolán et al. 2021a](#)), as the outflowing atmosphere would be asymmetric, likely featuring a comet tail-like structure.

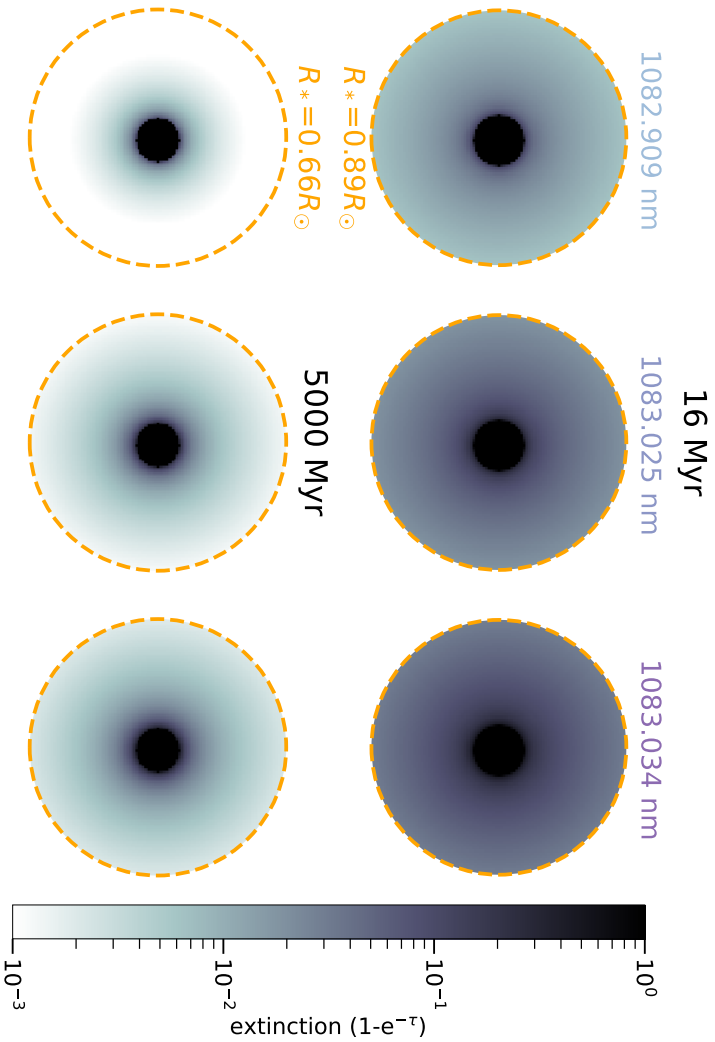


Figure 3.8: Plane-of-the-sky extinction contributions at 16 (upper-row) and 5000 Myr (lower-row), shown at mid transit. Each column shows the contribution of one of the three lines of the helium triplet. The dashed orange circle marks the stellar disk with respective radii of 0.89 and $0.66 R_\odot$ at ages 16 and 5000 Myr. The planetary parameters are those of our F2% model (see Table 3.4).

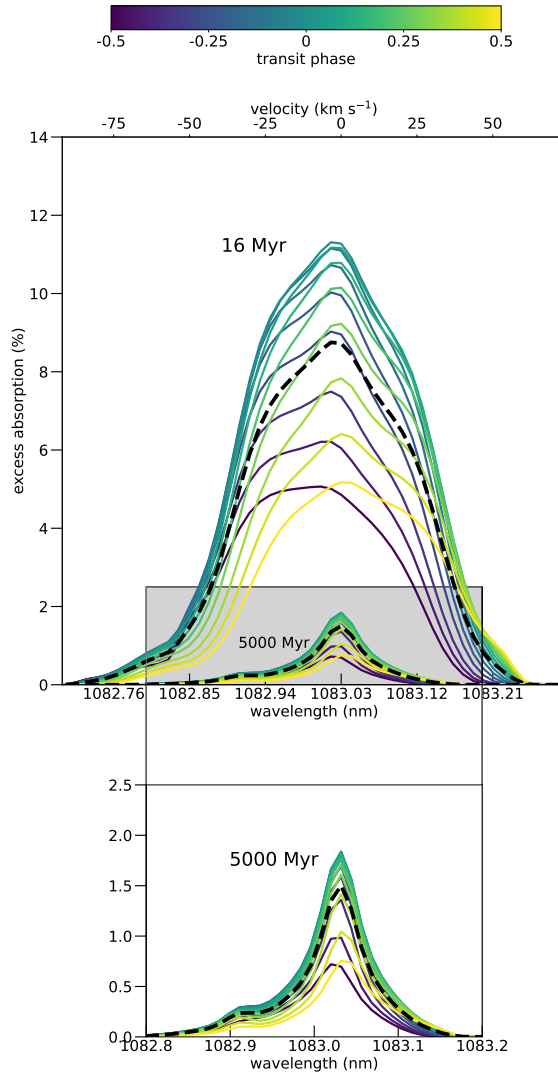


Figure 3.9: Helium 1083 nm transmission spectra as a function of time/transit phase as indicated by the colour bar. Transit phases of -0.5 and $+0.5$ correspond to the time of first and fourth contacts, respectively. The mean average of all spectra between these two phases is shown in dashed black. The upper-panel shows the spectra at a planetary age of 16 Myr while the lower-panel offers a closer look at the spectra at age 5000 Myr. The assumed planetary parameters are that of our model-set entitled F2% (see Table 3.4).

In practice, transit observations are integrated over a certain amount of time to obtain a sufficiently high signal-to-noise ratio. As the helium 1083 nm signature is then averaged out over time, the absorption from such an observation is weaker than the theoretical instantaneous 1083 nm signature at mid-transit. We account for this time-sampling effect by averaging our absorption profiles between T1 and T4, following [Dos Santos et al. \(2022\)](#). The black dashed spectra in [Figure 3.9](#) show these calculated mean averages.

The upper-panel of [Figure 3.10](#) shows the (T1-T4 phase-averaged) helium 1083 nm transmission spectra along planetary evolution. The lower-panel offers a closer look at the oldest age spectrum and its constituent contributions from each of the individual helium triplet lines. [Figure 3.11](#) displays the evolution of the T1-T4 phase-averaged equivalent width (upper-panel) and peak excess absorption (lower-panel) of these helium 1083 nm signatures for all four of our model sets. In our models, thermal broadening is negligible and the broad profiles and large equivalent widths, especially more noticeable at younger ages, are due to Doppler broadening. This is because there is more absorbing material at larger distances (and thus with larger velocities) in the 16 Myr old model than in older systems. Additionally, we see that the helium 1083 nm signature weakens with planetary evolution. The main cause of the larger 1083 nm absorption at younger ages is the larger amount of material in the triplet state obscuring the stellar disk during planetary transit (see, e.g., the density profiles in [Figure 3.7](#) and the extinction in [Figure 3.8](#)). Interestingly, we see in [Figure 3.10](#) very little variation in the 1083 nm absorption profile between ages 43 and 150 Myr, despite the reduction in atmospheric escape. This is because the stellar radius also drops from 0.74 to 0.64 R_{\odot} , hence the ratio of obscuring He(2^3S) to the stellar disk area remains similar at both ages.

3.5.3 Effect of helium abundance on 1083 nm observability

When comparing models with different abundances F2% and F10% in [Figure 3.11](#), we see a large change in the equivalent widths and peak excess absorptions. For example, model-set F2% (F10%) produces an equivalent width and peak excess absorptions of 0.013 nm (0.058 nm) and 6.6% (31.4%) at an age of 150 Myr, while at the later age of 5 000 Myr, the corresponding values are 0.0014 nm (0.007 nm) and 1.5% (7.4%). Although these models exhibited similar atmospheric escape hydrodynamics ([section 3.4.1](#)), our synthetic transit observations are very sensitive to the adopted helium abundance.

The F10% and F10%PostProc model sets show increased 1083 nm absorption going from 43 to 150 Myr while F2% maintains roughly the same absorption between these two ages, as discussed in the previous subsection.

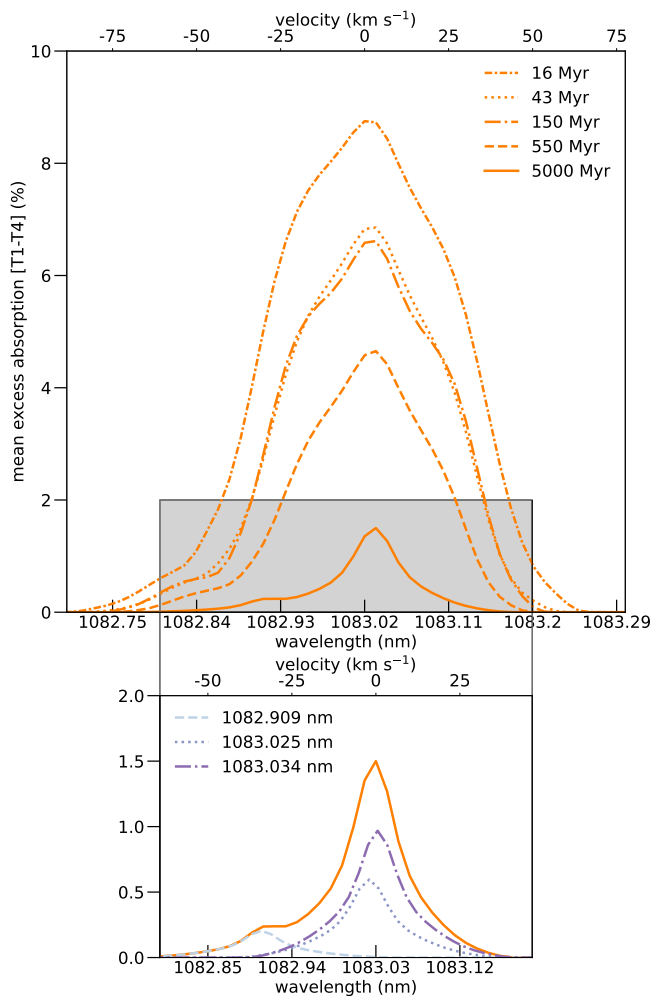


Figure 3.10: [Upper-panel] The helium 1083 nm transmission spectra averaged over phases between first and fourth contacts. The line-style relates each spectrum to its planetary age. [Lower-panel] A zoom-in of the grey shaded region in the upper-panel. The 5000 Myr transmission spectrum is shown by the solid line as well as its individual line contributions as shown by the legend. The planetary parameters are those of our F2% model (see Table 3.4).

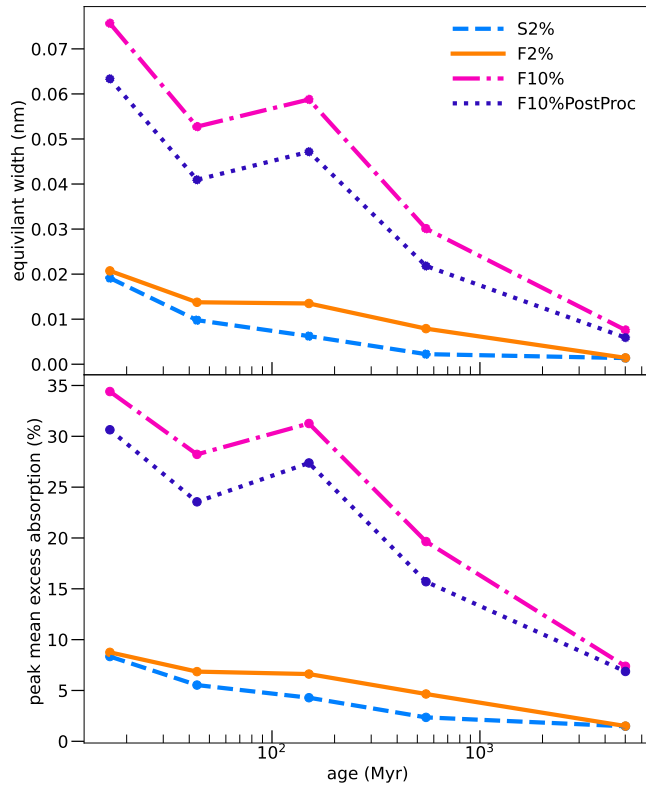


Figure 3.11: T1-T4 phase-averaged helium 1083 nm equivalent widths integrated over 1082.6-1083.35 nm (upper-panel) and peak excess absorptions (lower-panel) as a function of planetary evolution, for our model sets indicated in the legend (see Table 3.4).

The F2% model set exhibits a similar evolution of atmospheric escape to the F10% model, however unsurprisingly the latter has overall more He(2^3S) extinction and accordingly greater 1083 nm absorption. The larger ratio of obscuring He(2^3S) material relative to the stellar disk for F10% compared to the F2% model set emphasises the observational effect of the more drastic stellar disk area variation coinciding with a lesser variation in atmospheric escape between 43 and 150 Myr, leading to the bump in Figure 3.11 at 150 Myr for F10% and F10%PostProc models.

3.5.4 Effect of helium energetics on 1083 nm observability

Figure 3.11 shows similar transit properties for the two models F10% and F10%PostProc, with F10%PostProc having smaller and narrower absorptions. Interestingly, the inclusion of helium energetics impacts the resulting 1083 nm signature, however, as for the modelled hydrodynamics (section 3.4.2), the resulting variation is small over the modelled parameter space.

When excluding helium energetics, the missed heating from helium photoionisation and hydrogen photoionisation by helium produced photons is partially balanced by a larger availability of (stellar) photons capable of photoionising hydrogen, contributing to atmospheric heating (the F10%PostProc sets all photoionisation weighting factors to 1). 100% of the received stellar photons (bar those in the mid-UV due to their low energy) are then available to photoionise hydrogen. For a particular photoionisation, there is greater excess kinetic energy to heat the atmosphere than if the same photon was allowed to ionise He(1^1S). At older ages, the variation between the self-consistent and post-processing model is smaller on account of the reduced level of photoionisations.

3.6 Discussion and conclusions

3.6.1 Summary of main findings

In this paper, we investigated the evolution of atmospheric escape for highly irradiated $0.3M_{\text{Jup}}$ exoplanets with primordial hydrogen/helium atmospheres orbiting a K-dwarf star at 0.045 au, with the goal of predicting the evolution of their helium 1083 nm transits. Our model self-consistently solves the fluid dynamic equations in addition to the coupled equations for hydrogen ionisation balance and the helium 1^1S , 2^1S , 2^3S and He^+ states. For the transmission spectroscopy modelling of the helium triplet signature at 1083 nm, we use a ray tracing technique previously applied to Lyman- α and H- α transmission spectroscopy modelling (Allan & Vidotto 2019). We utilise evolving predictions of stellar flux and radius (Johnstone et al. 2021) and planetary

radius (Fortney & Nettelmann 2010) as input for our evolution modeling. We also explored how the He/H abundances and self-consistent inclusion and omission of helium energetics affect both the atmospheric escape and its 1083 nm absorption signature.

Our main conclusions regarding the hydrodynamics of escaping atmosphere are listed below:

- The heating processes which dominate are: photoionisation of neutral hydrogen by sEUV (36-92 nm), hEUV (10-36 nm) photons as well as by the 24.6 eV photon produced in the direct recombination to the helium 1^1S state. Although not dominant, heating arising from the photoionisation of He(1^1S) by hEUV photons is not negligible for abundances of 2% (Figure 3.5), and is more important for higher abundances (Figure 3.12).
- Neglecting helium heating contributions leads to a reduction of 21 and 45% in the net heating contribution at young and old ages, respectively, assuming a helium abundance of 0.1. See Figure 3.5.
- The majority of the heating affects the sub-sonic region of the atmosphere meaning that heating reductions with planetary evolution affects the mass-loss rate more so than the terminal velocity of the escaping atmosphere.
- Increasing the helium abundance from 2% to 10% results in a slightly slower outflow, with a smaller mass-loss rate (Figure 3.4). This does not strongly affect the hydrodynamics, but is important in the observability of the triplet (as we will discuss below).
- Omitting helium energetics in the hydrodynamics models leads to a lower mass loss and terminal velocity (Figure 3.4).

Regarding the population of the helium triplet and its observability, we found the following main conclusions:

- The dominant populating process for the helium triplet state is the recombination of ionised helium into the triplet state (Figure 3.6).
- The dominant depopulating process for the helium triplet state helium is de-excitation into the helium singlet state through a collision with a free electron (Figure 3.6).
- Although increasing the helium abundance from 2% to 10% does not affect the hydrodynamics, it substantially changes the observability of the transiting atmosphere. At an age of 5 Gyr, the (T1-T4 phase-averaged) peak excess absorption increases from 1.5% to 7.4% (see Figure 3.11).

When accounting for the evolution of the system, we showed that the diminishing XUV flux required to heat the planetary atmosphere combined with the growing gravitational force due to the shrinking planetary radii leads to the weakening of atmospheric escape as the planet evolves. As a consequence of a slower, less dense and less extended wind, the helium 1083 nm signature weakens overall with evolution (Figures 3.8, 3.10, 3.11).

We found that the strongest helium 1083 nm absorption occurs at the youngest ages. Our models predict that a very young ($\lesssim 150$ Myr) gas giant closely orbiting a K-dwarf star could produce a helium 1083 nm absorption of $\sim 4\%$ to $\sim 7\%$ assuming a helium abundance of 2% (if orbiting a slow or fast rotating star). This weakening with evolution, however, is not necessarily monotonic. For example, the transit depths and equivalent width of the planet at age 150 Myr are larger than those at 40 Myr for models with $\text{He}/\text{H} = 0.1$. This is due to a large drop in stellar radius corresponding with small decline of atmospheric escape.

3.6.2 Do we observe larger helium absorption at younger ages?

Our model suggests stronger helium 1083 nm absorption at younger ages. Is this higher absorption seen in the observations?

So far, there has been a limited number of helium 1083 nm transit observations of young systems. One difficulty is the greater stellar variability in helium 1083 nm at younger ages. Another difficulty is the small number of exoplanets known to transit a young (< 500 Myr) star, and in particular a K-type star best suited for 1083 nm detections. This currently small sample consists of super-Earths and mini-Neptunes, whose escaping atmospheres are intrinsically harder to detect than for larger planets.

In recent years, helium transit observations of a few young systems resulted in either non-detections or tentative detections possibly of stellar rather than planetary origin, namely of AU Mic b (Hirano et al. 2020), of the V1298 Tau planets (Gaidos et al. 2022; Vissapragada et al. 2021), of TOI 1807b and 2076b (Gaidos et al. 2023), and of the 400-Myr old mini-Neptune HD 63433c (Zhang et al. 2022b). Of these, only TOI 1807b and 2076b are thought to have K dwarf hosts, but these planets are rocky planets whose primary H-rich atmosphere might have already been lost. Zhang et al. (2023b, 2022a) recently reported successful helium 1083 nm detections for four young mini-Neptunes orbiting K dwarfs, with mean excess absorptions of $\sim 1\%$ in each.

It should be noted that the larger absorption predicted at young ages in our evolution models is not at odds with the current observations, as the current sample of observed young exoplanets orbiting K-dwarfs for which helium 1083 nm transmission spectroscopy has been performed does not yet include a gas giant planet. Hence, finding a system in which a larger radius

$1 - 2R_{\text{Jup}}$ close-in (< 0.1 au) exoplanet transits a young (< 150 Myr), ideally K dwarf star would be a better test to our evolution models. In a forthcoming work, we apply our modelling techniques for atmospheric escape and helium 1083 nm transmission spectroscopy to smaller, mini-Neptunes, more consistent with the current helium 1083 nm detections of young exoplanets.

Acknowledgements

APA and AAV acknowledge funding from the European Research Council (ERC) under the European Union’s Horizon 2020 research and innovation programme (grant agreement No 817540, ASTROFLOW). We thank several colleagues for discussions over this project: S. Carolan, D. Kubyshkina, J.S. Pineda, I. F. Shaikhislamov, A. Oklopčić, R. Allart and M. López Puertas. We gratefully thank the anonymous referee for their thorough analysis, insightful comments and suggestions that have greatly enhanced this work. This work has made use of data from the European Space Agency (ESA) mission *Gaia* (<https://www.cosmos.esa.int/gaia>), processed by the *Gaia* Data Processing and Analysis Consortium (DPAC, <https://www.cosmos.esa.int/web/gaia/dpac/consortium>). Funding for the DPAC has been provided by national institutions, in particular the institutions participating in the *Gaia* Multilateral Agreement.

Data Availability

The data described in this article will be shared on reasonable request to the corresponding author.

Appendix

Sensitivity to model free parameters

Two free parameters in our hydrodynamical models are the density and temperature at the base of the planetary atmosphere, assumed to be $\rho_0 = 4 \times 10^{-14}$ g cm $^{-3}$ and $T_0 = 1000$ K (see Section 3.2.1). We now discuss the model’s sensitivity to these values using two test models.

We test increasing the assumed base density by one order of magnitude, to $\rho_0 = 4 \times 10^{-13}$ g cm $^{-3}$. This larger base density causes the predicted mass-loss rate to increase by factors of 3.6 and 1.9 at ages of 16 and 5000 Myr, respectively. It only negligibly affects the terminal velocity (below 4% in all models). Hence, the hydrodynamics do not change significantly by varying the base density within a factor of 10 (i.e., at most by a factor of 3.6

in mass-loss rate affecting the youngest model). This is in agreement with [Murray-Clay et al. \(2009\)](#) who find their model’s hydrodynamic predictions to be insensitive to the assumed base density, so long as the chosen value results in an optical depth at the atmospheric base $\gg 1$. This is indeed true for the dominant H^0 sEUV photoionisation in our model for both of the base densities considered here. We also test raising the assumed base temperature to $T_0 = 2000$ K. This hotter base temperature causes the predicted mass-loss rate to increase by factors of 1.7 and 1.5 at young and old ages, respectively. As with the base density test, varying the base temperature only negligibly affects the terminal velocity (below 2% in all models).

However, we find that the variations in base density can cause changes beyond the uncertainties of observations in transit depth and EW at younger ages: we found increases by factors of 2.7 (1.8) in the EW and 2.4 (1.7) in the phase-averaged peak transit depth at ages of 16 (5000) Myr. For example, for the youngest age model, the peak transit depth obtained by our fiducial F10% model is 34%, while the increased-base density model results in a maximum depth of 81%. This is a change that could be observed. The sensitivity is because most of the $\text{He}(2^3\text{S})$ absorption takes place close to the planet. Because of such sensitivity, helium triplet transit observations can be used to constrain the atmospheric base density. However, it is interesting that this effect is not significant in the hydrodynamics (i.e., evaporation rates are not significantly altered by changes in base density). This is in stark contrast to isothermal models, in which the evaporation rate is directly proportional to base density. Raising the base temperature to 2000 K also affects the predicted observational results, albeit less so than the mentioned base density test. The increased base temperature leads to increases by factors of 1.6 (1.4) in the EW and 1.5 (1.4) in the peak transit depth at ages of 16 (5000) Myr.

Additional data on a helium abundance of 10%

Figure 3.12 shows the individual heating contributions for the F10% model. Compared to the F2% model (Figure 3.5), we see that heating due to helium unsurprisingly plays a more significant role for a greater helium abundance, however photoionisations of H^0 still dominates except in the very innermost atmosphere, where the photoionisation of $\text{He}(1^1\text{S})$ takes over, at both young and old ages.

The left panel of Figure 3.13 shows the resulting temperature profile for the F10% model, where we see the temperature is very similar to the F2% model (compare to Figure 3.7). The hydrodynamics of these models with two different abundances are very similar, reaching similar mass-loss rates, temperatures and velocities (with slightly lower speeds in the F10% model, as discussed in Section 3.4.1). This is a result of hydrogen photoionisation being the dominant driver of the atmospheric escape in both cases as

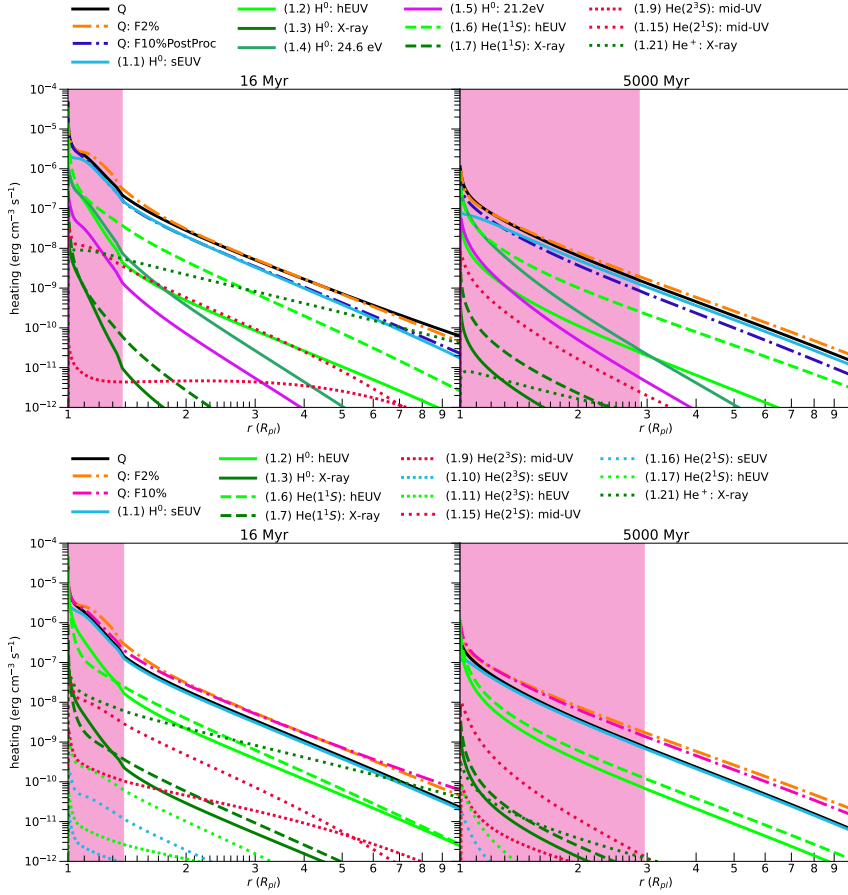


Figure 3.12: The same as the upper-panel of Figure 3.5, now showing individual heating components for our F10% (upper-panel) and F10%PostProc (lower-panel) model.

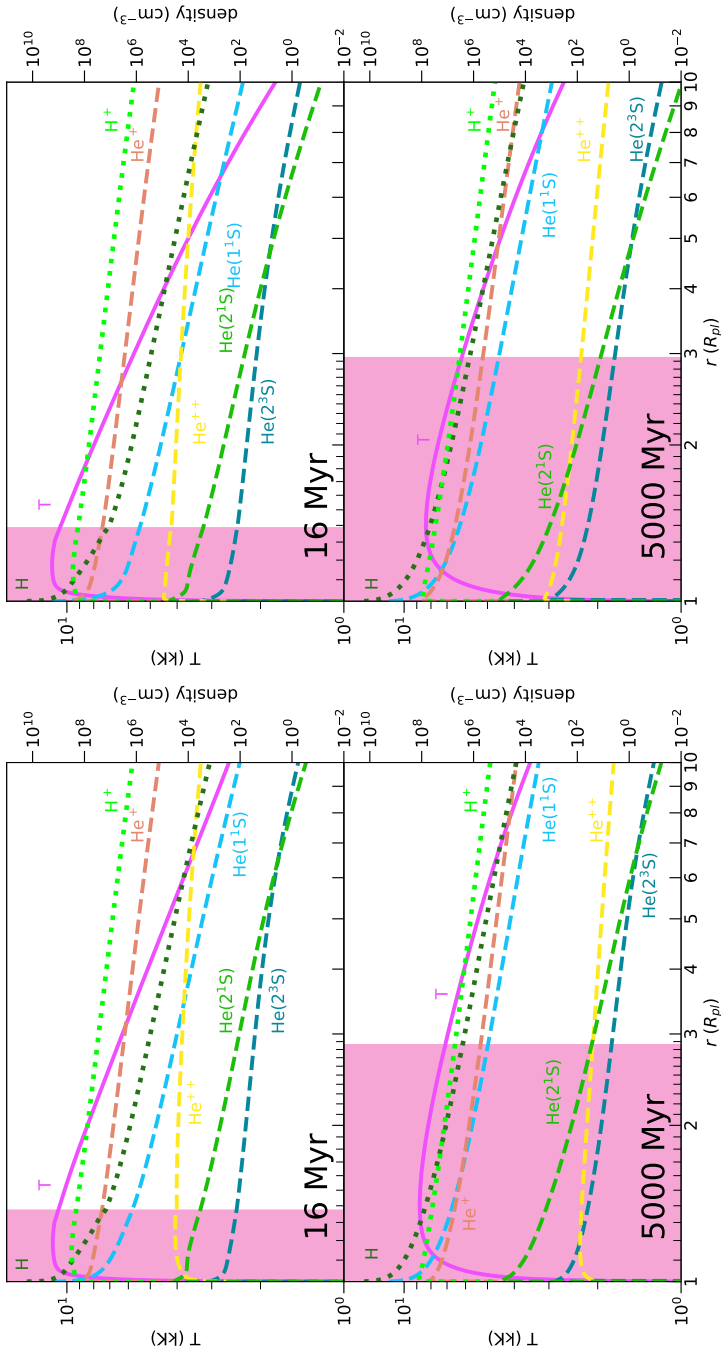


Figure 3.13: The same as Figure 3.7, now for our F10% (left-panel) and F10%PostProc (right-panel) models.

mentioned.

Additional data on omitting helium energetics

The right panel of Figure 3.13 shows the resulting temperature profile for the F10%PostProc model, where now we see more substantial differences in the temperature profile. While the F10% and F10%PostProc reach similar maximum temperatures, the latter exhibits a faster temperature decay. The lowered availability of potential absorbers for photoionisation heating (neutral hydrogen only as opposed to neutral hydrogen and helium), and the omission of photons released in helium transitions, are responsible for the swifter temperature decay.

4 | HELIUM ESCAPE SIGNATURES ARE GENERALLY STRONGEST DURING YOUNGER AGES BUT THIS AGE DEPENDENCE IS LOST IN THE DIVERSITY OF OBSERVED EXOPLANETS

A. P. Allan, A. A. Vidotto, 2025, *Monthly Notices of the Royal Astronomical Society*, Volume 539, Issue 3, May 2025, Pages 2144–2157.

Abstract

Highly irradiated exoplanets undergo extreme hydrodynamic atmospheric escape, due to their high level of received XUV flux. Over their lifetime, this escape varies significantly, making evolution studies essential for interpreting the growing number of observations of escaping planetary atmospheres. In a previous work, we modelled this evolving escape, alongside one of its observable tracers, the helium triplet transit signature at 1083nm. Using hydrodynamic and ray-tracing models, we demonstrated that atmospheric escape and the corresponding He I 1083 nm signature are stronger at younger ages, for a $0.3 M_J$ gas-giant. Yet, the current literature includes several young ($<1\text{Gyr}$) planets with weak or non-detections in He I 1083 nm. To understand this apparent discrepancy, we now perform detailed modelling for many of these systems. The resulting He I 1083 nm predictions align relatively well with the observations. From our two studies, we conclude that for any given planet, stronger atmospheric escape during younger ages produces deeper He I 1083 nm absorption. However, for a population of exoplanets, the relation between younger ages and stronger He absorptions is lost to the broad diversity of their various other system parameters. Accordingly, for the current sample of young, 1083nm-observed exoplanets, alternative trends take precedence. One such trend is that planets with deeper geometrical transits exhibit more favourable detections. Our modelling also agrees with the strong empirical trend in the literature between $EW \cdot R_*^2$ and $F_{\text{xuv}} \cdot R_{\text{pl}}^2 / \Phi_g$. Additionally, we show that the coupling between the lower and upper atmospheres is necessary for a robust prediction of the 1083nm signature.

4.1 Introduction

Exoplanets close in to their host star receive a high flux of X-ray and ultraviolet (XUV) radiation capable of heating their planetary atmosphere and ultimately driving its hydrodynamic escape. Numerous confirmed detections of escaping atmospheres have been made using the method of transit spectroscopy. This was first achieved via the hydrogen Lyman- α line for the hot-Jupiter HD 209458b (Vidal-Madjar et al. 2003). The helium triplet at 1083 nm (Seager & Sasselov 2000; Oklopčić & Hirata 2018) has since overtaken Lyman- α as the most popular tracer for escaping atmospheres (for review, see Dos Santos 2023). This near-infrared spectral feature is produced by helium in the metastable 2^3S state absorbing stellar photons resulting in the 2^3S to 2^3P transition. This observing strategy is still in its infancy, with the first space-based detection only happening in 2018 (Spake et al. 2018), swiftly followed by ground-based detections (Nortmann et al. 2018; Allart et al. 2018). Despite its novelty, there have now been over 50 helium triplet transit observations due to its ability to be observed using ground-based telescopes. Hence, population studies linking planetary parameters with the observed helium triplet absorption are now feasible (Krishnamurthy & Cowan 2024). Such studies benefit from homogeneous surveys obtained with the same instruments (Zhang et al. 2023b; Allart et al. 2023; Vissapragada et al. 2022; Orell-Miquel et al. 2024).

Unfortunately, observing escaping atmospheres with the helium triplet entails many difficulties, as proven by the currently greater number of non-detections than detections. The high uncertainty of the XUV flux received by the planet, a parameter which greatly affects both the escape and its observability, is one of the most difficult problems currently being faced. The ability of stellar variability to convincingly mimic the desired signature of planetary atmospheric escape is another. On the latter however, Krolkowski et al. (2024) show that the intrinsic stellar variability should not preclude detection of young exospheres, except at the youngest ages when the star is most active. The current scarcity of suitable close-in, young, transiting systems as well as poor constraints on their planetary masses also adds to the difficulty of observing and modelling atmospheric escape at young ages.

Despite the mentioned observational difficulties, younger ages (< 1 Gyr) remain a highly interesting phase in the context of planetary atmospheric escape, given that this is when the escape is strongest. At these ages, the high XUV flux and weaker gravitational force due to the ‘puffed up’ nature of younger exoplanets leads to a stronger atmospheric escape (Allan & Vidotto 2019). With time, the escape weakens due mainly to the reduction of XUV flux received as the star spins down (Vidotto et al. 2014) and the shrinking of the planetary radius as the planet cools (Fortney &

Nettelmann 2010). Hence, the first Gyr of evolution is when the most drastic atmospheric changes occur (Owen & Wu 2013). The extent to which a planetary atmosphere escapes depends on many factors, with the planetary gravity, the level of XUV flux received and the reservoir of atmospheric material all playing pivotal roles. In the most extreme cases, the primordial atmosphere can be lost entirely, changing the very nature of the planet (Lopez et al. 2012; Owen & Wu 2013; Fossati et al. 2017; Kubyskhina et al. 2018). Due to such cases, the process of extreme hydrodynamic escape is one of the leading theories currently offered to explain the sub-Jovian desert and radius gap (Fulton et al. 2017) apparent in the current population of observed exoplanets (Owen & Wu 2017; Jin & Mordasini 2018).

Given the importance of atmospheric escape at younger ages, studies are beginning to purposefully target young exoplanets for helium triplet observations. Zhang et al. (2023b) reported escaping helium in four <1 Gyr mini-Neptunes using Keck/NIRSPEC. Alam et al. (2024) set upper-limits due to non-detections in three <800 Myr sub-Jovian exoplanets with Keck II/NIRSPEC. Gathering published helium observations, Krishnamurthy & Cowan (2024) show that large planets have detections across young and old ages while small ($<2.6 R_{\oplus}$) planets only have detections at young ages. They attribute this to the total loss of the planetary atmosphere for smaller planets. The MOPYS (Measuring Out-flows in Planets orbiting Young Stars) project of Orell-Miquel et al. (2024) performed high-resolution spectroscopy observations with CARMENES (Quirrenbach et al. 2014) and GIARPS (Claudi et al. 2016) for 20 exoplanets. Their large scale project found that 0.1-1 Gyr-old planets do not exhibit more helium triplet and hydrogen H- α detections than older planets, in agreement with the study of Krishnamurthy & Cowan (2024). This absence of strong trend between planetary age and atmospheric escape signature is interesting considering that numerous theoretical studies escape predict escape to be strongest at the youngest ages. For example, the evolution studies of Allan & Vidotto (2019) and Allan et al. (2024) show clear trends between younger ages and stronger hydrogen (Lyman- α and H- α) and helium triplet absorption.

In this current work, we seek to clear up this apparent discrepancy. We do so by running self-consistent hydrodynamic escape models for numerous young planets which have helium triplet observations. In section 4.2, we outline our modelling approach. In section 4.3, we present our findings, discussing trends between planetary parameters and both the modelled and observed triplet absorption. Finally, we summarise our conclusions in section 4.4.

4.2 Modelling approach

We utilise two models in this work. The first being our hydrodynamic model, which self-consistently solves the fluid dynamic equations in addition to the coupled equations for hydrogen ionisation balance and helium state populations. It solves for transitions between the helium 1^1S , 2^1S , 2^3S and singly and doubly ionised states. The second is our ray-tracing model which utilises the atmospheric profiles and calculates the individual extinction by each of the lines of the helium triplet during a planetary transit. We refer the reader to [Allan et al. \(2024\)](#) for more in-depth descriptions of both models. The ray-tracing technique remains unchanged. In this current work, we outline only additions to our hydrodynamic model. The main additions can be summarised as follows. We now:

- model a sample of observed young systems (section 4.2.1), rather than the lifetime evolution of fictitious highly irradiated exoplanets ([Allan & Vidotto 2019](#); [Allan et al. 2024](#)).
- make a more physically-informed, system-dependant predictions for the conditions at the lower boundary of our modelled atmospheres (section 4.2.2).
- extend our modelled atmospheres to the minimum height required to fully encompass the stellar disk rather than $10R_{\text{pl}}$, given the smaller size of these modelled planets.

4.2.1 Sample of modelled systems

As previously discussed in section 4.1, young exoplanets are of particular interest when it comes to understanding the helium triplet transit signature both observationally and theoretically. Hence, we choose to model younger planets, with our chosen sample satisfying the following requirements:

- An age estimate below 1 Gyr¹.
- An orbital distance below 0.15 au.
- A host star of spectral-type K or G.
- A high-resolution helium triplet observation.

This selection process led us to 12 planets in our sample. Table 4.1 lists all of these planets along with their planetary parameters required as

¹We make an exception for TOI-2018b, given that it was initially presented as a young planet, although now has an updated, relatively young age estimate of 1.6 to 2.6 Gyr. TOI-1683b is a similar case, with [Zhang et al. \(2023b\)](#) quoting a young age of 500 ± 150 Myr while [Orell-Miquel et al. \(2024\)](#) recently pushed this back to $2_{-0.9}^{+1.3}$ Gyr.

Table 4.1: Properties of the planets considered in this work. Each planet has helium triplet transmission spectroscopy observations. The columns refer to planetary name, classification, age, mass, radius, orbital distance, and transit impact parameter and transit duration from first to fourth contact. Planetary mass values marked with superscripts ‘a’ and ‘b’ indicate that the mass was obtained via the mass-radius relation of [Chen & Kipping \(2017\)](#) and [Wolfgang et al. \(2016\)](#), respectively, due to lack of a precise radial velocity measurement.

name	classification	age (Myr)	M_{pl} (M_{\oplus})	R_{pl} (R_{\oplus})	a (AU)	b	t_{dur} (hours)	Reference
Wasp-52b	inflated hot-Saturn	400^{+300}_{-200}	137.9	14.0	0.027	0.60	1.81	(Kirk et al. 2022)
V1298 Tau c	proto-sub-Neptune	23 ± 4	26.7^{a}	5.5	0.082	0.35	4.66	(Alam et al. 2024)
TOI-1268b	hot-Saturn	110-380	96.3	9.1	0.072	0.42	4.00	(Pérez-González et al. 2024)
TOI-1683b	mini-Neptune	500 ± 150	8.0^{b}	2.3	0.036	0.85	1.28	(Zhang et al. 2023b)
K2-100b	Neptune desert dweller	750 ± 5	21.8	3.9	0.030	0.79	1.61	(Alam et al. 2024)
TOI-1430b	mini-Neptune	165 ± 30	7.0^{b}	2.1	0.070	0.44	2.71	(Zhang et al. 2023b)
TOI-2018b	super-Earth	2400^{+200}_{-800}	9.2	2.3	0.061	0.55	2.36	(Dai et al. 2023)
TOI-2076b	mini-Neptune	204 ± 50	9.0^{b}	2.6	0.063	0.34	3.25	(Zhang et al. 2023b)
HD 63433b	mini-Neptune	414 ± 23	5.3^{a}	2.2	0.072	0.38	2.93	(Alam et al. 2024)
HD 63433c	mini-Neptune	414 ± 23	7.3^{a}	2.7	0.146	0.37	4.10	(Zhang et al. 2022b)
TOI-560b	mini-Neptune	480-750	15.9	2.8	0.060	0.57	2.14	(Zhang et al. 2023b)
K2-136c	sub-Neptune	650 ± 70	18.1	3.0	0.110	0.31	3.45	(Mayo et al. 2023)

Table 4.2: Properties of the stars used in this work. The columns give the stellar spectral-type, age, mass, radius and the luminosity in each of the XUV and mid-UV bins (specified in the text). The first three host stars listed have their own SED from the literature. For the remainder, we utilise proxy SEDs from stars with similar spectral type and radius as indicated by the final column. MUSCLES series refers to the following works: France et al. (2016); Youngblood et al. (2016); Loyd et al. (2016). MUSCLES extension refers to Behr et al. (2023).

star	type	age (Myr)	M_* (M_\odot)	R_* (R_\odot)	$L_{X\text{-ray}}$ ($10^{-5}L_\odot$)	$L_{h\text{UV}}$ ($10^{-5}L_\odot$)	$L_{s\text{UV}}$ ($10^{-5}L_\odot$)	$L_{\text{mid-UV}}$ ($10^{-5}L_\odot$)	SED reference
Stars with an XUV SED available									
V1298 Tau	G2	23±4	1.10	1.34	91.16	18.62	8.59	591	(Duvvuri et al. 2023)
HD 63433	G5	414±23	0.99	0.91	2.04	1.75	2.55	2017	(Zhang et al. 2022b)
TOI-560	K4V	480-750	0.73	0.65	0.35	0.42	0.44	289	(Zhang et al. 2022a)
Stars requiring a proxy star									
K2-100	G0	750±5	1.15	1.24	1.31	1.13	3.05	664	<i>l</i> -Horologii
TOI-1268	K1/K2	110-380	0.96	0.92	0.72	1.05	1.20	517	<i>e</i> -Eridani
Wasp-52	K2	400 ⁺³⁰⁰ ₋₂₀₀	0.87	0.79	0.53	0.78	0.88	382	<i>e</i> -Eridani
TOI-1683	K0	500±150	0.69	0.64	0.34	0.50	0.57	247	<i>e</i> -Eridani
TOI-1430	K2V	165±30	0.85	0.78	0.52	0.76	0.87	376	<i>e</i> -Eridani
TOI-2076	K0	204±50	0.82	0.76	0.49	0.72	0.82	355	<i>e</i> -Eridani
TOI-2018	KV	2400 ⁺²⁰⁰ ₋₈₀₀	0.57	0.62	0.02	0.12	0.10	30	HAT-P-12
K2-136	K5.5	650±70	0.74	0.68	0.03	0.14	0.12	35	HAT-P-12
Proxy stars									
<i>l</i> -Horologii ²	G0V	600	1.34	1.13	1.31	1.13	3.05	664	(Sanz-Forcada et al. 2019)
<i>e</i> -Eridani	K2	600±200	0.82	0.74	0.47	0.68	0.77	335	MUSCLES series: [V2.2]
HAT-P-12	K5	2500±2000	0.73	0.70	0.03	0.15	0.13	38	MUSCLES extension: [V2.4]

² We used the same SED as Alam et al. (2024), in which the Sanz-Forcada et al. (2019) model was joined with the solar SED for the longer wavelengths.

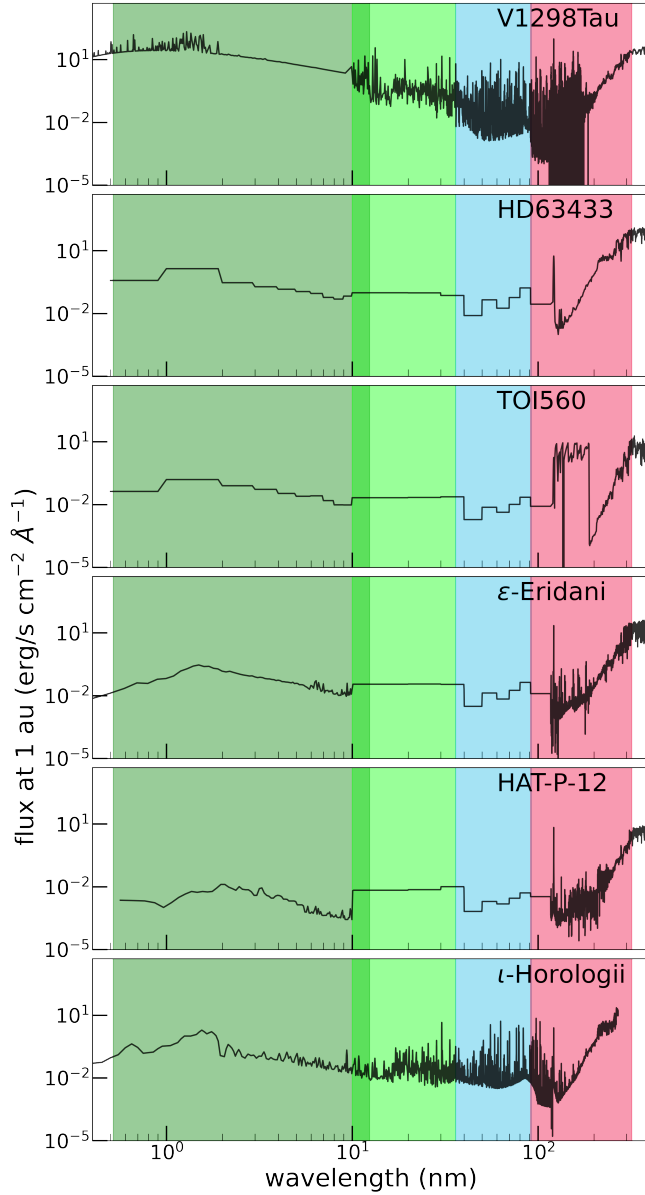


Figure 4.1: Stellar spectral energy distributions (SED's) adopted in our modelling. Table 4.2 lists the stellar parameters of each as well as the relevant reference. The shaded regions from left to right denotes the X-ray, hard-EUV, soft-EUV and mid-UV wavelength bins.

input to our modelling. Of all of the considered planets, only three of their host stars have a spectral energy distribution (hereby SED) published in the literature. For the remaining stars, we use their spectral type to assign them a proxy SED. We use the SED to calculate the stellar flux at the planet's orbital distance. Figure 4.1 displays each of the SEDs utilised. From left to right, they are binned into X-ray (0.517-12.4 nm), hard-EUV (10-36 nm), soft-EUV (36-92 nm) and mid-UV (91.2-320 nm) in accordance with [Allan et al. \(2024\)](#) and [Johnstone et al. \(2021\)](#). The resulting luminosities are listed in Table 4.2 along with other assumed stellar properties relevant to our modelling.

4.2.2 Determining the hydrodynamic atmospheric base

An important assumption of hydrodynamic escape models is the location of the upper atmospheric base, as well as its density and temperature. Usually, models are computed starting at the geometric radius of the planet, hereby R_{pl} . The sensitivity of the predicted hydrodynamic escape to boundary conditions assumed at the modelled upper atmospheric base (hereby R_{base}) has been studied by many. For example, the predicted atmospheric escape of the purely hydrogen, photons concentrated on a single energy, self-consistent, 1 D model of [Murray-Clay et al. \(2009\)](#) was shown to be reasonably insensitive to the assumed base density $\rho[R_{\text{base}}]$, base H-ionisation fraction $f_{\text{H}^+}[R_{\text{base}}]$ and their base temperature $T[R_{\text{base}}]$, so long as; $\tau[R_{\text{base}}] \gg 1$; $f_{\text{H}^+}[R_{\text{base}}] \ll 1$ and $T[R_{\text{base}}] \ll 10^4$ K. They do, however, note their solution to be highly sensitive to the height designated to the upper atmosphere base, with a 10% uncertainty in this producing as much as a factor of two variation in the predicted mass-loss rate. Using an order of magnitude calculation, they show the uncertainty in this height to be $\sim 10\%$, given that their R_{base} is set at $1R_{\text{pl}}$ rather $1.1R_{\text{pl}}$, where they find UV photons are absorbed. Indeed, applying the method later outlined in this section to the HD 209458b analogue of [Murray-Clay et al. \(2009\)](#), we reach only a slightly higher atmospheric base of $R_{\text{base}} = 1.18 R_{\text{pl}}$. Given their determined uncertainty of 10% in R_{base} , they determine their mass-loss rate predictions to include an uncertainty of at most a factor of two. For some of our considered sample of young exoplanets however, we calculate considerably larger relative values for R_{base} (see Table 4.3), raising the importance of the chosen height for the base of the upper atmosphere, due to its effect on the predicted atmospheric escape and resulting signatures. [Salz et al. \(2016b\)](#) reported similar findings to [Murray-Clay et al. \(2009\)](#) using the Pluto-Cloudy Interface (TPCI [Salz et al. 2015](#)), with sensitivities to $T[R_{\text{base}}]$ and $\rho[R_{\text{base}}]$ resulting in respective uncertainties of $<10\%$ and $<50\%$ in the predicted mass-loss rate.

We previously confirmed the discussed lower boundary sensitivities findings of [Murray-Clay et al. \(2009\)](#); [Salz et al. \(2016b\)](#) in our purely hydrogen,

Table 4.3: Upper atmospheric base properties, where the base is set at a pressure of 10 nanobar, and the density and temperature were calculated as explained in section 4.2.2. The final two columns give the base density assuming He/H number fractions of 0.1 and 0.02, respectively, with their difference arising from their mean molecular weights.

name	R_{base} (R_{pl})	$T[R_{\text{base}}]$ (K)	$\rho[R_{\text{base}}]$ (g cm^{-3})	$\rho[R_{\text{base}}]$ (g cm^{-3})
Wasp-52b	1.25	987	1.60e-13	1.30e-13
V1298 Tau c	1.43	829	1.90e-13	1.55e-13
TOI-1268b	1.16	676	2.33e-13	1.90e-13
TOI-1683b	1.51	666	2.37e-13	1.93e-13
K2-100b	1.65	1375	1.15e-13	9.35e-14
TOI-1430b	1.49	604	2.61e-13	2.13e-13
TOI-2018b	1.32	479	3.29e-13	2.68e-13
TOI-2076b	1.49	650	2.42e-13	1.98e-13
HD 63433b	1.77	729	2.16e-13	1.76e-13
HD 63433c	1.49	512	3.08e-13	2.51e-13
TOI-560b	1.26	541	2.91e-13	2.38e-13
K2-136c	1.18	402	3.92e-13	3.20e-13

photons concentrated at a single energy, self-consistent, 1 D model (Allan & Vidotto 2019). When including helium species and splitting the flux into various energy bins, we again found general agreement with the mentioned sensitivities (see appendix A of Allan et al. 2024). Interestingly however, we also noted our model to exhibit a strong sensitivity of the predicted helium triplet profile with the assumed boundary conditions, beyond the uncertainties of the observations (now demonstrated again in Appendix 4.4 for models of TOI-1286b and TOI-560b). For example, raising the assumed density at the base of the modelled atmosphere by an order of magnitude was found to increase the equivalent width of the predicted helium triplet by factors of 2.7 and 1.8 at respective ages of 16 Myr and 5 Gyr (Allan et al. 2024). This sensitivity has important implications in the context of modelling the observable helium triplet signature, particularly of younger planets and motivated us to better constrain the assumed boundary conditions at the base of our modelled upper atmosphere.

In order to achieve this, we utilise inputs from a lower atmosphere model. The lower and upper atmospheric models are coupled at a pressure $P[R_{\text{base}}]$ of 10 nanobar. We select this pressure to correspond to a height in the atmosphere at which heat from XUV photoionisation is sufficiently deposited. This chosen pressure was influenced by the few nanobar quoted in Murray-Clay et al. (2009, sketch in figure 8) for where UV photons are absorbed and Tang et al. (2024) who state that the photoionising high-energy flux

is deposited at a nanobar pressure. We note however that other studies assume greatly differing pressures at the base of their modelled escaping atmospheres, such as [Koskinen et al. \(2013\)](#) who select 1 μbar , based on photo-chemical calculations of HD 209458b ([Lavvas et al. 2014](#)). [Yan et al. \(2022\)](#) also assume a base pressure of 1 μbar , while [Lampón et al. \(2020\)](#) instead use 1 mbar. The ATES photoionization hydrodynamics code (ATmospheric EScape, [Caldioli et al. 2021](#)) follows the approach of [Salz et al. \(2016b\)](#) for the lower boundary conditions, assuming a total number density of 10^{14} cm^{-3} (corresponding to pressures around 14 μbar) at a modelled atmospheric base set to 1 R_{pl} . [Salz et al. \(2016b\)](#) highlight the slight inconsistency in beginning the simulation at 1 R_{pl} despite the assumed density being reached at a height above the planetary surface. This is currently a common inconsistency, present also in the previous versions ([Allan & Vittotto 2019](#); [Allan et al. 2024](#)) of the model presented here. Improving upon this by now coupling lower and upper atmospheric models, we utilise the lower atmosphere model of [Parmentier & Guillot \(2014\)](#). This analytical model provides the temperature-optical depth relation for planetary atmospheres that are heated both from below (intrinsic heat) and above (stellar irradiation), assuming a plane-parallel atmosphere inspired by Eddington’s approximation. As input we provide the planetary gravity g and the irradiated temperature, calculated using equation 1 of [Guillot \(2010\)](#). For all remaining inputs, we default to the standard values given in the [Parmentier & Guillot \(2014\)](#) model.

From the static model, we obtain atmospheric profiles of pressure P_s , temperature T_s , mean molecular weight μ_s , and optical depth τ_s where subscripts ‘s’ indicates static rather than hydrodynamic output profiles. We refer to the atmospheric height where $\tau_s = 2/3$ as the planetary photosphere, setting $R_{\text{photo}} = 1 R_{\text{pl}}$. Under the assumptions of hydrostatic equilibrium for an isothermal gas, we then calculate the height z above the photosphere at which our chosen $P[R_{\text{base}}] = 10$ nanobar is achieved:

$$z = -H_s \left(\ln(P[R_{\text{base}}]) - \ln(P[\tau_s = 2/3]) \right), \quad (4.1)$$

where $H_s = \frac{k T_s}{\mu_s m_{\text{H}} g}$ is the atmospheric scale height, with k being the Boltzmann constant and μ_s being the mean molecular weight in the lower static atmosphere. We set the base of our hydrodynamic atmosphere to occur at the height $R_{\text{base}} = 1 R_{\text{pl}} + z$, corresponding to a pressure of 10 nanobar. This height and the corresponding temperature and density (from the ideal gas law) required by our modelling are listed in Table 4.3 for each planet. For our sample, R_{base} spans from 1.16 to 1.77 R_{pl} , considerably above the standardly assumed 1 R_{pl} lower boundary condition used in our previous [Allan et al. \(2024\)](#) model version. While still inevitably making an assumption about the environment at the base of the atmosphere (namely the pressure being 10 nanobar), this approach allows for a more physically

informed estimate, given that the planetary gravity and the irradiated temperature now inform our choice of both the pressure and temperature for our hydrodynamic model.

As input for our ray-tracing model for predicting the helium triplet transit signature, we fuse the atmospheric profiles of the static atmosphere (spanning $1 R_{\text{pl}}$ to R_{base}) with the hydrodynamic atmosphere. In doing so, we assume that the fraction of helium in the triplet state within the innermost static atmosphere is constant and equal to the value predicted by the hydrodynamic atmosphere at R_{base} . Testing our ray-tracing model by assuming various constants for this fraction in the static atmosphere, we determine this value to only negligibly affect the resulting helium triplet profile predictions.

A comparison between the predicted triplet profiles obtained using the commonly used boundary conditions of $R_{\text{base}} = 1 R_{\text{pl}}$, $\rho[R_{\text{base}}] = 4 \times 10^{-14} \text{g cm}^{-3}$, $T[R_{\text{base}}] = 1000 \text{K}$ rather than those assumed in this work, is presented in section 4.4 of the appendix.

4.3 Results & discussion

4.3.1 General hydrodynamic predictions

Table 4.4 lists predicted properties for each of our modelled exoplanets; the mass-loss rate (\dot{m}), the wind terminal velocity (v_{term}), the peak of the temperature profile and the equivalent width and peak excess absorption of the helium triplet profiles. The adopted helium fraction has little effect on the predicted escape properties while naturally having a strong correlation on the corresponding observable helium signature. The mass-loss rate predictions appear to be strong relative to some recent studies of the same planets (Zhang et al. 2023b; McCreery et al. 2025). As discussed in more detail in section 4.4 of the Appendix, differing modelling natures are likely responsible for this noted discrepancy.

Overall, we find that the hydrodynamic behaviour of the escaping atmospheres modelled here follows that described previously in Allan et al. (2024), for an evolving, theoretical, $0.3 M_{\text{Jup}}$ planet closely orbiting a K-type star. Accordingly, we now only briefly discuss the dominant hydrodynamic processes.

For our entire exoplanet sample, heating within the majority of the modelled atmosphere is predominantly driven by the photoionisation of neutral hydrogen H^0 by sEUV photons. Within some inner region specific to each planet but extending out to $\lesssim 2 R_{\text{pl}}$ for all, alternative photoionisations dominate the heating. Assuming $\text{He}/\text{H}=0.02$, these are the photoionisations of H^0 by hEUV photons and by 24.6 eV photons (themselves emitted in direct recombinations to $\text{He}(1^1\text{S})$ from He^+). These photoionisations con-

Table 4.4: Atmospheric escape predictions for each of our planets. \dot{m} refers to the mass-loss rate. We define v_{term} as the velocity reached at $10 R_{\text{pl}}$. The hydrodynamic atmospheric temperature profile starts at $T[R_{\text{base}}]$, reaching a maximum temperature $\max(T)$ and cools off beyond that. EW refers to the equivalent width of the predicted helium triplet signature, while peak refers to its peak excess absorption. Predictions are giving first assuming a He/H number fraction of 0.1 and then 0.02.

name	\dot{m} (10^{12} g/s)	v_{term} (km/s)	$\max(T)$ (kK)	EW (mÅ)	peak (%)
He/H=0.1					
Wasp-52b	2.0	67	11.2	269	16.7
V1298 Tau c	6.5	31	11.1	147	7.4
TOI-1268b	0.5	23	10.1	49	4.9
TOI-1683b	3.4	27	9.9	16	1.5
K2-100b	7.6	34	11.3	23	1.2
TOI-1430b	1.9	21	7.6	8.4	1.0
TOI-2018b	0.3	11	4.6	5.5	0.9
TOI-2076b	2.0	23	8.4	7.6	0.8
HD 63433b	5.7	26	10.3	7.5	0.8
HD 63433c	1.4	20	7.3	4.8	0.7
TOI-560b	0.6	19	7.0	5.0	0.7
K2-136c	0.06	8	5.2	2.8	0.6
He/H=0.02					
Wasp-52b	2.6	69	11.3	113	8.8
V1298 Tau c	6.2	34	11.2	48	2.5
TOI-1268b	0.5	28	10.1	12	1.4
TOI-1683b	4.1	29	9.9	6.2	0.8
K2-100b	7.1	37	11.3	5.8	0.4
TOI-1430b	2.3	21	7.7	2.6	0.4
TOI-2018b	0.4	12	4.5	1.7	0.3
TOI-2076b	2.5	23	8.6	2.7	0.4
HD 63433b	8.6	26	10.5	3.7	0.5
HD 63433c	2.0	20	7.6	2.0	0.4
TOI-560b	0.6	21	6.6	1.2	0.2
K2-136c	0.06	8	4.1	0.6	0.2

tribute comparable heating rates within this mentioned inner atmospheric region. Assuming instead $\text{He}/\text{H}=0.1$, the hEUV photoionisation of H^0 and $\text{He}(1^1\text{S})$ are the strongest heaters within this region. The described heating behaviour is consistent with that shown in [Allan et al. \(2024\)](#), upper panels of figures 5 and B1). The non-negligible contribution of the 24.6 eV photon to atmospheric heating and consequent escape is of interest, given that it is often omitted from similar models.

Atmospheric heating is partially countered by cooling, with adiabatic expansion being the most effective cooling mechanism for each of the modelled planets. Lyman- α cooling also contributes substantially for the hotter planets, WASP-52b, V 1298 Tau and K2-100b. For these planets, Lyman- α cooling exceeds adiabatic cooling within a small inner region below where the outflow becomes supersonic, very similar to that shown for the younger (hotter) planet in [Allan et al. \(2024\)](#), lower panel of figure 5). This noted role of Lyman- α cooling for hotter exoplanets is in agreement with the models of [Murray-Clay et al. \(2009\)](#) and ATES ([Caldioli et al. 2021](#)).

4.3.2 He triplet transmission spectroscopy predictions

To model helium triplet transit signatures, we first compute the population of helium in the 2^3S state. This again follows a similar behaviour as that described in [Allan et al. \(2024\)](#). Namely, the recombination from ionised helium to the helium triplet state is the dominant populating pathway across all atmospheric heights. A major depopulating path is collisions with free electrons in to the $\text{He}(2^1\text{S})$ state. Photoionisations out of the triplet state mostly by mid-UV photons also contribute non-negligibly to the depopulation of the 2^3S state, in the more tenuous outer regions of the atmospheres.

Figures 4.2 displays our modelled helium triplet profiles for each considered planet. The solid and dashed lines were obtained by assuming constant number fractions of $\text{He}/\text{H}=0.1$ and 0.02 respectively. We average the predicted profiles for all phases between first and fourth contacts of the planetary transit, as done in [Allan et al. \(2024\)](#), in order to account for transit observations being integrated over a time sufficient to obtain a high signal-to-noise, rather than instantaneously at mid-transit. It is clear that there is great diversity in the shapes of the predicted profiles. The helium triplet consists of three lines, at 1083.034 nm, 1083.025 nm, and 1082.909 nm (wavelengths in air [Kramida et al. 2022](#)) where the first two are indistinguishable due to their proximity. It is interesting to note that for K2-100b, V1298 Tau c, WASP-52b all three lines blend together. This is the result of stronger Doppler broadening, with the atmospheric outflows of all three planets achieving fast velocities before the density falls beyond that required for the helium triplet profile to be affected. This is due to their relatively strong mass-loss rates combined with their fast terminal velocities,

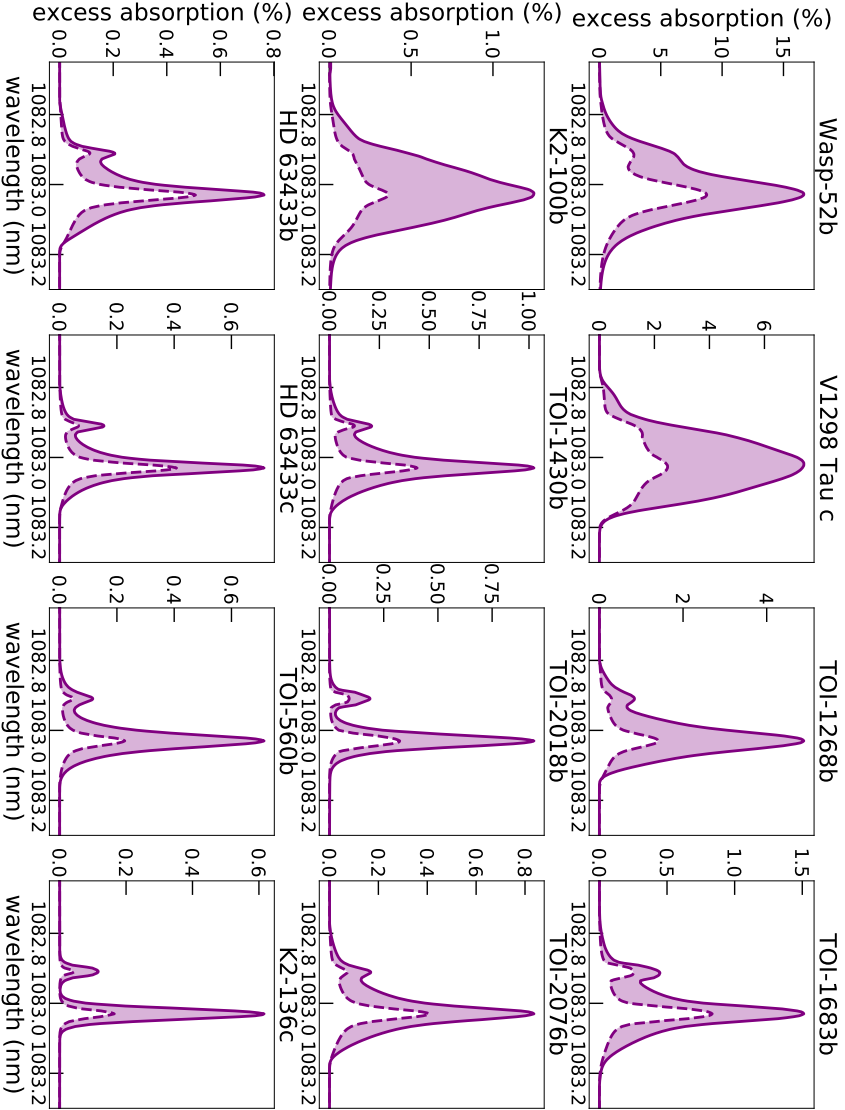


Figure 4.2: Model predictions of the helium 1083 nm transmission spectra for each planet, ordered by declining predicted absorption. The solid and dashed lines show models assuming helium to hydrogen number fractions of $\text{He}/\text{H}=0.1$ and 0.02 , respectively. The profiles are averaged over transit phases between first and fourth contacts. Note the strong variations between the various y-axes.

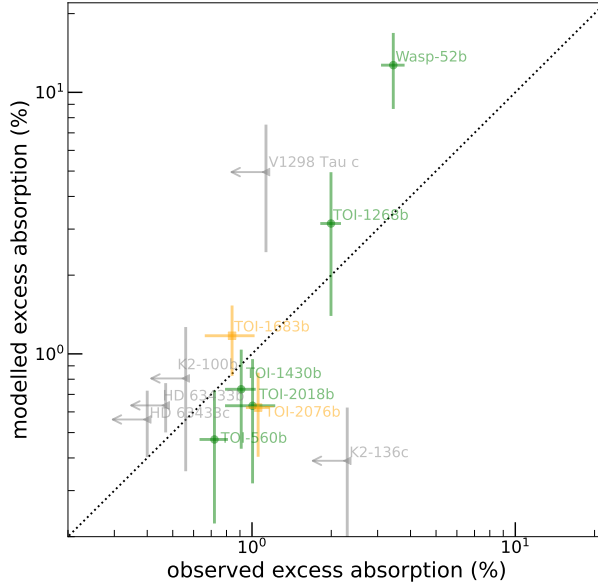


Figure 4.3: The relation between the observationally detected helium triplet excess absorption (green), conflicting detection (yellow) or upper limit due to non-detection (grey with arrow) with the modelled-predicted excess absorption for each planet. The diagonal dashed line indicates a perfect 1:1 match of the model prediction to the observation. Table 4.5 gives more detail on each observation. For each planet, the spread in the predicted excess absorption corresponds to assuming a He/H number fraction ranging from 0.02 to 0.1.

each above 30km/s (see Table 4.4). It is also worth highlighting that the assumed He/H fraction more strongly affects some of the predicted triplet profiles, as is the case for TOI-560b and TOI-1268b. While for HD 63433b and c, it has a much weaker effect.

We compare the model-predictions to the observed excess absorptions in figure 4.3. In this and subsequent figures, we distinguish between planets with confirmed detections, those with conflicting detections (see Table 4.5) and observational upper-limits due to non-detections, by the colours green, amber and grey. The vertical spread in the predicted excess absorption corresponds to assuming a He/H number fraction ranging from 0.02 to 0.1. Overall, figure 4.3 shows a positive agreement between the observations and model predictions.

Despite the overall agreement, for some planets, V 1298 Tau c in particular, there is disagreement between the model predicted and observed helium triplet profiles. While our model predicts strong 2 to 7% absorption assuming He/H respective fractions of 0.02 to 0.1, Alam et al. (2024) set

an upper limit of 1.1% with Keck II/NIRSPEC. There are various potential difficulties and limitations associated with performing helium triplet transit signatures of young exoplanets, any one of which could be responsible for this noted discrepancy. One particular difficulty is the presence of stellar activity, which is higher at such young ages. With an estimated age of 30 Myr, V 1298 Tau c is the youngest planet in our sample and a high level of activity of V 1298 Tau has been previously shown by [Krolikowski et al. \(2024\)](#) and [Vissapragada et al. \(2021\)](#) with, for example, flare detection. High stellar activity can produce significant variability in the chromospheric stellar helium triplet, which can both mask or mimic the helium triplet signature of escaping planetary material ([Krolikowski et al. 2024](#)). It can also introduce variability in the planetary escape signature itself by altering the level of XUV flux received. High stellar activity also complicates determining the planetary mass by affecting the radial velocity signatures. Accordingly, the literature currently offers no known planetary mass for the planets of V 1298 Tau, as is the case for five of the other young planets we model (see Table 4.1). In such cases, studies modelling the atmospheric escape and corresponding signatures must resort to mass-radius relations ([Chen & Kipping 2017](#)) in order to obtain a planetary mass estimate. However, such mass-radius relations are better suited to more mature planets. As [Poppenhaeger et al. \(2021\)](#) show, the uncertainty in the planetary masses of the V 1298 Tau system can have drastic effects on each planet's mass-loss rate and overall evolution. As a consequence, this could also affect the predicted helium transit signatures.

In addition to the mentioned observational difficulties associated with young ages, various limitations within the model can also cause discrepancy between the observed and predicted helium signatures. These limitations stem mostly from the hydrodynamic models 1–D nature, forcing the omission of various relevant physical processes. Star-planet interactions involving the stellar wind and planetary magnetic fields require 3–D magneto-hydrodynamic modelling. These interactions have been shown capable of strongly affecting the Lyman- α ([Carolan et al. 2021b](#); [Presa et al. 2024](#)) and helium triplet signatures ([Schreyer et al. 2024](#)) of planetary atmospheric escape. An interesting point related to this is that the three planets in our sample with the largest model-predicted mass-loss rates, K2-100b, HD 63433b and V 1298 Tau c, have tightly constrained non-detections for the helium triplet. We speculate that their non-detections could be due to stellar winds. It is known that stellar wind mass-loss rates increase with stellar X-ray fluxes ([Wood et al. 2002](#); [Vidotto 2021](#)) and that stellar winds can confine the extension of planetary atmospheres reducing the amount of absorption seen in spectroscopic transits ([Vidotto & Cleary 2020](#); [Carolan et al. 2021a](#)). It is therefore suggestive that V 1298 Tau, K2-100³ and

³for which ι -Horologii was used as a proxy (see table 4.2).

HD 63433, with their largest X-ray surface fluxes in our sample, could also generate strong stellar winds that would confine (or reduce the extension) of the helium-absorbing atmosphere. While beyond the scope of this work, the mentioned potential effects of stellar wind interactions on the observables is worth noting, particularly considering that the magnetic fields of both low-mass stars and gaseous exoplanets are expected to be strongest during their younger ages (Skumanich 1972; Vidotto et al. 2014; Kilmatis et al. 2024). Another possible problem in the model is in estimating the total helium abundance, which could in reality differ from that of our assumed constant He/H number fractions of 0.02 and 0.1. Finally, it is very important to have a robust characterisation of the stellar high-energy spectrum, due to its importance not only in driving the escape hydrodynamically, but also affecting the photoionisation of helium in the triplet state. Unfortunately, the stellar high-energy spectrum is rather difficult to obtain.

We highlight an interesting difference in the behaviour of the modelled hot-Saturns, WASP-52b and TOI-1268b, and the remaining smaller planets. In order for our model predicted triplet profiles of these two giants to reproduce their observed values, a low He/H number fraction of $\lesssim 2\%$ is required. Whereas $\gtrsim 10\%$ He/H is required for the remaining smaller planets. Planetary formation theory suggests that primordial planetary atmospheres accrete hydrogen and helium from the protoplanetary disk with He/H number fraction close to the solar value of ~ 0.1 (Coc et al. 2015). However, fits of various model to observed helium triplet data in the literature suggest sub-solar He/H for the escaping atmospheres of many exoplanets, including HD 189733b and GJ 3470b (Lampón et al. 2021). Such estimates have generally been made using single-fluid modelling with a constant He/H fraction assumed throughout the escaping atmosphere, as is the case for our model. Xing et al. (2023) however have performed multi-fluid modelling in order to demonstrate for HD 209458b, the escaping atmosphere can have sub-solar He/H even with an approximately solar helium and hydrogen abundances, due to mass-fractionation in the upper escaping atmosphere. Hence, fits suggesting low He/H does not necessarily mean sub-solar fractions of hydrogen and helium accreted during planetary formation. The preferential loss of hydrogen has also been shown capable of strongly enhancing the He/H fraction of planets on the upper edge of the radius valley (Malsky et al. 2023). These planets are susceptible to this given the loss of significant fractions of their initial atmosphere as mentioned in section 4.1. While considerably younger than the planets of the modelled grid of Malsky et al. (2023), our models apparent preference of higher He/H for smaller mini-Neptune relative to that for the hot-Saturns, could be explained by a similar enhancement. Given their relatively small reservoirs of atmospheric material and their strong predicted mass-loss rates, the enhancement of their He/H fraction to above that of the larger hot-Saturns may occur sufficiently quick to be noticeable even at such young ages. While a preferential loss of hydrogen

may also occur for larger hot-Saturn size planets, their large atmospheric reservoirs would likely prevent significant enhancement of He/H. In order to confirm this physical interpretation, both the expansion of the planet sample and evolutionary atmospheric escape modelling using a multi-fluid approach would be valuable.

4.3.3 Relations with the helium triplet signature

Many studies have sought relations between various planetary parameters and the helium triplet signature (Allart et al. 2023; Orell-Miquel et al. 2024; Krishnamurthy & Cowan 2024; Linssen et al. 2024; McCreery et al. 2025; Ballabio & Owen 2025). We now add to this discussion the insights gained from our work here. We do so by discussing relations (or lack thereof) between planetary parameters and the observed absorption (Figure 4.4), as well as the model-predicted absorptions (Figure 4.5).

From their homogeneous sample of eleven observations, Allart et al. (2023) noted a trend between stellar age and triplet absorption, but did not draw further conclusions on this given the small sample size and lack of precision in the age estimates. Orell-Miquel et al. (2024) instead found no clear trend with age in their larger survey, in agreement with the findings of Krishnamurthy & Cowan (2024), as mentioned in section 4.1. This lack of a clear trend is again shown in Figure 4.4a. On first glance, this may seemingly contradict our previous theoretical works, which modelled the atmospheric escape over the entire evolution of individual planets (Allan & Vidotto 2019; Allan et al. 2024). These theoretical studies both demonstrated a clear trend with younger ages and deeper absorptions. However, applying the same self-consistent hydrodynamic modelling to the diverse sample of observed young planets, it is clear that the resulting model predictions shown in Figure 4.5a, also exhibit no strong trend between age and absorption. This lack of trend with age is therefore in agreement with the current observations. Hence, for an individual planet along its evolution, its atmospheric escape and corresponding detectable signature are greatest at younger ages, as shown by the tracks of theoretical evolving $0.1 M_{\text{Jup}}$ planets orbiting an initially fast rotating K-dwarf at 0.045 au (Alam et al. 2024; Allan et al. 2024) in figure 4.5. However, for a diverse sample of exoplanets, both models and observations are in agreement that differences in other system parameters more strongly affect the resulting triplet signature, compared to the effect of system age. Hence, studies seeking to observe atmospheric escape should place such parameters above age in their consideration of potential targets.

One such property is the geometric transit depth given by $(R_{\text{pl}}/R_{\text{*}})^2$. Figures 4.4b and 4.5b show the relation between the geometric transit depth and the observed and predicted helium triplet excess absorptions, respectively. For *both* observed and model signatures, a relation is evident amongst the planets with detections. In each case, the strong detections of the hot-

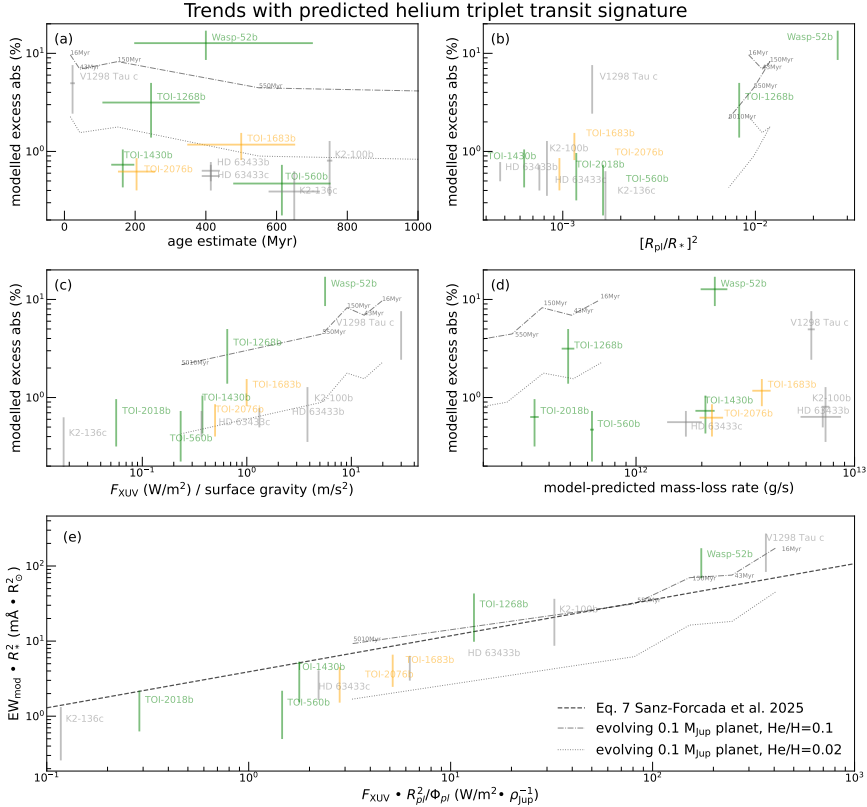


Figure 4.5: The same as Figure 4.4, now relating model-predicted rather than observed helium triplet parameters (y-axes) to various system parameters (x-axes). For each planet, the spread in the predicted excess absorption, the equivalent width EW_{mod} and the mass-loss rate corresponds to assuming a He/H number fraction ranging from 0.02 to 0.1. The dashed-dotted and dotted tracks are that of theoretical, evolving, 0.1 M_{Jup} planets with respective He/H number fractions of 0.1 and 0.02, orbiting an initially fast rotating K-dwarf at 0.045 au (Alam et al. 2024; Allan et al. 2024). Colour again indicates each planet’s observational outcome, with green for detections, amber for conflicting interpretations (see Table 4.5), and grey for non-detections.

Saturns WASP-52b and TOI-1268b are largely driving this trend. The planets with non-detections being to the lower end of the geometric transit depth scale, further strengthens this noted trend. Similarly, [Krishnamurthy & Cowan \(2024\)](#) note a preference for larger planetary radii amongst successful detections in their reanalysis of published studies. They suggest that the various non-detections for older systems with smaller planets are not surprising due to an insufficient accumulation of primordial atmosphere and their vulnerability to losing these atmospheres.

Another parameter which shows a positive trend with both the observed and modelled helium triplet signatures is the ratio of XUV flux, F_{xuv} to the planetary gravity (a popular proxy for the mass-loss rate). To obtain an F_{xuv} for each planet, we sum the individual X-ray, hEUV and sEUV fluxes, which depend on the respective stellar luminosities of these wavelength bins and the planet's orbital distance. In both the observed (figure 4.4c) and modelled (figure 4.5c) triplet signatures of planets with successful detections (coloured in green), a positive relation is evident. A large value for this ratio alone however is a poor indicator of a strong detection compared to a large geometric transit depth, as shown by the many non-detections (in grey) for planets with large XUV flux to gravity ratios. Furthermore, it is reliant upon the received XUV flux, a parameter which is greatly unknown for the majority of systems.

Interestingly, the systems with the strongest atmospheric escape rates as predicted by our hydrodynamic modelling have yielded non-detections (V1298 Tau c, K2-100b, HD 63433b) as seen in panel 4.4d. As discussed in section 4.3.2, these planets' host stars have the strongest X-ray surface fluxes of our sample, which implies that they also have stronger stellar winds that could potentially confine the extension of the helium-absorbing planetary atmospheres. Evidently, we do not find clear a trend between the predicted mass-loss rates and the predicted (figure 4.5d), nor the observed (figure 4.4d) helium absorptions. [Ballabio & Owen \(2025\)](#) recently demonstrated that the helium triplet excess absorption scales linearly with mass-loss rate, with all other things being equal. As many system properties vary substantially for the exoplanets of our sample (see tables 4.1 and 4.2), the lack of trend is to be expected. [Ballabio & Owen \(2025\)](#) also show that absorption is weaker for hotter atmospheric outflows. The high temperatures of K2-100b and HD 63433b with respective peaks of 11.3 and 10.3kK, could also have contributed to their predicted weak signatures, consistent with their tightly constrained non-detections. However, we also find that planets with even hotter peak temperatures and weaker escape rates such as WASP-52b are capable of producing strong absorptions, highlighting the importance of additional system parameters in affecting the resulting helium triplet signature.

In short, we find that a strong detection does not necessarily imply a strong rate of atmospheric escape nor does a weak or non-detection imply

a weak escape rate. This point is better illustrated by the tracks of the evolving, theoretical $0.1 M_{\text{Jup}}$ planets in figure 4.5. Despite the stronger mass-loss rate at the younger age of 43 Myr, the excess absorption is predicted to be stronger at 150 Myr (figure 4.5d). As explained previously in [Allan et al. \(2024\)](#), this is due to a larger ratio of planetary to stellar radii inputs adopted at the age of 150 Myr (figure 4.5b). While both planetary and stellar radii shrink substantially during the system’s early evolution, the more rapid decay of the stellar radius in this case results in a stronger helium detection despite a weaker escape at 150 Myr. Therefore, consideration of the stellar radius could be of benefit when selecting candidates for future helium detections, in addition to the more obvious XUV flux and planetary gravity.

[Zhang et al. \(2022a, section 5.3\)](#) relates an order-of-magnitude empirical estimate for planetary mass-loss rate to $EW_{\text{obs}} \cdot R_*$, where EW_{obs} is the equivalent width of the observed helium triplet profile. They do so by estimating the mass of obscuring helium triplet material. [Zhang et al. \(2023c\)](#) then demonstrated a positive relation between $EW_{\text{obs}} \cdot R_*$ and $F_{\text{XUV}}/\rho_{\text{XUV}}$ for a sample of helium observed exoplanets, the latter term arising from the energy-limited mass-loss approximation, with ρ_{XUV} being the average planetary density calculated using the XUV photosphere radius. [Sanz-Forcada et al. \(2025\)](#) noted the similar, strong, empirical relation:

$$EW_{\text{obs}} \cdot R_*^2 \propto F_{\text{XUV}} R_{\text{pl}}^2 / \Phi_g, \quad (4.2)$$

where $\Phi_g = GM_{\text{pl}}/R_{\text{pl}}$ is the planet gravitational potential with G being the gravitational constant, and R_{pl}^2/Φ_g is equivalent to the inverse average planet density. Figure 4.4e shows this relation for our considered sample of exoplanets.

Figure 4.5e shows the same trend, only now replacing EW_{obs} with our model-predicted equivalent width, EW_{mod} . In both cases, a clear trend is evident amongst the confirmed (green) and conflicted (yellow) detections. The theoretical individual planets are also seen to follow the trend of [Sanz-Forcada et al. \(2025\)](#) reasonably well as they evolve over time. Their evolution tracks highlight the importance of the size of the stellar disk in the y-axis term. The previously discussed observational enhancement at 150 Myr is descaled through multiplication with the stellar disk area, causing the y-axis values at the sampled ages to decrease chronologically, more consistent with their decreasing atmospheric escape.

Interestingly, the four planets with tightly constrained upper limits fall below the dotted line of the observational relation in Figure 4.4e, while their model predictions yield values closer to the general trend in Figure 4.5e. This could indicate an overestimated XUV flux, an underestimated planetary gravity, or the omission of important physical processes such as stellar wind interactions from the model, the latter being supported by the

high surface X-ray fluxes of their host stars, indicative of strong stellar winds (section 4.3.2). The non-simultaneity of the helium triplet observations and the stellar X-ray observations, as well as the EUV flux relying mostly on extrapolations from the X-ray, complicate the selection of the XUV flux. This important parameter strongly affects both the hydrodynamic escape and its resulting observables. On the possibility of underestimating the planetary gravities, three of these four planets have planetary masses obtained via mass-radius relation (see Table 4.1). Alternatively, the lower limit assumption of $\text{He}/\text{H}=0.02$ could also overestimate the true atmospheric helium abundance of these particular planets.

4.4 Conclusions

We applied our hydrodynamic model of atmospheric escape to a sample of young exoplanets which have helium triplet observations. We modelled their atmospheric escape as well as their corresponding helium triplet transit signature, achieving a good overall agreement between model and observation. From this work, we draw the following conclusions:

- For an individual planet along its evolution, its atmospheric escape and corresponding detectable signature are greatest at younger ages. However, for a diverse sample of exoplanets, differences in alternative parameters have a stronger effect on the resulting triplet signature, compared to the effect of age. This is seen both observationally and in our model predictions of the same systems.
- Our model predictions reproduce well the strong empirical trend of [Sanz-Forcada et al. \(2025\)](#): $EW \cdot R_*^2 \propto F_{\text{XUV}} \cdot R_{\text{pl}}^2 / \Phi_g$.
- Studies seeking to observe atmospheric escape should place parameters such as the geometric transit depth or $F_{\text{XUV}} \cdot R_{\text{pl}}^2 / \Phi_g$ above age in their consideration of potential targets for future helium triplet detections.
- Studies modelling the helium triplet transit signature should pay careful consideration to their choice of assumed lower boundary conditions. This is particularly the case when modelling small, mini-Neptune size planets for which the common assumption of setting the base of the modelled upper atmosphere to $1 R_{\text{pl}}$ can introduce large uncertainty in the predicted triplet profile.
- Our model predictions favour a higher He/H number fraction for smaller mini-Neptunes planets compared to hot-Saturns. This can be interpreted physically by the mini-Neptunes undergoing atmospheric escape with a preferential loss of hydrogen over helium in combination

with a sufficiently small reservoir of atmospheric material so that the previously escaped material can affect the current He/H ratio. Further observations and modelling of more of each class of planet would be needed to confirm such behaviour.

As the number of observations continues to grow, the known trends between various planetary parameters and the observed helium triplet signature of escape will become increasingly reliable, while new trends will no doubt be revealed. These trends can improve our approach of target selection for future observations.

Acknowledgements

We thank the anonymous referee for their insightful comments which have greatly improved this work. APA and AAV acknowledge funding from the European Research Council (ERC) under the European Union's Horizon 2020 research and innovation programme (grant agreement No 817540, ASTROFLOW). We thank several colleagues for helpful discussions over this project, particularly regarding the lower boundary conditions: Dr. Luca Fossati, Dr. James Owen, Dr. Carolina Villarreal D'Angelo.

Data Availability

The data described in this article will be shared on reasonable request to the corresponding author.

Appendix

Sensitivity to the assumed density at the base of the atmosphere

In order to emphasize the need for its careful selection, Figures 4.6 and 4.7 demonstrate the sensitivity of our model predicted atmospheric escape and its corresponding helium triplet signature to the density assumed at the base of the planetary atmosphere. Here, our calculations start at $R_{\text{base}} = 1 R_{\text{pl}}$ and we use $T[R_{\text{base}}] = 1000$ K. As discussed in section 4.2.2, our model exhibits a strong sensitivity of the predicted helium triplet profile with the assumed base density, beyond the uncertainties of the helium triplet observations. As shown in the appendix of Murray-Clay et al. (2009) and confirmed by our Allan & Vidotto (2019) model, for modelling considering

photons concentrated at a single energy bin (20 eV) and with a single possible absorber (neutral hydrogen), the predicted escape properties plateau to stable values for various assumed densities at the atmospheric base, once a sufficiently high density is reached, and an optical depth for photoionisations at the base of the model is above unity. The number of photons that penetrate the atmosphere is related to photoionisation and heating, which drives the planetary escape. However, with the inclusion of more photon energies and potential absorbers, this plateau behaviour does not occur at a reasonable base density (see top panels of Figures 4.6 and 4.7). This is because as we raise the base density, only some optical depths of possible photoionisations reach above unity, which implies that raising the base density increases the number of one of the possible photoionisations (affecting heating deposition at the lower part of the atmosphere) as is seen in the lower panels of figures 4.6 and 4.7, rather than a saturation of photoionisations being reached. Across a wide range of assumed base densities or pressures, the model remains sensitive to the choice of base density due to the number of occurrences of at least one of the potential photoionisations increasing.

Models assuming commonly used lower boundary conditions

In section 4.2.2 we outline our reasoning for choosing more physically motivated properties at the lower boundary of our modelled atmospheres. In section 4.3.2 we showed our predicted triplet signatures with our improved lower boundary assumptions. For comparison, in figure 4.8 we now show the model's predicted triplet signatures assuming the lower boundary conditions assumed in [Allan et al. \(2024\)](#) and more akin to that used in the current literature, $R_{\text{base}} = 1 R_{\text{pl}}$, $\rho[R_{\text{base}}] = 4 \times 10^{-14} \text{g cm}^{-3}$, $T[R_{\text{base}}] = 1000 \text{K}$.

Observational properties

Table 4.5 compiles observational data on all planets considered in this work. We consider only high-resolution observations. In the figures of relations of properties with the helium triplet signature in section 4.3.3, we choose only one representative observation for each planet. This is either the most recent, highest resolution detection, or most tightly constrained non-detection. The chosen observation for each planet is the first row to appear for each planet in table 4.5. Due to conflicting findings for the observations of TOI-2076b and TOI-1683b, we mark them in amber in figures 4.4 and 4.5.

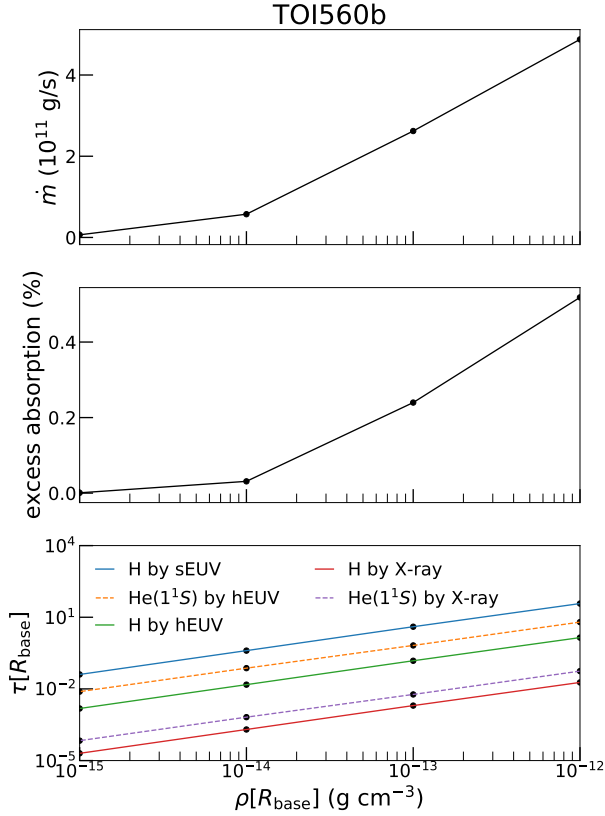


Figure 4.6: Sensitivity of the mass-loss rate (upper-panel) and the phase averaged helium 1083nm excess absorption (central-panel) to the assumed density at the base of the modelled atmosphere, while holding $R_{\text{base}} = 1 R_{\text{pl}}$ and $T[R_{\text{base}}] = 1000$ K constant. The remaining planetary parameters are that of TOI-560b, and assuming He/H=0.1. The lower panel displays optical depths to various photoionisations.

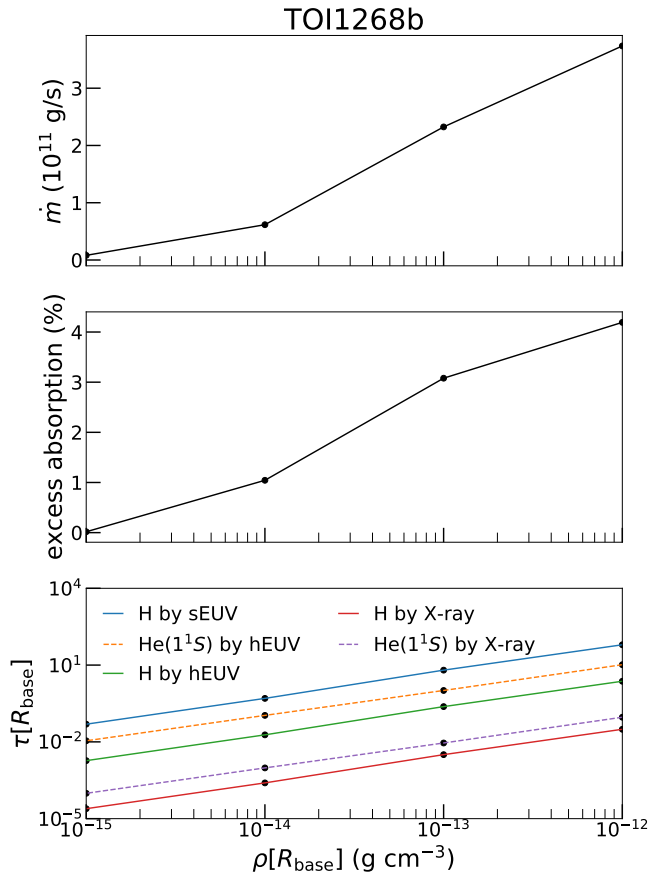


Figure 4.7: The same as figure 4.6 again assuming $R_{\text{base}} = 1 R_{\text{pl}}$ and $T[R_{\text{base}}] = 1000 \text{ K}$ and varying $\rho[R_{\text{base}}]$, while the remaining planetary parameters are now that of TOI-1268b.

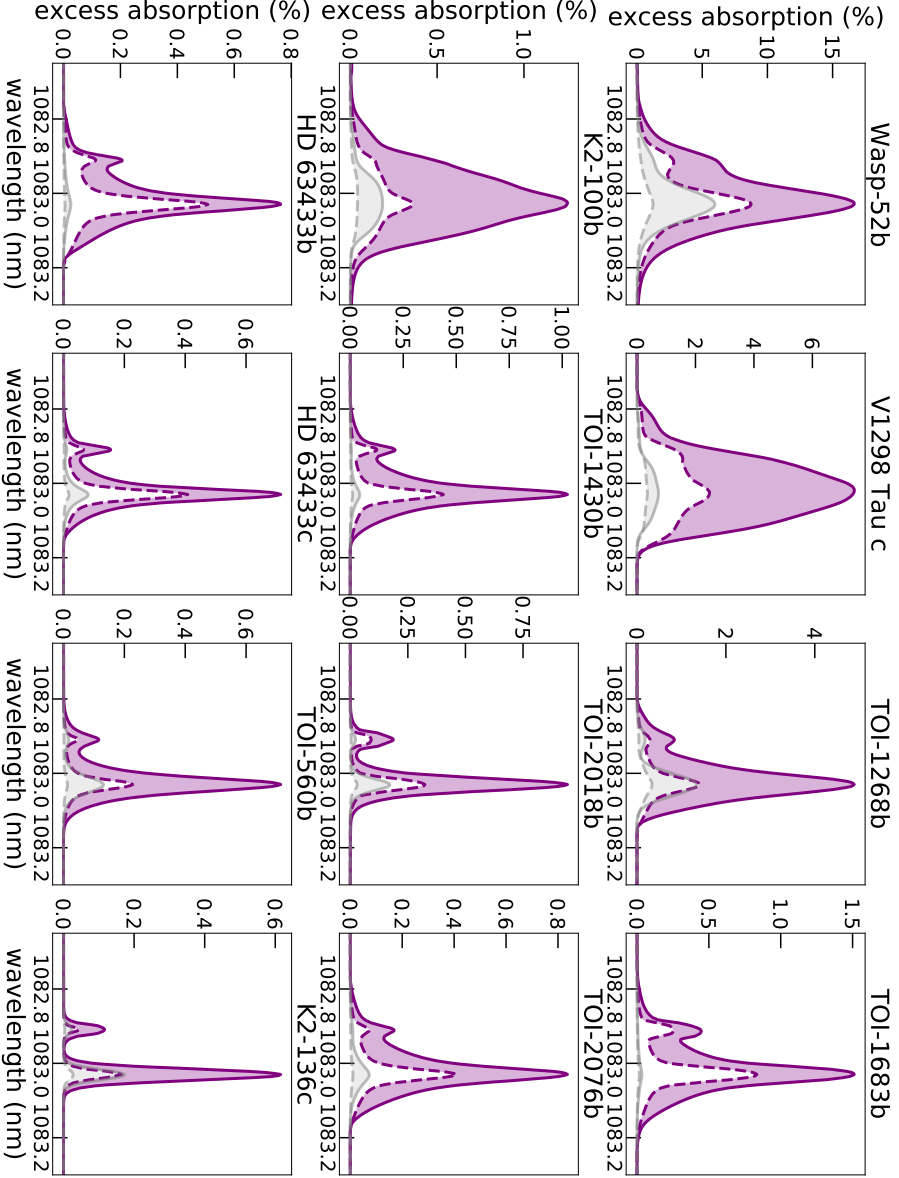


Figure 4.8: Comparison between the predicted triplet profiles with our calculated lower boundary conditions (purple, same as that in figure 4.2) and those predicted by reverting to the standardly assumed lower boundary conditions of $R_{\text{base}} = 1 R_{\text{p}}$, $\rho[R_{\text{base}}] = 4 \times 10^{-14} \text{ g cm}^{-3}$, $T[R_{\text{base}}] = 1000 \text{ K}$ (grey).

Table 4.5: Observational summary of the considered sample of exoplanets.

name	interpretation	peak abs (%)	EW (mÅ)	telescope	Reference
Wasp-52b	detect	3.44 ± 0.31	39.583 ± 1.4	Keck II/NIRSPEC	(Kirk et al. 2022)
V1298 Tau c	upper limit	< 1.13	< 8.49	Keck II/NIRSPEC	(Alam et al. 2024)
V1298 Tau c	upper limit	< 3.75	< 95.84	CARMENES	(Orell-Miquel et al. 2024)
TOI-1268b	detect	2 ± 0.16	19.1 ± 1.8	CARMENES	(Orell-Miquel et al. 2024)
TOI-1683b	detect	0.84 ± 0.17	8.5 ± 1.6	Keck/NIRSPEC	(Zhang et al. 2023b)
TOI-1683b	upper limit	< 0.7	-	CARMENES	(Orell-Miquel et al. 2024)
K2-100b	upper limit	< 0.56	< 4.44	Keck II/NIRSPEC	(Alam et al. 2024)
K2-100b	upper limit	< 1.2	< 5.7	IRD/Subaru	(Gaidos et al. 2020)
TOI-1430b	detect	0.91 ± 0.11	9.5 ± 1.1	CARMENES	(Orell-Miquel et al. 2023)
TOI-1430b	detect	0.64 ± 0.06	6.6 ± 0.5	Keck/NIRSPEC	(Zhang et al. 2023b)
TOI-2018b	detect	$1.02^{+0.19}_{-0.22}$	7.8 ± 1.5	CARMENES	(Orell-Miquel et al. 2024)
TOI-2076b	detect	1.01 ± 0.05	10.0 ± 0.7	Keck/NIRSPEC	(Zhang et al. 2023b)
TOI-2076b	upper limit	< 1.0	-	CARMENES	(Orell-Miquel et al. 2024)
HD 63433b	upper limit	< 0.47	< 2.52	Keck II/NIRSPEC	(Alam et al. 2024)
HD 63433b	upper limit	< 0.5	-	Keck II/NIRSPEC	(Zhang et al. 2022b)
HD 63433b	upper limit	< 0.34	< 2.0	CARMENES	(Orell-Miquel et al. 2024)
HD 63433c	upper limit	< 0.4	< 4.2	CARMENES	(Orell-Miquel et al. 2024)
HD 63433c	upper limit	< 0.5	-	Keck/NIRSPEC	(Zhang et al. 2022b)
TOI-560b	detect	0.72 ± 0.08	8.6 ± 0.6	Keck/NIRSPEC	(Zhang et al. 2023b)
TOI-560b	detect	0.64 ± 0.08	7 ± 0.4	Keck/NIRSPEC	(Zhang et al. 2022a)
K2-136c	upper limit	< 2.3	< 25	Subaru/IRD	(Gaidos et al. 2021)

Table 4.6: Ratios of the mass-loss rates reported in [McCreery et al. \(2025\)](#) relative to that predicted here, assuming both a high and low He/H fraction. *While we did not run He/H=0.01 models, we consider our He/H=0.02 models sufficient for this comparison, as the assumed fraction only minorly affects our hydrodynamic predictions (see Table 4.4), compared to the strong dependence with the mass-loss rates of [McCreery et al. \(2025\)](#), as explained in the text.

planet	ratio assuming He/H=0.1 (%)	ratio assuming He/H=0.01* (%)
WASP-52b	6–12	15–29
TOI-560b	3.3–22	10–66
TOI-1430b	0.08–0.48	0.4–1.9
TOI-1683b	0.03–0.63	0.2–4.2
TOI-2076b	0.08–0.2	0.2–0.4

Comparison of predicted mass-loss rates

It was mentioned in section 4.3.1 that our mass-loss rate predictions are strong relative to some recent studies of the same planets ([Zhang et al. 2023b](#); [McCreery et al. 2025](#)). The latter of these studies modelled various helium triplet observed exoplanets, including five planets common to our sample using the atmospheric escape code, P-WINDS ([Dos Santos et al. 2022](#); [Dos Santos & Vissapragada 2023](#), version 1.4.6). Table 4.6 shows that the mass-loss rates predicted here are considerably stronger than that found in [McCreery et al. \(2025\)](#). Our predictions also differ in that their mass-loss rate predictions are strongly dependent on the assumed He/H fraction, whereas our predictions are not. This is due to their mass-loss predictions involving modelling of the planets’ helium triplet profiles, which are strongly affected by the assumed abundance of helium. Whereas, our mass-loss rates are predicted purely by our hydrodynamic model and hence are only weakly affected by the assumed helium abundance as mentioned in section 4.3.1. In general, the different nature of the approaches taken in our studies makes it difficult to understand the reasons behind the noted mass-loss rate differences. For example, our model self-consistently outputs a mass-loss rate and atmospheric profiles of temperature and velocity, whereas the mass-loss rate and outflow temperature are free parameters in the set-up of [McCreery et al. \(2025\)](#). Both the temperature and the mass-loss rate (or base density) strongly affect the velocity and density profiles in models like theirs, which assume a constant temperature (or sound speed) throughout the atmospheric structure. Their approach however benefits from utilising helium triplet observations to retrieve good fits to the observed data, whereas, our purely forward-model predictions might not.

5

THE EFFECTS OF STELLAR ACTIVITY CYCLES ON PLANETARY ATMOSPHERIC ESCAPE AND THE HE I 1083 NM TRANSIT SIGNATURE

A. P. Allan, A. A. Vidotto, J. Sanz-Forcada, C. Villarreal D'Angelo.
Monthly Notices of the Royal Astronomical Society (now in press).

The He I 1083 nm transit signature is commonly used in tracing escaping planetary atmospheres. However, it can be affected by stellar activity, complicating detections and interpretations of atmospheric escape. We model how stellar activity cycles affect the atmospheric escape and He I 1083 nm signatures of four types of highly irradiated exoplanets, at 0.025 and 0.05 au, during minimum and maximum cycle phases. We consider two stars, exhibiting different cycle behaviours: the Sun and the more active star ι Hor, for which for the Sun, we use spectral irradiance observations. For ι Hor, we reconstruct its spectral energy distributions at minimum and maximum phases using X-ray observations and photospheric models. We show that over a modulated activity cycle, the release of extreme ultraviolet photons, responsible for atmospheric escape, varies substantially more than that of mid-UV photons, capable of photoionising He I (2^3S). This leads to consistently stronger helium signatures during maximum phases. We show that planets at the largest orbit are more affected by cycles, showing larger variations in escape rates and absorptions between minimum and maximum. We also confirm the counter-intuitive behaviour that, despite the fall-off in escape rate with orbital distance, the He I 1083 nm absorption is not significantly weaker at further orbits, even strengthening with orbital distance for some ι Hor planets. We partially explain this behaviour with the lower mid-UV fluxes at more distant orbits, leading to less He I (2^3S) photoionisations. Finally, we propose that stellar cycles could explain some of the conflicting He I 1083 nm observations of the same planet, with detections more likely during a phase of activity maximum.

5.1 Introduction

The 1083 nm helium triplet (hereby He I 1083 nm) signature, comprised of three individual lines centred on 1082.909, 1083.025, and 1083.034 nm in air, has fast become the most popular method for tracing escaping atmospheres of highly irradiated exoplanets (for recent analyses of the various detections and non-detections see [Orell-Miquel et al. 2024](#); [Krishnamurthy & Cowan 2024](#); [Sanz-Forcada et al. 2025](#); [McCreery et al. 2025](#)). Its near-infrared (nIR) wavelength benefits from being observable from the ground, a strong advantage over hydrogen’s Lyman- α line in the ultraviolet (UV), which is severely affected by absorption in the interstellar medium and requires space-based observations currently only possible with the Hubble Space Telescope ([Dos Santos 2023](#)). The He I 1083 nm triplet is produced by transitions from the 2^3S to the 2^3P state of neutral helium. The 2^3S state is metastable as radiative decays to the ground (1^1S) state are forbidden and hence greatly suppressed with a lifetime of 2.2 hours ([Drake 1971](#)).

Despite the success of the He I 1083 nm feature in studying escaping planetary atmospheres, stellar activity can also affect the observed signature, sometimes making it difficult to distinguish planetary from stellar contributions. Planets for which stellar activity has been proposed to influence their He I 1083 nm observations include the sub-Neptune TOI-2076b ([Gaidos et al. 2023](#)), hot-Jupiter HAT-P-32b ([Zhang et al. 2023a](#)) and HD 189733b ([Salz et al. 2018](#); [Guilluy et al. 2020](#); [Zhang et al. 2022c](#)). Various forms of stellar activity can affect He I 1083 nm either through direct He I(2^3S) variations in the stellar chromosphere ([Zirin 1975](#); [Sanz-Forcada & Dupree 2008](#)) or indirect variations of He I(2^3S) material in the escaping planetary atmosphere transiting across the stellar disk. On direct variations due to the star, [Mercier et al. \(2025\)](#) investigated temporal variability in the solar He I 1083 nm signature using multi-epoch observations, finding significant variability on timescales of minutes to days associated to telluric contamination and short-term stellar activity. They demonstrate that this observed solar He I 1083 nm variability should not significantly affect the inferred atmospheric escape properties of a strong 5% planetary absorption transit signature. [Krolikowski et al. \(2024\)](#) performed a similar temporal study of stellar He I 1083 nm variability for 10 young stars (with observational baselines ranging from minutes to years), cautioning that stronger variability in stars younger than 120 Myr, would likely preclude even significant planetary transit signatures without well-timed out-of-transit reference observations. In this work, we will focus on indirect variations of He I(2^3S) material coming from the escaping planetary atmosphere transiting across the stellar disk.

Stellar activity operates on three main timescales. In the shorter of these timescales, stellar flares operate on the order of hours to days. For observa-

tions of the star alone, these bursts of electromagnetic radiation can cause variations in the stellar He I 1083 nm, as has been found in He I 1083 nm observations of the Sun (Kuckein et al. 2015) and M dwarf stars (Fuhrmeister et al. 2020). He I 1083 nm observations performed during a planetary transit are also susceptible to variations from stellar flares. For example, Vissapragada et al. (2021) observed a flare over six high resolution spectra of V1298 Tau obtained with Habitable-zone Planet Finder (HPF Mahadevan et al. 2012b). This flare coincided with a planetary transit of V1298 Tau c, with the flare decay phase corresponding to an increase in the EW of the He I 1083 nm signature. However, they concluded that the enhancement was likely due to an increased population of He I (2^3S) in the stellar chromosphere rather than of a planetary origin. Supporting this interpretation, they were unable to detect the transit of V1298 Tau c at all using narrowband photometry centred on He I 1083 nm. A later higher-resolution non-detection of a transiting He I 1083 nm signature for V1298 Tau c (Alam et al. 2024) further supports this. However, 3-D hydrodynamic modelling performed for the hot-Jupiter WASP-69b, demonstrated that a stellar flare is also capable of enhancing the observed He I 1083 nm transit signature indirectly, through raising the planet’s atmospheric escape (Wang & Dai 2021a). Their modelled He I 1083 nm transit signature was temporarily weakened by an injected flare due to increased He I (2^3S) photoionisation before being enhanced after a few hours by which time the system had adjusted to a higher rate of atmospheric escape. Stellar activity in the form of stellar spots and bright facular or plage regions, also introducing short timescale variabilities, were shown to only weakly affect the He I 1083 nm transit signature, and is more likely to dilute rather than enhance it (Cauley et al. 2018). Hence, stellar spots, bright facular and plage regions should be less problematic to escaping helium planetary studies than other forms of stellar activity which can greatly influence the He I 1083 nm transit signature.

Over the full lifetime of a highly irradiated exoplanet, a much longer timescale for stellar activity, planetary atmospheric escape is known to vary substantially. As the system ages and the star spins down (Vidotto et al. 2014), the planetary atmospheric escape declines (Owen 2019; Allan & Vidotto 2019). This is due to the reducing XUV flux responsible for heating the atmosphere (Johnstone et al. 2021) and the shrinking planetary radius (Fortney & Nettelmann 2010). Consequently, the He I 1083 nm transit signature weakens over the evolution of the highly irradiated exoplanet, as shown previously in Allan et al. (2024).

An intermediary timescale between the mentioned short-term (hours to days) and long-term (planetary lifetime) timescales is also worth investigating, namely that related to stellar activity cycles. The Sun exhibits an activity cycle which causes its emitted XUV flux to vary cyclically, with a period of 11 years (Hathaway 2010). As will be discussed further in

section 5.2, XUV cycles of other stars can differ substantially from this. [Hazra et al. \(2020\)](#) previously showed, using solar XUV observations, that solar-like cyclic XUV variations can influence the atmospheric escape of hot-Jupiters. They demonstrated that variations in the strength of atmospheric escape introduces a cyclic nature to the hydrogen Lyman- α and H- α tracers of atmospheric escape, with H- α being more sensitive to the stellar activity cycle. Similarly, [Taylor et al. \(2025\)](#) recently demonstrated a sensitivity of the He I 1083 nm signature of the hot-Jupiter HD209458b to a Sun-like activity cycle also using solar XUV data. The effect of a Sun-like stellar activity cycle on the He I 1083 nm transit signature has however yet to be explored for an exoplanet beyond the archetypal hot-Jupiter HD209458b. Furthermore, how the signature is affected by XUV cycles beyond that of our Sun is another interesting avenue worth exploring (see section 5.4.3).

In this current work, we consider how stellar activity cycles affects the helium triplet signature of four different types of highly irradiated exoplanets at two orbital distances. In order to incorporate a stellar activity cycle, we take two different approaches for determining the stellar spectral energy distributions during minimum and maximum activity phases. The first approach described in section 5.2.1 considers a Sun-like activity cycle while our second approach considers the shorter cycle of ι Hor (section 5.2.2). Our method for modelling atmospheric escape and the He I 1083 nm signature using the 1-dimensional model of [Allan & Vidotto \(2025\)](#) is summarised in section 5.3. Our results are presented in section 5.4 along with relevant discussions in section 5.5.

5.2 Stellar XUV activity cycles

Although the activity cycle is better studied on the Sun, activity cycles also occur for other stars as made evident by monitoring programs such as that by the Mount Wilson ([Wilson 1978](#); [Baliunas et al. 1995](#)) and Lowell ([Hall et al. 2007](#)) observatories. [Boro Saikia et al. \(2018\)](#) more recently created a catalogue of 4454 cool stars exhibiting a cyclic nature using a combination of data from various surveys. The mentioned works all utilised the Ca II H&K lines with visible wavelengths (in air) of 3968.469 Å and 3933.663 Å respectively, both indicators of chromospheric activity. However, cycles have also been detected at X-ray wavelengths for a handful of stars: ι Hor ([Sanz-Forcada et al. 2013, 2019](#), see section 5.2.2 here), τ Boo ([Mittag et al. 2017](#)), HD 81809 ([Favata et al. 2008](#); [Orlando et al. 2017](#)), α Cen A & B ([Robrate et al. 2012](#); [Ayres 2020](#)), AB Dor ([Singh & Pandey 2024](#)), ϵ -Eri ([Coffaro et al. 2020](#)), 61 Cyg A & B ([Hempelmann et al. 2006](#); [Robrate et al. 2012](#)), and Proxima Cen ([Wargelin et al. 2024](#)). Activity cycle variations are larger towards higher-energy, lower wavelengths compared to the visible wavelengths of the Ca II H&K lines. In solar cycle 24 for example, the S-

Table 5.1: Binned luminosities in the X-ray, hEUV, sEUV and mid-UV bands for the minimum and maximum phases of the activity cycle of the Sun (upper part of the Table) and of ι Hor (bottom part of the Table). In the final row, the ratio of the maximum to minimum luminosity for each wavelength band is given.

	$L_{X\text{-ray}}$ (L_{\odot})	L_{hEUV} (L_{\odot})	L_{sEUV} (L_{\odot})	$L_{\text{mid-UV}}$ (L_{\odot})	EUV/mid-UV ratio
The Sun during cycle 24					
max	4.98e-07	2.36e-06	8.68e-07	1.97e-02	1.64e-04
min	1.35e-07	9.24e-07	5.87e-07	1.94e-02	7.80e-05
max/min	3.69	2.55	1.48	1.02	2.10
ι Hor					
max	3.33e-05	4.00e-05	2.81e-05	7.95e-02	8.56e-04
min	2.15e-05	3.98e-05	2.81e-05	7.95e-02	8.54e-04
max/min	1.55	1.00	1.00	1.00	1.00

index of the Ca II H&K activity indicators was $\sim 5.5\%$ larger during the phase of activity maximum compared to activity minimum (Egeland et al. 2017), while the integrated flux emitted from the soft X-ray bin (see Section 5.2.1) is a factor of ~ 4 times larger, with even larger variations at shorter wavelengths. Of the current few sample of stars with X-ray cycles, only older stars with low ratios of $L_{X\text{-ray}}/L_{\text{bol}}$ have been found to exhibit an X-ray cycle similar to that of the Sun, with large, smooth amplitude modulations evolving over similar decadal timescales. Younger, faster rotating stars with moderate to high $L_{X\text{-ray}}/L_{\text{bol}}$ ratios instead exhibit faster, more complex X-ray cycles with smaller variations, if a cycle is apparent at all (Ayres 2025). Oláh et al. (2016) previously set an age of 2-3 Gyr as a marker distinguishing between these two mentioned types of activity cycles.

In order to model hydrodynamically escaping planetary atmospheres, a good constraint on the XUV flux received by the planet is essential. Unfortunately, absorption by the interstellar medium and Earth's atmosphere complicates this, limiting observational EUV constraints to either nearby systems (France et al. 2016; Youngblood et al. 2016) or empirical reconstructions reliant on X-ray observations (Sanz-Forcada et al. 2011). It is often necessary to adopt an XUV flux based off a proxy star when modelling the atmosphere of a specific planet. For these reasons, observing stellar activity cycles in X-ray can substantially improve our understanding of how cyclic XUV behaviour affects planetary atmospheric escape and its observables.

5.2.1 The XUV cycle of the Sun

In order to obtain an XUV spectral energy distribution (hereby SED) during a minimum and maximum phase of the solar activity cycle, we can

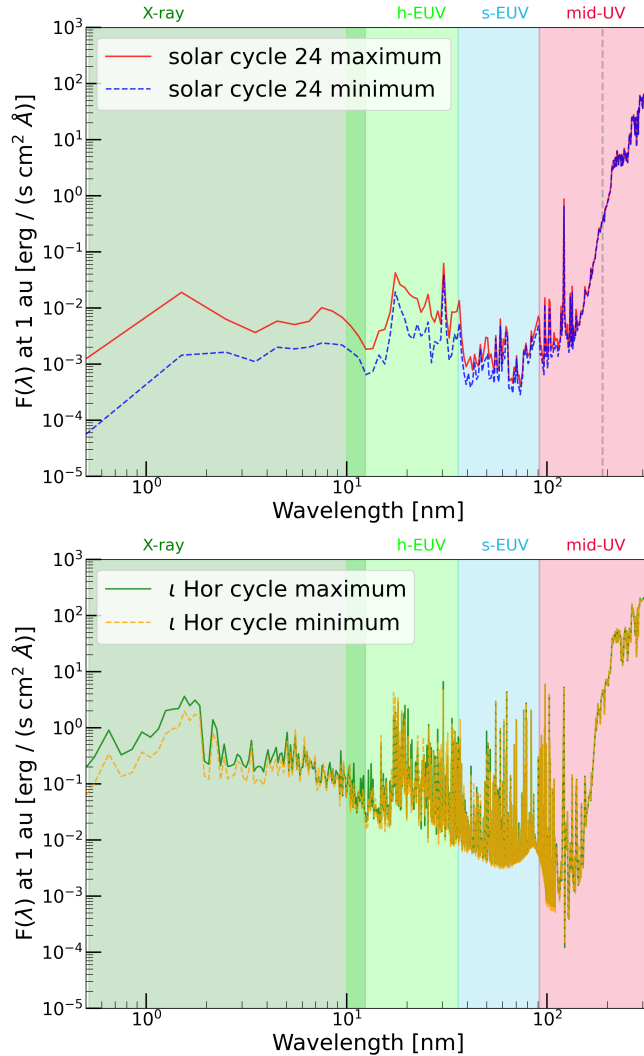


Figure 5.1: Upper panel: Solar SED at minimum and maximum phases of the solar activity cycle. The data at wavelengths below 189.5 nm (marked by the vertical grey line) were obtained with the SEE instrument while above with the SORCE instrument as described in section 5.2.1. Lower panel: Reconstructed SED of ι Hor during a minimum and maximum phase of the activity cycle, as described in section 5.2.2. The shaded regions common to both panels distinguish the wavelength bins used as input in our atmospheric escape model. From left to right they are X-ray (0.517-12.4 nm), hard-EUV (10-36 nm), soft-EUV (36-92 nm) and mid-UV (91.2-320 nm).

avail of numerous space-based spectral observations. In order to cover the wavelength range required by our atmospheric escape model, we combined datasets from two different observing missions. For wavelengths between 0.5-189.5 nm we utilise spectral irradiance measurements from the Solar EUV Experiment (SEE) instrument of the NASA Thermosphere Ionosphere Mesosphere Energetics Dynamics (TIMED) mission (Woods et al. 2005). For wavelengths between 189.5-320 nm, we use measurements obtained by the Solar Radiation and Climate Experiment (SORCE) NASA mission (Woods et al. 2021). Of the SORCE dataset, the data we use between 189.5-310 nm was obtained with the SOLar STellar Irradiance Comparison Experiment B (SOLSTICE-B) instrument while 310-320 nm was obtained by the Spectral Irradiance Monitor (SIM) instrument. We select datasets from each mission representing daily averages. In the XUV wavelengths for which we use the SEE observations, we select the Level 3 dataset which is filtered to remove flares as to focus our study on longer timescale variations. The SEE data have coverage from the year 2002 to present while the SORCE data cover 2003 to 2020. From their combined time coverage, we select solar cycle 24 for our analysis. As pointed out by Hazra et al. (2020), the variation across this particular cycle is relatively weak compared to other cycles in terms of sunspot number variation (Clette et al. 2014). In this sense, the resulting cyclic variation of planetary atmospheric escape and He I 1083 nm signature reported here for planets orbiting solar-like stars could be stronger, depending on the particular stellar cycle.

The upper panel of Figure 5.1 displays the resulting SEDs during a minimum phase (dashed-blue) and maximum phase (solid-red) of the Sun's activity cycle. We select January 1 2009 and April 1 2014 to represent the minimum and maximum phases of the activity cycle. The wavelength bins considered by our model set, distinguished by the background colour are soft X-ray (0.517–12.4 nm), hard-EUV (hEUV, 10–36 nm), soft-EUV (sEUV, 36–92 nm), and mid-UV (91.2–320 nm), consistent with Allan et al. (2024); Allan & Vidotto (2025). As previously mentioned, the activity cycle variation is greater towards shorter wavelengths. This is even more apparent in Figure 5.7 of Appendix 5.6, which displays the cyclic nature of the solar flux across each of our considered wavelength bins. The stronger cyclic variation at lower wavelengths is interesting in the context of observing planetary atmospheric escape using the helium triplet signature, as the higher energy XUV wavelengths which drive the escape vary substantially with the activity cycle, whereas the lower energy mid-UV photons capable of depopulating helium out of the 2^3s state via photoionisation exhibits negligible cyclic variation. The values of the binned fluxes for the solar activity minimum and maximum used in our modelling is given in Table 5.1.

5.2.2 The XUV cycle of ι Hor

The star ι -Hor is a young solar analogue of spectral type \sim F8V/G0V (Vauclair et al. 2008) with a detected X-ray cycle (Sanz-Forcada et al. 2013, 2019). Compared to the Sun it has a much shorter cycle period of only 1.6 years (Metcalfe et al. 2010) with smaller amplitude variations.

In order to study a stellar activity cycle differing from that of our Sun, we reconstruct the XUV SED of ι Hor during a minimum and maximum phase of its activity cycle. To achieve this, we utilise X-ray observations obtained by the XMM-Newton mission (Turner et al. 2001; Strüder et al. 2001) covering the star’s coronal cycle from Sanz-Forcada et al. (2019). We modelled the corona and transition region combining the information from UV lines from Sanz-Forcada et al. (2019) with the results of a 3-temperature fit to XMM-Newton EPIC spectra. We used the six highest observed fluxes in order to obtain the activity maximum SED in the X-ray, and conversely the lowest six fluxes for the activity minimum SED. The X-ray emission at the maximum was modelled with

$$\log T_{1,2,3}(\text{K}) = 6.18^{+0.06}_{-0.03}, 6.67^{+0.01}_{-0.01}, 6.96^{+0.01}_{-0.01}$$

and

$$\log EM_{1,2,3}(\text{cm}^{-3}) = 50.98^{+0.07}_{-0.09}, 51.23^{+0.02}_{-0.02}, 50.97^{+0.03}_{-0.03}.$$

At the minimum we got

$$\log T_{1,2,3}(\text{K}) = 6.10^{+0.03}_{-0.05}, 6.60^{+0.04}_{-0.02}, 6.87^{+0.03}_{-0.02}$$

and

$$\log EM_{1,2,3}(\text{cm}^{-3}) = 50.95^{+0.12}_{-0.07}, 50.97^{+0.07}_{-0.05}, 50.71^{+0.06}_{-0.15}.$$

The coronal and transition region contribution to the SED was then modelled as in other stars with no high-resolution X-rays data (see Sanz-Forcada et al. 2025).

For the photospheric contribution, we availed of synthetic modelling by Castelli & Kurucz (2003) adopting the model with $T=6250$ K, $\log g = 4.5$ and solar abundance. We find that this provides a good match to the HST/STIS spectra ranging 2600-2800 Å reported in Amazo-Gómez et al. (2023). We used the same model for maximum and minimum of the cycle. A stellar radius of $1.185 R_{\odot}$ was assumed in the mentioned ι Hor SED calculations, as well as in our ray-tracing model for predicting the He I 1083 nm planetary transit signature. In modelling the planetary atmospheric escape of these ι Hor-orbiting planets, a stellar mass of $1.16 M_{\odot}$ was assumed.

The lower panel of Figure 5.1 displays the resulting activity minimum and maximum SEDs of ι Hor, while Table 5.1 lists the luminosities in the wavelength bins relevant to our modelling. It is clear that the variation between our produced minimum and maximum activity SEDs are minor

Table 5.2: Planetary inputs assumed for each considered planet classification.

	sub-Neptune	Neptune-mass	Saturn-mass	HJ
$M_{\text{pl}} (M_{\text{Nep}})$	0.41	1.45	5.62	12.64
$R_{\text{pl}} (R_{\text{Nep}})$	0.55	1.04	2.34	3.92
$R_{\text{base}} (R_{\text{pl}})$	2.07	1.57	1.32	1.23
$g_{\text{surf}} (\text{m s}^{-2})$	14.98	14.92	11.45	9.15

and limited to the shorter wavelengths. This is unsurprising considering the smaller amplitude variation of the fast ι Hor activity cycle compared to that of the Sun.

5.3 Modelling planetary atmospheric escape and the He I 1083 nm transit signature

In modelling the planetary atmospheric escape and associated He I 1083 nm signatures presented in this work, we utilised the model previously presented in [Allan & Vidotto \(2025\)](#). This one dimensional model numerically solves the hydrodynamic atmospheric escape self-consistently, while simultaneously determining the population of helium in its 2^3S state as required for producing the He I 1083 nm signature. As described in [Allan & Vidotto \(2025, section 2.2\)](#), we again utilise the lower atmosphere model of [Parnentier & Guillot \(2014\)](#) in selecting the lower boundary conditions, setting the lower boundary of our hydrodynamic escape model for the upper atmosphere to occur at a pressure of 10 nbar. For each planet, we assume a constant He/H number density fraction of 0.1. In predicting the He I 1083 nm signatures, we utilise the ray-tracing model used in [Allan & Vidotto \(2025\)](#) and references therein. We assume a circular orbit and a transit along the centre of the stellar disk (impact parameter $b = 0$) resulting in a transit duration of $t_{\text{dur}} \approx \frac{2R_{\star}}{\sqrt{GM_{\star}/a}}$, where G is the gravitational constant and a is the planetary orbital distance. Depending on the stellar SED used, the stellar mass and radius, M_{\star} and R_{\star} is set to either that of the Sun or ι Hor.

In order to study how a stellar activity cycle affects the planetary atmospheric escape and the He I 1083 nm signature of a variety of exoplanets, we consider four different types of planets at two different orbital distances, 0.025 au and 0.05 au. We consider theoretical sub-Neptune (sub-Nep), Neptune-mass (Nep-mass), Saturn-mass (Sat-mass) and hot-Jupiter (HJ) exoplanets. Table 5.2 displays the assumed planetary masses and radii and the corresponding surface gravities. The assumed masses and radii were inspired by that of the sub-Neptune TOI-1430b ([Zhang et al. 2023b](#)), the Neptune-massed GJ436b ([von Braun et al. 2012](#)), Saturn-massed TOI-1268b

(Šubjak et al. 2022; Pérez-González et al. 2024) and hot-Jupiter HD209458b (Bonomo et al. 2017), all of which have had attempted He I 1083 nm transmission spectroscopy.

5.4 Findings of our study

5.4.1 The effect of a solar-like activity cycle on the atmospheric escape of highly irradiated exoplanets

In this section, we discuss how the solar-like activity cycle previously described in section 5.2.1 affects the planetary atmospheric escape predictions. Table 5.3 lists the predicted hydrodynamic escape properties of each modelled planet during either a maximum or minimum phase of the solar activity cycle, as indicated by the square brackets. The upper three panels of Figure 5.2 displays the relative variations in these hydrodynamic properties at a maximum phase of the activity cycle compared to a minimum, for the same orbital distance. Clearly, a solar-like activity cycle affects the atmospheric escape of the various types of highly irradiated exoplanets considered. For each of the modelled planets, the variation in mass-loss rate due to the activity cycle phase is substantial, with the smallest increase from the maximum to minimum phase being a factor of 1.68 for the sub-Neptune planet at 0.025 au, and the highest being a factor of 2 for the Neptune-mass planet at 0.05 au. While the terminal velocities are also influenced by the stellar activity cycle, their variations are considerably less than those of the mass-loss rates, with variations of only 1–2 km/s. The stronger dependence of the activity cycle with the mass-loss rates compared to the terminal velocities is due to the photoionisation heating occurring predominantly within the subsonic rather than the supersonic region of each of the modelled planetary atmospheres.

It is also apparent from Figure 5.2 that the activity cycle has a greater influence on the atmospheric escape of the more distant planets. This is reflected in the larger variations in mass-loss rate at the further orbital distance of 0.05 au (green cross) compared to that at 0.025 au (black circle), for all but the HJ planet. This stronger activity cycle influence at the further orbital distance is likely due to a transition in the efficiency of atmospheric escape. Going from higher to lower irradiation levels, atmospheric mass-loss rate is known to transition from the less efficient recombination-limited regime within which $\dot{m} \propto \sqrt{F_{\text{XUV}}}$ to the more efficient energy-limited escape regime where $\dot{m} \propto F_{\text{XUV}}$ (Murray-Clay et al. 2009; Owen & Alvarez 2016; Caldiroli et al. 2022). For the solar cycle 24 we consider in this work, the fraction of high-energy EUV flux¹ received by each planet during the activity

¹We find in our model that only the flux included in our hEUV and sEUV wavelength bins contribute to atmospheric heating and escape, hence for this discussion we consider

Table 5.3: Hydrodynamic escape predictions for planets orbiting a star with a solar-like activity cycle. For each property, the predicted value obtained during the maximum activity cycle is first given, followed by that for the minimum activity phase. \dot{m} refers to the planetary mass-loss rate, v_∞ the wind terminal velocity (velocity at the outermost edge of the modelled atmosphere) and T_{peak} to the peak of the non-isothermal atmospheric temperature profile.

	sub-Nep	Nep-mass	Sat-mass	HJ
0.025 au				
$\dot{m}[\text{max}]$ g/s	8.8e+12	2.7e+12	1.2e+12	7.8e+11
$\dot{m}[\text{min}]$ g/s	5.2e+12	1.5e+12	6.3e+11	4.3e+11
$v_\infty[\text{max}]$ km/s	68	67	64	61
$v_\infty[\text{min}]$ km/s	67	66	63	60
$T_{\text{peak}}[\text{max}]$ K	8782	8848	9349	9391
$T_{\text{peak}}[\text{min}]$ K	7028	7303	8452	8700
0.05 au				
$\dot{m}[\text{max}]$ g/s	2.1e+12	6.4e+11	2.5e+11	1.1e+11
$\dot{m}[\text{min}]$ g/s	1.1e+12	3.2e+11	1.3e+11	6.2e+10
$v_\infty[\text{max}]$ km/s	32	31	27	23
$v_\infty[\text{min}]$ km/s	30	28	25	22
$T_{\text{peak}}[\text{max}]$ K	5674	6064	8571	9134
$T_{\text{peak}}[\text{min}]$ K	4632	5142	8090	8869

maximum relative to activity minimum is 2.26. Hence, a corresponding mass-loss rate variation factor of 2.26 between activity cycle maximum and minimum would be indicative of energy-limited escape, as marked by the dashed-line in the upper panel of Figure 5.2. While a factor of $\sqrt{2.26} = 1.50$ would indicate recombination-limited escape, marked by the dotted-line. The predicted mass-loss rates exhibit activity cycle variation factors between 1.68-1.86 for the planets at 0.025 au and 1.74-1.98 for those at 0.05 au. The modelled atmospheric escape is hence between the energy-limited and recombination-limited regimes, with the closer orbiting planets being pushed closer to recombination-limited escape.

5.4.2 The effects of a solar-like activity cycle on the He I 1083 nm transit signature of highly irradiated exoplanets

It was shown in the previous subsection that a solar-like activity cycle can significantly affect the atmospheric escape of highly irradiated exoplanets. We now focus on the extent to which such atmospheric escape variations

only the activity cycle variation in the ‘EUV’ combined wavelength range of these two bins, omitting contributions from our X-ray bin.

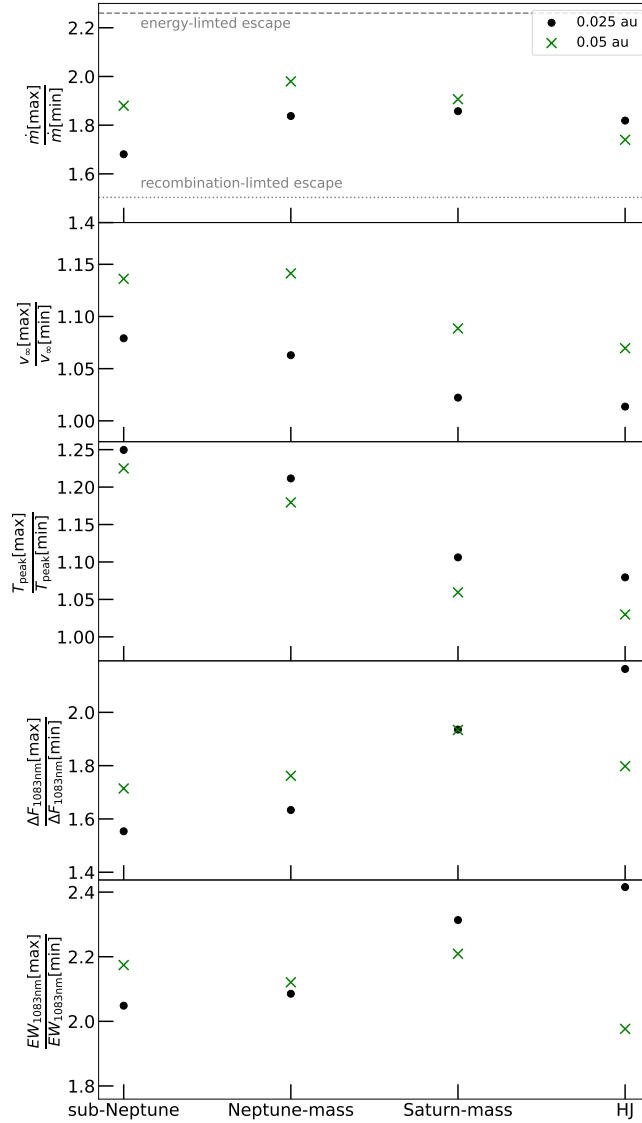


Figure 5.2: Maximum-to-minimum cycle variation in various properties of the escaping atmosphere for inner 0.025 au (circles) and outer 0.05 au (crosses) orbits around the Sun-like star. The absolute values of each parameter are listed in Table 5.3. The horizontal lines in the upper panel mark expected mass-loss rate variations based on the change in EUV flux for two different regimes of atmospheric escape as explained in the text.

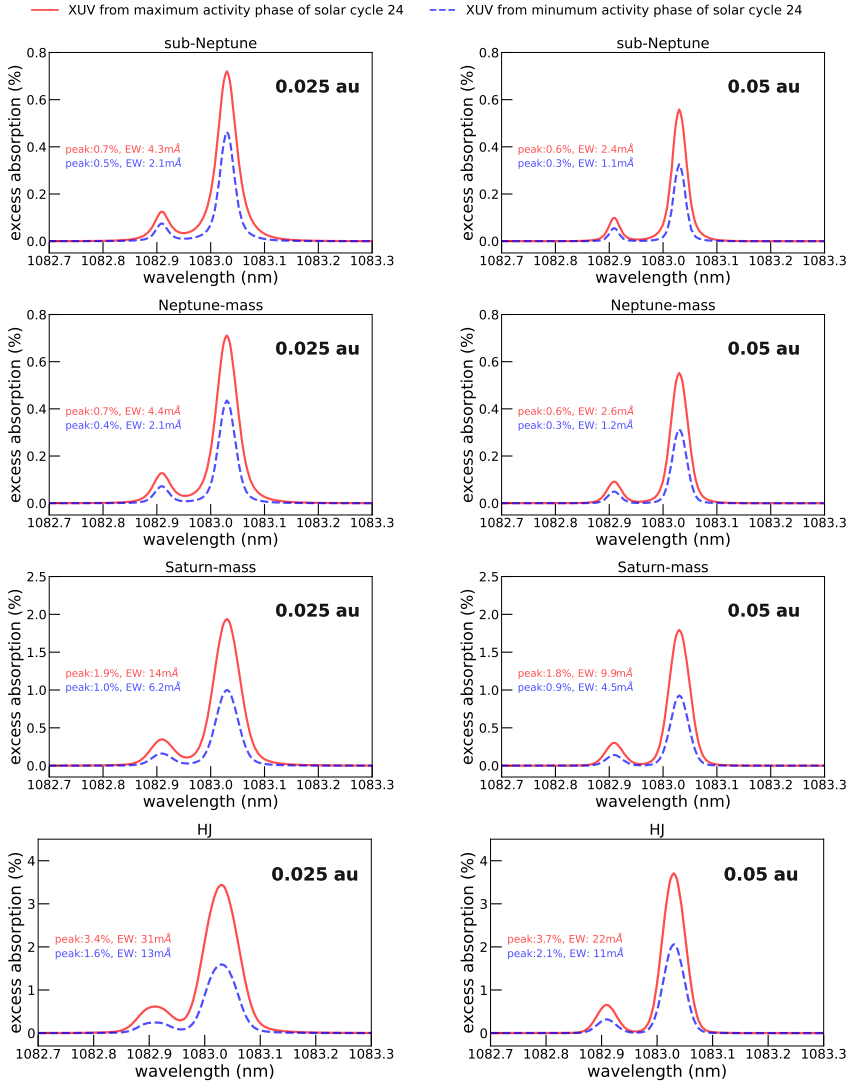


Figure 5.3: Predicted transit-phase-averaged helium triplet profiles assuming high energy fluxes consistent with maximum (red) and minimum (blue) stages during the solar activity cycle. The different rows correspond to the four different types of planets while the columns distinguish the assumed orbital distance. Note the differing y-scales for the differing planet types.

affect the planet’s observable He I 1083 nm transit signatures. Figure 5.3 displays the predicted transit-phase-averaged He I 1083 nm profiles for each modelled planet if observed during a maximum phase (red, solid line) or minimum phase (blue, dashed line) of a solar-like activity cycle. The profile’s peak excess absorption and equivalent width (EW) are listed in each panel. The factor by which these two properties vary from cycle maximum to minimum are shown in the lower two panels of Figure 5.2, respectively. Evidently, a solar-like activity cycle can significantly influence the He I 1083 nm transit signature of highly irradiated exoplanets. The stronger and faster atmospheric escape at a phase closer to the activity cycle maximum produces deeper, broader He I 1083 nm absorption features. Activity cycle variations of the Sun’s emitted mid-UV flux, capable of depopulating helium via photoionisation out of its metastable 2^3S state are insignificant relative to the larger variation in XUV fluxes, responsible for driving atmospheric escape, as shown previously in Figure 5.1 and Table 5.1. Hence, enhancement of the He I 1083 nm transit feature at activity cycle maximum by stronger atmospheric escape far outweighs the marginal He I 1083 nm weakening effect of slightly more mid-UV photons available to depopulate the observationally important He I (2^3S) state.

Despite atmospheric escape being naturally weaker at larger orbital distances (Table 5.3), the He I 1083 nm transit signature and popular ‘tracer of atmospheric escape’ interestingly weakens only slightly for planets orbiting further from a solar-like star (Figure 5.3), even strengthening for some of the modelled planets at further orbits of the more active ι Hor (as we will see in Figure 5.5). A similar non-monotonic behaviour of He I 1083 nm absorption with orbital distance was previously found by [Biassoni et al. \(2024\)](#), using the ATmospheric EEscape (ATES) model ([Caldirola et al. 2021](#)). [Biassoni et al. \(2024\)](#) proposed that larger extensions of the modelled atmosphere, which they set to the Hill radius $R_{\text{Hill}} \approx a \left(\frac{M_{\text{pl}}}{3M_{\star}} \right)^{1/3}$, is responsible for the cases of stronger He I 1083 nm absorption at further orbital distances. However, the modelled atmospheric extension of the model used here does not depend on the orbital distance. As mentioned in [Allan & Vidotto \(2025\)](#), the outer atmospheric extension is set to the minimum distance required for the modelled atmospheric grid to fully encompass the stellar disk during mid-transit, R_{\star} for a transit impact parameter of $b = 0$ as is assumed for the modelled transits here. Hence, an alternative explanation for the He I 1083 nm behaviour with orbital distance we find is required. We propose that the weaker mid-UV flux received by the planets at further orbital distances of the solar-like star is instead responsible. Mid-UV photons are capable of reducing the He I 1083 nm signature by photoionising helium out of its observationally important He I(2^3S) state ([Oklopčić 2019](#)). The weaker mid-UV flux received by the further orbiting planets can cause the helium in their weaker escaping atmospheres to be less effectively depopu-

lated out of its 2^3S state. To show this, Figure 5.4 displays the results of a demonstrative test case in which the mid-UV fluxes received by the Saturn-mass planets orbiting around the solar-like star during activity maximum is artificially suppressed by a factor of 1000 (solid profiles) compared to that found using $L_{\text{mid-UV}}$ of Table 5.1 (dashed profiles). Naturally, the test cases with suppressed mid-UV fluxes yield significantly stronger He I 1083 nm profiles compared to the profiles obtained using the true mid-UV fluxes (dashed profiles), despite their identical hydrodynamic escape predictions. This is because the lower number of mid-UV photons received leads to a reduction in photoionisations out of the He I(2^3S) state. Notably however, the mid-UV suppressed He I 1083 nm signature at 0.05 au is weaker than that at the closer orbital distance of 0.025 au. Hence, if the emitted solar flux at mid-UV wavelengths was significantly lower, the modelled planet's He I 1083 nm transit signature would better trace their atmospheric escape, being stronger at closer orbits where their escape is stronger. However, the He I 1083 nm behaviour with orbital distance is complex and is affected by more environmental properties than the mid-UV flux alone, as shown later in figure 5.6. A perhaps counter-intuitive result of the behaviour is that observational studies seeking to detect He I 1083 nm transit signatures may benefit from selecting targets orbiting further from stars with strong mid-UV fluxes, despite their weaker atmospheric escape.

5.4.3 Atmospheric escape with ι Hor as a stellar host

Figure 5.5 displays the predicted He I 1083 nm transit signatures obtained using the constructed activity maximum SED of ι Hor presented previously in section 5.2.2. Table 5.4 lists the hydrodynamic escape predictions for the same planets. Due to the similar EUV fluxes between the activity cycle minimum and maximum, our model predicts identical hydrodynamic and He I 1083 nm solutions, hence we do not compare predictions for activity maximum and minimum as done previously for the solar-like case in sections 5.4.1 and 5.4.2. Given the higher level of EUV radiation received by the planet (see table 5.1), the atmospheric escape of our modelled planets orbiting ι Hor is stronger than those orbiting the Sun. This is seen in their larger mass-loss rates and faster terminal velocities given in Table 5.4. For all modelled planets bar the sub-Neptune orbiting at 0.025 au, this stronger atmospheric escape yields larger equivalent widths for the He I 1083 nm signatures. This is due mostly to their significantly broader features arising from their faster atmospheric outflows. Despite their stronger atmospheric escape, the He I 1083 nm excess absorption for the sub-Neptune planets at both orbital distances and the Neptune-mass planet at 0.025 au is slightly below that found for the activity maximum solar case. The larger radius of $1.185R_{\odot}$ assumed for ι Hor is likely responsible, having a reducing effect on the predicted He I 1083 nm transit signature compared to when assum-

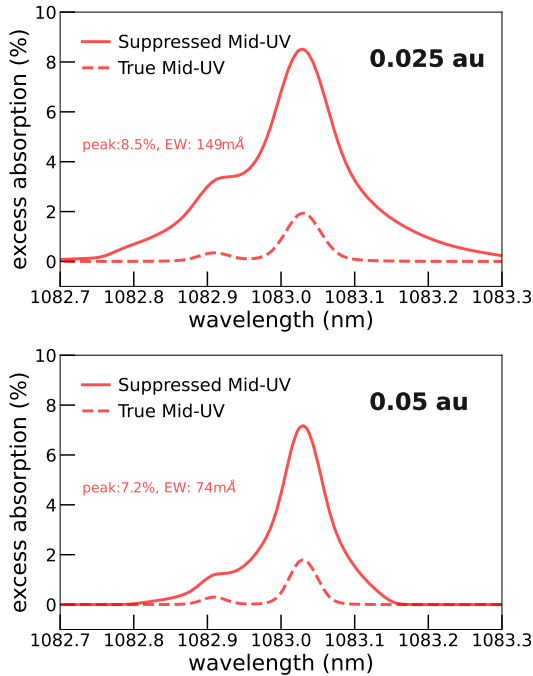


Figure 5.4: Demonstrative test suppressing the mid-UV flux received by the modelled Saturn-mass planet orbiting a solar-like star during a maximum phase of its activity cycle. For the mid-UV suppressed case (solid-line) the mid-UV flux capable of depopulating helium out of the 2^3S state has been reduced by a factor of 1000. The upper and lower panels correspond to orbital distances of 0.025 and 0.05 au, respectively. For comparison, the smaller He I 1083 nm profile of the original modelled signature with the true mid-UV flux is shown by the dashed profile.

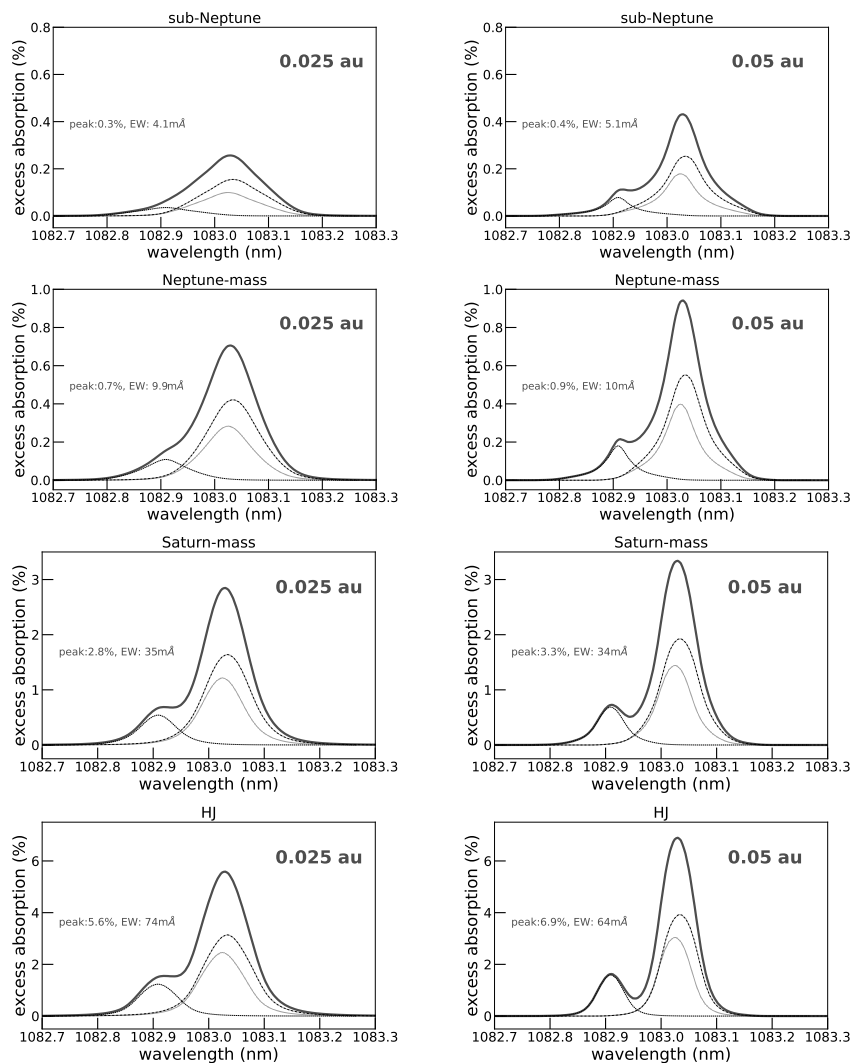


Figure 5.5: Predicted helium triplet profiles assuming high energy fluxes obtained from the SED of ι Hor previously presented in section 5.2.2. The three lighter, non-solid lines distinguish individual contributions from the three lines comprising the triplet.

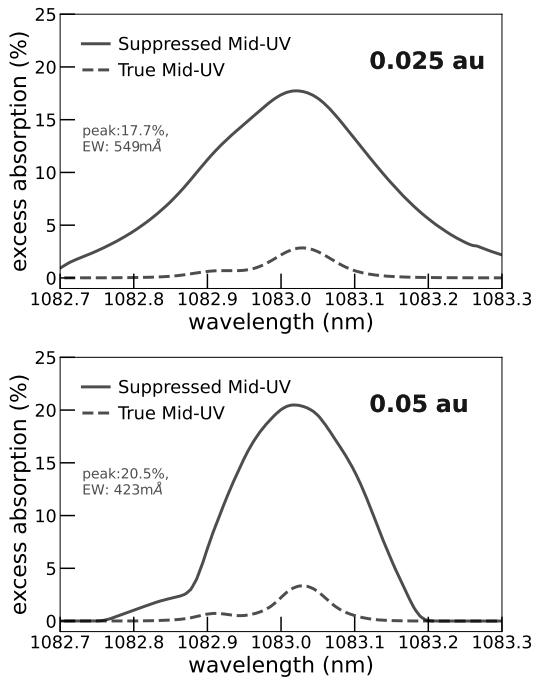


Figure 5.6: Demonstrative test of how suppressing the mid-UV flux received by the Saturn-mass planet orbiting ι Hor by a factor of 1000 affects the resulting He I 1083 nm transit signature. The figure set-up follows that in figure 5.4.

Table 5.4: Hydrodynamic escape predictions for planets orbiting ι Hor. The ‘maximum’ and ‘minimum’ activity phases presented in section 5.2.2 resulted in the same hydrodynamic predictions and hence are not distinguished here.

	sub-Nep	Nep-mass	Sat-mass	HJ
0.025 au				
\dot{m} g/s	2.2e+13	1e+13	5.4e+12	3.7e+12
v_∞ km/s	86	84	82	79
T_{peak} K	11225	11244	11262	11435
0.05 au				
\dot{m} g/s	1.2e+13	4.7e+12	2e+12	9.8e+11
v_∞ km/s	45	42	36	32
T_{peak} K	11016	10899	10832	10971

ing a smaller solar-sized stellar disk. This will particularly affect weaker He I 1083 nm signatures with less atmospheric He I (2^3S) material obscuring the stellar disk. The ~ 5 times larger mid-UV flux of ι Hor compared to the solar activity maximum will also contribute to weakening the ι Hor transit signatures, through raising the rate of photoionisations out of the 2^3S state.

The non-monotonic behaviour of the predicted He I 1083 nm signature with orbital distance discussed previously in section 5.4.2 is even more pronounced for planets orbiting ι Hor as seen in Figure 5.5. The predicted He I 1083 nm equivalent widths for the further 0.05 au orbiting planets are comparable to that of their closer orbiting 0.025 au counterparts despite their weaker atmospheric escapes. It was shown previously in Figure 5.4 that the weaker mid-UV flux at further orbital distance can cause unusual behaviour He I 1083 nm absorption with orbital distance, due to a reduced number of He I (2^3S) state photoionisations. Figure 5.6 presents a similar mid-UV suppression test, now assuming ι Hor as the stellar host. The lowered mid-UV flux He I 1083 nm profiles are again substantially stronger. In particular, they are significantly broader in the line wings due to absorption by He I (2^3S) in higher-up, faster-moving atmospheric material which otherwise would have been photoionised by mid-UV. While suppressing the mid-UV flux of ι Hor causes the He I 1083 nm equivalent width to fall with increasing orbital distance, the peak of the signature still does not fall with orbital distance. Hence, the mid-UV alone is not responsible for the cases of higher He I 1083 nm peaks at the further orbital distance of 0.05 au despite the weaker escape seen in figure 5.5. The drop in predicted mass-loss rates from an orbital distance of 0.025 au to 0.05 au is less for planets orbiting ι Hor compared to the Sun. This is a result of the stronger XUV emission of ι Hor causing the atmospheric escape for the closer orbiting models at 0.025 au to be further from the more efficient energy-limited

regime of atmospheric escape than the models orbiting the solar-like star at the same distance. This weaker relative fall-off in atmospheric escape with orbital distance for ι Hor orbiting planets complicates the behaviour of their He I 1083 nm transit signatures with orbital distance, compared to the planets orbiting the Sun-like star with atmospheric escape rates and He I 1083 nm signatures that are more sensitive to the orbital distance. Furthermore, as emphasised in [Biassoni et al. \(2024\)](#), the physics driving the strength of the He I 1083 nm transit signature is far from straightforward. The signature is reliant on the population of the He I (2^3S) state which itself is largely dependent on the mid-UV flux as discussed, in addition to the atmospheric temperature profile, the availability of He $+^2$ and free electrons³ and hence the XUV flux indirectly.

5.5 Discussion

5.5.1 A stellar XUV cycle can cause conflicting He I 1083 nm detections and non-detections of atmospheric escape

For both host stars, the He I 1083 nm profiles of the sub-Neptune and Neptune-mass planets are quite weak, contrary to their predicted mass-loss rates exceeding that of the Saturn-mass and HJ planets given in tables 5.3 and 5.4. Their comparatively weaker He I 1083 nm signatures despite their stronger atmospheric escape is a result of their smaller planetary radii (see [Allan & Vidotto 2025](#), Figures 4b and 5b). During a phase of stellar activity cycle minimum, with their He I 1083 nm signatures at their weakest, a He I 1083 nm transit observation may be sufficiently weak so as to be interpreted as a non-detection. It is feasible that such a non-detection would conflict with a positive detection made on a date closer to the maximum of the stellar activity cycle. The higher chance of a successful He I 1083 nm during the maximum phase of a stellar activity cycle is another possible explanation for the conflicting He I 1083 nm detections and non-detections reported for various planets in the literature; (Wasp-52b [Kirk et al. 2022](#); [Al-lart et al. 2023](#)), (TOI-2076b [Zhang et al. 2023b](#); [Gaidos et al. 2023](#)), (TOI-1683b [Zhang et al. 2023b](#); [Orell-Miquel et al. 2024](#)). While the predicted profiles of the larger Saturn-mass and HJ planets modelled here should be detectable even during activity minimum, their transit signatures could vary substantially with the cycle phase. Furthermore, Saturn-mass and HJ planets having with less atmospheric helium than that assumed here or

²required to populate He I (2^3S) via recombinations

³contributing to both populating He I (2^3S) via recombinations and depopulating via collisions

orbiting less XUV active hosts could also yield conflicting detections and non-detections as a result of a sufficiently varying stellar XUV cycle.

5.5.2 Comparing our model predictions to those in the literature

As mentioned in the introduction, [Hazra et al. \(2020\)](#) previously studied the effect of the Sun's activity cycle on the atmospheric escape of a HJ planet, finding similar general behaviours to those described previously in Section 5.4.1 for our similar HJ model at 0.05 au. Their predicted mass-loss rate for a HD209458b-like planet varies from $\sim 7.5 \times 10^{10}$ g/s to $\sim 1.5 \times 10^{11}$ g/s from similar phases of activity minimum and maximum of solar cycle 24 as considered here. These escape rates are comparable to the 6.2×10^{10} g/s and 1.1×10^{11} g/s predictions for our similar HJ model at 0.05 au. [Hazra et al. \(2020\)](#) additionally demonstrated that a solar-like activity cycle does not significantly affect the hydrogen Ly- α planetary transit signature. However, their excess absorption and equivalent widths predictions for the hydrogen H- α line varies by factors of 2.84 and 3.57 due to the activity cycle, more sensitive than the He I 1083 nm predictions found for all modelled planets in our work. The high sensitivity of H- α transit signature to stellar XUV cycles is due to the population of neutral hydrogen in the first excited state being highly responsive to changes in the atmospheric temperature.

In [Taylor et al. \(2025, section 3.5.1\)](#), the effects of applying a solar-like activity cycle to a HJ HD209458b-like planet on the predicted atmospheric escape and corresponding He I 1083 nm signature are discussed. The atmospheric mass-loss rates predicted by their model varies from 1.9×10^{10} g/s at activity minimum to 4.2×10^{10} g/s at activity maximum. Their predicted He I 1083 nm transit signature for the maximum phase of the activity cycle is similar to the HJ planet at 0.05 au in Figure 5.3, while that for activity minimum is notably weaker, peaking with an excess absorption of only $\sim 0.8\%$ (ours is 3.4%). A variety of potential reasons could produce the mentioned differences in predicted atmospheric escape and He I 1083 nm signatures, from slight variations in the assumed input parameters (in particular the received XUV and mid-UV fluxes to which both models are highly sensitive) as well as inherent differences in the hydrodynamic modelling approaches and treatment of the He I (2^3S) population. While a detailed comparison of the two modelling approaches is beyond the scope of this paper, both studies agree that a solar-like activity cycle in HD209458 would produce significant variability in the He I 1083 nm transit signature of its HJ planet due to strong variations in the planet's atmospheric escape.

5.6 Conclusions

In this work, we explored how stellar activity cycles can affect the atmospheric escape and He I 1083 nm signature of highly irradiated sub-Neptune, Neptune-mass, Saturn-mass and hot-Jupiter exoplanets. As described in sections 5.2.1 and 5.2.2, we considered two types of stellar activity cycles, first a solar-like activity cycle based on solar cycle 24, selected for its wavelength coverage suitable to our atmospheric escape modelling. We also reconstructed SEDs of the active star ι Hor during both a phase of activity maximum and minimum. Even though ι Hor shows an X-ray cycle, the resulting small variation in EUV flux does not change the modelled atmospheric escape and He I 1083 nm signatures.

We showed in section 5.4.1 that a solar-like activity cycle can strongly influence the atmospheric escape of highly irradiated exoplanets, with mass-loss rate predictions varying by factors of 1.68–1.98 for a phase of activity maximum compared to minimum. Substantial cyclic variations in the EUV flux are responsible for this activity cycle influence, with these high-energy photons heating the planetary atmospheres and driving their escape. This variable atmospheric escape with stellar activity cycle also impacts the resulting He I 1083 nm transit signatures, a popular tracer used in detecting exoplanetary atmospheric escape. Section 5.4.2 explores this, with the solar-like activity cycle causing the predicted He I 1083 nm signatures to vary by factors of 1.55–2.16 and 1.98–2.42 in their peak excess absorption and equivalent width, respectively. A solar-like activity cycle is also shown to have slightly greater influence on the atmospheric escape and helium signature of further orbiting planets (0.05 compared to 0.025 au). This is the result of a heightened sensitivity to the received EUV flux at lower irradiation levels, where the atmospheric escape is closer to the more efficient energy-limited regime.

Despite substantially weaker atmospheric escape at further orbital distances, the He I 1083 nm predictions of the planets orbiting at 0.05 au are not significantly weaker than those at 0.025 au. The behaviour of those planets orbiting the more active ι Hor star is even more extreme, exhibiting comparable or even slightly stronger He I 1083 nm features for the more distant planets, as shown in section 5.4.3. This unusual behaviour of the He I 1083 nm with the orbital distance was previously shown in the study of [Biassoni et al. \(2024\)](#). Here, we propose that lower mid-UV fluxes at more distant orbits leading to less photoionisations out of the He I (2^3S) state is causing this behaviour. At more distant orbits, the reduction in depopulation out of the observational important 2^3S state at least partially counterbalances the He I 1083 nm reducing effect of weaker atmospheric escapes.

From an observational standpoint, the He I 1083 nm behaviour with or-

bital distance leads to the counter-intuitive result that observational studies could benefit from performing He I 1083 nm transit spectroscopy for planets at further orbits, despite their weaker atmospheric escape rates. Whether the host star undergoes significant variations in its emitted XUV flux is also an important consideration for future observations. Granted there is sufficient XUV variation, timing a transit observation for a phase of activity maximum would raise the possibility of a successful detection. Stellar activity cycles could also help explain some of the conflicting He I 1083 nm detections and non-detections for the same planet, with detections being more likely during a phase of activity maximum. While time costly, detecting more and continual studying of known stellar activity cycles of planet hosts, particularly at XUV wavelengths, would greatly aid the current understanding of how stellar activity cycles are impacting planetary atmospheric escape and its associated signatures.

Acknowledgements

APA and AAV acknowledge funding from the European Research Council (ERC) under the European Union's Horizon 2020 research and innovation programme (grant agreement No 817540, ASTROFLOW). AAV acknowledges funding from the Dutch Research Council (NWO), with project number VI.C.232.041 of the Talent Programme Vici. JSF acknowledges support from the Agencia Estatal de Investigación del Ministerio de Ciencia e Innovación (AEI- MCINN) under grant PID2022-137241NB-C42. The authors thank Dr. E. Sandford for discussions on the available solar spectral irradiance data. The results presented in this document rely on data measured from the Thermosphere Ionosphere Mesosphere Energetics and Dynamics (TIMED) Solar EUV Experiment (SEE) and are available from the TIMED SEE website at <https://lasp.colorado.edu/see/data/>. The results presented in this document rely on data measured from the Solar Radiation Climate Experiment (SORCE) and are available at <https://lasp.colorado.edu/sorce/data/>. The TIMED SEE and SORCE data were accessed via the LASP Interactive Solar Irradiance Datacenter (LISIRD) (<https://lasp.colorado.edu/lisird/>).

Data Availability

The data described in this article will be shared on reasonable request to the corresponding author.

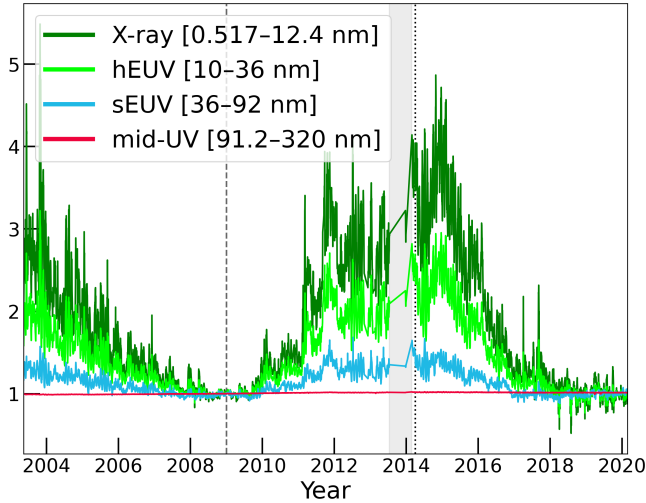


Figure 5.7: The cyclic nature of the flux of the Sun in our considered wavelength bins. Note that the mid-UV flux shows comparatively negligible cyclic variation. The data used are publicly available and obtained by the SEE instrument of the NASA (TIMED) mission as well as the NASA (SORCE) mission as described in the text. The different colours represent different wavelength bins over which the flux was integrated as indicated by the legend. The plotted values are normalised to the integrated flux within the same wavelength band on the date we assign to an activity minimum phase (vertical dashed line). The vertical dotted line indicates our assumed activity maximum and the grey shaded region indicates a period when there was an issue with the SORCE instruments and hence no available data.

Appendix

The XUV variation over the full solar cycle 24

In section 5.2.1, we describe how we utilise observational solar data in order to obtain fluxes in four different wavelength bins necessary for our model of atmospheric escape. For the sake of completeness, we now show in figure 5.7, the cyclic nature of the emitted high-energy flux over solar cycle 24, with the dates corresponding to the minimum and maximum phases we consider in our modelling marked by the dashed and dotted vertical lines, respectively.

BIBLIOGRAPHY

- Alam M. K., et al., 2024, *AJ*, 168, 102
- Allan A., Vidotto A. A., 2019, *MNRAS*, 490, 3760
- Allan A. P., Vidotto A. A., 2025, *MNRAS*, 539, 2144
- Allan A. P., Vidotto A. A., Villarreal D'Angelo C., Dos Santos L. A., Driessen F. A., 2024, *MNRAS*, 527, 4657
- Allan A. P., Vidotto A. A., Sanz-Forcada J., Villarreal D'Angelo C., 2025, (now in press with *MNRAS*),
- Allart R., et al., 2018, *Science*, 362, 1384
- Allart R., et al., 2019, *A&A*, 623, A58
- Allart R., et al., 2023, *A&A*, 677, A164
- Alonso-Floriano F. J., et al., 2019, *A&A*, 629, A110
- Amazo-Gómez E. M., et al., 2023, *MNRAS*, 524, 5725
- Ayres T. R., 2020, *ApJS*, 250, 16
- Ayres T., 2025, *AJ*, 169, 281
- Bailey E., Batygin K., 2018, *ApJ*, 866, L2
- Baliunas S. L., et al., 1995, *ApJ*, 438, 269
- Ballabio G., Owen J. E., 2025, *MNRAS*, 537, 1305
- Barnes J. R., Haswell C. A., Staab D., Anglada-Escudé G., 2016, *MNRAS*, 462, 1012
- Behr P. R., et al., 2023, *AJ*, 166, 35
- Bello-Arufe A., Cabot S. H. C., Mendonça J. M., Buchhave L. A., Rathcke A. D., 2022, *AJ*, 163, 96
- Ben-Jaffel L., 2008, *apj*, 688, 1352
- Benjamin R. A., Skillman E. D., Smits D. P., 1999, *ApJ*, 514, 307
- Bergeson S. D., et al., 1998, *Phys. Rev. Lett.*, 80, 3475
- Biassoni F., Caldiroli A., Gallo E., Haardt F., Spinelli R., Borsa F., 2024, *A&A*, 682, A115
- Black J. H., 1981, *MNRAS*, 197, 553
- Bonomo A. S., et al., 2017, *A&A*, 602, A107
- Boro Saikia S., et al., 2018, *A&A*, 616, A108
- Bouchy F., et al., 2025, *A&A*, 700, A10
- Bourrier V., Lecavelier des Etangs A., 2013, *A&A*, 557, A124
- Bourrier V., Lecavelier des Etangs A., Ehrenreich D., Tanaka Y. A., Vidotto A. A., 2016, *A&A*, 591, A121
- Bray I., Burgess A., Fursa D. V., Tully J. A., 2000, *A&AS*, 146, 481
- Brown R. L., 1971, *ApJ*, 164, 387
- Caldirolì A., Haardt F., Gallo E., Spinelli R., Malsky I., Rauscher E., 2021, *A&A*, 655, A30
- Caldirolì A., Haardt F., Gallo E., Spinelli R., Malsky I., Rauscher E., 2022, *A&A*, 663, A122
- Carolan S., Vidotto A. A., Loesch C., Coogan P., 2019, *MNRAS*, 489, 5784

- Carolan S., Vidotto A. A., Plavchan P., Villarreal D'Angelo C., Hazra G., 2020, *MNRAS*, **498**, L53
- Carolan S., Vidotto A. A., Villarreal D'Angelo C., Hazra G., 2021a, *MNRAS*, **500**, 3382
- Carolan S., Vidotto A. A., Hazra G., Villarreal D'Angelo C., Kubyschkina D., 2021b, *MNRAS*, **508**, 6001
- Castelli F., Kurucz R. L., 2003, in Piskunov N., Weiss W. W., Gray D. F., eds, IAU Symposium Vol. 210, Modelling of Stellar Atmospheres. p. A20 ([arXiv:astro-ph/0405087](https://arxiv.org/abs/astro-ph/0405087)), [doi:10.48550/arXiv.astro-ph/0405087](https://doi.org/10.48550/arXiv.astro-ph/0405087)
- Catling D. C., Kasting J. F., 2017, Atmospheric Evolution on Inhabited and Lifeless Worlds
- Cauley P. W., Redfield S., Jensen A. G., Barman T., Endl M., Cochran W. D., 2015, *ApJ*, **810**, 13
- Cauley P. W., Redfield S., Jensen A. G., 2017, *AJ*, **153**, 217
- Cauley P. W., Kuckein C., Redfield S., Shkolnik E. L., Denker C., Llama J., Verma M., 2018, *AJ*, **156**, 189
- Cauley P. W., Shkolnik E. L., Ilyin I., Strassmeier K. G., Redfield S., Jensen A., 2019, *AJ*, **157**, 69
- Cecchi-Pestellini C., Ciaravella A., Micela G., 2006, *A&A*, **458**, L13
- Cen R., 1992, *ApJS*, **78**, 341
- Charbonneau D., Brown T. M., Noyes R. W., Gilliland R. L., 2002, *ApJ*, **568**, 377
- Chen J., Kipping D., 2017, *ApJ*, **834**, 17
- Chen H., Rogers L. A., 2016, *ApJ*, **831**, 180
- Claudi R., et al., 2016, in Evans C. J., Simard L., Takami H., eds, Society of Photo-Optical Instrumentation Engineers (SPIE) Conference Series Vol. 9908, Ground-based and Airborne Instrumentation for Astronomy VI. p. 99081A ([arXiv:1611.07603](https://arxiv.org/abs/1611.07603)), [doi:10.1117/12.2231845](https://doi.org/10.1117/12.2231845)
- Claudi R., et al., 2017, *European Physical Journal Plus*, **132**, 364
- Clette F., Svalgaard L., Vaquero J. M., Cliver E. W., 2014, *Space Sci. Rev.*, **186**, 35
- Cloutier R., 2024, *arXiv e-prints*, p. [arXiv:2409.13062](https://arxiv.org/abs/2409.13062)
- Cloutier R., et al., 2018, *AJ*, **155**, 93
- Coc A., Petitjean P., Uzan J.-P., Vangioni E., Descouvemont P., Iliadis C., Longland R., 2015, *Phys. Rev. D*, **92**, 123526
- Coffaro M., et al., 2020, *A&A*, **636**, A49
- Craig N., et al., 1997, *ApJS*, **113**, 131
- Cubillos P. E., Fossati L., Koskinen T., Young M. E., Salz M., France K., Sreejith A. G., Haswell C. A., 2020, *AJ*, **159**, 111
- Czesla S., et al., 2022, *A&A*, **657**, A6
- D'Arpa M. C., et al., 2024, *A&A*, **692**, A77
- Dai F., et al., 2023, *AJ*, **166**, 49
- Daley-Yates S., Stevens I. R., 2019, *MNRAS*, **483**, 2600

- Debrecht A., Carroll-Nellenback J., Frank A., Blackman E. G., Fossati L., McCann J., Murray-Clay R., 2019, arXiv e-prints, p. [arXiv:1906.00075](#)
- Del Zanna G., Mason H. E., 2018, [Living Reviews in Solar Physics](#), **15**, 5
- Dere K. P., Del Zanna G., Young P. R., Landi E., Sutherland R. S., 2019, [ApJS](#), **241**, 22
- Donati J. F., et al., 2020, [MNRAS](#), **498**, 5684
- Dorn R. J., et al., 2023, [A&A](#), **671**, A24
- Dos Santos L. A., 2023, in Vidotto A. A., Fossati L., Vink J. S., eds, IAU Symposium Vol. 370, Winds of Stars and Exoplanets. pp 56–71 ([arXiv:2211.16243](#)), doi:10.1017/S1743921322004239
- Dos Santos L. A., Vissapragada S., 2023, p-winds, doi:10.5281/zenodo.10419485
- Dos Santos L. A., et al., 2022, [A&A](#), **659**, A62
- Dos Santos L. A., et al., 2023, [AJ](#), **166**, 89
- Dos Santos L. A., et al., 2025, arXiv e-prints, p. [arXiv:2507.07124](#)
- Drake G. W., 1971, [Phys. Rev.](#), **3**, 908
- Duvvuri G. M., Cauley P. W., Aguirre F. C., Kilgard R., France K., Bert-Thompson Z. K., Pineda J. S., 2023, [AJ](#), **166**, 196
- Egeland R., Soon W., Baliunas S., Hall J. C., Pevtsov A. A., Bertello L., 2017, [ApJ](#), **835**, 25
- Ehrenreich D., Désert J. M., 2011, [A&A](#), **529**, A136
- Ehrenreich D., et al., 2015, [Nature](#), **522**, 459
- Eikema K. S. E., Ubachs W., Vassen W., Hogervorst W., 1996, [Phys. Rev. Lett.](#), **76**, 1216
- Erkaev N. V., Kulikov Y. N., Lammer H., Selsis F., Langmayr D., Jaritz G. F., Biernat H. K., 2007, [Astronomy & Astrophysics](#), **472**, 329
- Esquivel A., Schneiter M., Villarreal D'Angelo C., Sgró M. A., Krapp L., 2019, [MNRAS](#), **487**, 5788
- Farret Jentink C., Bourrier V., Lovis C., Allart R., Chazelas B., Lendl M., Dumusque X., Pepe F., 2024a, [MNRAS](#), **527**, 4467
- Farret Jentink C., et al., 2024b, in Bryant J. J., Motohara K., Vernet J. R. D., eds, Society of Photo-Optical Instrumentation Engineers (SPIE) Conference Series Vol. 13096, Ground-based and Airborne Instrumentation for Astronomy X. p. 130967O ([arXiv:2405.18899](#)), doi:10.1117/12.3014420
- Favata F., Micela G., Orlando S., Schmitt J. H. M. M., Sciortino S., Hall J., 2008, [A&A](#), **490**, 1121
- Ferland G. J., Korista K. T., Verner D. A., Ferguson J. W., Kingdon J. B., Verner E. M., 1998, [PASP](#), **110**, 761
- Ferland G. J., et al., 2017, [Rev. Mexicana Astron. Astrofis.](#), **53**, 385
- Fleming B. T., et al., 2017, in Siegmund O. H., ed., Society of Photo-Optical Instrumentation Engineers (SPIE) Conference Series Vol. 10397, Society of Photo-Optical Instrumentation Engineers (SPIE) Conference Series. p. 103971A, doi:10.1117/12.2276138

- Fortney J. J., Nettelmann N., 2010, *Space Sci. Rev.*, **152**, 423
- Fossati L., et al., 2010, *ApJ*, **714**, L222
- Fossati L., et al., 2017, *A&A*, **598**, A90
- Fossati L., et al., 2022, *A&A*, **658**, A136
- France K., et al., 2016, *ApJ*, **820**, 89
- France K., et al., 2017, in Siegmund O. H., ed., Society of Photo-Optical Instrumentation Engineers (SPIE) Conference Series Vol. 10397, Society of Photo-Optical Instrumentation Engineers (SPIE) Conference Series. p. 1039713 ([arXiv:1709.06141](https://arxiv.org/abs/1709.06141)), doi:10.1117/12.2272025
- Fu G., et al., 2022, arXiv e-prints, p. [arXiv:2211.13761](https://arxiv.org/abs/2211.13761)
- Fuhrmeister B., et al., 2020, *A&A*, **640**, A52
- Fulton B. J., et al., 2017, *AJ*, **154**, 109
- Gaia Collaboration et al., 2016, *A&A*, **595**, A1
- Gaia Collaboration et al., 2022, arXiv e-prints, p. [arXiv:2208.00211](https://arxiv.org/abs/2208.00211)
- Gaidos E., et al., 2020, *MNRAS*, **495**, 650
- Gaidos E., Hirano T., Omiya M., Kuzuhara M., Kotani T., Tamura M., Harakawa H., Kudo T., 2021, *Research Notes of the American Astronomical Society*, **5**, 238
- Gaidos E., et al., 2022, *MNRAS*, **509**, 2969
- Gaidos E., et al., 2023, *MNRAS*, **518**, 3777
- Gallet F., Bouvier J., 2013, *A&A*, **556**, A36
- García Muñoz A., 2007, *planss*, **55**, 1426
- García Muñoz A., 2025, *A&A*, **698**, A199
- Gillet A., Garcia Munoz A., Strugarek A., 2023, arXiv e-prints, p. [arXiv:2309.08390](https://arxiv.org/abs/2309.08390)
- Ginzburg S., Schlichting H. E., Sari R., 2018, *MNRAS*, **476**, 759
- Güdel M., 2015, in European Physical Journal Web of Conferences. p. 00015, doi:10.1051/epjconf/201510200015
- Guillot T., 2010, *A&A*, **520**, A27
- Guilluy G., et al., 2020, *A&A*, **639**, A49
- Guilluy G., et al., 2024, *A&A*, **686**, A83
- Hale G. E., Ellerman F., Nicholson S. B., Joy A. H., 1919, *ApJ*, **49**, 153
- Hall J. C., Lockwood G. W., Skiff B. A., 2007, *AJ*, **133**, 862
- Hathaway D. H., 2010, *Living Reviews in Solar Physics*, **7**, 1
- Hazra G., Vidotto A. A., D'Angelo C. V., 2020, *MNRAS*, **496**, 4017
- Hempelmann A., Robrade J., Schmitt J. H. M. M., Favata F., Baliunas S. L., Hall J. C., 2006, *A&A*, **460**, 261
- Hirano T., et al., 2020, *ApJ*, **899**, L13
- Hui L., Gnedin N. Y., 1997, *MNRAS*, **292**, 27
- Indahl B., Wilson D., 2022, MANTIS: Monitoring Activity from Nearby sTars with uv Imaging and Spectroscopy, NASA Prop. ID 22-APRA22-121
- Indriolo N., Hobbs L. M., Hinkle K. H., McCall B. J., 2009, *ApJ*, **703**, 2131

- Ionov D. E., Pavlyuchenkov Y. N., Shematovich V. I., 2018, *MNRAS*, **476**, 5639
- Jackson A. P., Davis T. A., Wheatley P. J., 2012, *MNRAS*, **422**, 2024
- Jardine M., Collier Cameron A., Donati J.-F., Gregory S. G., Wood K., 2006, *MNRAS*, **367**, 917
- Jeffers S. V., Kiefer R., Metcalfe T. S., 2023, *Space Sci. Rev.*, **219**, 54
- Jensen A. G., Redfield S., Endl M., Cochran W. D., Koesterke L., Barman T., 2012, *ApJ*, **751**, 86
- Jensen A. G., Cauley P. W., Redfield S., Cochran W. D., Endl M., 2018, *AJ*, **156**, 154
- Jin S., Mordasini C., 2018, *ApJ*, **853**, 163
- Johnstone C. P., Güdel M., Brott I., Lüftinger T., 2015a, *A&A*, **577**, A28
- Johnstone C. P., et al., 2015b, *ApJ*, **815**, L12
- Johnstone C. P., Bartel M., Güdel M., 2021, *A&A*, **649**, A96
- Kasting J. F., Whitmire D. P., Reynolds R. T., 1993, *ICARUS*, **101**, 108
- Kawaler S. D., 1988, *ApJ*, **333**, 236
- Kempton E. M. R., et al., 2018, *PASP*, **130**, 114401
- Khodachenko M. L., Shaikhislamov I. F., Lammer H., Prokopov P. A., 2015, *ApJ*, **813**, 50
- Khodachenko M. L., Shaikhislamov I. F., Fossati L., Lammer H., Rumenskikh M. S., Berezutsky A. G., Miroshnichenko I. B., Efimov M. A., 2021a, *MNRAS*, **503**, L23
- Khodachenko M. L., Shaikhislamov I. F., Lammer H., Miroshnichenko I. B., Rumenskikh M. S., Berezutsky A. G., Fossati L., 2021b, *MNRAS*, **507**, 3626
- Kilmetis K., Vidotto A. A., Allan A., Kubyshkina D., 2024, *MNRAS*, **535**, 3646
- Kirk J., Alam M. K., López-Morales M., Zeng L., 2020, *AJ*, **159**, 115
- Kirk J., Dos Santos L. A., López-Morales M., Alam M. K., Oklopčić A., MacLeod M., Zeng L., Zhou G., 2022, *AJ*, **164**, 24
- Kislyakova K. G., et al., 2014, *A&A*, **562**, A116
- Koskinen T. T., Harris M. J., Yelle R. V., Lavvas P., 2013, *ICARUS*, **226**, 1678
- Kotani T., et al., 2018, in Evans C. J., Simard L., Takami H., eds, Society of Photo-Optical Instrumentation Engineers (SPIE) Conference Series Vol. 10702, Ground-based and Airborne Instrumentation for Astronomy VII. p. 1070211, doi:10.1117/12.2311836
- Kramida A., Yu. Ralchenko Reader J., and NIST ASD Team 2022, NIST Atomic Spectra Database (ver. 5.10), [Online]. Available: <https://physics.nist.gov/asd> [2022, December 7]. National Institute of Standards and Technology, Gaithersburg, MD.
- Krishnamurthy V., Cowan N. B., 2024, *AJ*, **168**, 30
- Krishnamurthy V., et al., 2021, *AJ*, **162**, 82

- Krolikowski D. M., Kraus A. L., Tofflemire B. M., Morley C. V., Mann A. W., Vanderburg A., 2024, *AJ*, **167**, 79
- Kubyshkina D., Fossati L., 2022, *A&A*, **668**, A178
- Kubyshkina D., Vidotto A. A., 2021, *MNRAS*, **504**, 2034
- Kubyshkina D., et al., 2018, *A&A*, **619**, A151
- Kubyshkina D., Vidotto A. A., Fossati L., Farrell E., 2020, *MNRAS*, **499**, 77
- Kuckein C., Collados M., Manso Sainz R., 2015, *ApJ*, **799**, L25
- Kulow J. R., France K., Linsky J., Loyd R. O. P., 2014, *ApJ*, **786**, 132
- Kurokawa H., Nakamoto T., 2014, *ApJ*, **783**, 54
- Lammer H., et al., 2009, *A&A Rev.*, **17**, 181
- Lampón M., et al., 2020, *A&A*, **636**, A13
- Lampón M., et al., 2021, *A&A*, **647**, A129
- Lavie B., et al., 2017, *A&A*, **605**, L7
- Lavvas P., Koskinen T., Yelle R. V., 2014, *The Astrophysical Journal*, **796**, 15
- Lecavelier Des Etangs A., et al., 2010, *aap*, **514**, A72
- Lecavelier des Etangs A., et al., 2012, *aap*, **543**, L4
- Linssen D. C., Oklopčić A., 2023, *A&A*, **675**, A193
- Linssen D. C., Oklopčić A., MacLeod M., 2022, *A&A*, **667**, A54
- Linssen D., Oklopčić A., MacLeod M., 2024, *arXiv e-prints*, p. [arXiv:2410.03228](https://arxiv.org/abs/2410.03228)
- Locci D., Petralia A., Micela G., Maggio A., Ciaravella A., Cecchi-Pestellini C., 2022, *psj*, **3**, 1
- Lopez E. D., Fortney J. J., 2013, *ApJ*, **776**, 2
- Lopez E. D., Fortney J. J., Miller N., 2012, *ApJ*, **761**, 59
- Loyd R. O. P., et al., 2016, *ApJ*, **824**, 102
- MacLeod M., Oklopčić A., 2022, *ApJ*, **926**, 226
- Mahadevan S., et al., 2012a, in McLean I. S., Ramsay S. K., Takami H., eds, Society of Photo-Optical Instrumentation Engineers (SPIE) Conference Series Vol. 8446, Ground-based and Airborne Instrumentation for Astronomy IV. p. 84461S ([arXiv:1209.1686](https://arxiv.org/abs/1209.1686)), [doi:10.1117/12.926102](https://doi.org/10.1117/12.926102)
- Mahadevan S., et al., 2012b, in McLean I. S., Ramsay S. K., Takami H., eds, Society of Photo-Optical Instrumentation Engineers (SPIE) Conference Series Vol. 8446, Ground-based and Airborne Instrumentation for Astronomy IV. p. 84461S ([arXiv:1209.1686](https://arxiv.org/abs/1209.1686)), [doi:10.1117/12.926102](https://doi.org/10.1117/12.926102)
- Malsky I., Rogers L., Kempton E. M. R., Marounina N., 2023, *Nature Astronomy*, **7**, 57
- Marconi A., et al., 2024, in Bryant J. J., Motohara K., Vernet J. R. D., eds, Society of Photo-Optical Instrumentation Engineers (SPIE) Conference Series Vol. 13096, Ground-based and Airborne Instrumentation for Astronomy X. p. 1309613 ([arXiv:2407.14601](https://arxiv.org/abs/2407.14601)), [doi:10.1117/12.3017966](https://doi.org/10.1117/12.3017966)

- Martin E. C., et al., 2018, in Evans C. J., Simard L., Takami H., eds, Society of Photo-Optical Instrumentation Engineers (SPIE) Conference Series Vol. 10702, Ground-based and Airborne Instrumentation for Astronomy VII. p. 107020A ([arXiv:1808.06024](https://arxiv.org/abs/1808.06024)), [doi:10.1117/12.2312266](https://doi.org/10.1117/12.2312266)
- Matsakos T., Königl A., 2016, *ApJ*, **820**, L8
- Mayo A. W., et al., 2023, *AJ*, **165**, 235
- Mayor M., Queloz D., 1995, *Nature*, **378**, 355
- Mazeh T., Holczer T., Faigler S., 2016, *A&A*, **589**, A75
- McCann J., Murray-Clay R. A., Kratter K., Krumholz M. R., 2019, *ApJ*, **873**, 89
- McCreery P., Dos Santos L. A., Espinoza N., Allart R., Kirk J., 2025, *ApJ*, **980**, 125
- McLean I. S., et al., 1998, in Fowler A. M., ed., Society of Photo-Optical Instrumentation Engineers (SPIE) Conference Series Vol. 3354, Infrared Astronomical Instrumentation. pp 566–578, [doi:10.1117/12.317283](https://doi.org/10.1117/12.317283)
- Mercier S. J., et al., 2025, arXiv e-prints, p. [arXiv:2507.21290](https://arxiv.org/abs/2507.21290)
- Metcalf T. S., Basu S., Henry T. J., Soderblom D. R., Judge P. G., Knölker M., Mathur S., Rempel M., 2010, *ApJ*, **723**, L213
- Mittag M., Robrade J., Schmitt J. H. M. M., Hempelmann A., González-Pérez J. N., Schröder K. P., 2017, *A&A*, **600**, A119
- Murray-Clay R. A., Chiang E. I., Murray N., 2009, *Astrophysical Journal*, **693**, 23
- Nail F., Oklopčić A., MacLeod M., 2024, *A&A*, **684**, A20
- Namekata K., Toriumi S., Airapetian V. S., Shoda M., Watanabe K., Notsu Y., 2023, *ApJ*, **945**, 147
- Norcross D. W., 1971, *Journal of Physics B Atomic Molecular Physics*, **4**, 652
- Nortmann L., et al., 2018, *Science*, **362**, 1388
- Oklopčić A., 2019, *ApJ*, **881**, 133
- Oklopčić A., Hirata C. M., 2018, *ApJ*, **855**, L11
- Oláh K., Kóvári Z., Petrovay K., Soon W., Baliunas S., Kolláth Z., Vida K., 2016, *A&A*, **590**, A133
- Orell-Miquel J., et al., 2023, *A&A*, **677**, A56
- Orell-Miquel J., et al., 2024, *A&A*, **689**, A179
- Orlando S., Favata F., Micela G., Sciortino S., Maggio A., Schmitt J. H. M. M., Robrade J., Mittag M., 2017, *A&A*, **605**, A19
- Osborn A., et al., 2023, *MNRAS*, **526**, 548
- Osterbrock D. E., Ferland G. J., 2006, *Astrophysics of gaseous nebulae and active galactic nuclei*
- Owen J. E., 2019, *Annual Review of Earth and Planetary Sciences*, **47**, 67
- Owen J. E., Alvarez M. A., 2016, *ApJ*, **816**, 34
- Owen J. E., Jackson A. P., 2012, *MNRAS*, **425**, 2931
- Owen J. E., Lai D., 2018, *MNRAS*, **479**, 5012
- Owen J. E., Wu Y., 2013, *ApJ*, **775**, 105

- Owen J. E., Wu Y., 2017, *ApJ*, **847**, 29
- Owen J. E., et al., 2023, *MNRAS*, **518**, 4357
- Palle E., et al., 2025, *Experimental Astronomy*, **59**, 29
- Parker E. N., 1958, *apj*, **128**, 664
- Parmentier V., Guillot T., 2014, *A&A*, **562**, A133
- Pepe F., et al., 2011, *A&A*, **534**, A58
- Pepe F., et al., 2021, *A&A*, **645**, A96
- Pérez-González J., Greklek-McKeon M., Vissapragada S., Saidel M., Knutson H. A., Linssen D., Oklopčić A., 2024, *AJ*, **167**, 214
- Pezzotti C., Eggenberger P., Buldgen G., Meynet G., Bourrier V., Mordasini C., 2021a, *A&A*, **650**, A108
- Pezzotti C., Attia O., Eggenberger P., Buldgen G., Bourrier V., 2021b, *A&A*, **654**, L5
- Poppenhaeger K., 2022, *MNRAS*, **512**, 1751
- Poppenhaeger K., Ketzler L., Mallonn M., 2021, *MNRAS*, **500**, 4560
- Presa A., Driessen F. A., Vidotto A. A., 2024, *MNRAS*, **534**, 3622
- Quirrenbach A., et al., 2014, in Ramsay S. K., McLean I. S., Takami H., eds, *Society of Photo-Optical Instrumentation Engineers (SPIE) Conference Series Vol. 9147, Ground-based and Airborne Instrumentation for Astronomy V*. p. 91471F, doi:10.1117/12.2056453
- Ribas I., Guinan E. F., Güdel M., Audard M., 2005, *ApJ*, **622**, 680
- Richey-Yowell T., et al., 2022, *ApJ*, **929**, 169
- Roberge W., Dalgarno A., 1982, *ApJ*, **255**, 489
- Robrade J., Schmitt J. H. M. M., Favata F., 2012, *A&A*, **543**, A84
- Rogers J. G., Gupta A., Owen J. E., Schlichting H. E., 2021, *MNRAS*, **508**, 5886
- Rumenskikh M. S., Shaikhislamov I. F., Khodachenko M. L., Lammer H., Miroschnichenko I. B., Berezutsky A. G., Fossati L., 2022, *ApJ*, **927**, 238
- Salz M., Banerjee R., Mignone A., Schneider P. C., Czesla S., Schmitt J. H. M. M., 2015, *A&A*, **576**, A21
- Salz M., Schneider P. C., Czesla S., Schmitt J. H. M. M., 2016a, *A&A*, **585**, L2
- Salz M., Czesla S., Schneider P. C., Schmitt J. H. M. M., 2016b, *A&A*, **586**, A75
- Salz M., et al., 2018, *A&A*, **620**, A97
- Sanz-Forcada J., 2022, *Astronomische Nachrichten*, **343**, e20008
- Sanz-Forcada J., Dupree A. K., 2008, *A&A*, **488**, 715
- Sanz-Forcada J., Micela G., Ribas I., Pollock a. M. T., Eiroa C., Velasco A., Solano E., Garcia-Alvarez D., 2011, *Astronomy and Astrophysics*, **6**, 10
- Sanz-Forcada J., Stelzer B., Metcalfe T. S., 2013, *A&A*, **553**, L6
- Sanz-Forcada J., Stelzer B., Coffaro M., Raetz S., Alvarado-Gómez J. D., 2019, *A&A*, **631**, A45
- Sanz-Forcada J., et al., 2025, *A&A*, **693**, A285

- Schreyer E., Owen J. E., Spake J. J., Bahroloom Z., Di Giampasquale S., 2024, *MNRAS*, **527**, 5117
- Schulik M., Owen J. E., 2025, *MNRAS*, **542**, 927
- Schwabe H., 1844, *Astronomische Nachrichten*, **21**, 233
- Seager S., Sasselov D. D., 2000, *ApJ*, **537**, 916
- Shaikhislamov I. F., Khodachenko M. L., Lammer H., Berezutsky A. G., Miroschnichenko I. B., Rumenskikh M. S., 2021, *MNRAS*, **500**, 1404
- Shematovich V. I., Ionov D. E., Lammer H., 2014, *A&A*, **571**, A94
- Singh G., Pandey J. C., 2024, *ApJ*, **966**, 86
- Skumanich A., 1972, *ApJ*, **171**, 565
- Spake J. J., et al., 2018, *Nature*, **557**, 68
- Spake J. J., Oklopčić A., Hillenbrand L. A., 2021, *AJ*, **162**, 284
- Spitzer L., 1978, Physical processes in the interstellar medium, [doi:10.1002/9783527617722](https://doi.org/10.1002/9783527617722).
- Sreejith A. G., et al., 2023, *ApJ*, **954**, L23
- Storey P. J., Hummer D. G., 1995, *MNRAS*, **272**, 41
- Strüder L., et al., 2001, *A&A*, **365**, L18
- Sun Y. R., Hu S.-M., 2020, *National Science Review*, **7**, 1818
- Szabó G. M., Kiss L. L., 2011, *ApJ*, **727**, L44
- Tang Y., Fortney J. J., Murray-Clay R., 2024, *ApJ*, **976**, 221
- Taylor A. R., Koskinen T. T., Argenti L., Lewis N., Huang C., Arfaux A., Lavvas P., 2025, *The Astrophysical Journal*, 989, 68
- Toriumi S., Airapetian V. S., 2022, *ApJ*, **927**, 179
- Tu L., Johnstone C. P., Güdel M., Lammer H., 2015, *A&A*, **577**, L3
- Turner M. J. L., et al., 2001, *A&A*, **365**, L27
- Vauclair S., Laymand M., Bouchy F., Vauclair G., Hui Bon Hoa A., Charpinet S., Bazot M., 2008, *A&A*, **482**, L5
- Verner D. A., Ferland G. J., Korista K. T., Yakovlev D. G., 1996, *ApJ*, **465**, 487
- Vidal-Madjar A., Lecavelier des Etangs A., Désert J. M., Ballester G. E., Ferlet R., Hébrard G., Mayor M., 2003, *Nature*, **422**, 143
- Vidal-Madjar A., et al., 2004, *apj*, **604**, L69
- Vidotto A. A., 2021, *Living Reviews in Solar Physics*, **18**, 3
- Vidotto A. A., Cleary A., 2020, *MNRAS*, **494**, 2417
- Vidotto A. A., Jatenco-Pereira V., 2006, *ApJ*, **639**, 416
- Vidotto A. A., et al., 2014, *MNRAS*, **441**, 2361
- Vidotto A. A., et al., 2018, *MNRAS*, **481**, 5296
- Villarreal D'Angelo C., Schneiter M., Costa A., Velázquez P., Raga A., Esquivel A., 2014, *MNRAS*, **438**, 1654
- Villarreal D'Angelo C., Esquivel A., Schneiter M., Sgró M. A., 2018, *MNRAS*, **479**, 3115
- Vissapragada S., et al., 2020, *AJ*, **159**, 278
- Vissapragada S., et al., 2021, *AJ*, **162**, 222
- Vissapragada S., et al., 2022, *AJ*, **164**, 234

- Wang L., Dai F., 2021a, *ApJ*, 914, 98
- Wang L., Dai F., 2021b, *ApJ*, 914, 99
- Wargelin B. J., Saar S. H., Irving Z. A., Slavin J. D., Ratzlaff P., do Nascimento J.-D., 2024, *ApJ*, 977, 144
- Watson A. J., Donahue T. M., Walker J. C. G., 1981, *icarus*, 48, 150
- Wiese W. L., Fuhr J. R., 2009, *Journal of Physical and Chemical Reference Data*, 38, 565
- Wilson O. C., 1968, *ApJ*, 153, 221
- Wilson O. C., 1978, *ApJ*, 226, 379
- Wolfgang A., Rogers L. A., Ford E. B., 2016, *ApJ*, 825, 19
- Wood B. E., Müller H.-R., Zank G. P., Linsky J. L., 2002, *ApJ*, 574, 412
- Wood B. E., Redfield S., Linsky J. L., Müller H.-R., Zank G. P., 2005, *ApJS*, 159, 118
- Woods T. N., et al., 2005, *Journal of Geophysical Research (Space Physics)*, 110, A01312
- Woods T. N., Harder J. W., Kopp G., McCabe D., Rottman G., Ryan S., Snow M., 2021, *Solar Physics*, 296, 127
- Wytttenbach A., et al., 2020, *A&A*, 638, A87
- Xing L., Yan D., Guo J., 2023, *ApJ*, 953, 166
- Yan F., Henning T., 2018, *Nature Astronomy*, 2, 714
- Yan D., Seon K.-i., Guo J., Chen G., Li L., 2022, *ApJ*, 936, 177
- Yelle R. V., 2004, *icarus*, 170, 167
- Yeo K. L., Krivova N. A., Solanki S. K., 2014, *Space Sci. Rev.*, 186, 137
- Youngblood A., et al., 2016, *ApJ*, 824, 101
- Zhang M., Knutson H. A., Wang L., Dai F., Oklopčić A., Hu R., 2021, *AJ*, 161, 181
- Zhang M., Knutson H. A., Wang L., Dai F., Barragán O., 2022a, *AJ*, 163, 67
- Zhang M., et al., 2022b, *AJ*, 163, 68
- Zhang M., Cauley P. W., Knutson H. A., France K., Kreidberg L., Oklopčić A., Redfield S., Shkolnik E. L., 2022c, *AJ*, 164, 237
- Zhang Y., et al., 2022d, *A&A*, 666, A47
- Zhang Z., et al., 2023a, *Science Advances*, 9, eadf8736
- Zhang M., Knutson H. A., Dai F., Wang L., Ricker G. R., Schwarz R. P., Mann C., Collins K., 2023b, *AJ*, 165, 62
- Zhang M., Dai F., Bean J. L., Knutson H. A., Rescigno F., 2023c, *ApJ*, 953, L25
- Zirin H., 1975, *ApJ*, 199, L63
- Šubjak J., et al., 2022, *A&A*, 662, A107
- von Braun K., et al., 2012, *ApJ*, 753, 171

ENGLISH SUMMARY

Almost 6000 exoplanets, or planets orbiting a star other than our Sun, have been confirmed. Due to observational biases in their detection techniques, many of these exoplanets are orbiting very close to their host star. Consequently, they receive strong levels of high-energy irradiation from their host star, rendering them vulnerable to atmospheric escape. This process, driven by heating from atmospheric photoionisation, has the ability to drastically affect the planet's composition and overall evolution. In the most extreme cases, it can cause a planet to lose its atmosphere entirely. This has led to atmospheric escape becoming one of the leading theories for explaining observed phenomena such as the 'radius valley', an observed dearth of close-in 1.5-2 R_{\oplus} -sized planets. By this explanation, planets with radii placing them below the valley are believed to have lost their atmospheres while those above still have theirs.

Observationally, escaping exoplanetary atmospheres can be, and indeed have been, detected. This is achieved using a method called transmission spectroscopy, in which light from a star observed over a specific wavelength range is absorbed by the obscuring planet and its atmosphere during a planetary transit. The hydrogen Lyman- α line at 1215.67 Å, studied in Chapter 2 of this thesis, was previously the most popular feature used for performing such observations. Given the high abundance of hydrogen in exoplanetary atmospheres, this feature is capable of extremely deep transit absorptions, as was highlighted by the famous case of warm-Neptune GJ 436b. However, the Lyman- α line core is unusable to atmospheric escape studies due to absorption by the interstellar medium and contamination by Earth's geocorona. Additionally, space-based UV telescopes such as the Hubble Space Telescope are required to make such observations. These shortcomings have allowed for the more accessible He I(2^3S) triplet feature at 1083 nm in the nIR, studied in Chapters 3 to 5, to overtake Lyman- α as the most popular tracer of atmospheric escape. However, given its relatively novel application to atmospheric escape, there is room to better our understanding of the environments which produce strong He I 1083 nm detections, with the current observations so far yielding more non-detections than detections.

The projects presented in this thesis employed a theoretical approach to the study of exoplanetary atmospheric escape. We developed a 1-D, self-consistent, theoretical model to numerically solve the hydrodynamical escape of exoplanetary atmospheres. Initially our escape model assumed a hydrogen-only atmosphere and used a monochromatic flux for the received high-energy stellar radiation, as described in Chapter 2. Substantial modifications were since made for the subsequent H-He model presented in Chapter 3. These model upgrades were necessary in order to facilitate solving the atmospheric population of the observationally important He I(2^3S) state self-consistently with the hydrodynamic escape.

The first two studies of this thesis focus on the long-term evolution of atmospheric escape and the associated observable signatures. They both demonstrate that the escape of the exoplanetary atmospheres, and their associated transit signatures, are strongest during the earlier evolution of a planet's lifetime. This is the result of a planet receiving a larger flux of high-energy radiation while younger, resulting in greater atmospheric heating, as well as the more inflated planetary radius reducing the gravitational force acting on atmospheric material.

In the following study of Chapter 4, we applied our modelling approach to predict the atmospheric escape of twelve young exoplanets which already had attempted He I 1083 nm transmission spectroscopy. Our forward-model predictions of their atmospheric escape and helium signatures aligned relatively well with their observed helium transit detections and non-detections. Most notably however this study showed that, as the title indicated, while *helium escape signatures are generally strongest during younger ages* (as demonstrated earlier in Chapter 3), *this age dependence is lost in the diversity of observed exoplanets*. In other words, while the atmospheric escape and the 1083 nm observability of an individual planet is stronger during its younger years, focusing future observations on the population of younger planets is not an optimal approach. Instead, placing greater emphasis on other important parameters such as a large geometric transit would be more rewarding going forward.

In the most recent study of Chapter 5, we again studied the evolution of atmospheric escape of highly irradiated exoplanets, but instead over a much shorter timescale, that of a stellar activity cycle. Over such a cycle, the release of EUV photons, those responsible for driving atmospheric escape, varies substantially more than that of mid-UV photons which are capable of photoionising He I (2^3S). In our atmospheric escape modelling, we considered the activity cycle of two stars, the Sun for which we utilised daily spectral observations, and ι Hor for which we reconstructed spectral energy distributions at a minimum and maximum phase of its activity cycle. Our model predictions showed that a star with substantial activity cycle variations such as the Sun can enhance planetary atmospheric escape and the corresponding He I 1083 nm transit signature during a maximum activity phase. We proposed that this unaccounted for stellar influence could explain some of the conflicting He I 1083 nm observations that have been reported in the literature, with positive detections being more likely during a phase of activity maximum.

Overall, this thesis can be briefly summarised as a theoretical study into the hydrodynamic atmospheric escape of highly irradiated exoplanets, performed using 1-D, self-consistent, numerical modelling. How this atmospheric escape evolves over a planet's lifetime, how observable hydrogen and helium transit signatures are affected, and the influence a stellar activity cycle can have, are the main topics of exploration.

NEDERLANDSE SAMENVATTING

Bijna 6000 exoplaneten, ofwel planeten die rond een andere ster dan onze zon draaien, zijn bevestigd. Door observationele vooringenomenheid in onze detectietechnieken draaien veel van deze exoplaneten zeer dicht om hun moederster. Daardoor ontvangen ze grote hoeveelheden hoogenergetische straling van hun moederster, waardoor ze kwetsbaar zijn voor ontsnapping uit de atmosfeer. Dit proces, aangestuurd door verhitting door atmosferische foto-ionisatie, kan de samenstelling en algehele evolutie van de planeet drastisch beïnvloeden. In de meest extreme gevallen kan het ertoe leiden dat een planeet zijn atmosfeer volledig verliest. Dit heeft ertoe geleid dat ontsnapping uit de atmosfeer een van de belangrijkste theorieën is geworden voor het verklaren van waargenomen verschijnselen zoals de 'radiusvallei', een waargenomen tekort aan planeten dicht bij hun moederster $1.5-2 R_{\oplus}$ groot. Volgens deze verklaring wordt aangenomen dat planeten met een straal die zich onder de vallei bevindt, hun atmosfeer hebben verloren, terwijl planeten erboven die nog hebben.

Ontsnappende exoplanetaire atmosferen kunnen observationeel worden gedetecteerd, en dat is ook gebeurd. Dit wordt bereikt met behulp van een methode genaamd transmissiespectroscopie, waarbij licht van een ster, waargenomen over een specifiek golflengtebereik, wordt geabsorbeerd door de verduisterende planeet en zijn atmosfeer tijdens een planetaire transit. De waterstof Lyman- α -lijn op 1215.67 \AA , bestudeerd in Hoofdstuk 2 van dit proefschrift, was voorheen het meest populaire kenmerk dat werd gebruikt voor dergelijke observaties. Gezien de hoge abundantie van waterstof in exoplanetaire atmosferen, is dit kenmerk in staat tot extreem diepe transitabsorpties, zoals werd benadrukt door het beroemde geval van de warme Neptunus GJ 436b. De kern van de Lyman- α -lijn is echter onbruikbaar voor studies naar atmosferische ontsnapping vanwege absorptie door het interstellair medium en vervuiling door de geocorona van de aarde. Bovendien zijn UV ruimtetelescopen, zoals de Hubble-ruimtetelescoop, nodig om dergelijke observaties te doen. Deze tekortkomingen hebben ervoor gezorgd dat de meer toegankelijke He I (2^3S) tripletstructuur op 1083 nm in het nIR, bestudeerd in de Hoofdstukken 3 tot 5, Lyman- α heeft ingehaald als de meest populaire tracer voor atmosferische ontsnapping. Gezien de relatief nieuwe toepassing ervan voor atmosferische ontsnapping, is er echter ruimte om ons begrip van de omgevingen die sterke He I 1083 nm detecties opleveren te verbeteren. De huidige waarnemingen hebben tot nu toe meer niet-detecties dan detecties opgeleverd.

De projecten die in dit proefschrift worden gepresenteerd, maakten gebruik van een theoretische benadering van de studie van atmosferische ontsnapping uit exoplaneten. We ontwikkelden een 1-D, zelfconsistent, theore-

tisch model om de hydrodynamische ontsnapping uit exoplanetaire atmosferen numeriek te berekenen. Aanvankelijk ging ons ontsnappingsmodel uit van een atmosfeer die uitsluitend uit waterstof bestond en gebruikte het een monochromatische flux voor de ontvangen hoogenergetische stellaire straling, zoals beschreven in Hoofdstuk 2. Sindsdien zijn er substantiële wijzigingen aangebracht in het daaropvolgende H-He-model, gepresenteerd in Hoofdstuk 3. Deze modelupgrades waren nodig om de atmosferische populatie van de observationeel belangrijke He I(2^3S)-toestand zelfconsistent met de hydrodynamische ontsnapping te kunnen bepalen.

De eerste twee studies van dit proefschrift richten zich op de langetermijnevolutie van atmosferische ontsnapping en de bijbehorende waarneembare signaturen. Ze tonen beide aan dat de ontsnapping uit de exoplanetaire atmosferen, en de bijbehorende transitsignaturen, het sterkst zijn tijdens de eerste evolutiefase van de levensduur van een planeet. Dit is het gevolg van het feit dat een planeet op jongere leeftijd een grotere flux van hoogenergetische straling ontvangt, wat resulteert in zowel een grotere opwarming van de atmosfeer, als een grotere planetaire straal die de zwaartekracht op atmosferisch materiaal vermindert.

In de opeenvolgende studie in Hoofdstuk 4 hebben we onze modelleringsaanpak toegepast om de atmosferische ontsnapping te voorspellen van twaalf jonge exoplaneten waarop al He I 1083 nm transmissiespectroscopie was geprobeerd. Onze voorwaartse modelvoorspellingen van hun atmosferische ontsnapping en heliumsignaturen kwamen relatief goed overeen met hun waargenomen heliumtransitdetecties en niet-detecties. Het meest opvallende aan deze studie is echter dat, zoals de titel al aangaf, *heliumontsnappingssignaturen over het algemeen het sterkst zijn tijdens jongere leeftijden* (zoals eerder aangetoond in Hoofdstuk 3), *althoewel deze leeftijdsafhankelijkheid verloren gaat in de diversiteit van waargenomen exoplaneten*. Met andere woorden, hoewel de atmosferische ontsnapping en de waarneembaarheid van een individuele planeet op 1083 nm sterker zijn tijdens de jongere jaren, is het niet optimaal om toekomstige observaties te richten op de populatie van jongere planeten. In plaats daarvan moet er meer nadruk worden gelegd op andere belangrijke parameters, zoals een grote geometrische transit.

In de meest recente studie van Hoofdstuk 5 bestudeerden we opnieuw de evolutie van atmosferische ontsnapping van sterk bestraalde exoplaneten, maar dan over een veel kortere tijdschaal, die van een stellaire activiteitscyclus. Gedurende zo'n cyclus varieert de uitstoot van EUV-fotonen, die verantwoordelijk zijn voor atmosferische ontsnapping, aanzienlijk meer dan die van mid-UV-fotonen die in staat zijn om He I (2^3S) te foto-ioniseren. In onze modellering van atmosferische ontsnapping hebben we rekening gehouden met de activiteitscyclus van twee sterren: de zon, waarvoor we dagelijkse spectrale waarnemingen gebruikten, en ι Hor, waarvoor we spectrale energieverdelingen reconstrueerden tijdens een minimale en maximale fase van

zijn activiteitscyclus. Onze modelvoorspellingen lieten zien dat een ster met aanzienlijke variaties in de activiteitscyclus, zoals de zon, planetaire atmosferische ontsnapping en de bijbehorende transitsignatuur van He I 1083 nm tijdens een maximale activiteitsfase kan versterken. Wij opperden dat deze onverklaarde stellaire invloed een verklaring zou kunnen zijn voor een aantal van de tegenstrijdige He I 1083 nm-waarnemingen die in de literatuur zijn gerapporteerd, waarbij positieve detecties waarschijnlijker zijn tijdens een fase van maximale activiteit.

Over het geheel genomen kan dit proefschrift kort worden samengevat als een theoretische studie naar de hydrodynamische atmosferische ontsnapping van sterk bestraalde exoplaneten, uitgevoerd met behulp van 1D, zelfconsistente, numerieke modellering. De belangrijkste onderwerpen van onderzoek zijn hoe deze atmosferische ontsnapping zich ontwikkelt gedurende de levensduur van een planeet, hoe waarneembare waterstof- en heliumtransitsignaturen worden beïnvloed en welke invloed een stellaire activiteitscyclus kan hebben.

PUBLICATIONS

First-author publications

- Evolution of atmospheric escape in close-in giant planets and their associated Ly- α and H- α transit predictions
A. P. Allan, A. A. Vidotto
Monthly Notices of the Royal Astronomical Society
Volume 490, Issue 3, December 2019, Pages 3760–3771
- Evolution of helium triplet transits of close-in gas giants orbiting K-dwarfs
A. P. Allan, A. A. Vidotto, C. Villarreal D’Angelo, L. A. Dos Santos, F. A. Driessen
Monthly Notices of the Royal Astronomical Society
Volume 527, Issue 3, January 2024, Pages 4657–4676
- Helium escape signatures are generally strongest during younger ages but this age dependence is lost in the diversity of observed exoplanets
A. P. Allan, A. A. Vidotto
Monthly Notices of the Royal Astronomical Society
Volume 539, Issue 3, May 2025, Pages 2144–2157

Publications in press

- The effects of stellar activity cycles on planetary atmospheric escape and the He I 1083 nm transit signature
A. P. Allan, A. A. Vidotto, J. Sanz-Forcada, C. Villarreal D’Angelo
Accepted in *Monthly Notices of the Royal Astronomical Society*.

Contributing author publications

- Characterizing a world within the hot-Neptune desert: Transit observations of LTT 9779 b with the Hubble Space Telescope/WFC3
B. Edwards, Q. Changeat, A. Tsiaras, **A. P. Allan** and 26 others
The Astronomical Journal
Volume 166, Issue 4, October 2023, Page 158
- Non-detections of Helium in the Young sub-jovian planets K2-100b, HD 63433b, and V1298 Tau c
M. K. Alam, J. Kirk, L. A. Dos Santos, P. McCreery, **A. P. Allan**, J. E. Owen, A. A. Vidotto, R. Allart, V. Bourrier, N. Espinoza
The Astronomical Journal
Volume 168, Issue 3, September 2024, Page 102
- Magnetic field evolution of hot exoplanets
K. Kilmetsis, A. A. Vidotto, **A. P. Allan**, D. Kubyshkina
Monthly Notices of the Royal Astronomical Society
Volume 535, Issue 4, December 2024, Pages 3646–3655

CURRICULUM VITAE

While I was born in Alloa, Scotland in 1997, I grew up in Westmeath, in the Midlands of Ireland. I enjoyed my time in school, attending the local CBS in Mullingar. In the later years, my classes in physics (Mr. Coyle) and applied mathematics (Mr. Corroon) particularly interested me.

After finishing my schooling in 2015, I decided to apply my growing interest in science to a Bachelors in General Science at Trinity College Dublin (TCD), selecting the subjects of mathematics, physics and chemistry. In the third year, I opted to specialise in physics and astrophysics. During the fourth and final year, I had the good fortune of working under the supervision of Aline Vidotto for my research project. This was my first immersion in to the field of modelling the escaping atmospheres of exoplanets. I graduated from TCD in 2019 with a first class honours for my Bachelors in Physics and Astrophysics and was also awarded a Trinity gold medal. In order to grow the foundations of our earlier research into a scientific paper, I worked at TCD as a research assistant over the summer that followed. Having decided that I wanted to stay on the path of astrophysical research, I then joined Jose Groh's Massive Stars and Supernovae research group at TCD. This proved to be an excellent experience and I thoroughly enjoyed the research I was doing which involved modelling spectral features in the outflows of massive stars and supernovae rather than exoplanetary atmospheres. This concluded in 2021 when I graduated from TCD with a Masters in Science in the School of Physics.

I then moved to the Netherlands, beginning my PhD at Leiden University under the supervision of Aline Vidotto in the September. I was excited to experience living outside of Ireland and to pick up from where my previous research with Aline had left off. We set out with a plan of incorporating the 1083 nm helium triplet transit signature and tracer of atmospheric escape into our model. Giving its ability to be observed using ground-based telescopes, this helium feature was fast detecting atmospheric escape in highly irradiated exoplanets. Over the course of my PhD I was incredibly fortunate to attend many engaging conferences both within the Netherlands and beyond. Personal highlights include the International Astronomical Union General Assembly in Busan, Republic of Korea, Exo-atmospheres at Les Houches, France, both in 2022, and the 4th Advanced School on Exoplanetary Science in Vietri sul Mare, Italy in 2023.

After receiving my doctorate, I plan on utilising many of the skills my PhD experience has given me, which I can only hope will lead to a career as enjoyable and fulfilling as that of an astrophysics PhD researcher.

ACKNOWLEDGEMENTS

I would like to first sincerely thank my supervisor Aline Vidotto for always been patient, generous and kind in your guidance and support. Your enthusiasm towards research is infectious and made our meetings something I always looked forward to. Thanks also to the many members of Aline's research group that I have been fortunate enough to work alongside. Thanks for helping me to see my research from other perspectives, and for all the helpful advice and stimulating conversations, both astrophysical in nature and otherwise. Similar thanks go to my many collaborators as well as those who made the Leiden exoplanet community so welcoming. Thanks to my Mullingar friends for consistently encouraging me through the PhD. Your visits here and my visits back have meant a lot. Thanks also to the many friends I made over my time in Dublin. You each made those times something I look back on very fondly. To the friends I made in Leiden, thank you all for the memories of the Kaiser Lounge, Borrels, parties and trips away, and for the countless games of falafel played. Rob, Amanda and Gopal, moving to the Netherlands was made less intimidating and more exciting by sharing that unforgettable experience with you. Ciarán, Sill, Joey, Martje, Thijs, Elia, Karin and Casper, trying to keep up with you all on cycles and runs was somehow always very enjoyable. Alessia, Silvia and Josh, you made everything more fun and memorable. To my friends from Cosmos United and Den Haag GAA, playing alongside you all has been amazing. Cian and Niamh, your move over was a very nice addition to my Leiden experience. Alfred, Andres, Javier, Mira, Nina and Zorry, our fun plans together could always take my mind away from my work when needed. A special thanks to my two paranympths Osmar and Kevin. You have both been terrible darts players over the years but have been great friends. Mam, Dad, Clodagh and my extended family, thank you for the continuous support, for celebrating each milestone with me and for the many calls and visits. Finally, thank you Nerea for been there for me throughout. You have been a great support, particularly in the busier phases. Getting to know the Netherlands with you mainly through the form of searching for the best gluten-free restaurants has been an absolute joy.

